

Glacial-interglacial perturbations in the global carbon cycle

Andy J. Ridgwell

submitted for the degree of Doctor of Philosophy
on this day, 1st February, 2001

© This copy of the dissertation has been supplied on condition that anyone who consults it is understood to recognize that its copyright rests with the author and that no quotation from the dissertation, nor any information derived therefrom, may be published without the author's prior, written consent.

with thanks to ...

Andy Watson
(for supervising)

David Archer, Olivier Marchal, Natalie Mahowald, Michel Crucifix
(for providing data sets, model code, and other such goodies)

Maureen Raymo
(for fruitful discussions regarding the Big Picture)

Natural Environmental Research Council
(for stumping up the readies)

*Muppet, Shelly, Jo, Connor, Kirsten, Mark, Anna, Rosa, Millie, Laura, Andi, Joysey, Josh,
Ed, Emma, Andy, Liz, Dave, Bethan, Dougal, Dom, Sophie, Bernard, Quentin*
(for providing welcome distractions primarily of a liquid nature, without which ...
... I might have finished much earlier)

three Compaq Alpha DC20 workstations
(for carrying out double precision floating point operations very quickly indeed)

the players and management of Norwich City FC
(for putting on a weekly display of such unrivalled hopelessness
that any severity of modelling setback was placed into true perspective)

Banham Rum Cask
(7.4% by volume)

and

Jo
(for all sorts of things)

***To retain respect for either models or sausages,
one must not watch too carefully what goes into them***

Adapted from a remark attributed to Otto Von Bismarck,
1st chancellor of the German Empire, 1871-1890.

Abstract. A flexible representation of the global carbon cycle is developed for use on multi-millennial time-scales, based upon the cycling within the ocean of carbon and alkalinity, together with the essential nutrients; phosphate, silicic acid, and iron. The diagenetic alteration of calcium carbonate (CaCO_3) and opal in deep-sea sediments is explicitly considered, with primary biogeochemical interactions between oceanic and sedimentary reservoirs accounted for. Material preserved in the sediments is allowed to accumulate to form synthetic sediment records. This enables a wide variety of paleoceanographic observations to be directly employed in helping to constrain the processes driving the evolution of the carbon cycle over the course of the late Quaternary.

A test harness for use in the investigation of the observed glacial-interglacial variability in the concentration of atmospheric carbon dioxide ($x\text{CO}_2$) is constructed by marrying the biogeochemical framework developed here with a zonally-averaged representation of ocean circulation. Potential mechanisms are evaluated on a dynamic (i.e., time-stepping) basis by reconstructing variability in the relevant model boundary conditions over the past 400,000 years. Model results suggest that a key role is played in initial deglacial $x\text{CO}_2$ rise by declining aeolian iron supply to the Southern Ocean. With sea ice limits also varied in this region, it is also possible to account for the glacial-interglacial variability in much of the paleoceanographic record either side of the Antarctic Polar Front. However, none of the mechanisms considered here, even operating in concert, are able to reproduce the full magnitude of observed deglacial $x\text{CO}_2$ rise whilst simultaneously meeting constraints dictated by the sedimentary CaCO_3 record. It is, therefore, likely that any combination of changes in; equatorial up-welling, high latitude surface ocean stratification, and the oceanic nitrogen cycle, play an additional and important role.

Contents

Introduction	1
<i>SUE: An ocean biogeochemical framework</i>	7
2.1 Introduction	7
2.2 Model description	8
2.2.1 Framework overview	8
2.2.1.1 Ocean configuration and circulation	8
2.2.1.2 Overall biogeochemical cycling scheme	8
2.2.1.3 Carbonate system thermodynamics	10
2.2.1.4 Numerical scheme	10
2.2.2 Ocean-atmosphere gas exchange	10
2.2.2.1 Ocean-atmosphere CO ₂ exchange	10
2.2.2.2 Ocean-atmosphere O ₂ exchange	11
2.2.3 Biological new production	11
2.2.3.1 Phosphate uptake model	12
2.2.3.2 Nutrient half-saturation constants	13
2.2.3.3 'Redfield' and derived chemical export ratios	13
2.2.4 Remineralization within the water column	16
2.2.4.1 Particulate organic matter	16
2.2.4.2 Calcite	17
2.2.4.3 Aragonite	18
2.2.4.4 Opal	19
2.2.5 Iron biogeochemical cycling	22
2.2.6 Carbon-13	24
2.2.6.1 Fractionation within the aqueous carbonate system	24
2.2.6.2 Fractionation during ocean-atmosphere gas exchange	24
2.2.6.3 Fractionation during biological fixation of organic carbon	25
2.2.6.4 Fractionation during the formation of calcium carbonate	26
<i>The simulation of deep-sea sediments</i>	27
3.1 Introduction	27
3.2 Modelling deep-sea sediments	28
3.2.1 Bioturbation	29
3.2.1.1 Bioturbation model description	29
3.2.1.2 Inert tracer profile simulation	30
3.2.1.3 ¹⁴ C age profile simulation	30
3.2.1.4 Scheme choice	33
3.2.2 Porosity	33
3.2.3 Numerical implementation of diagenesis	34
3.2.4 Sedimentary diagenesis of CaCO ₃	35
3.2.4.1 Look-up table implementation	35
3.2.4.2 The location of CaCO ₃ dissolution	35
3.2.5 Sedimentary diagenesis of biogenic opal	36
3.2.5.1 A model for sedimentary opal diagenesis	36
3.2.5.2 Look-up table implementation	39
3.2.5.3 Model validation	40
3.3 Synthetic deep-sea sediment cores	43
3.3.1 Synthetic sediment core construction	43
3.3.2 The application of synthetic sediment cores to paleoclimatic analysis	44

3.3.2.1	<i>Sediment distribution analysis</i>	44
3.3.2.2	<i>Single core analysis</i>	45
3.3.2.3	<i>CaCO₃ lysocline transition zone</i>	46
<i>Modelling the pre-industrial state</i>		49
4.1	<i>Introduction</i>	49
4.2	<i>Ocean structure and circulation</i>	50
4.2.1	<i>Derivation of basic ocean structure</i>	51
4.2.2	<i>Physical boundary conditions</i>	52
4.2.3	<i>Derivation of basic ocean circulation</i>	53
4.2.3.1	<i>Convective processes</i>	53
4.2.3.2	<i>Eddy diffusivity</i>	54
4.2.4	<i>The addition of deep-sea sediments</i>	54
4.3	<i>Biogeochemical configuration</i>	54
4.3.1	<i>Geochemical boundary conditions</i>	54
4.3.1.1	<i>Dissolved chemical input to the ocean</i>	55
4.3.1.2	<i>The delivery of aeolian material to the ocean</i>	55
4.3.1.3	<i>Neritic sediment accumulation</i>	55
4.3.2	<i>Biological productivity</i>	56
4.3.3	<i>Fe biogeochemical cycling</i>	56
4.3.4	<i>“Nutrient trapping”</i>	56
4.4	<i>The ‘present-day’ in SUE1608</i>	57
4.4.1	<i>Ocean tracer fields</i>	60
4.4.1.1	<i>Temperature and salinity</i>	60
4.4.1.2	<i>Phosphate</i>	60
4.4.1.3	<i>Silicic acid</i>	60
4.4.1.4	<i>Dissolved oxygen</i>	61
4.4.1.5	<i>Total dissolved iron</i>	61
4.4.1.6	<i>δ¹³C^{DIC}</i>	62
4.4.2	<i>The biological pump</i>	62
4.4.3	<i>Sediment composition</i>	65
4.5	<i>An improved representation of the Southern Ocean and global Si cycling</i>	66
4.5.1	<i>Sedimentary opal distributions</i>	66
4.5.2	<i>Re-evaluation of the opal diagenesis module</i>	66
4.6	<i>Summary</i>	70
<i>Perturbations to the system</i>		71
5.1	<i>Introduction</i>	71
5.2	<i>Evidence for glacial-interglacial variability of the global carbon cycle</i>	72
5.3	<i>Uncertainties in model response to perturbations of the carbon cycle</i>	73
5.3.1	<i>The ‘Harvardton Bear Equilibrium Index’</i>	73
5.3.2	<i>The ‘Archer Abiotic xCO₂’ test</i>	75
5.3.3	<i>Implications for this present study</i>	75
5.4	<i>Model evaluation of mechanisms for glacial-interglacial xCO₂ variability</i>	75
5.4.1	<i>Sea level</i>	76
5.4.2	<i>Ocean surface temperatures</i>	78
5.4.3	<i>Wind speed driven air-sea gas transfer</i>	80
5.4.4	<i>Sea ice extent</i>	82
5.4.5	<i>Ocean circulation</i>	84
5.4.6	<i>Terrestrial carbon storage</i>	84
5.4.7	<i>Neritic sediment storage</i>	86
5.4.7.1	<i>The ‘Coral Reef Hypothesis’</i>	88
5.4.7.2	<i>Introducing the ‘Opal Extraction Model’</i>	90
5.4.8	<i>Dissolved silica supply to the ocean</i>	90
5.4.8.1	<i>Aeolian flux</i>	90
5.4.8.2	<i>Riverine fluxes</i>	90
5.4.8.3	<i>Oceanic Si cycling and the ‘Silica Hypothesis’</i>	92
5.4.9	<i>The ‘Iron Hypothesis’</i>	93

5.4.10	<i>The nitrogen hypothesis</i>	95
5.5	<i>The role of the Southern Ocean</i>	97
5.5.1	<i>Glacial-interglacial variability in dust deposition</i>	97
5.5.2	<i>The role of changes in seasonal sea ice extent</i>	100
5.6	<i>Towards the complete picture</i>	103
5.7	<i>The sequence of events surrounding Termination I</i>	107
5.8	<i>What ultimately drives the deglacial rise in atmospheric CO₂?</i>	108
	Conclusions	111
	References	113
Appendix I	: Carbonate system thermodynamics	125
Appendix II	: Insolation	129
Appendix III	: Opal diagenesis core data	131
Appendix IV	: Model parameter values (baseline scenario)	133
Appendix V	: Model source code, plus example parameter & results files	CD-ROM

Introduction

There is abundant geological evidence on the Earth's surface, particularly in characteristic landforms and drift sediments, that in the relatively recent geologic past global climate was very much colder than at present, with extensive ice sheets covering much of higher northern hemisphere latitudes [Imbrie and Imbrie, 1979]. In fact, such evidence points to there having been more than one cold episode, each punctuated by periods of relatively warm climatic conditions. Once this interpretation had become generally accepted during the 19th century, the search started for an explanation as to why these events should have occurred at all. On the basis that periods of low solar insolation would result in a cooling of the planet (thus allowing ice sheets to grow) variations in the amount of sunlight received was the obvious starting point. Initial explanatory theories included sun spot cycles, the existence of dust clouds in space through which the Earth might pass (therefore attenuating solar radiation) and in a similar vein, major sub-aerial volcanic eruptions. However, none of these could be reasonably tested at that time and had little supporting evidence. It was not until the French mathematician Joseph Adhémar, noting that the Earth's orbit is elliptical rather than spherical that the first true astronomical theory was born. Adhémar proposed that the precession of the equinoxes would produce antagonistic variations in insolation received by the two hemispheres during winter with ice ages occurring alternately in each, a full cycle taking 22 thousand years (ka) to complete.

Later that same century, a Scotsman, James Croll, realized that Adhémar had overlooked the fact that the shape of the Earth's orbit (eccentricity) varied over time, a detail which could potentially hold the key. Croll calculated orbital eccentricity for the past 3 Ma and determined a cyclicity of approximately 100 ka. The occurrence of ice ages was still linked to the precession of the equinoxes as postulated by Adhémar, but now the envelope of eccentricity modified the precessional cycle, such that when eccentricity was close to zero no ice age would occur in either hemisphere. However, since variations in eccentricity produced only very minor changes in the annual radiation budget of the Earth Croll considered that this was not sufficient to drive the ice ages, and therefore invoked positive feedbacks in the climate system through changes in surface albedo. Although widely welcomed at the time, this theory gradually fell out of acceptance as circumstantial geological evidence started to accumulate, with indications that the last ice age might have ended as recently as ~10 ka BP (Before Present), rather than the ~70 ka BP predicted by Croll.

No further progress was made with astronomical descriptions of the ice ages until during the first half of the 20th century when Milutin Milankovitch, a Serbian

mathematician, constructed a theoretical framework for describing the distribution of insolation over the Earth's surface as a function of three orbital properties (precession, obliquity, and eccentricity). Not only did Milankovitch apply this to the present-day but was also able to make calculations for any point in time during the past 650 ka. Noting that summertime melting appeared to be the key season in controlling the growth of modern glaciers, he suggested that it was insolation levels during this half of the year that was critical to the control of ice ages rather than the winter months as had previously been assumed. This received strong support through the remarkable match made between summer insolation calculated at 65°N and variability in the reconstructed terminal limits of Alpine glaciers.

It was not until the late '60s and early '70s with the advent of sufficiently-sensitive analytical techniques for determining isotopic composition that Milankovitch's astronomical theory of the ice ages would be confirmed. Sediment cores recovered from the deep sea had already confirmed earlier geological evidence based upon glacial till sequences. Measurements of the abundance ratio of the stable isotopes ^{18}O and ^{16}O ($\delta^{18}\text{O}$) contained within foraminiferal calcite now revealed the occurrence of as many as 7 major ice age cycles (Figure 1). Location of the Brunhes-Matuyama magnetic reversal (then dated to around 730 ka BP) in particularly long sediment sequences allowed the period of the cycles to be estimated at around 100 ka, matching that of orbital eccentricity. Further support for the theory came with the realization that variations in $\delta^{18}\text{O}$, (particularly in benthic foraminifera) must reflect changes in global ice volume. Finally, spectral analysis of this ice volume proxy verified the presence of primary periods of variability occurring at 100 ka and 41 ka, corresponding to the orbital components of eccentricity and obliquity. Furthermore, the presence of not one but two precessional peaks (23 ka and 19 ka) was revealed by the sediment core data, an orbital feature not previously predicted by calculations.

From the very outset, the most problematic aspect of Milankovitch's astronomical theory of ice ages has been that eccentricity, which appears to match the frequency of the glacial-interglacial cycles, is far weaker than either precessional or obliquity orbital components in terms of the spectral power of insolation variability. Indeed, variations in eccentricity alter annual radiation received by the Earth by less than 0.1% [Imbrie *et al.*, 1993]. With the use of computers as a standard scientific tool in the mid 1970s, possible climatic mechanisms that could produce such a non-linear response began to be investigated with complex numerical models. The first such model calculated increases in global ice volume simply in proportion to an insolation (50°N summer) deficit [Calder, 1974]. Non-linearities in ice

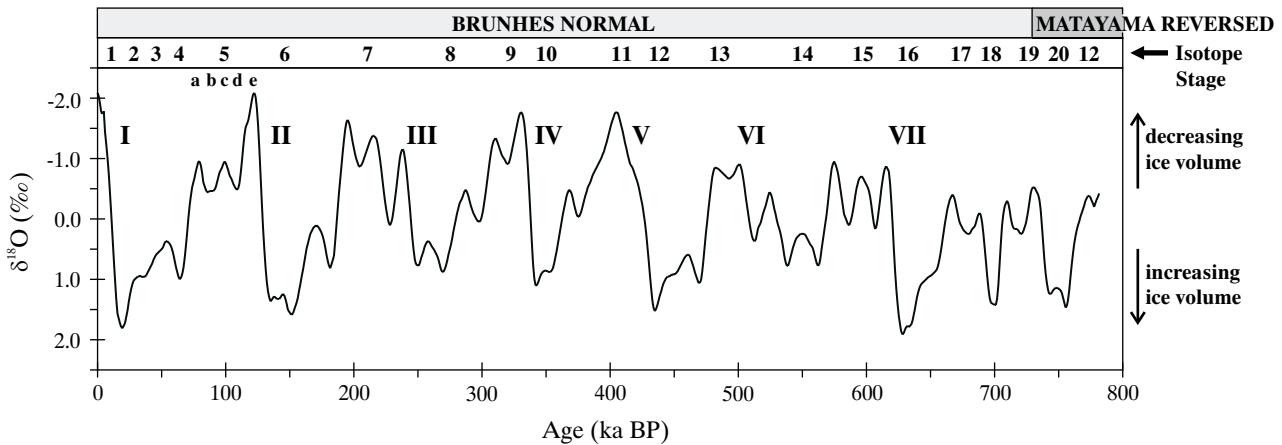


Figure 1-1 The SPECMAP stacked marine $\delta^{18}\text{O}$ record [Imbrie *et al.*, 1984], where increasing $\delta^{18}\text{O}$ values approximately scale with increasing global ice volume. Labeled are the Marine Isotope Stages after Shackleton and Opdyke [1973] (with Stage 5 sub-divided 'a' through 'e') together with the location of the Brunhes-Matuyama magnetic reversal, taken at 730 ka BP [Imbrie *et al.*, 1984]. Also marked are the last 7 major glacial terminations, labelled "I" through "VII".

sheet response were represented by taking a different proportionality for melt-back than for growth. Remarkably, this model produces a distinct 100 ka cycle in spite of the relatively low power at the corresponding period inherent in the forcing. A similar formulation, but with non-linearities in ice sheet response now represented explicitly was presented by Imbrie and Imbrie [1980], proving a fruitful basis for further development [Pisias and Shackleton, 1984; Sniieder, 1985]. This model improved upon the overall sawtooth shape of the glacial-interglacial cycles of that produced by Calder [1974]. Other simple methods were also found of accounting for much of the variance contained within the marine $\delta^{18}\text{O}$ record directly from insolation, including multivariate regression [Berger *et al.*, 1981] and astronomical climate index [Kukla *et al.*, 1981] models, and through consideration of albedo-radiation feedbacks [Wigley, 1976].

One direction of development taken from these initial studies was in what were often highly abstracted models of the Earth system. In these, 100 ka cycles were variously obtained through stochastic resonance [Matteucci, 1989], the selective frequency amplification of an internal oscillation [Le Trent and Ghil, 1983; Van der Shuijs *et al.*, 1996], as a free-running oscillation driven by an inherent climatic instability [Saltzman, 1987, 1990; Saltzman and Maasch, 1988, 1990, 1991; Saltzman and Sutera, 1984, 1987; Saltzman and Verbitsky, 1992, 1993, 1994a,b; Saltzman *et al.*, 1993], or through the existence of multiple thresholds prescribed within the system [Paillard, 1998]. Insolation forcing was still important in all of these, although in some cases its role in the glacial-interglacial cycles was reduced to little more than phase-locking of internal oscillations.

An alternative approach brought to bear on the glacial-interglacial cycle question was to represent key processes within the climate system in an explicit and

mechanistic fashion. The element suspected to play the predominant role was that of the cryosphere [Calder, 1974] (including its interaction with other components of the climate system). On this basis, Weertman [1976] modelled the (northern hemisphere) cryosphere as a simple equilibrium ice sheet atop a plastic crust. Although significant changes in ice volume were found when this model system was forced with variable (summer 50°N) insolation, no clear 100 ka cycle was produced. Models comprising just atmospheric, ocean, or coupled ocean-atmosphere components similarly failed [Brickbat *et al.*, 1999; Short *et al.*, 1991; Suarez and Held, 1976], as did coupling an atmospheric component to the ice sheet [Pollard, 1978]. However, the introduction of a realistic time scale for isostatic bedrock adjustment, either explicitly or mechanistically through representation of mantle elasticity or viscoelasticity allowed an ice volume signal with a clear ~ 100 ka period to be obtained [Birchfield *et al.*, 1981; Deblonde and Peltier, 1991; Pollard, 1982; Oerlemans, 1980, 1982]. Having achieved this, the next area of deficiency in predicted ice volume (compared to the marine $\delta^{18}\text{O}$ record) concerned the glacial terminations, which tended to be rather sluggish and with incomplete deglaciation occurring. Additional mass wasting parameterizations were therefore introduced to correct for this such as that of ice calving [Clark and Pollard, 1998; Deblonde and Peltier, 1990, 1991, 1993; Hughes, 1992; Oerlemans, 1991; Pollard, 1983]. In contrast, simulating glacial inception was much less problematic, with adequate representation of continental topology often sufficient to allow the initiation of ice sheets during periods of low summer insolation [Birchfield *et al.*, 1982; Deblond and Peltier, 1990, 1991, 1993; Ledley and Chu, 1995; Tarasov and Peltier, 1997]. Recent studies have also highlighted the potential importance of vegetation-albedo feedbacks in this process [de Noblet *et al.*, 1996; Gallimore

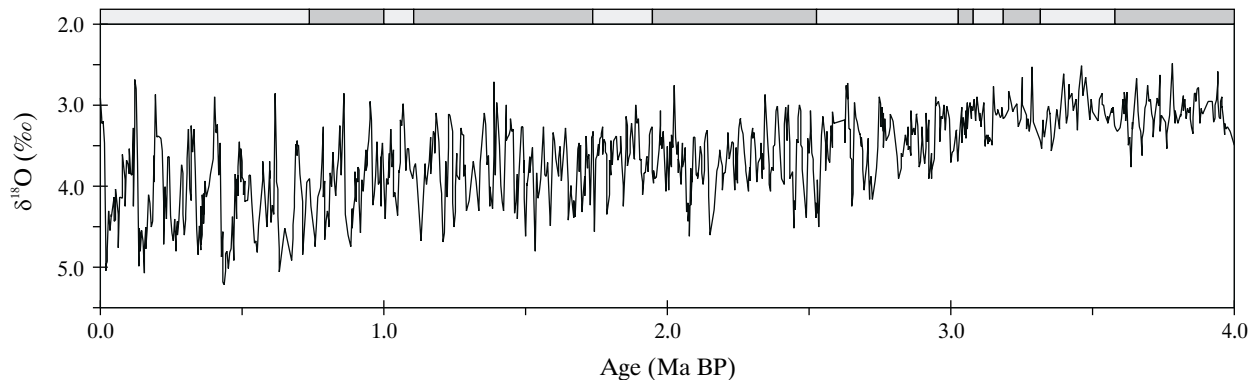


Figure 1-2 The benthic $\delta^{18}\text{O}$ record of Ocean Drilling Program site 659 [Tiedemann *et al.*, 1994]. Shown at top are the approximate occurrences of the different magnetic polarity epochs over the length of this record.

and Kutzbach, 1996]. Building upon the promising response obtained by interactions between ice sheets and the underlying bedrock models have gradually attained increasing complexity as additional climate components (such as full atmospheric energy balance models and representations of ocean heat transport and storage) have been added. In particular, considerable advances have been made in our understanding of glacial-interglacial climate dynamics through the development of models of ‘intermediate complexity’ such as those of Deblonde, Peltier and co-workers [Deblonde and Peltier, 1990, 1991, 1992, 1993; Peltier and Marshall, 1995; Tarasov and Peltier, 1997] and the LLN model of André Berger and co-workers [Berger and Loutre, 1997a,b; Berger *et al.*, 1990, 1993, 1998, 1999; Li *et al.*, 1998a,b; Loutre and Berger, 2000]. However, even relatively advanced models such as these fall noticeably short of being able to fully account for the 100 ka glacial-interglacial cycles. Clearly there must be some important climatic factor still missing.

The climatic fluctuations of the last ~ 800 ka are only a part of a longer-term evolution in the dynamics of the Earth’s climate, which has seen substantial change over the course of much of the late Cenozoic [Driscoll and Haug, 1998; Raymo and Ruddiman, 1992; Ruddiman and Raymo, 1988]. Figure 1-2 shows part of a marine $\delta^{18}\text{O}$ record covering the last 5 Ma [Tiedemann *et al.*, 1994]. Again taking (benthic) $\delta^{18}\text{O}$ primarily as a proxy for global volume it can be seen that up until about ~ 3.1 Ma BP, climate appeared relatively stable, with little variability in global ice volume (probably similar to that of the present interglacial). After this point there was a clear downward trend, with the amplitude of fluctuations steadily increasing. This continued to around 2.5 Ma BP when the first major northern hemisphere glacial event occurred [Shackleton *et al.*, 1984]. A relatively extended period ensued thereafter, with ice ages reoccurring with a period of about 41 ka and with maximum ice volume perhaps half that of the more recent 100 ka cycles [Clark and Pollard, 1998]. Finally, somewhere during the interval 1.5 to 0.7 Ma

BP there was a transition to the establishment of 100 ka glacial-interglacial cycles. In an attempt to characterize the nature of this final transition a wide variety of spectral and statistical techniques have been brought to bear. These have ranged from relatively simple spectral [Mudelsee and Schulz, 1997; Pisias and Moore, 1981] and bispectral methods [Hagelberg *et al.*, 1991; Rutherford and D’Hondt, 2000], through multitaper-based techniques [Birchfield and Ghil, 1993; Mann and Lees, 1996; Park and Maasch, 1993; Saltzman and Verbitsky, 1992], to probability density functions [Maasch, 1988; Matteucci, 1990; Mudelsee and Statterger, 1997] and more recently, wavelet analysis [Bolton *et al.*, 1995; Lau and Weng, 1995]. However, these techniques have often been at odds with each other regarding the details of the rate of change and timing of the mid point of the transition. Statistical methods also generally fail to illuminate the underlying physical processes responsible for the change in the dynamics of the climate system at this time, although there have been suggestions that a key role was played by the tropics [Rutherford and D’Hondt, 2000].

Various explanations have been offered to account for aspects of the inferred evolution of the Earth’s climate system over the late Cenozoic. For the initial onset of ice age cycles around 2.5 Ma BP, favourite among these has been tectonic changes, particularly the emergence of the Isthmus of Panama with possible associated disruption of ocean circulation patterns [Hay, 1996], and the deepening of the Fram and Denmark Straits [Hay, 1993, 1996]. However, the timing of these events place them too early to have had a direct effect, with the results of ocean and atmospheric circulation models often not supporting a significant role [Hay, 1996; Maslin *et al.*, 1998; Raymo and Ruddiman, 1992]. Uplift of the Tibetan plateau may also have had an influence in producing climatic conditions conducive to the growth of ice sheets through its distorting influence on atmospheric circulation in the northern hemisphere [Raymo and Ruddiman, 1992; Ruddiman and Raymo, 1992]. For the transition from 41 to 100 ka periodicity, a gradual

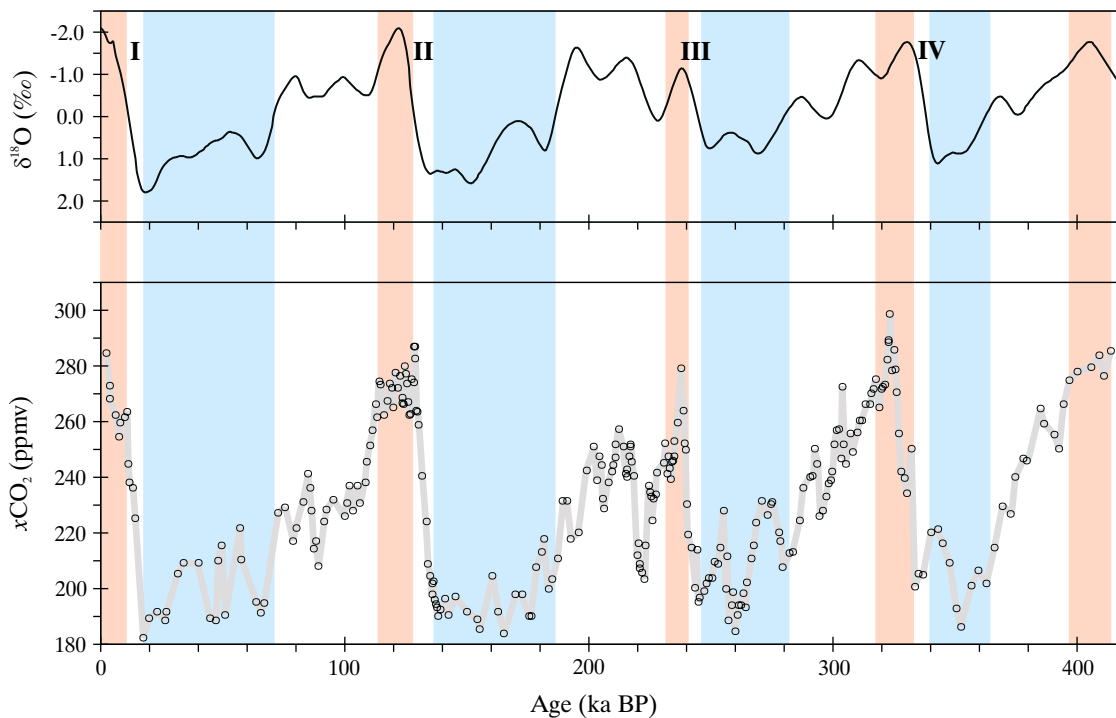


Figure 1-3 Approximate correspondence between glacial-interglacial variations in the concentration of atmospheric CO_2 [Petit et al., 1999] and changes in ice volume (as indicated by the SPECMAP $\delta^{18}\text{O}$ record [Imbrie et al., 1984]). Interglacials are highlighted in red with deep glacial periods in blue.

transformation of continental regolith has been proposed, with the formation of ice sheets characterized by much greater height and volume only enabled by the eventual erosion of the underlying sediment substrate down to the bedrock [Clark and Pollard, 1998; Clark et al., 1999]. However, such explanations tend to be difficult to critically assess and are not entirely convincing as sole agents. Once again, one must suspect that an additional key component of the climate system has not yet been accounted for.

Past records of atmospheric composition, in the form of microscopic bubbles trapped within the crystalline structure of ice buried in the ice caps of both hemispheres, has sparked a revolution in thinking regarding the long-term dynamics of the climate system. Ice cores recovered from Greenland and Antarctica during the early 1980s and analysed for air bubble CO_2 content showed that atmospheric CO_2 levels at the time of last glacial were some $\sim 30\%$ lower than during the late Holocene [Nefel et al., 1988; Oeschger et al., 1984]. Cores were soon extracted from much greater depths, extending the record first back beyond the last interglacial period (the Eemian) [Barnola et al., 1987; Jouzel et al., 1993; Lorius et al., 1990] and then finally, four complete glacial-interglacial cycles were revealed by the Vostok core [Petit et al., 1999]. Results demonstrated that the pattern was regularly repeated, with relatively high CO_2 levels (~ 280 ppmv) during interglacials and low levels (~ 190 ppmv) during the deepest

glacial periods (Figure 1-3). On the basis that the presence of CO_2 in the atmosphere effectively retards the loss from the Earth to space of radiation at infrared wavelengths [IPCC, 1990], it was immediately recognized that such past variability in CO_2 concentrations might have played an important role in the ice age cycles [Barnola et al., 1987; Broccoli and Manabe, 1987].

The potential importance of variations in CO_2 concentrations in determining the envelope of the ice age cycles has been demonstrated by numerous modelling studies. For instance, the addition of a CO_2 -dependent forcing to one of the earliest insolation-driven climate models produces a significant improvement in the evolution of simulated ice volumes [Pisias and Shackleton, 1984]. Other abstracted models confirmed that relatively realistic ~ 100 ka cycles could be generated by accounting for the influence of CO_2 [Lindzen, 1986; Saltzman, 1987, 1990, Saltzman and Maasch, 1988; Saltzman and Verbitsky, 1994]. Mechanistic (intermediate complexity) climate models also exhibited an evolution in ice volume over the course of the 100 ka glacial-interglacial cycles significantly more in line with paleoclimate reconstructions upon the addition of external CO_2 forcing [Berger et al., 1998, 1999; Li et al., 1998a; Loure and Berger, 2000]. This improvement can be demonstrated more quantitatively through spectral analysis. Without applied variability in CO_2 forcing, model spectral power

centred about a period of ~ 100 ka is in fact split into two peaks corresponding to periods of ~ 95 and ~ 125 ka [Ridgwell *et al.*, 1999], closely following the character of eccentricity [Muller and MacDonald, 1997a,b,c]. There is also considerable (unwanted) power centred around the ~ 413 ka eccentricity component. In contrast, model response where changes in CO_2 levels are accounted for exhibit a single peak corresponding to ~ 100 ka with little power at lower frequencies, consistent with the spectral characteristics of marine $\delta^{18}\text{O}$ records [Ridgwell *et al.*, 1999].

The potential importance of CO_2 also extends to the evolution of the climatic system over the late Cenozoic. Uplift of the Tibetan plateau over this period may have resulted in increased chemical weathering and/or increased net organic carbon burial, producing a gradual draw-down in atmospheric CO_2 [France-Lanord and Derry, 1997; Raymo, 1994; Raymo and Ruddiman, 1992; Raymo *et al.*, 1988]. This is illustrated once again by climate models driven by a long-term reduction in CO_2 forcing component, which are able to reproduce both the onset of ~ 41 ka ice age cycle around ~ 2.5 Ma BP, together with the transition between 41 and 100 ka periodicity with an associated increase in cycle amplitude [Saltzman and Maasch, 1991; Saltzman and Verbitsky, 1992, 1993, 1994].

What processes at work within the earth system then drive the observed glacial-interglacial variability in the concentration of atmospheric CO_2 ... ?

SUE: An ocean biogeochemical framework

2.1 Introduction

On time scales of decades and less the terrestrial biosphere exerts a significant control on atmospheric composition with a pronounced seasonal signal, primarily due to variability in the balance between uptake and release of CO_2 by the terrestrial biosphere [IPCC, 1990]. However, at some 39000 GtC the reservoir of dissolved carbon in the oceans is over 13 times that of the atmosphere and terrestrial biosphere put together [IPCC, 1994]. Thus, the mechanisms responsible for longer-term variability in the concentration of atmospheric CO_2 are more likely to involve the ocean. For this reason, models of the global carbon cycle used in the context of glacial-interglacial change are rooted in numerical representation of the oceanic carbon cycle.

Exchange of CO_2 between the ocean and atmosphere depends on the difference in molar fraction of gaseous CO_2 in the atmosphere ($x\text{CO}_2$) and in the surface ocean (assumed to be equal to its fugacity ($f\text{CO}_2$)). In the absence of any significant change in terrestrial ecosystem carbon storage, in weathering rates of silicate rocks, or in volcanic out-gassing of CO_2 , it is the mean ocean surface $f\text{CO}_2$ (area-weighted and modified by local wind speed) that determines the value of $x\text{CO}_2$. $f\text{CO}_2$ in turn is primarily a function of the concentration of total dissolved inorganic carbon (DIC), alkalinity (ALK), salinity (S), and temperature (T) at the ocean surface. Volk and Hoffert [1985] recognized three main cycles of transformation of state and translocation within the ocean system which act to vertically (and horizontally) partition DIC and ALK and thus determine surface ocean $f\text{CO}_2$. These three processes were termed ‘pumps’, and comprise;

- The ‘solubility pump’, whose action arises through the strong temperature-dependence of the solubility of gaseous CO_2 in water, with cold water exhibiting a much lower $f\text{CO}_2$ than warmer water. Thus, all other things being equal, warm oceanic regions will tend to be sources of CO_2 to the atmosphere and cold regions sinks. The concentration of atmospheric CO_2 is therefore related to mean sea surface temperature (SST).
- The ‘soft tissue pump’, whose effect is due to the removal of dissolved inorganic carbon from surface waters through its photosynthetic fixation by phytoplankton, and is subsequent export in the form of particulate organic carbon (POC) into deeper waters, where it is largely remineralized back into DIC. Through this action there is a vertical partitioning of DIC within the ocean with reduced surface concentrations. The concentration of atmospheric CO_2 is consequently inversely related to the strength of operation of this pump.
- The ‘carbonate pump’, whose effect arises in a similar way to that of the soft tissue pump, except that the particulate phase in question is calcium carbonate (CaCO_3). In the production of CaCO_3 by certain species of phyto- and zoo-plankton and subsequent export, alkalinity is changed in a 2:1 ratio with DIC. The resultant alkalinity partitioning in the ocean more than counteracts the effect on $f\text{CO}_2$ of that due to DIC. The concentration of atmospheric CO_2 therefore scales with the strength of the operation of this pump.

At a minimum, any description of the global carbon cycle must resolve these three separate ‘pumps’. However, the functioning of the real system is considerably more complicated than painted by this rather idealized picture. For instance, the soft tissue pump tends to ‘leak’, with a component of organic carbon primary production advected in a dissolved organic form as opposed to a pure vertical transport of particulates settling under the influence of gravity. The action of the soft tissue pump also results in a partitioning of alkalinity through the base capacities of the organic nutrients nitrate (NO_3^-) and phosphoric acid (PO_4^{3-}). This acts to slightly enhance the influence of the soft tissue pump on $x\text{CO}_2$. Regional variability in sea surface salinity (SSS) modifies the effect of the solubility pump, while regional differences in ocean surface wind speed and sea ice cover exert strong controls on the rate of gas transfer, thus influencing $x\text{CO}_2$. Finally, interactions between the ocean and underlying sediments plays an important role in influencing whole-ocean chemical and nutrient inventories on longer time scales.

Model structure is inevitably a trade-off between the degree of comprehensivity to which mechanisms within the global carbon cycle are represented, the spatial and temporal resolution of the model, simulation length, and actual model run-time. For a given requirement of simulation length together with practical and computational resource-driven limits on run-time, model structure is constrained by process complexity and spatial and temporal resolution. Additional constraints arise through deficiencies in our understanding of aspects of ocean biogeochemical cycling and in available data coverage and quality. Even so, there is no single solution in terms of a hypothetical ‘optimal’ model. Instead, model construction is inevitably a rather subjective ‘art’.

2.2 Model description

For investigation of potential mechanisms driving the observed glacial-interglacial variability in $x\text{CO}_2$, a new numerical description of the (oceanic) global carbon cycle is developed in this study; a model named “SUE”.

2.2.1 Framework overview

The model structure of SUE is shown schematically in Figure 2-1. SUE is essentially a biogeochemical framework of interactions important to the operation of the global carbon cycle operating on both an intra-ocean basis and across the interfaces linking atmosphere, ocean and deep-sea sediments. Ocean configuration and circulation are simply prescribed. As such, there is no feedback on the physical ocean from biogeochemistry and resulting atmospheric composition. Ocean-sediment interactions are described in Chapter 3. Typical model parameter values are summarized in Appendix IV. Full source code and example parameter files are attached on CD-ROM (Appendix V).

2.2.1.1 Ocean configuration and circulation

SUE is not tied to any particular ocean configuration but rather is developed as a flexible biogeochemical framework able to utilize any practical configuration of world ocean. In this, it is assumed that the ocean can be represented by a two-dimensional array of c horizontal regions or zones (hereafter referred to as ‘grid points’), divided vertically into l vertical layers, giving a total of $c \times l$ distinct oceanic volumes (‘cells’). To fully define the model physical ocean structure all that remains are the latitudinal and longitudinal boundaries (or alternatively the area) of each grid point region, together with the depth of the base of each ocean layer. Ocean circulation is defined by a set of mass flows between adjoining cells, from which the translocation of dissolved tracer species (such as DIC, ALK, and nutrients) can be calculated. Rather than prescribe entire ocean temperature (T) and salinity (S) fields as is usual in box model studies, temperature and salinity are advected along with other ocean tracers. Only SST and SSS boundary conditions must there be prescribed.

Many of the primary determinants of deep-sea sedimentary composition (such as CaCO_3 saturation state, and biogenic material rain rates) are depth-dependent. Assumption of a uniform depth for the ocean would then degrade the overall dynamics of ocean-sediment interaction [Keir, 1995]. In addition, the value of any comparison made between model sediments and observations will be reduced. The representation of deep sea sediments therefore follows previous schemes where the ocean floor is defined at each grid point according to a hypsographic curve [Munhoven and Francois, 1994, 1996; Sundquist, 1990; Walker and Opdyke, 1995], derived from actual (inferred) topography [ETOPO5, 1988] on either a mean regional or global basis. These continuous bathymetric profiles are discretized into a series of m separate depth bands at each grid point, with which an individual module handling ocean-sediment interactions is associated. The sediment module depth bands need not

rigidly correspond to the depth intervals of ocean layers, with the result that changes in sea level can alter the depth in the ocean at which the sediments lie.

2.2.1.2 Overall biogeochemical cycling scheme

The model biogeochemical scheme is based around the cycling of three primary nutrients limiting to biological productivity; phosphate (PO_4), silicic acid (H_4SiO_4), and iron (Fe). Primary processes relating the intra-ocean cycling and ocean-sediment exchange of these nutrients in addition to dissolved inorganic carbon (DIC), alkalinity (ALK), and dissolved oxygen (O_2), are considered. Biogeochemical cycling is assumed to be representative of the ‘open ocean’ environment, with no explicit consideration of coastal or shelf processes (other than through highly parameterized representations of the accumulation and erosion of CaCO_3 and opal in neritic sediments – see 5.4.7). Carbon (as CO_2) and O_2 are exchanged with a ‘well-mixed’ atmosphere across the air-sea interface.

Nutrients, together with DIC and ALK, are taken out of solution in the sunlit surface ocean layer through biological action, and exported in particulate form (particulate organic matter (POM), CaCO_3 , and opal) to deeper layers. As it settles through the water column, such material is subject to remineralization processes, resulting in the release of dissolved constituent species back to the ocean. Export of nutrients and carbon may also occur in the form of dissolved organic material (DOM). In this case, removal and transport is through ocean advection and mixing rather than gravitational settling. Dissolved iron in the ocean is considered in the form of a single species which is ultimately available for biological uptake at the ocean surface. In addition to surface biological removal dissolved Fe may also be taken out of solution throughout the ocean as a result of the scavenging action of settling particulate matter. Fe may therefore be subsequently released at depth back into solution not only through the normal operation of the ‘soft tissue pump’, but also liberated as the scavenging agents themselves are remineralized.

Biogenic and detrital material reaching the ocean floor may undergo diagenetic alteration (releasing further dissolved species to the ocean) and/or (semi-) permanent burial. The dissolution flux and thus fractional preservation of CaCO_3 and opal is represented mechanistically (Chapter 3). As an initial approximation, POM is preserved in a simple fraction, while Fe (whether in organic or inorganic form) reaching the sediments is assumed to be completely preserved along with detrital matter. Loss of material through burial in the sediments must be balanced over the long-term by supply to the ocean from continental weathering and geothermal processes (in the case of DIC, ALK, PO_4 , and H_4SiO_4) together with aeolian input at the surface (Fe and H_4SiO_4).

The two stable isotopes of carbon (^{12}C and ^{13}C) are treated separately, with all significant fractionation processes involving transformations of carbon state taken into account. However, many of the most important fractionation processes discriminating between the stable isotopes of oxygen (^{16}O , ^{17}O , and ^{18}O) are associated with the operation

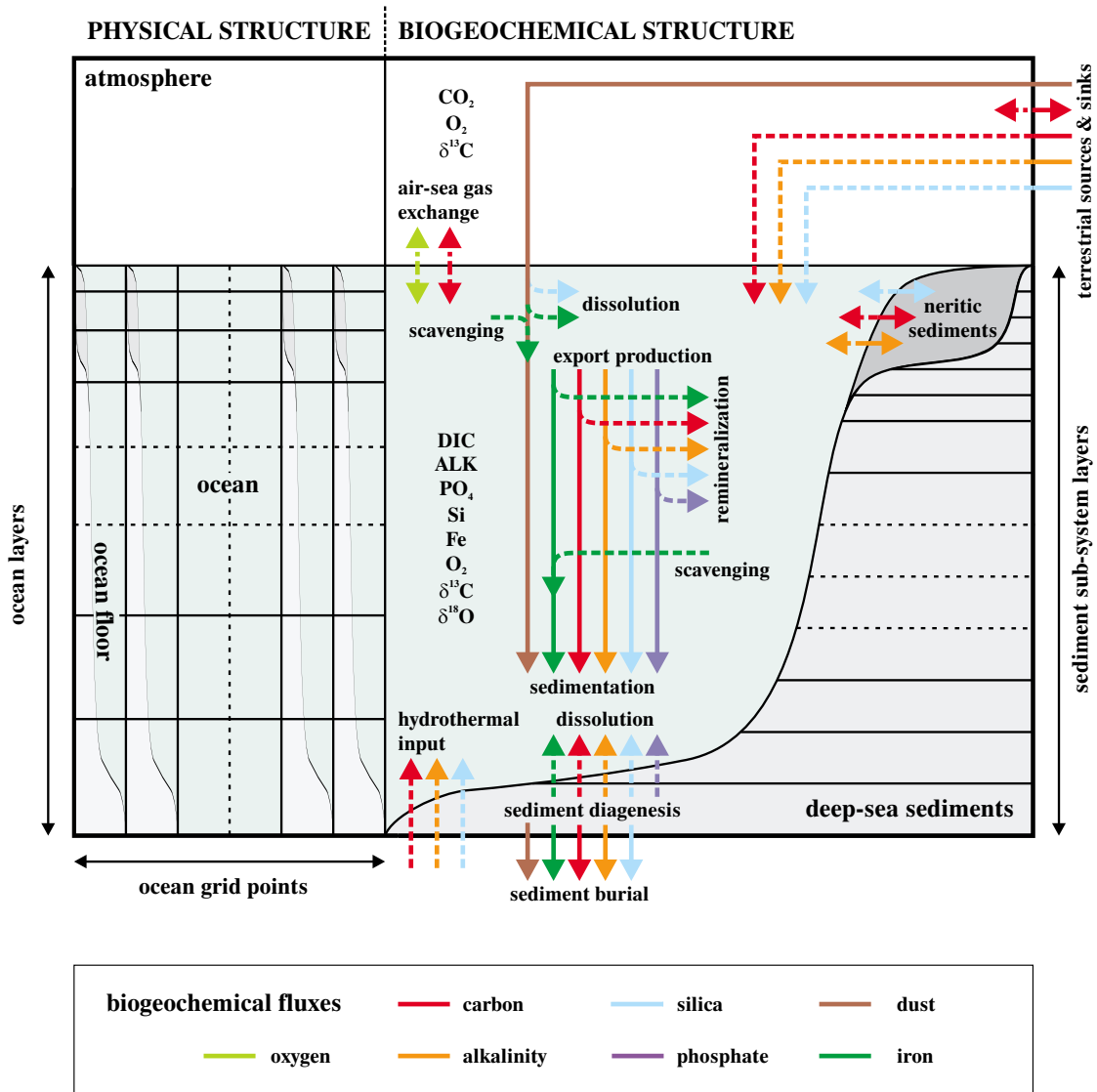


Figure 2-1. Schematic representation of the global carbon cycle model “SUE”. Solid biogeochemical fluxes are shown as solid lines, dissolved fluxes are dashed lines, and gaseous fluxes as dotted lines.

of the hydrological cycle and terrestrial ecosystems, neither of which are explicitly represented in SUE. ^{18}O is therefore included only as a passive tracer. As such, it takes a (uniform) value throughout the ocean-atmosphere system set according to SPECMAP [Imbrie *et al.*, 1984] for any point in time.

2.2.1.3 Carbonate system thermodynamics

In order to calculate important variables such as the fugacity of CO_2 in the surface ocean, or the degree of under-saturation of CaCO_3 in the deep sea, the equilibrium state of the aqueous carbonate system must be known. A solution for this is approximated numerically given the concentrations of DIC, ALK, H_4SiO_4 , and PO_4^{3-} , together with ambient temperature, salinity, and pressure. The thermodynamical scheme is outlined in Appendix I.

2.2.1.4 Numerical scheme

The incarnation of SUE presented here is rooted in mean annual ocean circulation in common with many other carbon cycle models. Equations describing intra-ocean and ocean-atmosphere processes are solved numerically within a forward-time finite difference framework. However, while this and similar schemes are numerically stable for ocean models having a relatively thick (≥ 150 m) surface ocean layer (e.g., Broecker and Peng [1986], Keir [1988]), instabilities in the air-sea exchange of CO_2 can arise if a much thinner surface ocean layer is assumed. The time step for intra-ocean and ocean-atmosphere processes is therefore allowed to take a value much shorter than 1 year. Problems can also arise with regards to the description of biological new production in the surface ocean, where there can be a danger of nutrient depletion below zero occurring [Sarmiento *et al.*, 1993]. A separate sub-step is therefore used for this, nested within that for the ocean-atmosphere system as a whole. Deep-sea sedimentary processes are solved strictly at an annual time step, and are asynchronously coupled with the ocean across the sediment-ocean interface at this same period.

2.2.2 Ocean-atmosphere gas exchange

In addition to being linked through ocean transport, surface ocean cells are geochemically coupled via the atmosphere. A single ‘well-mixed’ box is assumed on the basis of the relatively rapid rate of atmospheric mixing between the hemispheres compared with typical time scale of CO_2 concentration adjustment to changes in sources and sinks [IPCC, 1990]. Exchange of $^{12}\text{CO}_2$, $^{13}\text{CO}_2$, and O_2 between atmosphere and ocean across the air-sea interface is considered.

2.2.2.1 Ocean-atmosphere CO_2 exchange

Carbon cycle models have often used a prescribed gas transfer coefficient, taken to be uniform over the entire ocean surface [Heinze *et al.*, 1991, 1999; Maier-Reimer, 1993; Maier-Reimer and Hasselmann, 1987; Marchal *et al.*, 1998b; Yamanaka and Tajika, 1996]. The value assumed for this coefficient (typically between 0.05 and 0.07 $\text{mol m}^{-2} \mu\text{atm}^{-1} \text{a}^{-1}$) is taken consistent with ^{14}C observations [Broecker *et al.*,

1985]. Although wind speeds actually exhibit substantial spatial heterogeneity [Broecker *et al.*, 1985], on the basis that the effect of sea ice cover at high latitude regions would act so as to largely cancel out the influence of the higher wind speeds found there Siegenthaler and Joos [1992] supported the use of this uniform coefficient. However, on glacial-interglacial time scales both wind speed and sea ice extent are likely to vary significantly and independently of each other. It has been suggested that changes in either or both of these ocean surface boundary conditions may account for much of the observed atmospheric CO_2 record [Keir, 1993; Stephens and Keeling, 2000]. For this reason the influence of wind speed and sea ice extent on the mean gas transfer coefficient is taken into account at each grid point. The gas transfer coefficient is represented as an explicit function of wind speed in a similar manner to Aumont *et al.* [1999], utilizing an empirical description of gas exchange coefficient [Wanninkhof, 1992]. This relationship is then corrected for the application of long-term mean rather than instantaneous wind speeds [Wanninkhof, 1992]. In this, the flux density across the air-sea interface of each cell is

$$f_{\text{atm} \rightarrow \text{ocn}}^{\text{CO}_2} = K \cdot (p\text{CO}_2 - f\text{CO}_2) \quad (2-1)$$

where $p\text{CO}_2$ is the partial pressure of CO_2 in the atmosphere, taken to be equal to its molar fraction ($x\text{CO}_2$) for a mean atmospheric pressure of 1 atm, and $f\text{CO}_2$ is the fugacity of CO_2 in the surface ocean. K is a gas transfer coefficient, expressed

$$K = k_{\text{av}} \cdot Q \quad (2-2)$$

where k_{av} is the gas transfer velocity or piston velocity for appropriate for long-term average wind speeds (in m s^{-1}), and Q is the Henry’s Law constant for CO_2 in seawater (calculated from Weiss [1974], and converted into units of $\text{mol m}^{-3} \mu\text{atm}^{-1}$). k_{av} is given by

$$k_{\text{av}} = l \cdot \left[2.5 \cdot (a + b \cdot T + c \cdot T^2) + 0.38 \cdot u_{\text{av}}^2 \right] \cdot \left(\frac{Sc}{660} \right)^{-0.5} \quad (2-3)$$

where a , b , and c are empirical constants, taking values of 0.5246, 1.6256×10^{-2} , and 4.9946×10^{-4} , respectively, l is a scaling constant of value 2.778×10^6 , T is the temperature in $^{\circ}\text{C}$, u_{av} is the long-term average wind speed (m s^{-1}), and Sc is the Schmidt number for CO_2 in sea water, which can be approximated by

$$Sc = a - b \cdot T + c \cdot T^2 - d \cdot T^3 \quad (2-4)$$

where a , b , c , and d are empirical constants, taking values of 2073.1, 125.62, 3.6267, and 0.043219, respectively [Wanninkhof, 1992].

In order to calculate the net exchange of CO_2 between the atmosphere and ocean, assuming that sea ice represents an impenetrable barrier to gaseous diffusion [Sarmiento *et al.*, 1992] the flux density across the air-sea interface is simply multiplied by the ice-free area, and summed over all grid points

$$F_{\text{air} \rightarrow \text{sea}}^{\text{CO}_2} = \sum_c \left(f_{\text{air} \rightarrow \text{sea}(c)}^{\text{CO}_2} \cdot (A_{(c)} - A_{\text{ice}(c)}) \right) \quad (2-5)$$

Where $A_{(c)}$ and $A_{\text{ice}(c)}$ are the appropriate total and sea ice areas, respectively, corresponding to grip point c .

2.2.2.2 Ocean-atmosphere O_2 exchange

Unlike CO_2 , dissolved oxygen concentrations ($[\text{O}_2]$) are not buffered by the presence of a complex chemical reservoir so that $[\text{O}_2]$ in the surface ocean is often close to equilibrium with the atmosphere. The simplifying assumption is therefore often made in carbon cycle models that strict equilibrium is always maintained [Bolin *et al.*, 1983; Maier-Reimer, 1993; Yamanaka and Tajika, 1996]. However, this doesn't necessarily hold true in regions where vigorous convective overturning takes place such that the residence time of water at the surface may be too short for full equilibration with the atmosphere to take place [Heinze *et al.*, 1999]. A simple restoring scheme is therefore adopted, weighted by the fractional ice-free area

$$[\text{O}_2]_{\text{new}} = [\text{O}_2]_{\text{old}} + \frac{(A_{\text{tot}} - A_{\text{ice}})}{A_{\text{tot}}} \cdot ([\text{O}_2]_{\text{eqm}} - [\text{O}_2]_{\text{old}}) \cdot \frac{\Delta t}{\tau_{\text{O}_2}} \quad (2-6)$$

where $[\text{O}_2]_{\text{new}}$ is the new concentration of dissolved O_2 after exchange with the atmosphere, $[\text{O}_2]_{\text{old}}$ is the old value before any exchange, and $[\text{O}_2]_{\text{eqm}}$ is the theoretical concentration of O_2 in the ocean in equilibrium with an atmospheric partial pressure ($p\text{O}_{2(\text{atm})}$) of 0.2096 atm, given by

$$[\text{O}_2]_{\text{eqm}} = Q_{\text{O}_2(\text{T,S})} \cdot p\text{O}_{2(\text{atm})} \quad (2-7)$$

where $Q_{\text{O}_2(\text{T,S})}$ is the Henry's Law constant for O_2 as a function of temperature and salinity in the surface ocean [Millero and Sohn, 1992]. The model time step is Δt , with τ_{O_2} , the restoring time for $[\text{O}_2]$ assigned a default value of 30 days.

2.2.3 Biological new production

Numerous mechanistic schemes for representing biological productivity in the surface ocean based on a multi-component description of ecosystem structure and nutrient cycling have been developed to date [Aksnes *et al.*, 1995; Andersen *et al.*, 1987; Fasham *et al.*, 1990]. These range in complexity from single nutrient and single phytoplankton component systems operating within a homogeneous surface ocean layer, to systems of multiple nutrients and trophic levels, all coupled to a 1D physical model. The export flux of particulate biogenic matter out of the surface layer in these models is derived from primary productivity taking into account various recycling and transformation processes within the euphotic zone. Although such schemes have been incorporated into global carbon cycle models their computational demands make their use in extended model runs problematic. In addition, they are often not particularly

generalized and may require site-specific tuning [Hurt and Armstrong, 1996, 1998].

Much simpler is to attempt to estimate new (export) production directly from available surface nutrient concentrations, a tactic used in many carbon cycle models. Of limited use in addressing the glacial-interglacial question in this regard are schemes where export production is calculated to effectively 'restore' surface ocean nutrient concentrations to some pre-determined value (e.g., Marchal *et al.* [1998b], Murnane *et al.* [1999], Najjar *et al.* [1992]). Alternatively, export production may be parameterized as a function of a single nutrient (usually PO_4), modified by terms representing Michaelis-Menten kinetic nutrient limitation, together with some or all of light, temperature, and mixed layer depth [Bacastow and Maier-Reimer, 1990; Heinze *et al.*, 1991; Maier-Reimer, 1993]. Recently, the effect of additional limiting nutrients (H_4SiO_4 and Fe) have also been considered [Archer and Johnson, 2000; Archer *et al.*, 2000; Heinze *et al.*, 1999; Lefèvre and Watson, 2000; Watson *et al.*, 2000]. However, common to all of these schemes is the calculation of a single value of whole-community organic carbon export. While this is sufficient in terms of the organic carbon pump alone, CaCO_3 and opal production remain to be estimated. The magnitude of CaCO_3 export flux together with its 'rain ratio' with respect to particulate organic carbon (POC), plays a critical role in controlling the alkalinity balance of the ocean and thus in determining $x\text{CO}_2$ [Archer and Maier-Reimer, 1994]. For this reason it is undesirable to assume an invariant ratio of CaCO_3 :POC new production over the glacial-interglacial cycles. Not only is reproducing the observed spatial heterogeneity in rain ratios (at least to a first order) a precondition for effective simulation of Holocene sediments, being able to account for differences in this ratio during glacial times facilitates verification of the mechanism(s) assumed for glacial-interglacial change through comparisons between observed and model Last Glacial Maximum (LGM) sediment distributions. Similar arguments also apply for opal:POC. Unfortunately, since ecosystem structure is fundamental in determining such ratios there is no simple means of deriving their values from a total POC flux [Shaffer, 1993], although (highly parameterized) attempts have been made taking into account ambient nutrient and temperature conditions [Archer *et al.*, 1999a,b, 2000; Heinze *et al.*, 1999; Maier-Reimer, 1993].

A new computationally-efficient scheme for surface ocean biological production is presented here. In the manner in which it seeks to estimate export production out of the euphotic zone directly from surface physical and chemical conditions (as opposed to via a full ecosystem model) it is similar to that of Maier-Reimer [1993]. However, a significant departure is made in that production arising from two distinct classes of phytoplankton is considered; siliceous phytoplankton ("SP") and non-siliceous phytoplankton ("NSP"), following Egge and Aksnes [1992]. SP (typified by open ocean diatom species such as *Thalassiosira oceanica*) are assumed to be solely responsible for the production of opal, and as a result are limited by the availability of H_4SiO_4 . In contrast, NSP (typified by open ocean coccolithophorids

such as *Emiliana huxleyi*, but including the bulk of pico- and nano-phytoplankton species), have no such silicic acid limitation and are assumed to be the sole producers of CaCO_3 . Both classes are affected by ambient $[\text{PO}_4]$ and $[\text{Fe}]$, temperature, and light. In the absence of any nutrient limitation (and assuming a stable water column and adequate insolation levels) siliceous phytoplankton tend to dominate the phytoplankton community [Egge, 1998]. SP are therefore characterized in the model by a relatively high (export) productivity. NSP tend to generally comprise somewhat smaller species with productivity much more tightly controlled by grazing, and are therefore characterized by relatively low productivity. Obviously this is highly simplistic, with no explicit representation of the role played by zooplankton or of the microbial loop [Taylor and Joint, 1990]. In addition, the important contribution made to POC export in regions such as the Southern Ocean by high productivity non-siliceous bloom-forming species such as *Phaeocystis antarctica* [Elderfield and Rickaby, 2000] will not be captured. However, such a scheme is still able to capture the first order contrast in the observed CaCO_3 :POC rain ratio between different oceanic regions as will be demonstrated later (4.4.2).

Although the biological scheme is based around nutrient limitation by PO_4 , H_4SiO_4 , and Fe, present-day surface nutrient distributions suggests that the availability of nitrate (NO_3) is likely to be generally more limiting to phytoplankton growth than PO_4 [McElroy, 1983; Tyrrell, 1999]. However, considering the complexity of the oceanic NO_3 cycle no explicit representation is incorporated in SUE at present, although account is still taken of the contribution made to alkalinity partitioning in the ocean by NO_3 cycled through the ‘soft tissue pump’ [Broecker and Peng, 1982].

2.2.3.1 Phosphate uptake model

Net uptake fluxes (in units of $\text{mol PO}_4 \text{ kg}^{-1} \text{ a}^{-1}$) within the euphotic zone by siliceous phytoplankton ($u_{\text{SP}}^{\text{PO}_4}$) and non-siliceous phytoplankton ($u_{\text{NSP}}^{\text{PO}_4}$) are based upon the ‘law of the minimum’ for multiple nutrient limitation [Aksnes et al., 1994], and described by

$$u_{\text{SP}}^{\text{PO}_4} = u_{0,\text{SP}}^{\text{PO}_4} \cdot \text{MIN}\left(k_{\text{SP}}^{\text{PO}_4}, k_{\text{SP}}^{\text{H}_4\text{SiO}_4}, k_{\text{SP}}^{\text{Fe}}\right) \cdot \mu_{(I)} \cdot \mu_{(T)} \quad (2-8a)$$

$$u_{\text{NSP}}^{\text{PO}_4} = u_{0,\text{NSP}}^{\text{PO}_4} \cdot \text{MIN}\left(k_{\text{NSP}}^{\text{PO}_4}, k_{\text{NSP}}^{\text{Fe}}\right) \cdot \mu_{(I)} \cdot \mu_{(T)} \quad (2-8b)$$

where $u_{0,\text{SP}}^{\text{PO}_4}$ and $u_{0,\text{NSP}}^{\text{PO}_4}$ are uptake rates ($\text{mol PO}_4 \text{ kg}^{-1} \text{ a}^{-1}$) in the absence of any nutrient limitation for SP and NSP, respectively, and treated as optimizable parameters. $\mu_{(I)}$ is a factor accounting for the effects ambient solar insolation has on new production, while $\mu_{(T)}$ is similar, but for temperature. A realistic treatment of light limitation is complex, requiring consideration of the depth distribution of phytoplankton in the water column, effects of self-shading and photo-inhibition, and an estimate of the depth of the mixed layer [Andersen et al., 1987; Taylor et al., 1991; Tyrrell and Taylor, 1996], all of which are beyond the scope of the current model. A simple (normalized) insolation factor is therefore used (detailed in Appendix II). $\mu_{(T)}$ is defined

$$\mu_{(T)} = e^{(aT)} \quad (2-9)$$

such that $\mu_{(T)}$ takes a value of unity at a temperature of 0°C . A Q_{10} -type dependence is assumed, with the scalar a given by [Aksnes et al., 1995]

$$a = \ln\left(\frac{Q_{10}}{10}\right) \quad (2-10)$$

Following Eppley [1972] Q_{10} for phytoplankton growth of 1.88 is assumed, giving $a = 0.063$. No distinction is made between the two phytoplankton groups in terms of their temperature response [Aksnes et al., 1995].

The ‘ k ’ terms in (2-8a) represent Michaelis-Menten kinetic limitation of uptake [Aksnes and Egge, 1991; Dugdale, 1967]

$$k_{\text{SP}}^{\text{PO}_4} = \frac{[\text{PO}_4]}{K_{\text{S,SP}}^{\text{PO}_4} + [\text{PO}_4]} \quad (2-11)$$

$$k_{\text{SP}}^{\text{H}_4\text{SiO}_4} = \frac{[\text{H}_4\text{SiO}_4]}{K_{\text{S,SP}}^{\text{H}_4\text{SiO}_4} + [\text{H}_4\text{SiO}_4]} \quad (2-12)$$

$$k_{\text{SP}}^{\text{Fe}} = \frac{[\text{Fe}]}{K_{\text{S,SP}}^{\text{Fe}} + [\text{Fe}]} \quad (2-13)$$

where K_{S} values in the three equations are the half-saturation constants for the respective nutrients. The NSP terms are similar, except that there is no H_4SiO_4 limitation.

Strictly speaking, Michaelis-Menten limitation kinetics and the associated use of half-saturation constants are not directly applicable to a model of this type. Reported constants are calculated on the basis of growth rate of individual phytoplankton cells, whereas SUE seeks to predict net nutrient removal throughout the euphotic zone (and with it, export production). It is likely that export production has no simple relationship with primary production. Indeed, a tendency for export production to increase more rapidly with increasing primary production than primary production itself has been reported [Aksnes and Wassmann, 1993]. However, for want of a suitable alternative, this concise and easily interpretable parameterization is adopted for the purpose of this present study.

Integrating net uptake ((2-8a) and (2-8b)) over the depth of the euphotic zone (D_{euph}) and total ice free area gives the total net uptake rate from each oceanic region (in units of $\text{mol PO}_4 \text{ a}^{-1}$)

$$U_{\text{SP}}^{\text{PO}_4} = u_{\text{SP}}^{\text{PO}_4} \cdot 1027 \cdot \left(1 - (A_{\text{tot}} - A_{\text{ice}})\right) \cdot D_{\text{euph}} \quad (2-14a)$$

$$U_{\text{NSP}}^{\text{PO}_4} = u_{\text{NSP}}^{\text{PO}_4} \cdot 1027 \cdot \left(1 - (A_{\text{tot}} - A_{\text{ice}})\right) \cdot D_{\text{euph}} \quad (2-14b)$$

where the mean density of sea water is assumed to be 1027 kg m^{-3} . Finally, (steady state) export production out of the euphotic zone is simply equal to net uptake. Partitioning this export into particulate (POP) and dissolved organic phosphate (DOP) forms, gives

$$Fnp_{SP}^{POP} = \lambda_{SP} \cdot U_{SP}^{PO_4} \quad (2-15a)$$

$$Fnp_{NSP}^{POP} = \lambda_{NSP} \cdot U_{NSP}^{PO_4} \quad (2-15b)$$

and

$$Fnp_{SP}^{DOP} = (1 - \lambda_{SP}) \cdot U_{SP}^{PO_4} \quad (2-16a)$$

$$Fnp_{NSP}^{DOP} = (1 - \lambda_{NSP}) \cdot U_{NSP}^{PO_4} \quad (2-16b)$$

Where λ_{SP} and λ_{NSP} are the export partitioning coefficients for SP and NSP, respectively.

2.2.3.2 Nutrient half-saturation constants

Phytoplankton nutrient half saturation constants are derived from values observed in both incubation and whole-ocean ecosystem studies. These values are summarized in Table 2-1, and adopted on the following basis

Phosphate

The PO_4 half saturation constant for siliceous phytoplankton ($K_{S,SP}^{PO_4}$) is taken from the diatom value used by *Aksnes et al.* [1995]. Coccolithophorids have been observed to exhibit a higher affinity for phosphate than do diatoms [*Aksnes et al.*, 1994; *Egge* 1998]. The PO_4 half saturation constant for non-siliceous phytoplankton ($K_{S,NSP}^{PO_4}$) is therefore assigned a value some 50% lower than that assumed for siliceous phytoplankton in order to reflect this difference.

Silicic acid

The half-saturation constant for siliceous phytoplankton is taken to be $4 \mu\text{mol kg}^{-1}$, consistent with kinetic experiments on single and diatoms and natural assemblages suggest a value for $K_{S,SP}^{H_4SiO_4}$ in the range $0.5\text{-}5.0 \mu\text{mol kg}^{-1}$ [*Dugdale et al.*, 1995; *Officer and Ryther*, 1980].

Iron

Assigning globally representative half-saturation constant values for Fe is much more problematic than for the macro-nutrients. While *Sunda and Huntsman* [1995] reported K_S^{Fe} values for several typical oceanic diatom

species, their experimental system was heavily EDTA-buffered with results reported on a calculated dissolved Fe^{II} scale. It is unwise to utilize the results of such a system directly [*Gerringa et al.*, 2000; *Muggli et al.*, 1996]. More applicable are results of Fe additions made to natural systems when the concentration of Fe tends to be operationally defined and thus substantially equivalent to the total dissolved Fe scale considered in SUE. Incubation enrichment experiments on equatorial Pacific samples indicate a whole-community K_S^{Fe} of $0.12 \text{ nmol kg}^{-1}$ [*Coale et al.*, 1996b; *Fitzwater et al.*, 1996], while similar experiments conducted at the equator and 15°N are consistent with values of 0.035 and $0.22 \text{ nmol kg}^{-1}$, respectively [*Price et al.*, 1994]. More recent enrichment incubation experiments carried out by *Takeda* [1998] are consistent with a value for K_S^{Fe} of $0.25\text{-}0.75 \text{ nmol kg}^{-1}$ for oceanic waters of all three main HNLC zones, while *Hutchins and Bruland* [1998] suggest values characterizing the California coastal up-welling regime lie anywhere in the range $0.02\text{-}1.0 \text{ nmol kg}^{-1}$ (depending on the precise details of the operational definition of [Fe] chosen). A value of $K_{S,diat}^{Fe}$ of $0.125 \text{ nmol kg}^{-1}$ is therefore chosen generally consistent with these estimates and assuming that most of the observed changes in primary production is due to diatoms. On the basis that *Sunda and Huntsman* [1995] observed half-saturation values for *T. oceanica* approximately twice that for *E. huxleyi*, $K_{S,NSP}^{Fe}$ is taken to be 50% lower than that of $K_{S,SP}^{Fe}$.

2.2.3.3 'Redfield' and derived chemical export ratios

While (2-15a) and (2-15b) together predict particulate PO_4 export from the euphotic zone the export of other biogeochemically important nutrient and non-nutrient chemical species, such as H_4SiO_4 , Fe, CO_2 , and alkalinity (from Ca^{2+} and NO_3^-) must now be derived. The organic or inorganic components of particulate matter export are related directly (or via an intermediary) to phosphate export, by a series of characteristic ratios. For SP, these relationships are

$$Fnp_{SP}^{POC} = r_{SP}^{POC:POP} \cdot Fnp_{SP}^{POP} \quad (2-17)$$

$$Fnp_{SP}^{ALK} = -0.7 \cdot r_{SP}^{PON:POP} \cdot Fnp_{SP}^{POP} \quad (2-18)$$

$$Fnp_{SP}^{POFe} = r_{SP}^{POFe:POC} \cdot Fnp_{SP}^{POC} \quad (2-19)$$

$$Fnp_{SP}^{opal} = r_{SP}^{opal:POC} \cdot Fnp_{SP}^{POC} \quad (2-20)$$

where $r_{SP}^{x:y}$ is a molar ratio linking constituent x to y . For NSP, they are

$$Fnp_{NSP}^{POC} = r_{NSP}^{POC:POP} \cdot Fnp_{NSP}^{POP} \quad (2-21)$$

$$Fnp_{NSP}^{ALK} = -0.7 \cdot r_{NSP}^{PON:POP} \cdot Fnp_{NSP}^{POP} + 2 \cdot r_{NSP}^{CaCO_3:POC} \cdot Fnp_{NSP}^{POC} \quad (2-22)$$

Table 2-1 Nutrient Half-saturation Values for the Two Phytoplankton Groups Considered in SUE

Phytoplankton group	Nutrient	K_S value
Siliceous	PO_4	$0.1 \mu\text{mol kg}^{-1}$
Siliceous	H_4SiO_4	$4.0 \mu\text{mol kg}^{-1}$
Siliceous	Fe	$0.125 \text{ nmol kg}^{-1}$
Non-siliceous	PO_4	$0.05 \mu\text{mol kg}^{-1}$
Non-siliceous	H_4SiO_4	n/a
Non-siliceous	Fe	$0.0675 \text{ nmol kg}^{-1}$

$$Fnp_{NSP}^{POFe} = r_{NSP}^{POFe:POC} \cdot Fnp_{NSP}^{POC} \quad (2-23)$$

The proportions of C and N to P in POM are characterized by observed mean ratios (the so-called ‘Redfield’ ratios), with $r_{POC:POP}^{POC}$ and $r_{PON:POP}^{PON}$ taking values of 106:1 and 16:1, respectively [Redfield *et al.*, 1963]. The same ratios are assumed for POM derived from both SP and NSP. Net oxygen production in the euphotic zone is assumed to be in a fixed ratio to phosphate export, with $O_2:P$ of 177:1.

Recent studies have indicated profound physiological effects on phytoplankton of iron availability aside from the direct influence on growth rate. For instance, phytoplankton have been observed to take up Fe in an apparent ‘luxuriant’ manner when ambient Fe availability is high [Sunda *et al.*, 1991; Sunda and Huntsman, 1995]. A second physiological change manifests itself through the molar ratio of cellular carbon to frustular opal in diatoms, with the apparent efficiency of silicic acid utilization (per unit carbon fixed) increasing with iron availability. Where available H_4SiO_4 is limiting to diatom growth, therefore, enhanced iron supply may enable increased diatom organic carbon export without any concurrent increase in opal export. This has important implications both for the operation of the global carbon cycle and for the paleoclimatic interpretation of sedimentary opal content and accumulation rates in deep sea sediment cores [Anderson *et al.*, 1998; Boyle, 1998; Takeda, 1998; Watson *et al.*, 2000]. The export ratios $r_{SP}^{POFe:POC}$, $r_{NSP}^{POFe:POC}$, and $r_{SP}^{opal:POC}$ are therefore defined as functions of Fe availability. Although Fe availability was previously thought to have relatively little influence on the ratios linking C, N, and P [Greene *et al.*, 1991], nitrate utilization appears to be significantly greater per unit carbon fixed under Fe-replete conditions [Cullen, 1995; Hutchins and Bruland, 1998; Hutchins *et al.*, 1998; Muggli *et al.*, 1996; Takeda, 1998]. Since there is no explicit consideration of NO_3 in SUE and little quantitative information is currently available concerning changes in $H_4SiO_4:PO_4$ uptake, no dependence of [Fe] on either $r_{POC:POP}^{POC}$ or $r_{PON:POP}^{PON}$ is considered.

Export $CaCO_3:POC$ ratio

The export ratio of $CaCO_3:POC$ from non-siliceous phytoplankton ($r_{NSP}^{CaCO_3:POC}$) is left as an optimizable parameter in the model. $CaCO_3$ in SUE is resolved in calcitic and aragonitic components. Although there is little available data for aragonite export, sediment trap measurements suggest that aragonite constitutes at least 12% of the total $CaCO_3$ sinking flux at a depth of 667 m in the equatorial Atlantic [Berner and Honjo, 1981], but can be as high as 24% at 100 m in the North Pacific [Betzer *et al.*, 1984]. Aragonite is therefore assumed to constitute ~5% of $CaCO_3$ export production, equivalent to ~10% at 1000 m depth as a result of rapid reduction in calcite fluxes through the mesopelagic zone (see 2.2.4.2).

While the value of $r_{NSP}^{CaCO_3:POC}$ is itself invariant and spatially uniform the overall, $CaCO_3:POC$ export ratio comprises export from both SP (contributing POC only) and NSP (contributing both POC and $CaCO_3$). Temporal or

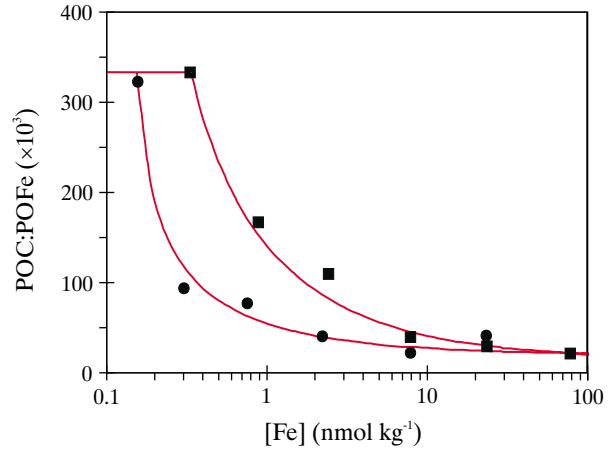


Figure 2-2 Model relationship for the export ratio of POC:POFe (i.e., the reciprocal of $r_{POFe:POC}^{POFe}$), for both siliceous phytoplankton (upper line) and non-siliceous phytoplankton (lower line) as functions of the concentration of total dissolved iron ([Fe]). Observational data for *T. oceanica* (filled squares) and *E. huxleyi* (filled circles) are from Sunda and Huntsman [1995].

spatial variability in the balance between SP and NSP productivity (for instance, due to changes in the availability of H_4SiO_4) can thus give rise to variability in the net $CaCO_3:POC$ export ratio.

Export POC:POFe ratio

Export POC:POFe ratios are related to Fe availability empirically in the model based on culture results reported by Sunda and Huntsman [1995]. Their theoretical free Fe^{II} (Fe') scale is converted to the equivalent in total dissolved iron ([Fe]) used in SUE by assuming that the half saturation constant for diatoms on the $[Fe']$ scale of ~0.004 $nmol\ kg^{-1}$ [Sunda and Huntsman, 1995], can be equated directly to the estimated value for NSP of 0.125 $nmol\ kg^{-1}$ of [Fe] derived earlier (2.2.3.2). A simple power law function is used, with the observed behaviour of *T. oceanica* taken to be representative of SP, and *E. huxleyi* of NSP [Sunda and Huntsman, 1995]. Assuming that there is no fractionation between Fe and C components of POM primary production within the euphotic zone, Fe:C export ratios for the two phytoplankton groups are set equal to these cellular relationships. A threshold level is imposed and set at the maximum observed efficiency of iron utilization [Sunda and Huntsman, 1995]; a value of some 3 $\mu mol\ Fe\ (mol\ C)^{-1}$ for both $r_{SP}^{POFe:POC}$ and $r_{NSP}^{POFe:POC}$. The relationships thereby obtained (Figure 2-3) are

$$r_{SP}^{POFe:POC} = \frac{1}{\text{MIN}(333000, 15000 + 115623 \cdot ([Fe] - 0.125)^{-0.65})} \quad (2-24a)$$

and

$$r_{NSP}^{POFe:POC} = \frac{1}{\text{MIN}(333000, 20000 + 31805 \cdot ([Fe] - 0.125)^{-0.65})} \quad (2-24b)$$

where $[\text{Fe}]$ is the total dissolved iron concentration in units of nmol kg^{-1} .

Export opal:POC ratio

Incubation and ocean patch studies have reported changes in the cellular uptake ratios of $\text{H}_4\text{SiO}_4:\text{C}$ and $\text{H}_4\text{SiO}_4:\text{NO}_3$ by HNLC-type phytoplankton assemblages upon the addition of iron [Hutchins and Bruland, 1998; Takeda, 1998; Watson et al., 2000], summarized in Table 2-2. Fe-stressed diatoms are also visibly more heavily silicified [Hutchins et al., 1998; Leynaert et al., 1993]. This increase in diatom $\text{H}_4\text{SiO}_4:\text{C}$ with decreasing Fe-availability has been suggested to be due to the order of cell cycle events, where silicic acid uptake only occurs in a phase just prior to cellular division [Pondaven et al., 1999]. If division is delayed through Fe-limitation, the length of time available for opal deposition is longer, thus resulting in a higher degree of diatom silicification. If this is the case, a reasonable starting point in relating $\text{H}_4\text{SiO}_4:\text{C}$ uptake to ambient $[\text{Fe}]$ would be to assume that this ratio is proportional to Fe-stress as defined by the reciprocal of the relevant Michaelis-Menten kinetic term (2-16), to give

$$r_{\text{SP}}^{\text{H}_4\text{SiO}_4:\text{C}} = r_{0,\text{SP}}^{\text{H}_4\text{SiO}_4:\text{C}} \cdot \frac{1}{k_{\text{Fe}}} \quad (2-25)$$

where $r_{0,\text{SP}}^{\text{H}_4\text{SiO}_4:\text{C}}$ is the ratio of $\text{H}_4\text{SiO}_4:\text{C}$ uptake under Fe-replete conditions. The singularity at $[\text{Fe}] = 0$ is removed by adding a fixed offset ($[\text{Fe}]_{\text{off}}$) to the value of ambient $[\text{Fe}]$.

The observed decrease in diatom $\text{H}_4\text{SiO}_4:\text{C}$ with increasing Fe availability (Table 2-3) can be reasonably reproduced with $K_S^{\text{Fe}} = 0.25 \text{ nmol kg}^{-1}$, and applying an offset in ambient $[\text{Fe}]$ of $0.125 \text{ nmol kg}^{-1}$.

Given their very different biogeochemical natures, a high degree of differential recycling between opal and POC within the euphotic zone is likely [Dugdale et al., 1995; Dugdale and Wilkerson, 1998]. Changes in the degree of diatom silicification may alter the magnitude of this differential, such as through changes in sinking rate [Boyle, 1998; Muggli et al., 1996], grazing susceptibility, or the ‘quality’ of frustuline opal (and thus solubility and/or dissolution rate). However, for simplicity the export opal:POC ratio ($r_{\text{SP}}^{\text{opal:POC}}$) will be assumed to scale linearly with the cellular $\text{H}_4\text{SiO}_4:\text{C}$ uptake ratio. The export ratio can therefore be written

$$r_{\text{SP}}^{\text{opal:POC}} = r_{0,\text{SP}}^{\text{opal:POC}} \cdot \frac{K_S^{\text{Fe}} + ([\text{Fe}] + [\text{Fe}]_{\text{off}})}{([\text{Fe}] + [\text{Fe}]_{\text{off}})} \quad (2-26)$$

where $r_{0,\text{SP}}^{\text{opal:POC}}$ is now the export opal:POC ratio under Fe-replete conditions. The form of this relationship is shown in Figure 2-3. The magnitude of differential recycling within the euphotic zone represented by the implicit scale factor linking $r_{0,\text{SP}}^{\text{opal:POC}}$ to $r_{0,\text{SP}}^{\text{H}_4\text{SiO}_4:\text{C}}$ is poorly quantified, and has been variously estimated to be in the range 1.25 to 3.0 depending on assumptions made regarding grazing [Dugdale et al., 1995; Dugdale and Wilkerson, 1998]. $r_{0,\text{SP}}^{\text{opal:POC}}$ is therefore left as an optimizable parameter in the model.

Table 2-2 Observed Dependence of Molar Uptake Ratios upon Iron Availability

Identifier and location	Treatment	$[\text{Fe}]$ (nmol kg^{-1})	$\text{H}_4\text{SiO}_4:\text{NO}_3$	$\text{H}_4\text{SiO}_4:\text{C}$	Growth rate (d^{-1})	Reference
#1 - Big Sur 1997A	Control	0.1-0.5 ¹	1.6	0.27	0.30	Hutchins and Bruland [1998]
	Fe addition	2.5	0.8	0.21	0.68	
#2 - Big Sur 1996	Control	0.06-0.3 ¹	2.7	0.39	0.70	Hutchins and Bruland [1998]
	Fe addition	10	1.1	0.24	0.94	
#3 - Ano Nuevo 1995	Control	1.5-2.6 ¹	1.0	n/a	0.44	Hutchins and Bruland [1998]
	Fe addition	10	0.9	n/a	0.37	
#4 - Southern Ocean	Control	0.16	2.3	n/a	0.13	Takeda [1998]
	Fe addition	1.2	0.95	n/a	0.43	
#5 - Subarctic North Pacific	Control	0.22	2.6	n/a	0.14	Takeda [1998]
	Fe addition	1.1	1.2	n/a	0.49	
#6 - Equatorial Pacific	Control	<0.05	1.3	n/a	0.06	Takeda [1998]
	Fe addition	0.46	0.45	n/a	0.48	
	Fe addition	0.72	0.45	n/a	0.79	
#7 - Southern Ocean	Control	0.06	n/a	0.36±0.015	n/a	Watson et al. [2000]
	Fe addition	0.3-3.0 ²	n/a	0.18±0.1	n/a	

¹ Control Fe concentration are presented as a range of estimates, depending on the analytical method employed [Hutchins and Bruland, 1998].

2.2.4 Remineralization within the water column

Much of particulate biogenic material exported out of the euphotic zone is remineralized within the water column before it can reach the sediments. Material returned to solution in the mesopelagic zone has the potential to be rapidly returned to the surface, which in the case of nutrients such as PO_4 , NO_3 , H_4SiO_4 , and Fe has obvious implications for surface productivity. The magnitude of the remaining particulate fraction reaching the sediments ultimately exerts an important control on oceanic inventories of nutrients, DIC, and ALK. An adequate representation of remineralization processes within the water column is therefore critical to any description of the global carbon cycle, particularly over glacial-interglacial time scales. In the following sections, a reference depth z_0 is defined at the base of the euphotic zone, where the settling flux of particulate constituent x is equal to the total export flux

$$F_{set(z_0)}^x = Fnp_{SP}^x + Fnp_{NSP}^x \quad (2.27)$$

For dissolved organic matter, remineralization proceeds according to a simple characteristic decay rate [Marchal *et al.*, 1998b; Najjar *et al.*, 1992] as it is transported through the ocean. No distinction is made between semilabile and refractory components [Yamanaka and Tajika, 1997].

2.2.4.1 Particulate organic matter

The processes involved in the remineralization of particulate organic matter (POM) within the water column are extremely complex, including such factors as the repackaging and aggregation/dispersal of particles, bacterial and

Table 2-3 Observed and Model-estimated Relative Changes in $\text{H}_4\text{SiO}_4:\text{C}$ Uptake From Comparatively Iron-deplete to Iron-replete Conditions

Identifier ¹	observed $\frac{\text{H}_4\text{SiO}_4:\text{C}_{\text{deplete}}}{\text{H}_4\text{SiO}_4:\text{C}_{\text{replete}}}$	model $\frac{\text{H}_4\text{SiO}_4:\text{C}_{\text{deplete}}}{\text{H}_4\text{SiO}_4:\text{C}_{\text{replete}}}$
#1	1.29	1.27-1.92 ²
#2	1.63	1.59-2.35 ²
#3	1.00 ³	1.10-1.15 ²
#4	1.58 ³	1.58
#5	1.42 ³	1.43
#6	1.89 ³	>1.70 ⁴
#7	2.00	2.03

¹ (see Table 2-2)

² Depending upon assumptions made regarding the exact value of [Fe] in the experimental control.

³ Estimated from published changes in $\text{H}_4\text{SiO}_4:\text{NO}_3^-$. Care must therefore be taken in using these values, since there is also a significant dependence of $\text{H}_4\text{SiO}_4:\text{NO}_3^-$ on [Fe].

⁴ Assuming control [Fe] < 0.05 nmol kg⁻¹.

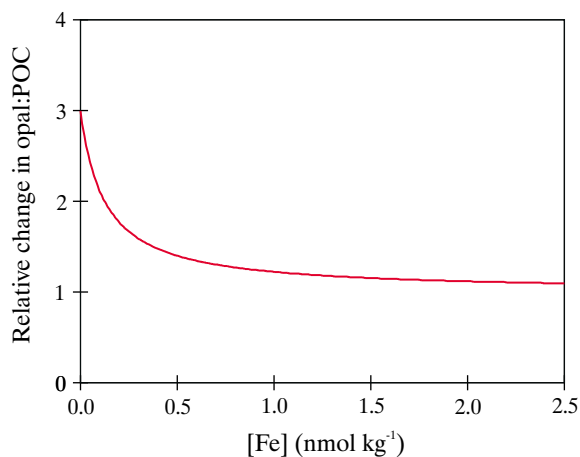


Figure 2-3 Change in siliceous phytoplankton opal:POC export relative to $r_{SP,0}^{\text{opal:POC}}$, as a function of the concentration of total dissolved iron ([Fe]).

zooplankton ecology and the occurrence of rapid export events following phytoplankton blooms [Kriest and Evans, 1999; Shaffer, 1993]. Simple empirical functions are therefore utilized in global carbon cycle models. Various schemes have been proposed, typically based on exponential [Volk and Hoffert, 1985] or power law [Martin *et al.*, 1987; Suess, 1980] functions in which the remaining (un-remineralized) fraction of the initial POM export flux is related directly to the depth in the water column. Of these, the parameterization of Martin *et al.* [1987], derived from a series of sediment trap measurements made during the 'VERTEX' programs and covering the uppermost 2000 m in the eastern equatorial Pacific tends to be fairly ubiquitous (e.g., Maier-Reimer [1993], Yamanaka and Tajika [1996]). However, sediment trap studies suggest that remineralization deeper than this is much less extensive than extrapolation of the Martin *et al.* [1987] function might suggest (Figure 2-4). Since any significant underestimation of POM rain rate to the sediments would reduce the component of CaCO_3 dissolution driven by *in situ* POM remineralization [Archer and Maier-Reimer, 1994] and thus disrupt global alkalinity, Archer *et al.* [1996, 1998] modified the Martin *et al.* [1987] function (Figure 2-4). Although this is in good agreement with deeper (> 2000 m) sediment trap observations, it tends to deviate a little from the VERTEX data at mesopelagic depths.

A slightly different function is adopted which assumes that a fraction of POM settles through the water column essentially unaltered, either due to rapid settling and/or a recalcitrant composition. The remaining fraction is degraded according to a simple power law. The settling flux of particulate organic phosphorus (POP) is therefore defined

$$F_{set(z)}^{\text{POP}} = F_{set(z_0)}^{\text{POP}} \quad z \leq z_0 \quad (2.28a)$$

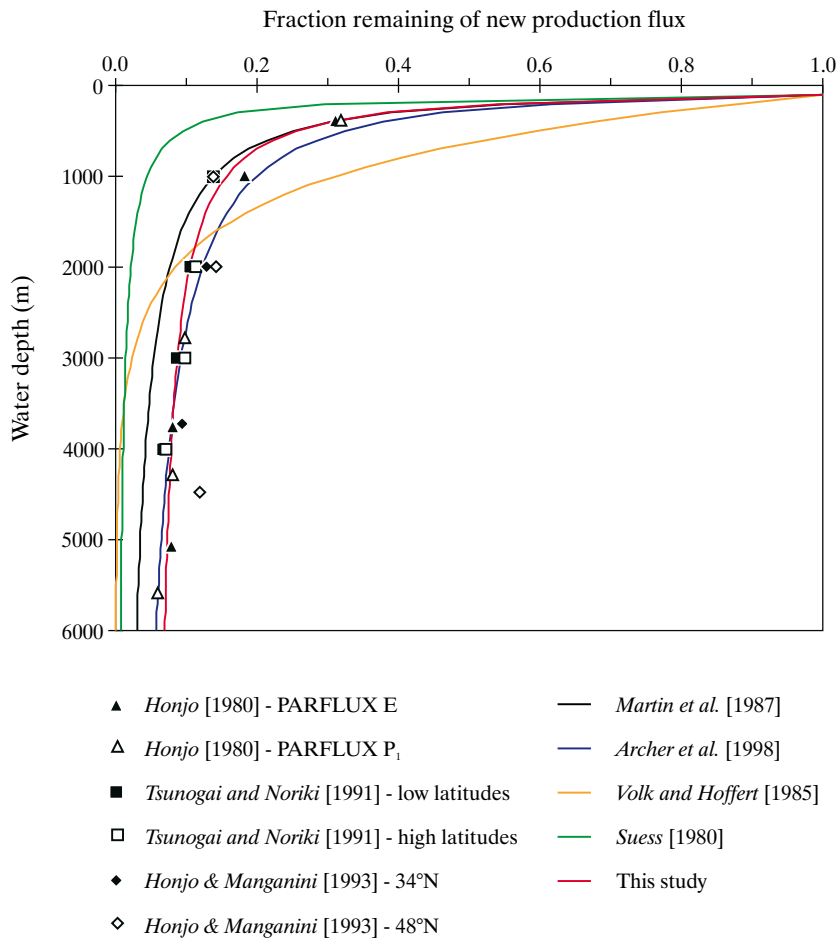


Figure 2-4 Model particulate organic matter remineralization profiles (solid lines) together with observed flux profiles (symbols). Observed profiles comprise a series of discrete flux measurements made by trap deployments over a range of depths. All profiles are normalized to unity at 100 m depth, which for measured profiles is carried out by assuming that the profile in between the shallowest available trap and 100 m depth obeys the *Martin et al.* [1987] curve.

$$F_{set(z)}^{POP} = F_{set(z_0)}^{POP} \cdot$$

$$\left(0.05 + 0.95 \cdot \left(\frac{100 + (z - z_0)}{100} \right)^{-0.950} \right) \quad z > z_0 \quad (2.28b)$$

As shown in Figure 2-4, this gives a reasonable compromise solution, consistent with observations of both mesopelagic and bathypelagic flux profiles.

Constant ratios linking C, Fe, and N to P during the remineralization of POM are assumed throughout the water column, taking values equal to those characterizing mean export production (2-17 to 2-23). The remineralization of POM involves the oxidation of organic compounds, a process that requires the availability of oxygen (or an alternative electron donor). Dissolved oxygen is assumed to be depleted within the water column in a 177:1 molar ratio with the quantity of phosphate released. To prevent depletion of O_2 below zero in regions characterized by poor ventilation

and/or high surface productivity, a minimum threshold is prescribed (taken to be $25 \mu\text{mol kg}^{-1}$) below which no further depletion is allowed. POM continues to be remineralized in the model though, somewhat analogous to remineralization fuelled through denitrification (although nitrogen cycling is not explicitly represented).

2.2.4.2 Calcite

Calcite has been the only polymorph of CaCO_3 explicitly considered in global carbon cycle models to date. Its remineralization within the water column invariably proceeds in accordance with an exponentially decreasing flux profile, taking an e -folding depth sometimes as short as 2 km [*Heinze et al.*, 1999; *Maier-Reimer*, 1993], although studies where model alkalinity fields are fitted to observed data suggest a higher value in the region of 3-3.5 km [*Marchal et al.*, 1998b; *Yamanaka and Tajika*, 1996]. However, *Milliman et al.* [1999] concluded that 40-80% of CaCO_3 export dissolved at depths

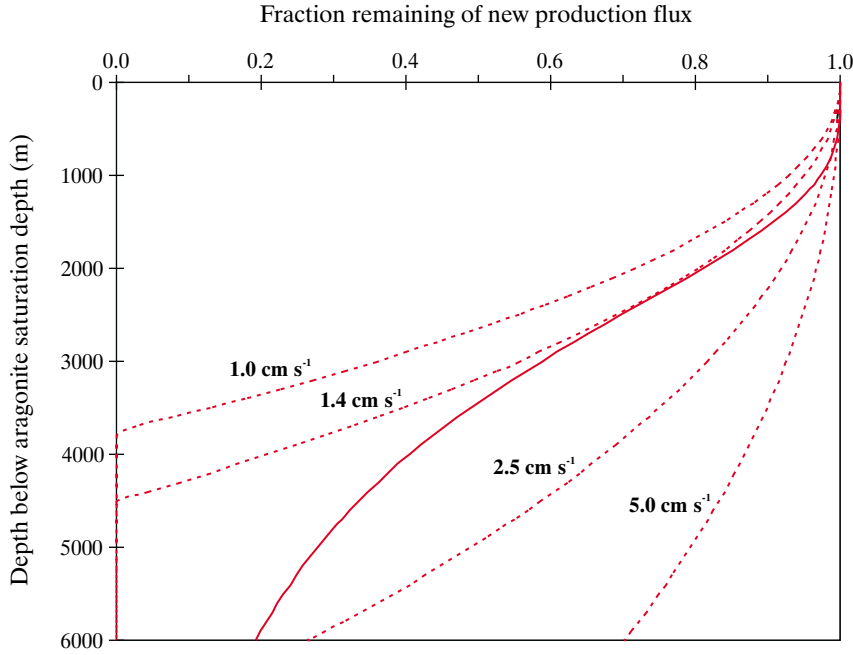


Figure 2-5 Aragonite remineralization profiles for; (a) initial size classes characterized by sinking rates of 1.0, 1.4, 2.5, and 5.0 cm s^{-1} [Byrne *et al.*, 1984] (dashed lines), (b) overall remineralization profile assuming an initial size distribution between these four classes of 2:2:3:3 (solid line).

shallower than about 1 km, while dissolution was inconsequential below this, perhaps due to the rapid dissolution of coccoliths in the guts of grazing zooplankton. This can be parameterized by the assumption of a fixed fraction of calcite export production with reaches the deep ocean without alteration, with the remainder subject to remineralization [Archer *et al.*, 1998]. The magnitude of the remineralizable fraction together with its remineralization scale length are chosen consistent with the general conclusions of Milliman *et al.* [1999], and more specifically, with the sediment trap observations of Martin *et al.* [1993] over the upper-most 1000 m. The calcite settling flux is therefore defined

$$Fset_{(z)}^{\text{calcite}} = Fset_{(z_0)}^{\text{calcite}} \quad z \leq z_0 \quad (2-29a)$$

$$Fset_{(z)}^{\text{calcite}} = Fset_{(z_0)}^{\text{calcite}} \cdot \left(0.4 + 0.6 \cdot e^{\left(\frac{-(z-z_0)}{500} \right)} \right) \quad z > z_0 \quad (2-29b)$$

2.2.4.3 Aragonite

The remineralization of aragonite within the water column is based on the analysis of Byrne *et al.* [1984]. Their theoretical profiles of flux decrease with depth below the aragonite saturation horizon can be reasonably well fitted with a simple power function (Figure 2-5)

$$f_{(z)}^{\text{aragonite}} = f_{(z_{\text{sat}})}^{\text{aragonite}} \cdot \left(1 - \left(\frac{(z - z_{\text{sat}})}{z_l} \right)^2 \right) \quad (2-30)$$

where $f_{(z)}^{\text{aragonite}}$ is the aragonite flux at depth z , $f_{(z_{\text{sat}})}^{\text{aragonite}}$ is the aragonite flux at the base of the photic zone, z_{sat} is the depth of the aragonite saturation horizon, and z_l is a scale depth for remineralization, depending on the initial size/settling rate. A net remineralization profile in the ocean can then be defined given the depth of the aragonite saturation horizon together with an estimate of the initial size distribution of sinking particles. Unfortunately, the latter piece of information is extremely poorly quantified. Aragonite export is therefore assumed to be comprised of a mixture of the four species considered by Byrne *et al.* [1984], *Culierina columnella*, *Limaclina bullmoldes*, *Limacina helicina*, and *Limacina inflata*. The initial export flux is partitioned 2:2:3:3 (by mass) between these, giving 40% of the flux as > 1 mm diameter particles, and 60% as $< 500 \mu\text{m}$, reasonably consistent with observations of aragonite flux size distributions [Berner and Horjo, 1981; Bryne *et al.*, 1984]. The remineralization of each initial class size is summed and the total flux fitted as a function of depth below the aragonite saturation horizon (Figure 2-5). The aragonite settling flux is therefore defined

$$Fset_{(z)}^{aragonite} = Fset_{(z_0)}^{aragonite} \quad z \leq z_{sat} \quad (2-31a)$$

$$Fset_{(z)}^{aragonite} = Fset_{(z_0)}^{aragonite} \cdot \left(1 - \left(\frac{z - z_{sat}}{1000} \right)^{0.25} \cdot \left(1 - e^{\left(\left(\frac{-(z - z_{sat})}{1400} \right)^{4.5} \right)} \right) \right) \quad z > z_{sat} \quad (2-31b)$$

2.2.4.4 Opal

In initial studies incorporating Si cycling into a global carbon cycle model the remineralization of opal within the water column was described with a simple exponential depth function, taking a somewhat arbitrary e -folding length of order 10 km [Heinze *et al.*, 1999; Maier-Reimer, 1993]. More recently, noting the importance of temperature in the control of dissolution rates, Gnanadesikan [1999] proposed a more realistic scheme. In this, the dissolution rate of opal, r^{opal} (d^{-1}) was described by

$$r^{opal} = 1.32 \times 10^{16} \cdot e^{\left(\frac{-11481}{T} \right)} \quad (2-32)$$

where T is the absolute temperature. Opaline particles were assumed to settle through the water column at a uniform rate of 50 $m d^{-1}$. While Erez *et al.* [1982] concluded that variations in silicic acid concentrations were not the main control on opal dissolution rates, this was on the basis of first-order dissolution kinetics, an assumption which has now been called into question [Van Cappellen and Qiu, 1997b]. A new scheme is therefore developed here, able to account explicitly for the dependence of opal remineralization of both ambient temperature and concentration of H_4SiO_4 .

Model formulation

The description of opal remineralization is based empirically on the thermodynamic studies of Van Cappellen and Qiu [1997a,b] (see 3.2.5.1 for more details). Primary controls are assumed to be ambient temperature and the concentration of silicic acid, together with the settling velocity of the material. No account is taken of changes in surface reactivity which may occur during transit down through the water column, such as may arise through a general reduction in surface roughness or the removal of reactive sites at surface defects [Van Cappellen and Qiu, 1997b]. Bacteria may also play an important role in controlling the dissolution rate of diatom frustules, which strongly depends on the presence or absence of a protective organic coating [Bidle and Azam, 1999; Kamatani, 1982]. However, since the bacterial degradation of this layer appears to be substantially complete within a matter of only 1-2 days [Bidle and Azam, 1999], bacterial influence may be confined to pelagic and mesopelagic regions.

The rate of release of silicic acid within an ocean layer l resulting from the dissolution of biogenic opal settling through the water column, $Fdis_{(l)}^{opal}$ ($mol a^{-1}$), is described by

$$Fdis_{(l)}^{opal} = r_{(l)}^{opal} \cdot k_0^{opal} \cdot Fset_{(l)}^{opal} \cdot \Delta t_{(l)} \quad (2-33)$$

where k_0^{opal} is a base opal dissolution rate pertaining to ambient conditions of 0°C and complete under-saturation with respect to the solid phase, $Fset_{(l)}^{opal}$ is the settling flux of opal into the layer ($mol a^{-1}$), and $\Delta t_{(l)}$ is the residence time of this opal within the layer. $r_{(l)}^{opal}$ is a normalized dissolution rate (described in 3.2.5.1) characterized by a Q_{10} value of 2.3 for under-saturated conditions, consistent with the dissolution experiments of Kamatani [1982] and given by

$$r_{(l)}^{opal} = 0.225 \cdot \left(1 + \frac{T_{(l)}}{15} \right) \cdot u_{(l)}^{opal} + 0.775 \cdot \left(\left(1 + \frac{T_{(l)}}{400} \right)^4 \cdot u_{(l)}^{opal} \right)^{9.25} \quad (2-34)$$

where $u_{(l)}^{opal}$ is the degree of under-saturation of the solid phase (3.2.5.1).

The value for K_0^{opal} is derived from observed diatom dissolution rates. From laboratory studies, Nelson *et al.* [1976] found a mean dissolution rate in small centric diatoms under different growth conditions equivalent to 0.134 d^{-1} at 20°C, while two acid-washed coastal species (also measured at 20°C) dissolved at a rate of 0.074 d^{-1} [Kamatani, 1982]. Dissolution rates can also be estimated in the field from observations of the increase in sediment trap head-space [H_4SiO_4]. In this way, Brzezinski and Nelson [1995] calculated the dissolution rate of trapped material at $0.07 \pm 0.03 d^{-1}$ at $\sim 19^\circ C$, while Blain *et al.* [1999] estimated rates of 0.068, 0.085, 0.075, and 0.065 d^{-1} from a series of four different deployment depths. If conditions of complete under-saturation (i.e., $u^{opal} = 1.0$) are assumed, and dissolution rates corrected to $T = 0^\circ C$ (estimated from Levitus *et al.* [1994c] where not reported) and taking a Q_{10} value of 2.3, a mean value across all these studies of 0.019 d^{-1} is obtained.

Analysis of sediment trap series suggests settling rates of opal material ranging from 32 to 200 $m d^{-1}$ [Blain *et al.*, 1999; Honjo and Manganini, 1993; Takahashi, 1986]. In the absence of any tighter observational constraint a uniform sinking rate of 125 $m d^{-1}$ is assumed following Pondaven *et al.* [1998]. The residence time $\Delta t_{(l)}$ (d) is then given by

$$\Delta t_{(l)} = \frac{th_{(l)}}{125} \quad (2-35)$$

where $th_{(l)}$ is the thickness (m) of the l th ocean layer.

Model evaluation

A number of studies have reported opal settling fluxes at multiple depths measured at the same geographical location, which in theory could be used to validate the remineralization model. However, there are a number of serious complications in the interpretation of opal sediment trap observations which are likely to significantly reduce their utility in such validation;

- Since the ocean is everywhere under-saturated with respect to biogenic opal, opal caught in sediment traps will continue to dissolve throughout the period of trap deployment. While recent studies make use of traps that

have been filled with high density brine solution in order to help quantify *in situ* dissolution (Blain *et al.* [1999]; Brzezinski and Nelson [1995]; Honjo and Manganini [1993]), early studies took no account of such losses (Honjo [1980]; Noriki and Tsunogai [1986]; Takahashi [1986]). Thus, account must be taken of the potential for the underestimation of settling fluxes by less sophisticated trap designs.

- Sinking fluxes may be modified by the random mesoscale eddy field through which the particles settle [Siegel *et al.*, 1990], an effect which can be manifested as an 'inverted' flux profiles (i.e., where measured fluxes *increase* with depth despite continued dissolution). Even where flux measurements have been made by free-floating traps (e.g., Blain *et al.* [1999]) there is likely to be some residual hydrodynamic distortion.
- Temporal variability in export production (such as associated with phytoplankton blooms) may cause problems in short term trap deployments. For instance, flux profiles which strongly increase with depth can arise should the traps be deployed at such a time that the uppermost trap samples post-bloom conditions while deeper ones still sample bloom conditions.
- In mesopelagic trap deployments, increased capture rates of radiolarians with depth may also produce inverted-type profiles [Blain *et al.*, 1999].
- Any decrease in surface reactivity as opal dissolves in the water column may lead to the influence of surface to deep contrasts in ambient temperature and $[H_4SiO_4]$ being overestimated. In particular, the microbial degradation of protective organic coatings on diatom frustules [Bidle and Azam, 1999; Kamatani, 1982] may significantly bias measurements made by near-surface trap deployments.

Studies reporting opal settling flux profiles used in the validation of the water-column dissolution model are detailed in Table 2-4 and the data shown in Figure 2-6. These data sets have been selected on the basis of there being no obvious distortion due to hydrodynamical or seasonal factors. For instance, some studies report a strongly increasing trend of $CaCO_3$ flux with depth [Honjo, 1980; Honjo and Manganini, 1993], suggestive of hydrodynamical distortion, while the character of the flux profile recorded by Brzezinski and Nelson [1995] associated with a bloom event

was noticeably different to that observed during the remainder of the year. These are therefore omitted from further consideration.

The water column opal remineralization scheme (2-33) is run for each of the validation sites. Temperature and $[H_4SiO_4]$ profiles in the water column for these locations are taken from Levitus *et al.* [1994c] and Conkright *et al.* [1994], respectively. A base dissolution rate constant (K_0^{opal}) of $0.019 d^{-1}$ is assumed, along with a uniform settling rate of $125 m$. The mean residence time of opal in the traps is taken to be equal to half of the total trap collection time. Opal dissolves continuously according to ambient conditions during this period and is assumed 'lost' in cases where the corresponding sediment trap measurements take no account of *in situ* dissolution. Predicted apparent settling fluxes (i.e., simulated measurements) are shown in Figure 2-6a. While the model is generally successful in approximating the apparent depth-invariance observed in many of the sediment trap studies, there are notable failures. Firstly, there is a pronounced intermediate-depth maximum in profile #2 whose magnitude is not well reproduced by the model. However, this profile can be reproduced by doubling the value of K_0^{opal} to 0.038, only slightly higher than the range of reported dissolution rates allow for. Secondly, dissolution in series #5 is seriously overestimated. In this case the profile can only be reproduced with a combination of lower values for both K_0^{opal} and settling velocity. Interestingly, the magnitude of the dissolution rate constant so required is similar to that observed from kinetic studies on core-top opal [Van Cappellen and Qiu, 1997b]. It is possible that the unusually long trap deployment period (98 days) [Honjo, 1980; Honjo *et al.*, 1982] might have resulted in geochemical conditions within the layer of accumulating trap material approaching that found in the benthic environment. If so, a combination of the presence of detrital silicate matter and local enrichment in ambient $[H_4SiO_4]$ may be acting so as to suppress the dissolution rate.

For comparison, the equivalent model predictions using the parameterization of Gnanadesikan [1999] are shown in Figure 2-6b. While some of the sediment trap data is consistent with this model over the upper most ~2500 m of the water column, there is a prominent negative trend with depth below this, contrary to observations. An improved fit is possible if a more rapid settling rate is adopted, although it is beyond this particular scheme's capability to fit either of data sets #2 and #5, regardless of assumptions made regarding settling rate.

Predicted opal remineralization profiles for the same six locations (Table 2-4) are shown in Figure 2-7. It can be seen that there are interesting regional contrasts in the degree of remineralization which occurs within the water column. The lowest degrees of remineralization are predicted for regions characterized by relatively low temperatures and high concentrations of silicic acid throughout the water column, such as found in the north Pacific (#6) and the Southern Ocean (#1). In contrast, a relative high degree of remineralization occurs throughout the water column in the low- and mid-latitude Atlantic (#4 and #5) where, despite temperatures rapidly decreasing with depth below the

Table 2-4 Biogenic Opal Flux Sediment Trap Data

Identifier	Location	Reference
#1	61.5°S, 150.5°E	Noriki and Tsunogai [1986]
#2	31.7°N, 124.6°W	Noriki and Tsunogai [1986]
#3	17.5°N, 117.0°W	Noriki and Tsunogai [1986]
#4	34°N, 21°W	Honjo and Manganini [1993]
#5	13°N, 54°W	Honjo [1980], Honjo <i>et al.</i> [1982]
#6	50°N, 145°W	Takahashi [1986]

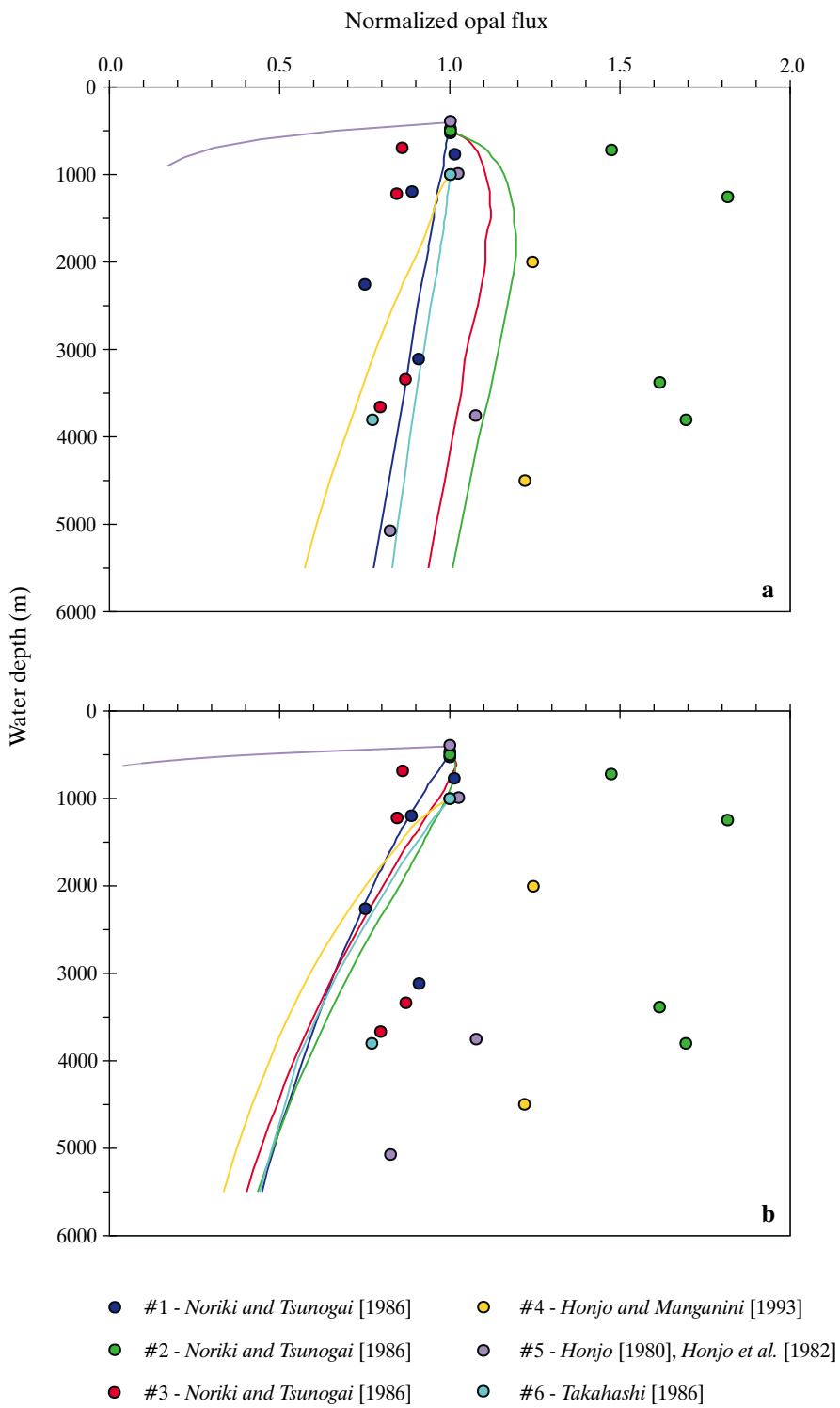


Figure 2-6 Apparent opal settling fluxes recorded by arrays of sediment traps, normalized to the value recorded in the uppermost trap of each array (filled symbols) and compared with model-predicted opal fluxes, normalized in a similar way (solid lines of a corresponding colour). Model results are shown for both the scheme developed here (a), and that of Gnanadesikan [1999] (b).

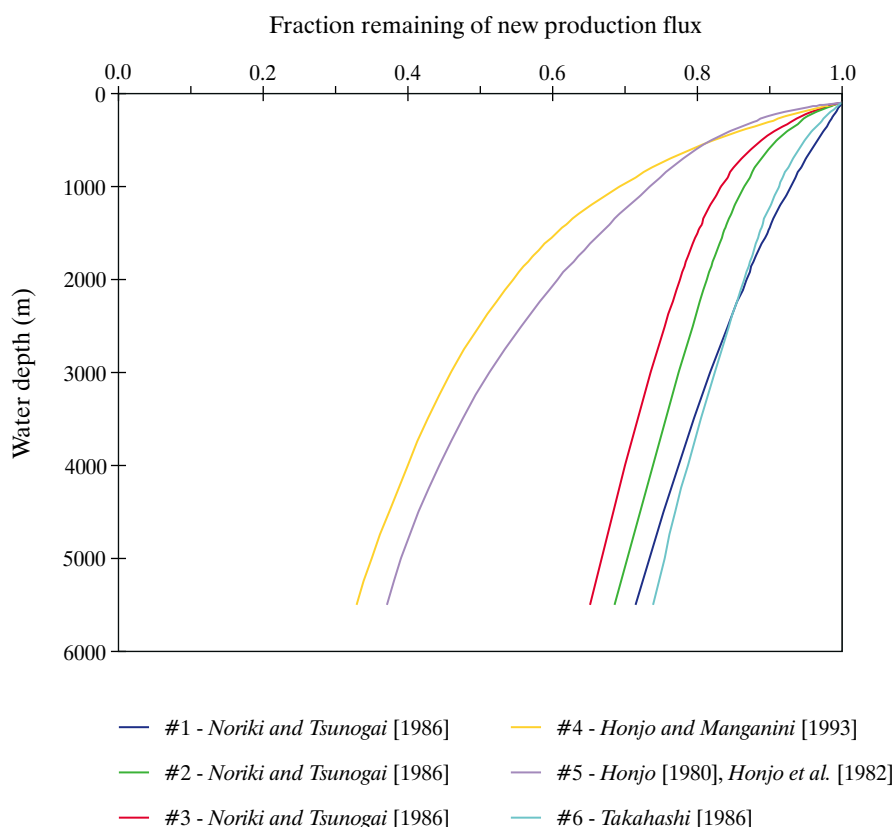


Figure 2-7 Model-predicted opal dissolution profiles, for each of the site locations detailed in Table 2-4. Opal rain rates are normalized to the flux at 100 m depth.

surface, $[H_4SiO_4]$ remains comparatively low and thus conditions highly under-saturated. Low- and mid-latitude Pacific regions (#2 and #3) are also characterized by high temperatures and low $[H_4SiO_4]$ at the surface. However, little remineralization occurs below the mesopelagic zone despite cold, high $[H_4SiO_4]$ deep ocean conditions.

2.2.5 Iron biogeochemical cycling

The behaviour of iron in the ocean is highly complex, involving transformations between various particulate, dissolved, and complexed phases [Donaghay et al., 1991; Johnson et al., 1997; Gerringa et al., 2000]. The dynamic equilibrium state of such a system is strongly affected by such factors as pH [Jickells, 1999; Jickells and Spokes, in press; Kuma et al., 1996], temperature, insolation levels [Jickells and Spokes, in press; Kuma et al., 1996; Sunda and Huntsman, 1995], and the presence of organic compounds able to bind to Fe (ligands) [Johnson et al., 1997; Rue and Bruland, 1997; Sunda and Huntsman, 1995]. Qualitative knowledge regarding the role of these (and further) factors is currently still in its infancy. SUE therefore considers a single 'total

dissolved' iron phase, substantially equivalent to the operational definition in ocean Fe measurements [de Baar and de Jong, in press]. In this way, the values of Fe-related variables and parameters in the model should be directly comparable to those measured in both the ocean and laboratory seawater systems.

On the basis of the similarity between observed profiles of dissolved iron and nitrate in the upper 2000 m of the water column, the first-order biogeochemical behaviour of iron in the ocean has been considered to parallel that of other organic nutrients (PO_4 and NO_3) [Johnson et al., 1997]. That is to say, like PO_4 and NO_3 , Fe is taken up in a set ratio with carbon by phytoplankton (2-20, 2-23), exported as a component of (particulate) organic matter from the euphotic zone, and subsequently released back into dissolved form during remineralization within the water column. In common with other model studies [Archer and Johnson, 2000; Lefèvre, and Watson, 1999; Watson and Lefèvre, 1999], therefore, the basic biogeochemical scheme used for Fe follows that for PO_4 . However, the extremely low solubility and high reactivity of free Fe in solution under typical seawater conditions results in it being readily scavenged out of

solution by the rain of particulate debris settling through the water column [Johnson *et al.*, 1997]. This scavenging has previously been represented by a simple characteristic residence time for dissolved Fe, assumed to be uniform in value throughout the ocean [Archer and Johnson, 2000; Johnson *et al.*, 1997; Lefèvre and Watson, 1999]. Intuitively, though, the scavenging rate should be directly related to the flux density of settling particulate material. SUE therefore scales local residence times inversely with particulate flux densities. Previous studies have also considered the ubiquitous presence of a Fe-binding ligand [Archer and Johnson, 2000; Lefèvre and Watson, 1999; Watson and Lefèvre, 1999], which acts so as to effectively prevent any further scavenging when Fe concentrations fall below that of the ligand [Johnson *et al.*, 1997]. While the action of ligands in retaining Fe in solution, particularly in the surface ocean is undoubtedly critical [Rue and Bruland, 1997], the exact nature, global distribution, and lifetime of these compounds is still far from being adequately elucidated. The presence of Fe-binding ligands is therefore omitted from the current model. Fe previously scavenged higher up in the water column is released back into solution if the host material is remineralized.

In the ocean interior the total change in the Fe inventory of each ocean cell (mol a⁻¹) can be written

$$\Delta M_{\text{tot}}^{\text{Fe}} = \Delta M_{\text{ocn}}^{\text{Fe}} + \Delta M_{\text{remin}}^{\text{Fe}} - \Delta M_{\text{scav}}^{\text{Fe}} \quad (2-36)$$

where $\Delta M_{\text{ocn}}^{\text{Fe}}$ is the net change due to ocean advection, convective adjustments, and (horizontal and vertical) diffusivity, and $\Delta M_{\text{remin}}^{\text{Fe}}$ represents Fe both liberated from organic compounds through the remineralization of POM and from Fe scavenged by particulate matter further up in the water column and subsequently released through the remineralization of the scavenger substrate. $\Delta M_{\text{remin}}^{\text{Fe}}$ is defined

$$\begin{aligned} \Delta M_{\text{remin}}^{\text{Fe}} = & r^{\text{POFe:POC}} \cdot \left(F_{\text{set}_{\text{in}}}^{\text{POC}} - F_{\text{set}_{\text{out}}}^{\text{POC}} \right) + \\ & \frac{F_{\text{set}_{\text{in}}}^{\text{POC}} - F_{\text{set}_{\text{out}}}^{\text{POC}}}{F_{\text{set}_{\text{in}}}^{\text{POC}}} \cdot F_{\text{scav}_{\text{POC,in}}}^{\text{Fe}} + \\ & \frac{F_{\text{set}_{\text{in}}}^{\text{opal}} - F_{\text{set}_{\text{out}}}^{\text{opal}}}{F_{\text{set}_{\text{in}}}^{\text{opal}}} \cdot F_{\text{scav}_{\text{opal,in}}}^{\text{Fe}} + \\ & \frac{F_{\text{set}_{\text{in}}}^{\text{cal}} - F_{\text{set}_{\text{out}}}^{\text{cal}}}{F_{\text{set}_{\text{in}}}^{\text{cal}}} \cdot F_{\text{scav}_{\text{cal,in}}}^{\text{Fe}} + \\ & \frac{F_{\text{set}_{\text{in}}}^{\text{arg}} - F_{\text{set}_{\text{out}}}^{\text{arg}}}{F_{\text{set}_{\text{in}}}^{\text{arg}}} \cdot F_{\text{scav}_{\text{arg,in}}}^{\text{Fe}} \end{aligned} \quad (2-37)$$

where $r^{\text{POFe:POC}}$ is the mean ratio of Fe:C in POM, and $F_{\text{set}_{\text{in}}}^{\text{POC}}$ and $F_{\text{set}_{\text{out}}}^{\text{POC}}$ are the settling fluxes of POC into and out of the cell, respectively (mol a⁻¹). $F_{\text{scav}_{\text{POC,in}}}^{\text{Fe}}$ is the flux of scavenged Fe associated with POC into the cell, with the scavenged fluxes associated with opal (“opal”), calcite (“cal”), and aragonite (“arg”), similarly designated.

$\Delta M_{\text{scav}}^{\text{Fe}}$ is the loss (mol a⁻¹) of Fe due to scavenging by settling particulate matter

$$\begin{aligned} \Delta M_{\text{scav}}^{\text{Fe}} = & k_{\text{scav}_{\text{POC}}}^{\text{Fe}} \cdot f_{\text{set}_{\text{out}}}^{\text{POC}} \cdot M^{\text{Fe}} + \\ & k_{\text{scav}_{\text{opal}}}^{\text{Fe}} \cdot f_{\text{set}_{\text{out}}}^{\text{opal}} \cdot M^{\text{Fe}} + \\ & k_{\text{scav}_{\text{cal}}}^{\text{Fe}} \cdot f_{\text{set}_{\text{out}}}^{\text{cal}} \cdot M^{\text{Fe}} + \\ & k_{\text{scav}_{\text{arg}}}^{\text{Fe}} \cdot f_{\text{set}_{\text{out}}}^{\text{arg}} \cdot M^{\text{Fe}} \end{aligned} \quad (2-38)$$

where $k_{\text{scav}_{\text{POC}}}^{\text{Fe}}$ is the scavenging rate of Fe by POC (a⁻¹ (mol m⁻² a⁻¹)⁻¹), with scavenging rates associated with opal (“opal”), calcite (“cal”), and aragonite (“arg”), similarly designated, and M the inventory of Fe within the cell (mol). $f_{\text{set}_{\text{out}}}^{\text{POM}}$ is the particulate matter flux density out of the cell (mol m⁻² a⁻¹) defined by

$$f_{\text{set}_{\text{out}}}^{\text{Fe}} = \frac{F_{\text{set}_{\text{out}}}^{\text{Fe}}}{A} \quad (2-39)$$

where A is the horizontal cross-sectional area of the cell (m²).

For the surface ocean layer, the mass balance is

$$\Delta M_{\text{tot}}^{\text{Fe}} = \Delta M_{\text{ocn}}^{\text{Fe}} + \Delta M_{\text{aeolian}}^{\text{Fe}} - \Delta M_{\text{scav}}^{\text{Fe}} - \Delta M_{\text{np}}^{\text{Fe}} \quad (2-40)$$

where $\Delta M_{\text{aeolian}}^{\text{Fe}}$ is the aeolian input of dissolved Fe from dust deposited to the surface, and $\Delta M_{\text{np}}^{\text{Fe}}$ is the loss of Fe due to biological uptake (and subsequent export)

$$\Delta M_{\text{np}}^{\text{Fe}} = r^{\text{POFe:POC}} \cdot F_{\text{np}}^{\text{POC}} \quad (2-41)$$

where $F_{\text{np}}^{\text{POC}}$ is the export flux of POC from the surface.

The aeolian input of dissolved Fe, $\Delta M_{\text{aeolian}}^{\text{Fe}}$ can be simply written

$$\Delta M_{\text{aeolian}}^{\text{Fe}} = \frac{1}{55.6} \cdot F_{\text{esol}}^{\text{dust}} \cdot F_{\text{frac}}^{\text{dust}} \cdot F_{\text{dep}}^{\text{dust}} \quad (2-42)$$

where $F_{\text{esol}}^{\text{dust}}$ is the mass fraction of aeolian Fe soluble in sea water, $F_{\text{frac}}^{\text{dust}}$ is the mass fraction of Fe in aeolian dust, and $F_{\text{dep}}^{\text{dust}}$ is the deposition flux of dust to the surface ocean (g a⁻¹). The mean relative atomic mass of Fe, used to convert between mass and molar fluxes is taken to be 55.8 g mol⁻¹.

The mass fraction of Fe in aeolian dust ($F_{\text{frac}}^{\text{dust}}$) can be reasonably assumed to be equal to the mean crustal abundance of 3.5% [Duce and Tindale, 1991]. However, estimating a representative global value for $F_{\text{esol}}^{\text{dust}}$ is much more problematic. Indeed, estimates reported for the solubility of aerosol Fe range over a full 3 orders of magnitude from <0.013 % to 55% [Jickells and Spokes, in press]. The most important controlling factor in determining overall solubility of Fe in sea water is likely to relate to the balance of aeolian material deposited between ‘wet’ and ‘dry’ deposition routes, as the solubility of Fe in rainwater (~14%) is considerably higher than that of Fe in seawater (0.1-1.0%) [Jickells and Spokes, in press]. However, the effective solubility of Fe in sea water via the ‘wet’ deposition route is reduced by the precipitation of insoluble iron

(hydr-)oxide phases associated with the pH change, to perhaps ~0.3-6.8% [Jickells and Spokes, in press; Spokes and Jickells, 1996]. Final solubility is also likely to be affected by the degree of remoteness of an oceanic region from dust source area, as the lability of iron in aerosols is enhanced through pH cycling within clouds [Spokes and Jickells, 1996]. Given these complications together with uncertainties regarding the balance between wet and dry dust deposition routes, $Fesol^{dust}$ is treated as an optimizable parameter, whose value(s) is chosen in order to be broadly consistent with the estimate of global mean solubility of Jickells and Spokes [in press] (0.8-2.1%).

A second important factor affecting overall aerosol iron solubility concerns the degree of system loading. For instance, Zhuang *et al.* [1990] showed that the soluble metal fraction decreased dramatically with increasing total iron content in seawater, while Spokes and Jickells [1996] found that solution concentrations were highly nonlinear with particulate loading. These effects may be related to (re-)adsorption of dissolved iron onto aerosol surfaces [Chester *et al.*, 1993]. A degree of 'self-scavenging' by aerosols in the ocean surface layer is therefore implemented in SUE. This implicitly produces an apparent Fe solubility which exhibits an inverse dependence on both [Fe] and dust flux, qualitatively consistent with observations. The surface ocean Fe mass balance (2-42) is now modified

$$\Delta M_{aeolian}^{Fe} = \frac{1}{55.6} \cdot Fesol^{dust} \cdot Ffrac^{dust} \cdot Fdep^{dust} - kscav_{dust}^{Fe} \cdot fdep^{dust} \cdot M^{Fe} \quad (2-43)$$

where $kscav_{dust}^{Fe}$ is a 'self-scavenging' rate constant (in units of $a^{-1} (g m^{-2} a^{-1})^{-1}$), and $fdep^{dust}$ is the dust deposition flux density ($g m^{-2} a^{-1}$) defined by

$$fdep^{dust} = \frac{Fdep^{dust}}{A} \quad (2-44)$$

Finally, aeolian iron not dissolved in the surface ocean is assumed to pass through the water column without further dissolution.

2.2.6 Carbon-13

As an aid to elucidating the function of the present-day global carbon cycle together with the causes of glacial-interglacial change, all major ^{13}C fractionation processes are represented within SUE. These relate to the dissolution equilibria within the aqueous carbonate system, biological fixation of both organic and inorganic carbon, and air-sea gas exchange.

In the subsequent sections, the following conventions will be adopted. From the ratio of the concentration of ^{13}C to ^{12}C in bulk matter

$$R(C) = \frac{[^{13}C]}{[^{12}C]} \quad (2-45)$$

a fractionation factor is defined for any process, α where the chemical or physical state of carbon is transformed

$$\alpha(C \rightarrow C') = \frac{R(C)}{R(C')} \quad (2-46)$$

The fractionation associated with this process is more commonly written

$$\varepsilon = \alpha - 1 \quad (2-47)$$

where ε is quoted in units per mil (‰).

2.2.6.1 Fractionation within the aqueous carbonate system

The equilibrium partitioning of ^{13}C between the three primary reservoirs of the aqueous carbonate system is calculated explicitly (Figure 2-8). In this treatment, the net ^{13}C isotopic signature of $CO_{2(aq)}$ ($\delta^{13}C^{CO_{2(aq)}}$) is derived from bulk DIC ($\delta^{13}C^{DIC}$) by considering the fractionation with respect to both HCO_3^- and CO_3^{2-} and calculated in proportion to their relative aqueous concentrations [Marchal *et al.*, 1998b; Yamanaka and Tajika, 1996]. Although Zhang *et al.* [1995] suggested that the presence of ion complexes in seawater prevent this simple approach being valid, the error in this method is <0.2‰ under typical oceanic conditions. This scheme has the advantage over the use of a single empirical temperature-dependent function linking $\delta^{13}C^{CO_{2(aq)}}$ and $\delta^{13}C^{DIC}$ (e.g., Mook *et al.* [1974]) in that it is able to additionally account for the influence on $\delta^{13}C^{CO_{2(aq)}}$ of changes in ALK, DIC, and pressure (depth).

Equilibrium fractionation factors within the surface ocean carbonate system are adapted from Zhang *et al.* [1995], with fractionations α_1 and α_2 derived by correcting the observed fractionations $HCO_3^- \rightarrow CO_{2(g)}$ and $CO_3^{2-} \rightarrow CO_{2(g)}$, respectively, for the dissolution fractionation between $CO_{2(g)}$ and $CO_{2(aq)}$ (α_β). Writing in per mil notation, these become

$$\varepsilon_1 = -41.92 + 0.114 \cdot T \quad (2-48)$$

$$\varepsilon_2 = -24.07 + 0.057 \cdot T \quad (2-49)$$

where T is the ambient temperature (K). The fractionation between DIC and $CO_{2(aq)}$ can then be estimated from

$$\varepsilon_\Sigma = \frac{\varepsilon_1 \cdot [HCO_3^-] + \varepsilon_2 \cdot [CO_3^{2-}]}{[CO_2] + [HCO_3^-] + [CO_3^{2-}]} \quad (2-50)$$

2.2.6.2 Fractionation during ocean-atmosphere gas exchange

The one-way ocean \rightarrow atmosphere and atmosphere \rightarrow ocean fractionation factors, $\alpha_{o \rightarrow a}$ and $\alpha_{a \rightarrow o}$, respectively (Figure 2-8) are defined [Siegenthaler and Munnich, 1981]

$$\alpha_{o \rightarrow a} \equiv \alpha_\Sigma \cdot \alpha_k \quad (2-51)$$

$$\alpha_{a \rightarrow o} \equiv \alpha_\beta \cdot \alpha_k \quad (2-52)$$

where α_β is the equilibrium CO_2 solubility fractionation factor [Zhang *et al.*, 1995], equivalent to

$$\varepsilon_{\beta} = -2.65 + 0.005 \cdot T \quad (2-53)$$

and α_k is the kinetic fractionation factor associated with CO_2 diffusion across the boundary layer. A value of -0.88‰ is assumed for ε_k , consistent with both the experimental measurements of *Zhang et al.* [1995] and theoretical calculation of *Siegenthaler and Munnich* [1981]. A (sea water) correction is made to $\varepsilon_{a \rightarrow o}$ [*Zhang et al.*, 1995], to give final descriptions for one-way ocean \rightarrow atmosphere and atmosphere \rightarrow ocean fractionation

$$\varepsilon_{o \rightarrow a} = \varepsilon_{\Sigma} - 0.88\text{‰} \quad (2-54)$$

$$\varepsilon_{a \rightarrow o} = \varepsilon_{\beta} - 1.08\text{‰} \quad (2-55)$$

2.2.6.3 Fractionation during biological fixation of organic carbon

The fractionation of ^{13}C during the formation of organic matter in the surface ocean is usually described by a fixed factor, typically assigned a value between -20 and -22‰ in global carbon cycle models [*Heinze*, 1994; *Maier-Reimer*, 1993; *Yamanaka and Tajika*, 1996]. However, the isotopic signature of organic constituents in marine plankton appears to vary strongly as a function of both latitude and SST [*Rau et al.*, 1989] against a background of relatively constant $\delta^{13}\text{C}^{\text{DIC}}$. Recent field and experimental observations suggests that the ambient concentration of $\text{CO}_{2(\text{aq})}$ (itself a function of temperature) is a more important denominator [*Rau et al.*, 1992]. The isotopic composition of POC ($\delta^{13}\text{C}^{\text{POC}}$) is therefore parameterized with an explicit dependence on $[\text{CO}_{2(\text{aq})}]$. The model of *Rea et al.* [1996] is adapted, assuming that the isotopic signature of exported POC reflects that of phytoplankton biomass. $\delta^{13}\text{C}^{\text{POC}}$ is therefore defined

$$\delta^{13}\text{C}^{\text{POC}} = \delta^{13}\text{C}^{\text{CO}_{2(\text{aq})}} - \varepsilon_f + (\varepsilon_f - \varepsilon_d) \cdot \frac{Q_s}{c_e} \cdot \left(\frac{r}{D_T \cdot (1 + r/r_k)} + \frac{1}{P} \right) \quad (2-56)$$

Where ε_f and ε_d are fractionation factors associated with enzymic intercellular C fixation and $\text{CO}_{2(\text{aq})}$ diffusion, respectively, c_e is the ambient concentration of $\text{CO}_{2(\text{aq})}$ (in units of mol m^{-3}), r is the surface area equivalent cell radius, r_k is the reacto-diffusive length, Q_s the $\text{CO}_{2(\text{aq})}$ uptake rate per cell surface area, P is the cell wall permeability to $\text{CO}_{2(\text{aq})}$, and D_T is the temperature-sensitive diffusivity of $\text{CO}_{2(\text{aq})}$ in seawater given by

$$D_T = 5019 \times 10^{-6} \cdot e^{\left(\frac{-E_d}{RT} \right)} \quad (2-57)$$

where E_d is the activation energy of diffusion, R is the gas constant, and T the temperature (K). Parameter values are those used by *Rea et al.* [1996], with the exception of r and Q_s which follow *Rea et al.* [1997]. These parameters are summarized in Table 2-5.

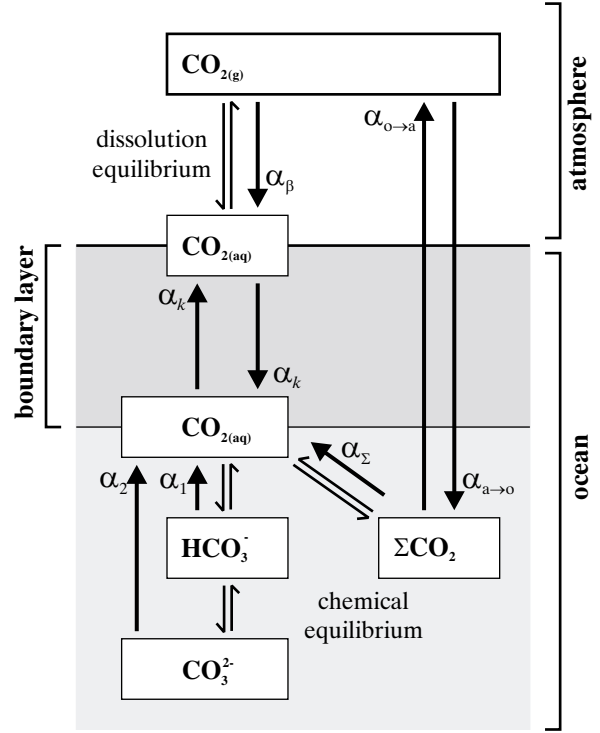


Figure 2-8 Schematic diagram of ocean-atmosphere ^{13}C and aqueous carbonate system fractionation, adapted from *Yamanaka and Tajika* [1996].

The description of $\delta^{13}\text{C}^{\text{POC}}$ (2-56) can be simplified

$$\delta^{13}\text{C}^{\text{POC}} = \delta^{13}\text{C}^{\text{CO}_{2(\text{aq})}} - \varepsilon_f + (\varepsilon_f - \varepsilon_d) \cdot \frac{K_Q}{[\text{CO}_{2(\text{aq})}]} \quad (2-58)$$

where

$$K_Q = 1027 \cdot Q_s \cdot \left(\frac{r}{D_T \cdot (1 + r/r_k)} + \frac{1}{P} \right) \quad (2-59)$$

and with $[\text{CO}_{2(\text{aq})}]$ now in units of mol kg^{-1} . Finally, K_Q is approximated assuming that factors such as cell size are invariant

$$K_Q = 2.829 \times 10^{-10} - 1.788 \times 10^{-7} \cdot T + 3.170 \times 10^{-5} \cdot T^2 \quad (2-60)$$

Despite the scheme of *Rau et al.* [1996,7] being able to successfully explain the main observational $\delta^{13}\text{C}^{\text{POC}}$ trend in the ocean, variations in $[\text{CO}_{2(\text{aq})}]$ alone cannot account for the residual scatter and the more extreme outlying values [*Goericke and Fry*, 1994; *Rau et al.*, 1989, 1997]. Variability in vital factors such as cell size, growth rate, cell membrane

permeability, and diffusion rate will all affect the intercellular availability of $\text{CO}_{2(\text{aq})}$ and thus overall fractionation [Hinga *et al.*, 1994]. Unfortunately, such parameters are not available in the simple biological model employed in SUE. However, since the biological scheme does differentiate between two distinct classes of phytoplankton (siliceous and non-siliceous) it is possible to represent species-specific factors, at least to a first order. While Rau *et al.* [1996, 1997] adopt an intermediate value of 25‰ for the enzymatic isotope fractionation factor associated with intracellular C fixation (ϵ_f), they note that it may actually range from 20 to 29‰. Indeed, Hinga *et al.* [1994] observed that $\delta^{13}\text{C}^{\text{POC}}$ in the diatom *Skeletonema costatum* was lower by some 8-10% compared to the coccolithophorid *Emiliania huxleyi* under identical growth conditions, possibly largely due to species differences in carbon fixation pathways [Falkowski, 1991]. Different values of ϵ_f associated with the two different classes of phytoplankton are therefore adopted, taking default values of 25% and 20%, for siliceous and non-siliceous classes, respectively.

2.2.6.4 Fractionation during the formation of calcium carbonate

The formation of the carbonate tests of coccolithophorids and foraminifera and the shells of pteropods typically involves a degree of ^{13}C fractionation an order of magnitude less than that in the fixation of organic carbon. The ‘carbonate pump’ (2.1.1) therefore plays only a relatively minor role in determining spatial heterogeneity in $\delta^{13}\text{C}^{\text{DIC}}$ compared to action of the ‘soft tissue pump’. However, since the permanent removal of carbon from the ocean is predominantly in the form of CaCO_3 [Sarmiento and Sundquist, 1992], CaCO_3 cycling is likely to be important in the long-term (glacial-interglacial) regulation of ^{13}C in the system. For this reason alone it is necessary to represent the fractionation $\text{DIC} \rightarrow \text{CaCO}_3$. To reproduce paleoceanographic foraminiferal $\delta^{13}\text{C}$ tracer signals observed in deep-sea sediments will also require a realistic treatment of the fractionation pathway $\text{DIC} \rightarrow \text{CaCO}_3^{\text{foram}}$.

Coccolith calcite and pteropod aragonite is assumed to make up bulk sedimentary CaCO_3 . Simple

temperature-dependent fractionation following Mook [1986] is assumed for this

$$\epsilon_{\text{HCO}_3^-(\text{aq}) \rightarrow \text{CaCO}_3^{\text{cal}}} = \frac{4232.0}{T} + 1510 \quad (2-61a)$$

$$\epsilon_{\text{HCO}_3^-(\text{aq}) \rightarrow \text{CaCO}_3^{\text{arg}}} = \frac{4232.0}{T} + 16.90 \quad (2-61b)$$

In contrast, foraminiferal calcite is assumed not to contribute to the bulk sediment, but instead is treated as a tracer tied to bulk calcite (and as such does not contribute to mass transfer within the system). The simplest description of foraminiferal calcite $\delta^{13}\text{C}$ would be to assume an identical fractionation behaviour to bulk calcite. However, recent culture and modelling studies [Spero *et al.*, 1997; Wolf-Gladrow *et al.*, 1999a,b; Zeebe *et al.*, 1999] suggest that the concentration of carbonate ions ($[\text{CO}_3^{2-}]$) has an important controlling influence on fractionation. Empirically-determined relationships linking planktonic foraminiferal $\delta^{13}\text{C}$ to $[\text{CO}_3^{2-}]$ under conditions of constant DIC [Spero *et al.*, 1997] are therefore adopted (with reported shell $\delta^{13}\text{C}$ corrected for experimental $\delta^{13}\text{C}^{\text{DIC}}$). For the spinose *Orbulina universa*, $\delta^{13}\text{C}^{\text{cal}}$ is taken to be the mean of high light and dark responses (in a 50:50 proportion), while for the non-spinose *Globigerina bulloides*, $\delta^{13}\text{C}^{\text{cal}}$ is taken to be the mean of 12th and 13th chamber values [Spero *et al.*, 1997]. For *Orbulina universa* the resulting $\text{DIC} \rightarrow \text{CaCO}_3^{\text{foram}}$ fractionation can be written

$$\epsilon_{\Sigma\text{CO}_2 \rightarrow \text{CaCO}_3^{\text{foram}}} = +1.795 - 0.006 \cdot [\text{CO}_3^{2-}] \text{‰} \quad (2-62)$$

while for *Globigerina bulloides* it is

$$\epsilon_{\Sigma\text{CO}_2 \rightarrow \text{CaCO}_3^{\text{foram}}} = -0.135 - 0.013 \cdot [\text{CO}_3^{2-}] \text{‰} \quad (2-63)$$

where $[\text{CO}_3^{2-}]$ is the carbonate ion concentration in units of $\mu\text{mol kg}^{-1}$. As a default, *Globigerina bulloides* is assumed to represent the planktonic foraminiferal tracer in SUE. In the absence of comparable experimental data for benthic species the relationship for *Globigerina bulloides* is also used for the benthic foraminiferal tracer.

Table 2-5 Parameters Used in the ^{13}C POC Fractionation Model

Parameter	Value	Units
ϵ_f	20 to 29	‰
ϵ_d	0.7 ¹	‰
Q_s	1.62×10 ⁻⁷	mol C m ⁻² s ⁻¹
r	5.00×10 ⁻⁵	m
E_d	19510	J mol ⁻¹
R	8.3143	J K ⁻¹ mol ⁻¹

¹ ϵ_d has a small temperature dependence in reality, but is assumed here to be constant.

The simulation of deep-sea sediments

3.1 Introduction

Deep-sea sediments play a critical role in global biogeochemical cycles. Particulate material delivered to, or formed at the ocean surface and which is not removed whilst settling through the water column will eventually reach the ocean floor, forming a surficial 'fluff' layer at the ocean-sediment interface. Much of this material undergoes diagenetic alteration as it is gradually incorporated deeper into the sediments. Such post-depositional changes involve a multitude of interacting physical (diffusion, advection), biological (bioturbation, metabolism) and chemical (dissolution, oxidation, reduction) processes, often characterized by rapid rate constants and operating on a fine spatial scale. By nature of the extremely remote and hostile location of the benthic environment, many of these processes are poorly characterized. Modelling the diagenetic alteration of material within deep-sea sediments is therefore no easy task and can be numerically expensive. Global carbon cycle models have therefore often simply returned all settling material reaching the ocean floor instantaneously back to the ocean (in dissolved form). However, there are a number of compelling reasons for the explicit representation of the deep-sea sediment system, particularly for application to glacial-interglacial change;

- Dissolved chemical species formed through diagenetic alteration processes may escape the sediments by diffusing out across the sediment-water interface into the ocean. Solid material not transformed in this way will be eventually buried. This burial represents a 'sink' for the chemical constituents of that material. For the system as a whole to be at steady state, such sinks must be balanced by inputs to the ocean-atmosphere, such as via continental weathering or volcanic out-gassing. A simplified system where there are no sources or sinks of a species is considered to be 'closed' with respect to this species. The dynamical response of a closed system is found to be very different from that of an open one where there is a continual throughput [Hotinski *et al.*, 2000; Kump, 1993; Sigman *et al.*, 1998]. Particularly where the species in question are potentially limiting nutrients, carbon, or alkalinity, a closed system may not capture the long-term dynamics of the global carbon cycle, and will thus not be capable of correctly accounting for the observed glacial-interglacial variability in atmospheric CO₂.
- The explicit consideration of the diagenetic alteration of material delivered to the deep-sea floor allows for realistic estimation of the fractionation preservation of this material in the sediments, and therefore of surface sediment composition. Comparisons between model and observed distributions of major solid constituents (CaCO₃, opal, detrital material) provides a powerful diagnostic for optimizing or validating components of the overall system model.
- Finally, representation of deep-sea sediments enables an extensive synthetic sedimentary record to be built up over the course of the model simulation. Perturbations to the system will be recorded as down-core variations in sediment solid and/or isotopic properties. Contrasting artificial sediment tracer signals with those derived from actual cores recovered from the ocean floor provides additional constraints for elucidating the mechanisms involved in glacial-interglacial change [Berger *et al.*, 1996].

Deep-sea sediments and their biogeochemical interaction with the ocean are therefore included as a key component within SUE. However, although sediments in the model are considered at all depths (including the pelagic zone) the schemes used for ocean-sediment interaction are strictly applicable only to the benthic environment. As such, there is no explicit consideration of shelf sedimentary processes. The diagenetic alteration of CaCO₃ (separately as both calcite and aragonite) and opal are all represented, with the first order effects of bioturbation and sediment compaction accounted for. However, there is no similar mechanistic representation of processes relating to the diagenetic alteration of particulate (or dissolved) organic matter or detrital particles.

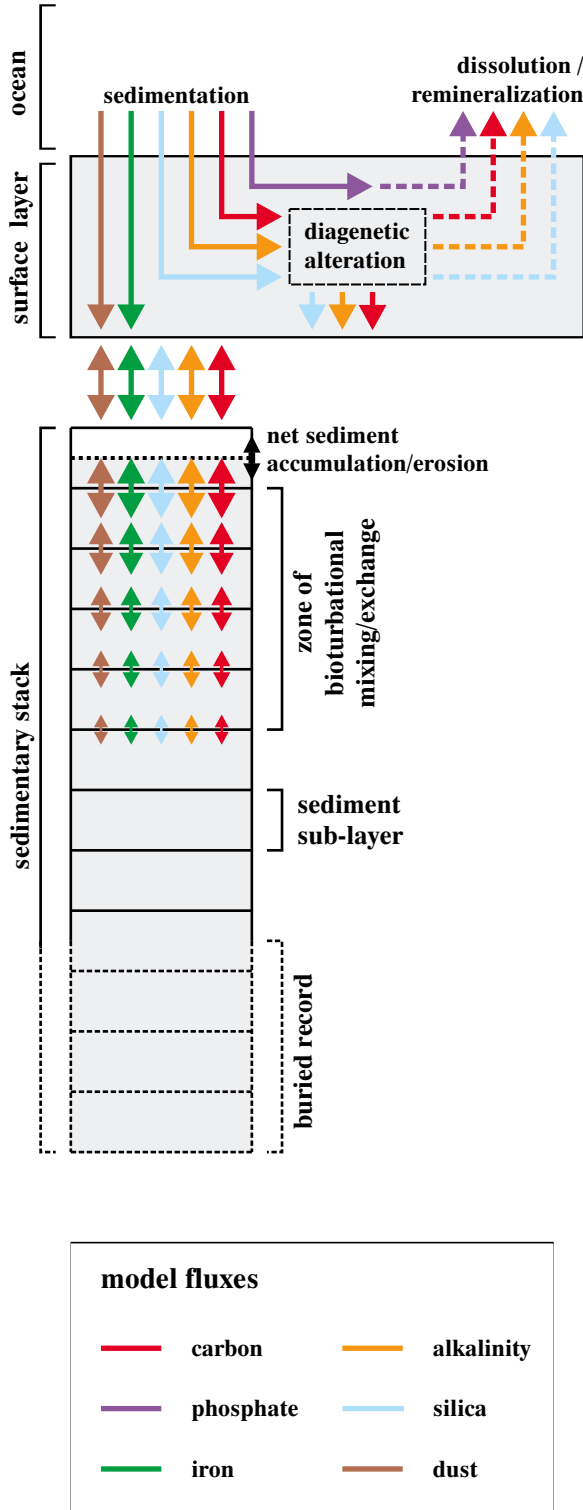


Figure 3-1 Schematic representation of the sedimentary module within SUE.

3.2 Modelling deep-sea sediments

The deep-sea sediment module used in SUE is shown schematically in Figure 3-1. The system comprises a single surface layer underlain by a series of sub-layers. The surface layer represents the upper zone of the sediment where bioturbation effectively homogenizes solid composition with respect to depth, and where the most important diagenetic processes of interest to this present study take place. Solid material which is preserved and exported out of this surface layer (i.e., ‘buried’) is stored in sedimentary sub-layers lying immediately below. These sub-layers are prescribed a thickness of 1 cm, representing a trade-off between simulated down-core sediment resolution and computational running and storage costs. In addition to the advective transfer of solids between the surface layer and upper-most sediment stack sub-layer (arising from net sedimentary accumulation/erosion) a diffusive-like transfer is prescribed between adjacent sediment layers. This represents the vertical mixing of solids due to biological activity.

Sediment composition within the surface layer is calculated via a simple mass balance and operated asynchronously with the ocean-atmosphere module, such that at time $t = t + 1$

$$M_{(t+1)}^S = M_{(t)}^S + \Delta M_{(t)}^S + Fbal^S \quad (3-1)$$

where $M_{(t)}^S$ is the mass of solid component S in the surface layer, and $\Delta M_{(t)}^S$ is the change in mass of this component calculated as the net flux across the sediment-ocean interface

$$\Delta M_{(t)}^S = Fsed_{(t)}^S - Fdis_{(t)}^S \quad (3-2)$$

where $Fsed_{(t)}^S$ is the sedimentation (or settling) flux of solid material at the ocean-sediment interface, and $Fdis_{(t)}^S$ is the flux to the ocean of dissolved species derived from the diagenetic alteration of S within the surface layer. $Fbal^S$ is a balancing flux, calculated according to the criterion that there must be no net change in the thickness of the surface layer. Where a net flux across the sediment-water interface results in a volume surfeit of material in the surface layer, a correction is made by removing material from the surface layer and transferring it to the top sub-layer of the sediment stack. Conversely, where the net flux results is a volume deficit, material is removed from the top of the sediment stack and added to the surface layer. This is formally written

$$Fbal^S = -\frac{\sum_S \Delta V_{(t)}^S}{\sum_S V_{(t)}^S} \cdot (M_{(t)}^S + \Delta M_{(t)}^S) \quad \sum_S \Delta V_{(t)}^S > 0 \quad (3-3a)$$

$$Fbal^S = +\frac{\sum_S \Delta V_{(t)}^S}{\sum_S V_{(t)}^S} \cdot M_{(t)}^S \cdot \frac{\sum_S V_{(t)}^S}{\sum_S V_{(t)}^S} \quad \sum_S \Delta V_{(t)}^S < 0 \quad (3-3b)$$

where $M_{(t)}^S$ is the mass of component S in the uppermost sediment stack sub-layer. Equivalent volumes (V) for the mass of each component are defined

$$V^S = \frac{M^S}{\rho^S \cdot \phi} \quad (3-4)$$

where ρ^S is the density of (solid) component S , and ϕ is the sediment porosity. This transferal procedure is more complicated in practice than this description suggests, since the uppermost sub-layer in the sediment stack has a finite capacity. The situation therefore arises that the effective volume of material to be added to this sub-layer is greater than its remaining (un-filled) capacity. In this case, the incomplete sub-layer is filled first, after which a new sub-layer is created immediately above, which accepts the remaining material. Conversely, when there is a surface deficit, the effective volume of material required may be greater than that remaining within the uppermost sub-layer. All the material in this sub-layer is therefore removed first and the sub-layer destroyed. The residual deficit is then made up by removing material from the new uppermost sub-layer. A simple alternative to this 'open-topped' stack arrangement would be that of an 'open-bottomed' stack [Heinze *et al.*, 1999]. In this scenario all the sub-layers are always complete, with excess material permanently lost or gained from the base. However, this is not only more computationally demanding to implement but is numerically diffusive.

Solid components represented in the sediments include calcite, aragonite, and opal, who all share a biogenic origin in the surface ocean and whose fractional preservation in the sediments is represented explicitly (3.2.4 and 3.2.5). Detrital matter derived from aeolian deposition at the ocean surface is also represented, although it is assumed to act conservatively within the sediments, and no release either H_4SiO_4 (from silicates) or dissolved Fe (from Fe-bearing ore and silicate minerals) is considered. Finally, in order to allow glacial-interglacial variability in the isotopic composition of particulate organic carbon to be recorded, POM is simply added to the sediment in a fixed ratio with the flux of material reaching the sediment surface, acting conservatively thereafter. A mean fractional preservation of the POM settling flux of 5% is chosen, consistent with estimates of ~3-7% in deep-sea sediments [Archer *et al.*, submitted; Tromp *et al.*, 1995]. Since the system is not open with respect to PO_4 , the carbon and phosphorous components of buried POM (together with associated alkalinity) are artificially returned in dissolved form to the overlying surface ocean.

In addition to the representation of solid sedimentary components, a number of isotopic and 'colour' tracers (both conservative and non-conservative) are considered in the sediment module. An isotopic composition for calcite and aragonite is considered, with ^{13}C added and removed in proportion to changes in the solid fraction. This proportionality takes a ratio whose value is determined by fractionation processes associated with formation in the ocean surface (2-61a and 2-61b) upon initial deposition to the sediments. Removal from the surface through dissolution or transfer between layers proceeds simply according to a ratio equal to the mean bulk isotopic composition in the layer(s) where the material resides. ^{14}C is treated in a similar

manner, with the exception that it is decayed with a half life of 5.73 ka. ^{13}C in POC is treated in a similar manner to ^{13}C in $CaCO_3$. 'Colour' (artificial numerical) tracers are also considered, and used to represent properties such as the age of solid calcite, foraminiferal $\delta^{13}C$ (with planktonic and benthic isotopic signatures considered separately), and foraminiferal $\delta^{18}O$ (again resolved into planktonic and benthic species). These are tied to a solid fraction and treated in a similar manner to that for bulk ^{13}C , with the exception that the depositional value of benthic and planktonic foraminiferal $\delta^{13}C$ follow (2-62) and (2-63), while benthic and planktonic foraminiferal $\delta^{18}O$ take an isotopic value equal to mean oceanic $\delta^{18}O$, itself prescribed according to the SPECMAP stack [Imbrie *et al.*, 1984]. A final colour tracer is used to represent ash depositional events (3.2.1.2).

At the start of a model run, all sediment modules are initialized with the surface layer and 100 sub-layers entirely composed of detrital material. Steady state is typically reached throughout the ocean with respect to the solid composition in surface sediments on an order of 100 ka.

3.2.1 Bioturbation

The vertical (and horizontal) mixing of solid material in the surface zone of deep-sea sediments by the action of benthic organisms (termed 'bioturbation') plays an important role in the dynamical behaviour of the global carbon cycle. For instance, perturbations in ocean chemistry or biological export may lead to the erosion of surface $CaCO_3$. Previously buried material can then be exhumed from depth through bioturbational mixing, thus effectively replenishing the material in the sediment surface [Archer *et al.*, 1998; Boudreau, 1994]. If the perturbation continues for an extended period a significant mass of material may eventually be brought to the surface and eroded in this way, thus affecting global ocean chemistry [Archer *et al.*, 1998]. Bioturbation also has important consequences for the interpretation of paleoceanographic proxies [DuBois and Prell, 1988; Ruddiman *et al.*, 1980; Schiffelbein, 1984; Trauth, 1998]. Down-core tracer profiles (such as foraminiferal calcite $\delta^{13}C$ or $\delta^{18}O$) associated with a perturbation event can be 'smeared out' by vertical mixing. This degrades the resolution of the phase information which can be obtained from recovered cores, complicating the analysis of causal links between different processes operating within the system [Boudreau, 1994; Hutson, 1980]. The apparent magnitude of a perturbation event can also be significantly diminished. Implementation of an adequate sedimentary bioturbation scheme is therefore desirable both for realism in model-generated sediment cores and in capturing system dynamics.

3.2.1.1 Bioturbation model description

The mechanistic action of benthic organisms leads to the movement of solid material within the surface zone of the sediment. This transfer can occur in both horizontal and vertical planes, may be highly selective in terms of size fraction or chemical composition, and take place throughout a large range of spatial and temporal scales, from an almost

continuous local transport to highly episodic occurrences over an extended distance. The nature of individual disturbances will depend on the animal species involved through behavioural characteristics such as mode of feeding, locomotion, and shelter [Soetaert *et al.*, 1996; Wheatcroft *et al.*, 1990; Wheatcroft, 1992]. The abiotic benthic environment also has an important influence, particularly in terms of food source availability [Legeleux *et al.*, 1994; Trauth *et al.*, 1997]. Various detailed mechanistic treatments of bioturbation have been proposed [Soetaert *et al.*, 1996; Wheatcroft *et al.*, 1990; Trauth, 1998]. However, such schemes are computationally expensive and require knowledge of benthic ecology which cannot be prognostically provided by SUE. A highly simplified representation of bioturbational mixing in deep sea sediments is therefore required.

The simplest possible treatment is to assume the presence of a relatively thick surface layer, homogeneous in composition over its entire depth [Berger and Heath, 1968; Munhoven and Francois, 1996]. Such schemes typically assume a thickness of 10 cm for this layer, representing the approximate depth to which deep-sea sediments are often observed to be predominantly 'well-mixed' [Boudreau, 1994; Ikehara *et al.*, 2000; McManus *et al.*, 1995]. However, vertical resolution can be improved by assuming that the effect of bioturbation can be modelled as an quasi-diffusive process [Pope *et al.*, 1996; Wheatcroft *et al.*, 1990] and therefore ignoring the effects of non-local mixing [Boudreau, 1994; Legeleux *et al.*, 1994; Soetaert *et al.*, 1996; Wheatcroft, 1992]. In this, the surface sediment zone is discretized into a series of sub-layers with mixing between adjacent layers characterized by a prescribed biodiffusion coefficient [Archer, 1991; Guinasso *et al.*, 1975; Officer and Lynch, 1983; Walker and Opdyke, 1995].

A variety of simple bioturbational schemes are evaluated here for application in SUE. Potential parameterizations are constrained by the configuration of the sediment module (Figure 3-1) to comprise a homogeneous surface layer overlying a sequence of 1 cm thick stacked layers. The mixing rate between pairs of sub-layers is determined by a biodiffusion coefficient which decreases with depth determined by a profile which can be varied in both shape and magnitude. In the following sections the results from just two of these schemes are presented. The first (designated

"10 cm only") is the simplest, consisting of just a 10 cm thick surface layer with no deeper mixing. The second ("5 cm plus deep mixing") is adapted from Peng *et al.* [1979], and comprises a 5 cm thick surface layer with deeper mixing below this. This deep mixing follows an exponentially-decreasing profile of *e*-folding length 1 cm, with a maximum mixing rate (at the base of the surface layer) of 16 cm² ka⁻¹.

3.2.1.2 Inert tracer profile simulation

Sub-aerial volcanic events tend to produce airborne ejecta such as ash and pumice in discrete rather transitory pulses. Since the time scale for its deposition to the deep-sea floor is short compared to the residence time of material in the bioturbated zone, the input to the sediments of ash and pumice can be assumed to be effectively instantaneous. An additional advantage of such material as a bioturbation tracer is that it is relatively inert, thus acting conservatively. If a constant sediment accumulation rate is assumed, down-core profiles of ash and pumice concentration will depend only on the details of bioturbational mixing. Modelling such profiles allows different bioturbation schemes to be evaluated.

Table 3-1 details a number of deep-sea sediment cores taken from the Pacific and Indian oceans where down-core concentrations of (62-125 μm) volcanic ash and pumice have been measured [Ruddiman *et al.*, 1980]. The sediment module is run once for each of these cores with bulk-matter deposition fluxes chosen to give the appropriate observed sediment accumulation rate. After sediment 'spin-up', an impulse addition of a 'colour' tracer (representing the input of volcanic material) is made to the sediment surface. Figure 3-2 shows the results of this exercise for the "10 cm only" and "5 cm plus deep mixing" mixing schemes. It can be seen that while the first scheme can reproduce tracer profiles in cores characterized by relatively high sedimentation rates (>2 cm ka⁻¹), it tends to over-estimate peak concentrations at lower rates. The second scheme, however, produces a reasonable fit under all sedimentation conditions. There is a general failure in both these and other schemes evaluated (not shown) to produce adequate mixing of tracer deeper than the level of impulse addition (the observed 'tail' to the right of the maximum tracer concentration). While prescribing stronger biodiffusion at depth can partly alleviate this mis-match it also seriously reduces peak concentrations. The inability to reproduce this feature highlights one of the deficiencies of a simple quasi-diffusional model, that of the role of non-local mixing events.

3.2.1.3 ¹⁴C age profile simulation

A second test of mixing scheme involves the use of down-core measurements made of ¹⁴C age. Core ERDC-92 is chosen for this analysis, having already been extensively characterized in terms of mixing and accumulation regime by Peng *et al.* [1979]. The sediment sub-model is run assuming apparent (i.e., ¹⁴C age-derived) sedimentation rates of 2.3 cm ka⁻¹ before 6 ka BP and 1.2 cm ka⁻¹, thereafter [Peng *et al.*, 1979]. No dissolution of CaCO₃ is prescribed, consistent with the shallow location of this core. CaCO₃ deposited to the

Table 3-1 Ash and Pumice Tracer Sediment Core Details

Core	Tracer	Sediment accumulation rate (cm ka ⁻¹)
V19-28	Ash	7.00
V19-29	Ash	7.00
V29-39	Ash	0.50
V29-40	Ash	0.50
RC17-126	Ash	2.00
E48-23	Pumice	2.50

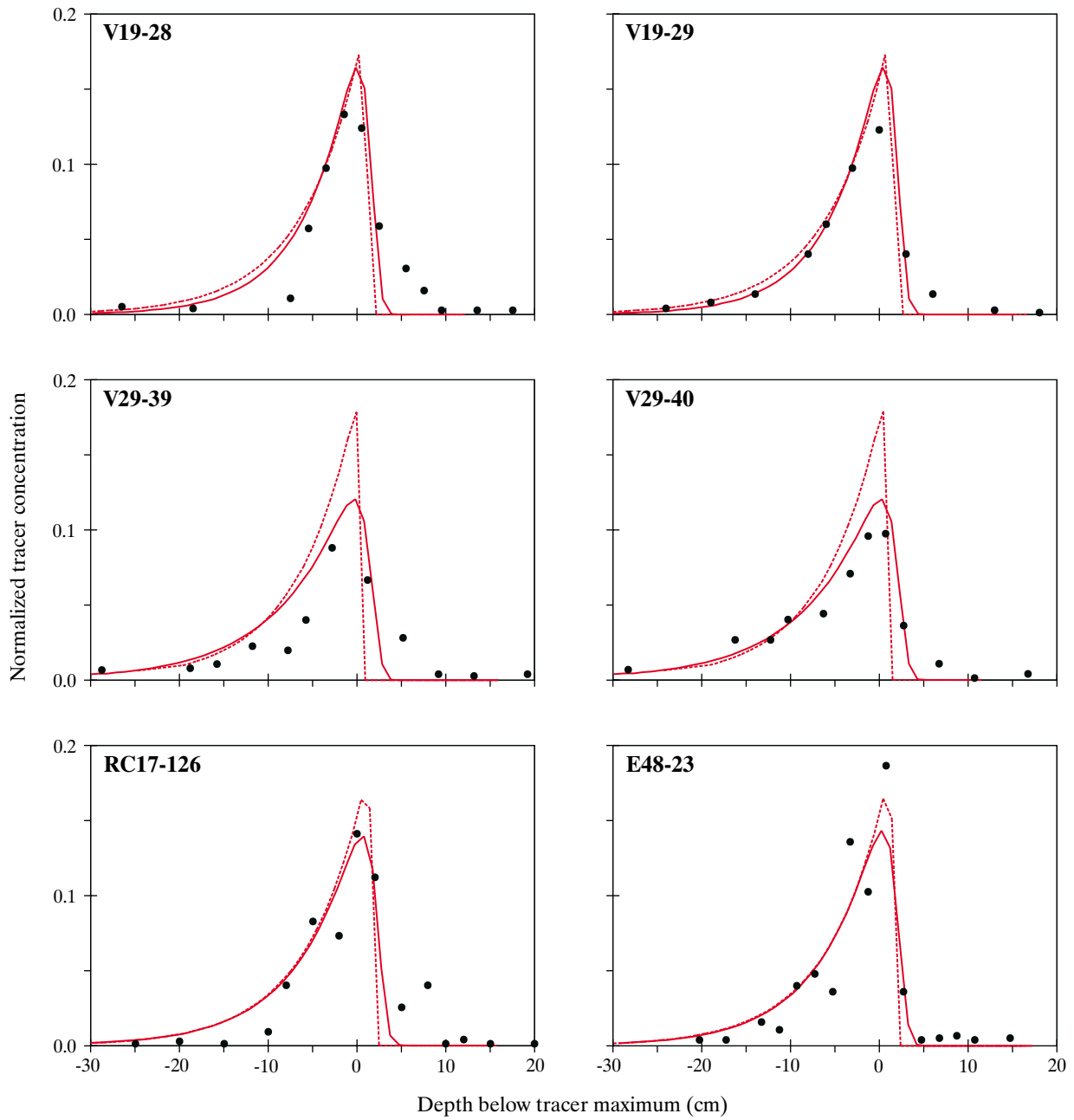


Figure 3-2 Model down-core ‘colour’ tracer profiles (solid and dotted red lines, corresponding to the schemes “5 cm plus deep mixing” and “10 cm only”, respectively) compared to observed ash and pumice concentrations (filled circles). All tracer concentrations are shown normalized to unit integrated volume.

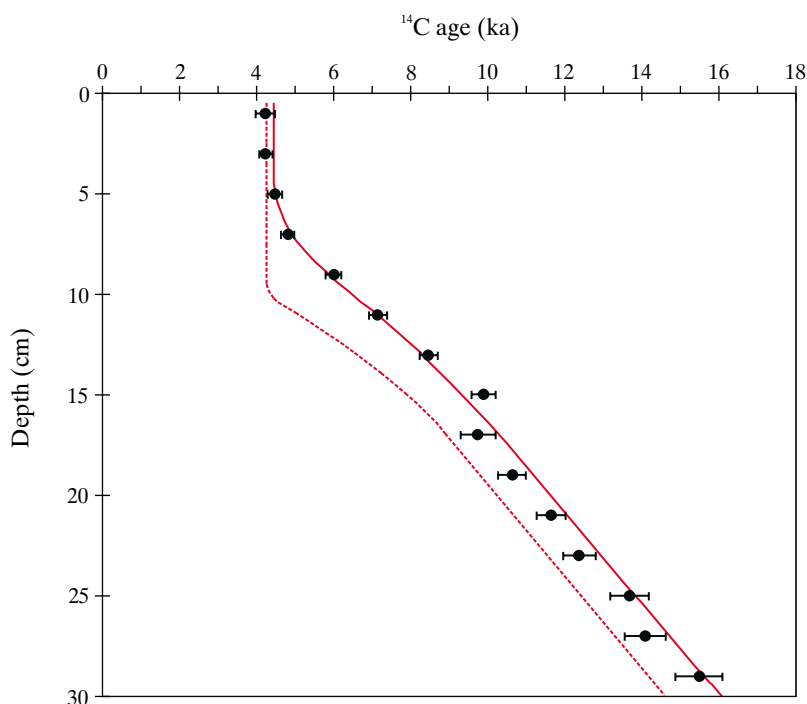


Figure 3-3 Model down-core CaCO_3 ^{14}C age tracer profiles (solid and dotted red lines, corresponding to the schemes “5 cm plus deep mixing” and “10 cm only”, respectively) compared to observations from core ERDC-92 [Peng *et al.*, 1979] (filled circles with error bars).

sediment surface in the model is assigned a ^{14}C age of 0.4 ka, in order to account for surface water aging [Keir and Michel, 1993; Oxburgh, 1998; Peng *et al.*, 1979]. The results from the same two bioturbation schemes as presented before are shown in Figure 3-3, and compared to observations. While both correctly reproduce the observed core-top ^{14}C age, the simple “10 cm only” scheme is noticeably less successful in reproducing the deeper age profile.

The “5 cm plus deep mixing” scheme is also evaluated against four ^{14}C profiles presented by Broecker *et al.* [1991], with corrections made for the surface ocean ^{14}C reservoir age as before. Core details, including apparent accumulation rates used to constrain the sediment module are listed in Table 3-2. The results of this exercise are shown in Figure

3-4, demonstrating that the mixing scheme is able to capture core-top ^{14}C ages and down-core profile of core FAM527-3, while introducing only a relatively small age offset (~ 0.5 ka) in cores EN66-21 and ERDC-92. However, the model significantly under-predicts ^{14}C ages in TT154-5. This apparently somewhat mixed success might be a direct consequence of the different oceanographic locations of the cores; while the other three cores come from either relatively shallow depths or from the Atlantic, TT154-5 is from the mid-depth Pacific. As such, it is likely to be bathed in water under-saturated with respect to CaCO_3 [Archer, 1996a]. A significant fraction of the (young ^{14}C age) CaCO_3 rain is therefore likely to dissolve upon reaching the surface and before being incorporated into the well-mixed layer, leading

Table 3-2 Radiocarbon Profile Sediment Core Details

Core	Latitude	Longitude	Depth (m)	Sediment accumulation rate (cm ka^{-1})	Reference
FAM527-3	36.8°N	33.3°W	2600	2.9	Nozaki <i>et al.</i> [1977]
ERDC-92	2.2°S	157.0°E	1598	1.8	Berger and Killingley [1982], Peng <i>et al.</i> [1979]
EN66-21	4.2°N	20.6°W	3995	1.4	DuBois and Prell [1988]
TT154-5	10.3°S	111.3°W	3225	0.8	Broecker <i>et al.</i> [1991]

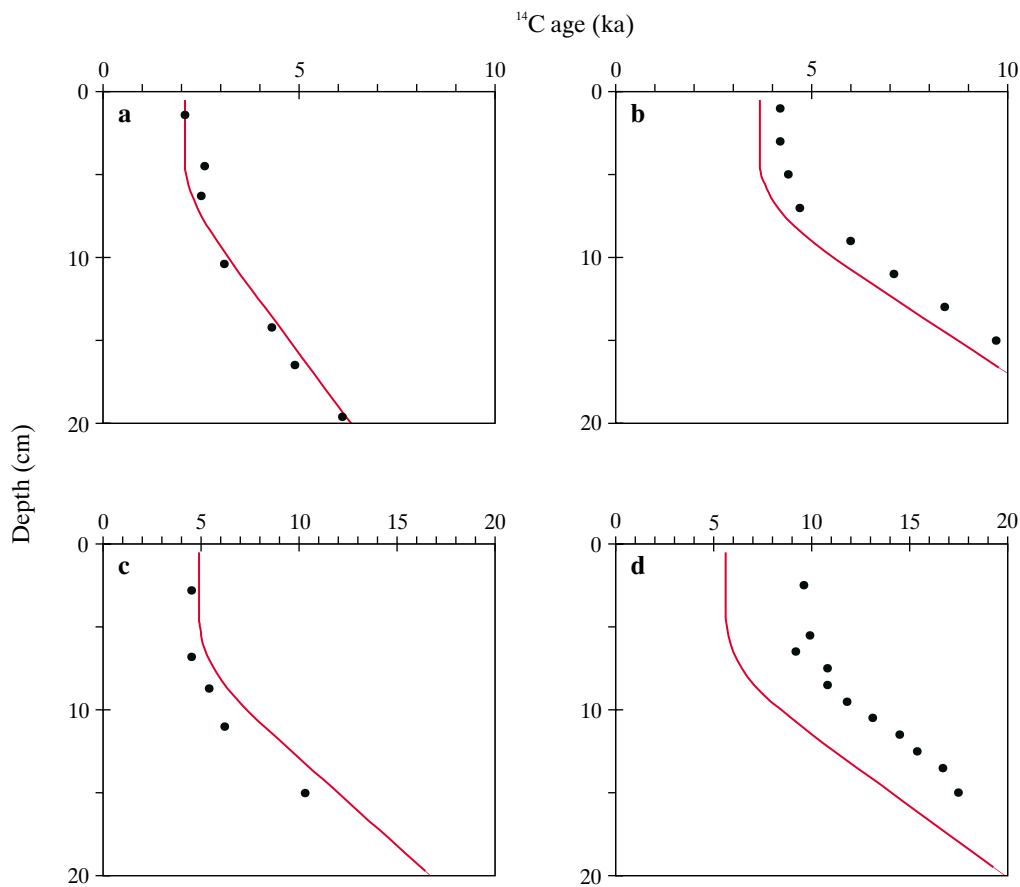


Figure 3-4 Model down-core CaCO_3 ^{14}C age tracer profiles (solid red lines, corresponding to the scheme “5 cm plus deep mixing”) compared to observations from cores FAM527-3 (a), ERDC-92 (b), EN66-21 (c), and TT154-5 (d), all designated by filled circles.

to a higher-than expected ^{14}C age [Broecker *et al.*, 1991, 1999b; Oxburgh, 1998]. That the simple test used here assumes that no dissolution of CaCO_3 takes place is the probable cause of this discrepancy. A secondary effect contributing to model-observation mismatch may be insufficient elapsed time since the LGM for a new steady-state to have been established. This is supported by an anti-correlation between the degree of ^{14}C age mis-match and sediment accumulation rate. Only for the fastest sediment accumulation rate (FAM527-3) would it have been possible for virtually all trace of LGM conditions to have been erased over the entire depth of the observed profile.

3.2.1.4 Scheme choice

Although carrying an additional computational burden associated with it, the “5 cm plus deep mixing” scheme appears to perform better than the simpler “10 cm only” parameterization. However, the performance of both of these is significantly better than that of other schemes tested, such as the power law mixing parameterization of Walker and Opdyke [1995]. The “5 cm plus deep mixing” scheme is

therefore adopted as default in SUE. Although some models have introduced a dependence of sediment mixing rates on ocean depth or POM rain rates [Archer *et al.*, in press; Muehlen and Francois, 1996], the chosen parameterization is applied uniformly to all sediments throughout the model ocean as an initial step.

3.2.2 Porosity

The porosity of deep-sea sediments can affect diagenetic behaviour through scaling the vertical accumulation rates (which in turn determines the mean time spent by material in the sub-surface zone of intense diagenetic alteration), and by controlling the diffusivity of dissolved species within the sediment matrix. Although there appears to be some dependence of porosity on sediment composition [Archer *et al.*, 1979; Martin *et al.*, 1991], for simplicity, a single empirically-derived sediment porosity profile is utilized in this study.

Figure 3-5 shows porosity profiles estimated from *in situ* microelectrode resistivity measurements in a number of

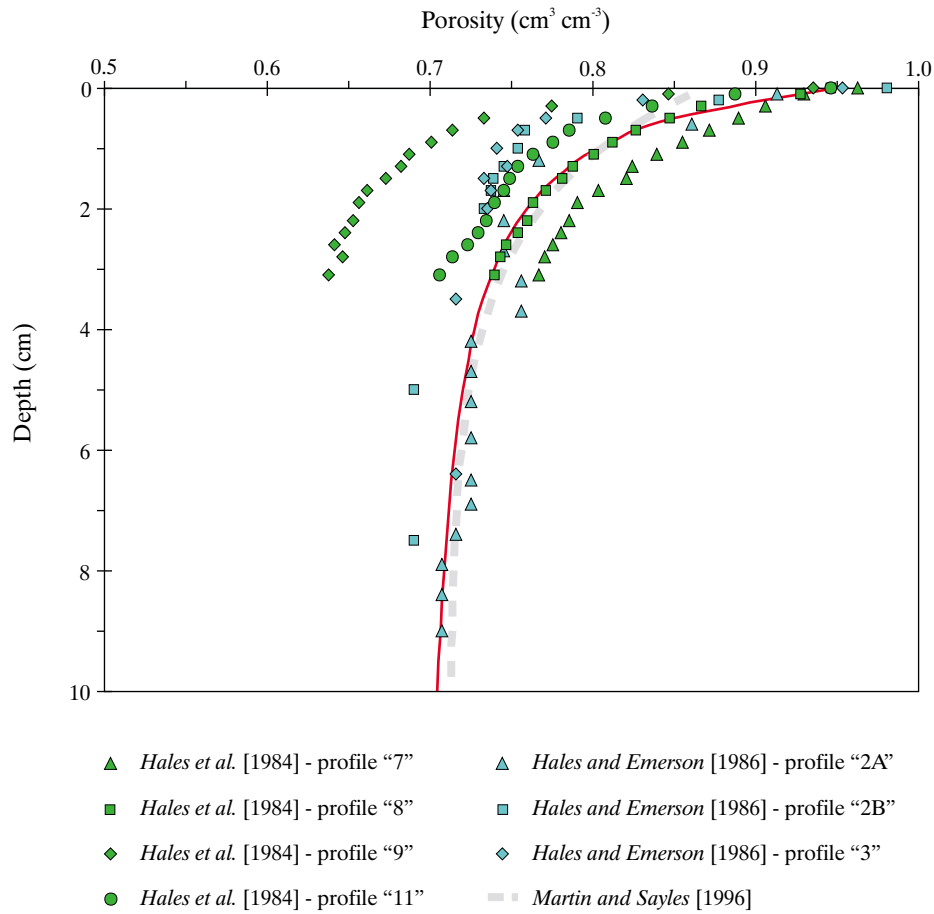


Figure 3-5 Model sediment down-core porosity profile (continuous line) compared with observations.

equatorial Pacific [Hales and Emerson, 1996] and north Atlantic cores [Hales et al., 1994], together with a mean equatorial Atlantic profile [Martin and Sayles, 1996]. Assuming porosities at the surface of 0.95 and 0.70 $\text{cm}^3 \text{cm}^{-3}$ at depth, all these observations can be reasonably be described by

$$\phi_{(z)} = 0.69 + 0.26 \cdot (1.0 + z)^{-1.2} \quad (3-5)$$

where $\phi_{(z)}$ is the porosity at depth z (cm) in the sediment. This gives a mean porosity of $\sim 0.89 \text{ cm}^3 \text{cm}^{-3}$ over the uppermost 0.5 cm, consistent with Hensen et al. [1998], and an overall profile similar to models use by Heinze et al. [1999] and Jahnke et al. [1997]. The 5 cm thick surface layer in the sediment module is therefore assigned a porosity of 0.776 $\text{cm}^3 \text{cm}^{-3}$, with 0.705 $\text{cm}^3 \text{cm}^{-3}$ applied uniformly to all sub-layers.

3.2.3 Numerical implementation of diagenesis

The diagenetic alteration of material in deep-sea sediments is in essence a 1-D reaction-diffusion system. Numerical stability considerations in the solution of such a system

dictate a minimum time step for the required vertical resolution [Moldrup et al., 1996] such that explicit application over a global scale for extended time model runs is problematic. While elegant schemes have been developed for rapid approximation of a quasi-steady solution [Archer, 1991, Archer et al., in press], there are alternative methodologies for the efficient encapsulation of complex diagenetic behaviour.

On the basis of a set of simplifying assumptions, Sigman et al. [1998] successfully reduced the dimensionality of a complex model of CaCO_3 diagenesis to a system defined by only 2 independent variables. A multi-variate polynomial fit was derived from this and subsequently employed within a global carbon cycle model. However, if the number of variables considered essential for a reasonable representation of system behaviour exceeds this, it becomes difficult to construct an equivalent regression surface. Alternatively, a representation of the solution surface can be obtained by training a neural network on the underlying numerical model. Unfortunately, the protracted ‘training’ times required by neural networks will tend to curtail their use where the parameter space is large. A simple ‘look-up’ table approach is therefore introduced here for the

representation of sedimentary diagenetic behaviour, whereby required values of state are obtained through linear interpolation on a regular grid of pre-calculated values within an n -dimensional space, where n is the number of parameters defining the system.

3.2.4 Sedimentary diagenesis of CaCO₃

Sedimentary diagenesis of CaCO₃ follows *Archer* [1991]. In this model, the dissolution of CaCO₃ within a 10 cm thick surface zone is considered, driven both by the overlying ocean chemistry and as a result of remineralization of POC within the sediments. The assumption is made that POC reaching the sediments is completely reduced under oxic conditions. Numerical solution is achieved via a relaxation method within a vertically discretized system. While no account is taken of anoxic conditions produced at depth or resulting from a high ratio of POC rain rate to ocean dissolved oxygen concentrations, this scheme has proved successful in a number of previous global carbon cycle models [*Archer*, 1996a; *Archer et al.*, 1998; *Heinze et al.*, 1999]. For application in SUE, several minor modifications are made. Firstly, to ensure internal model consistency, the same representation of carbonate chemistry as that of the oceanic component is used (Appendix I). Secondly, a single down-core porosity is assumed, independent of sediment composition (3.2.2).

3.2.4.1 Look-up table implementation

In the *Archer* [1991] model, CaCO₃ dissolution flux density across the sediment-water interface ($fdis^{CaCO_3}$) is primarily a function of ocean depth (D), the bottom-water concentration of total dissolved inorganic carbon ([DIC]), alkalinity ([ALK]), and dissolved oxygen ([O₂]), the mass fraction of CaCO₃ in the sediments (c^{CaCO_3}), and the flux density of particulate organic matter delivered to the sediment surface ($fsed^{POC}$). The look-up table function for such a system can be written

$$fdis^{CaCO_3} = L(D, [DIC], [ALK], c^{CaCO_3}, [O_2], fsed^{POC}) \quad (3-6)$$

where L is a function for linear interpolation within an n -dimensional space. However, the six-dimensional space defined by these variables does not easily yield a manageable look-up table. Parameter space dimensionality can be reduced considering that it is carbonate ion concentration that directly determines CaCO₃ dissolution rates rather than DIC and ALK individually. A variable representing the degree of under-saturation (dCO_3) is therefore introduced following *Sigman et al.* [1998], defined as the difference between ambient [CO₃²⁻] and the local saturation value for CaCO₃. The spanning space is collapsed through the substitution of [DIC] and [ALK] by a single descriptive variable (dCO_3)

$$fdis^{CaCO_3} = L(D, dCO_3, c^{CaCO_3}, [O_2], fsed^{POC}) \quad (3-7)$$

A further dimensional reduction is made by assuming a uniform dissolved oxygen concentration throughout the

ocean (taken to be 200 μmol kg⁻¹). This is justified on the basis of the relatively weak dependence of $fdis^{CaCO_3}$ on [O₂] under typical benthic conditions (of order 0.01% (μmol kg⁻¹)⁻¹). The CaCO₃ dissolution flux density is now a much simpler function of just four variables;

$$fdis^{CaCO_3} = L(D, dCO_3, c^{CaCO_3}, fsed^{POC}) \quad (3-8)$$

The spanning set of look-up table parameters are detailed in Table 3-3. Spanning ranges are generally chosen to cover conditions found in the benthic environment, with step intervals relaxed where $fdis^{CaCO_3}$ is only weakly non-linear with a particular parameter.

Since both forms of biogenic CaCO₃ are resolved in SUE two look-up tables must be generated, one for calcite and the other for aragonite. For the dissolution of calcite, parameter values are taken from *Archer* [1996a] for the order of dissolution (4.5) and dissolution rate constant (1.0 d⁻¹). The dissolution rate constant for aragonite is assumed to be the same, but a slightly lower value of 4.2 is used for the reaction order [*Keir*, 1980]. Artificially separating the dissolution of calcite and aragonite in this way presents the problem of how dissolution forcing due to POC remineralization is partitioned between the two polymorphs. As a crude approximation $fsed^{POC}$ is split between the calcite and aragonite diagenetic systems in proportion to their relative mass abundance in the sediments, giving

$$fdis^{cal} = L\left(D, dCO_3^{cal}, c^{cal}, \frac{c^{cal}}{c^{cal} + c^{arg}} \cdot fsed^{POC}\right) \quad (3-9a)$$

$$fdis^{arg} = L\left(D, dCO_3^{arg}, c^{arg}, \frac{c^{arg}}{c^{cal} + c^{arg}} \cdot fsed^{POC}\right) \quad (3-9b)$$

3.3.4.2 The location of CaCO₃ dissolution

In terms of CaCO₃ mass balance it makes no difference from where in surface sediments material is dissolved. However, this is not true for qualities of CaCO₃ that may vary with time such as ¹³C and ¹⁴C isotopic composition. A number of different end-member models have been proposed to qualitatively describe the effect of dissolution on such properties [*Broecker et al.*, 1991; *Oxburgh and Broecker*, 1993], namely; “interface” dissolution, where the dissolution of settling CaCO₃ takes place in the surficial fluff layer before any downwards mixing occurs; “homogeneous” dissolution, where settling CaCO₃ is first homogenized into the intensely bioturbated zone prior to dissolution; and “sequential” or

Table 3-3 CaCO₃ Diagenesis Look-up Table Spanning Set

Parameter	Spanning range	Spanning step	Units
dCO_3	-100 to 100	1	μmol kg ⁻¹
D	0 to 10000	1000	m
$fsed_{POC}$	0 to 50	1	μmol cm ² a ⁻¹
c_{CaCO_3}	10 to 100	10	%

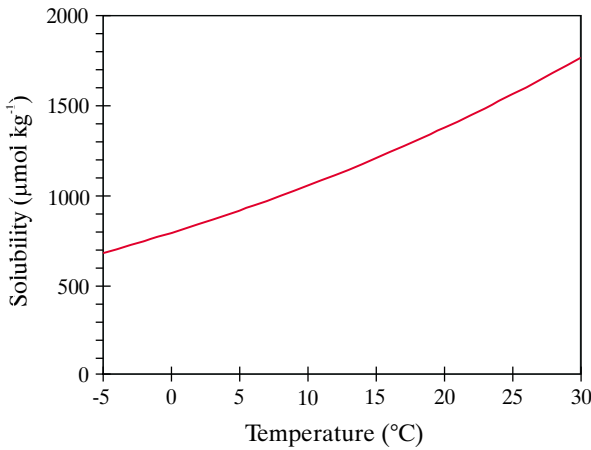


Figure 3-6 Dependence of opal solubility on temperature [Van Cappellen and Qiu, 1997a].

“one pass” dissolution, where CaCO_3 is initially mixed into the surface layer, but ‘ages’, becoming less susceptible to dissolution with time. On the basis of observed ^{14}C ages, interface dissolution of CaCO_3 has generally been considered to be the dominant process [Broecker *et al.*, 1991, 1999b; Keir and Michel, 1993; Oxburgh and Broecker, 1993; Oxburgh, 1998] although there has been some recent support for the action of an ageing-like process [Martin *et al.*, 2000]. Dissolution of CaCO_3 within the sediment module is therefore assumed to take place before mixing into the surface zone occurs according to the ‘interface’ dissolution model. If the dissolution flux is less than the rain flux, the remaining material is then incorporated into the surface mixed layer, while if the dissolution flux is greater than the rain flux additional material is removed from the mixed layer to make up this shortfall (up to a volume equal to the entire CaCO_3 surface layer inventory if necessary).

3.2.5 Sedimentary diagenesis of biogenic opal

Despite its importance to both the dynamics of the global carbon cycle and in the interpretation of paleoceanographic proxies of past change, the factors determining the preservation of opal in deep-sea sediments are poorly understood [Archer *et al.*, 1993]. As a result, there have been few previous global carbon cycle models in which the ocean Si cycle has been comprehensively represented [Archer *et al.*, 2000; Heinze *et al.*, 1999]. A new description of sedimentary opal diagenesis is presented here, developed empirically from recent observations and laboratory analyses of opal dissolution and thermodynamics in a series of cores taken from the Southern Ocean [Rabouille *et al.*, 1997; Van Cappellen and Qiu, 1997a,b].

3.2.5.1 A model for sedimentary opal diagenesis

The system for the diagenetic alteration of opal within deep-sea sediments can be restricted to the uppermost 10 cm since little net diffusion of H_4SiO_4 is observed below this depth [Rabouille *et al.*, 1997; Sayles *et al.*, 1996; Van Bennekom *et al.*, 1988]. A further simplifying assumption is made in that the concentration of opal is constant with depth, again in line with observations [Rabouille *et al.*, 1997; Schluter and Sauter, 2000; Van Bennekom *et al.*, 1988]. The system is vertically discretized into 0.2 cm thick sub-layers with down-core sediment porosity following (3-5), and solved on a finite-difference basis. However, considering that the relaxation time of solutes in the system is several orders of magnitude faster than for the solids [Rabouille and Gaillard, 1990], pore-water H_4SiO_4 concentrations are solved for in isolation. Steady-state is assumed to have been obtained when the dissolution flux across the sediment-water interface changes by less than 0.001% between time steps. The two individual components of the reaction-diffusion system are defined as follows.

Diffusion of H_4SiO_4

Correcting for tortuosity [Ullman and Aller, 1982] the *in situ* diffusion of H_4SiO_4 at depth z in the sediment is described by

$$D_{\text{sed}(z)} = (\phi_{(z)})^{(n-1)} \cdot D_{\text{SW}} \quad (3-10)$$

where D_{SW} is the molecular diffusivity of H_4SiO_4 in free seawater, taken as $4.59 \times 10^{-6} \text{ cm}^2 \text{ s}^{-1}$ at 0°C and adjusted for the actual bottom-water temperature after Hensen *et al.* [1998]

$$D_{\text{SW}} = 4.59 \times 10^{-6} + 1.74 \times 10^{-7} \cdot (T_{\text{SW}} - 273.15) \quad (3-11)$$

where T_{SW} is the temperature of the bottom-water (K), ϕ_z is the porosity at depth z (3-5), and n is a correlation factor taking a value of 2.5 typical for deep-sea sediments [Hensen *et al.*, 1998; Ullman and Aller, 1982]. Compared with molecular diffusion of H_4SiO_4 , bioturbation and advection (due to sediment accumulation) play no significant role in aqueous transport within the sediment [Schink *et al.*, 1975] and are thus omitted.

Dissolution of biogenic opal

Dissolution of opal (in units of $\text{mol cm}^{-3} \text{ opal a}^{-1}$) at depth z in the sediment proceeds according to

$$R_{(z)}^{\text{opal}} = k_{(z)}^{\text{opal}} \cdot \rho^{\text{opal}} \cdot [1 - \phi_{(z)}] \cdot c_{(z)}^{\text{opal}} \quad (3-12)$$

where $k_{(z)}^{\text{opal}}$ is a dissolution rate constant (a^{-1}), ρ^{opal} the density of opal (mol cm^{-3}), $\phi_{(z)}$ sediment porosity ($\text{cm}^3 \text{ cm}^{-3}$), and $c_{(z)}^{\text{opal}}$ the solid fraction of opal ($\text{cm}^3 \text{ cm}^{-3}$) as a proportion of sediment solids. Traditionally, opal dissolution rate has been assumed to be a linear function of the degree of under-saturation [Archer *et al.*, 1993, 2000; Rabouille and Gaillard, 1990; Rabouille *et al.*, 1997; Schink *et al.*, 1975]

$$k_{(z)}^{\text{opal}} = a \cdot u_{(z)}^{\text{opal}} \quad (3-13)$$

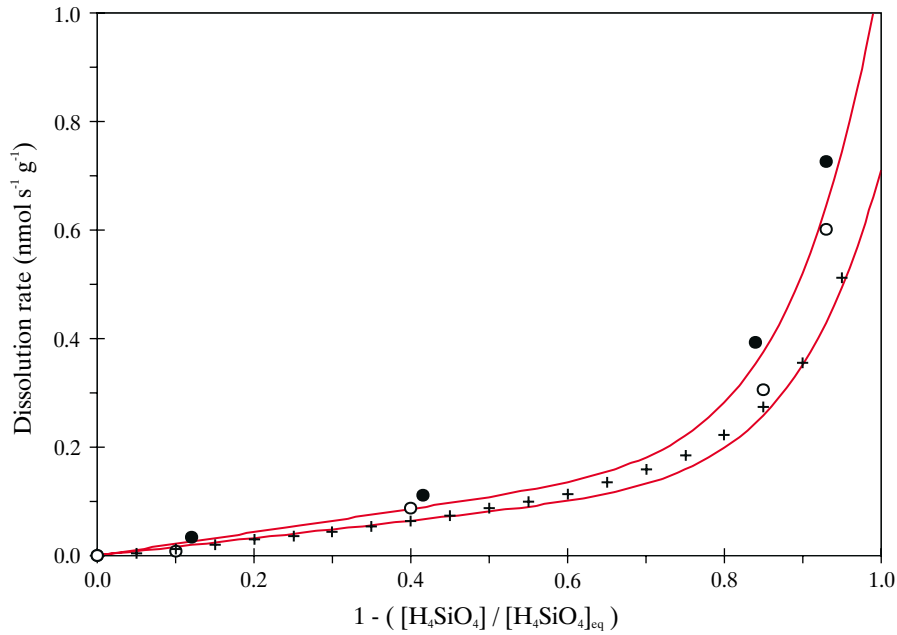


Figure 3-7 Opal dissolution rate as a function of degree of under-saturation (u^{opal}). Directly measured (at 5°C) dissolution rates are shown as filled (for core KYB05) and unfilled (KTB06) circles, respectively, together with estimated (at 0°C) dissolution rates marked by crosses [Van Cappellen and Qiu, 1997b]. Calculated dissolution rates using (3-16) are shown for temperatures of 5°C (top line) and 0°C (bottom line).

where a is a constant and $u_{(z)}^{\text{opal}}$ is the degree of local pore-water under-saturation with respect to the solid phase

$$u_{(z)}^{\text{opal}} = \frac{[\text{H}_4\text{SiO}_4]_{\text{eq}(z)}^{\text{opal}} - [\text{H}_4\text{SiO}_4]_{(z)}}{[\text{H}_4\text{SiO}_4]_{\text{eq}(z)}^{\text{opal}}} \quad (3-14)$$

where $[\text{H}_4\text{SiO}_4]_{(z)}$ is the pore water concentration of silicic acid and $[\text{H}_4\text{SiO}_4]_{\text{eq}(z)}^{\text{opal}}$ the equilibrium (saturation) concentration with respect to opal. $[\text{H}_4\text{SiO}_4]_{\text{eq}(z)}^{\text{opal}}$ can be estimated empirically [Van Cappellen and Qiu, 1997a] by

$$\log_{10}([\text{H}_4\text{SiO}_4]_{\text{eq}(z)}^{\text{opal}}) = 6.44 - \frac{968}{T} \quad (3-15)$$

where T is the absolute temperature (Figure 3-6). Although a dependence of $[\text{H}_4\text{SiO}_4]_{\text{eq}(z)}^{\text{opal}}$ on $p\text{H}$ has also been observed [Van Cappellen and Qiu, 1997a], errors arising from omission of this effect are unlikely to be more than $\sim 5\%$ under typical pore-water conditions.

Contrary to the common assumption of linear dissolution kinetics (3-13) Van Cappellen and Qiu [1997b] found that the relationship describing dissolution rate appeared to become highly nonlinear as u^{opal} approached unity. As shown in Figure 3-7, estimated and directly observed dissolution rates [Van Cappellen and Qiu, 1997b] can be crudely represented by an equation of the form

$$R^{\text{opal}} = 0.16 \cdot \left(1 + \frac{T}{15}\right) \cdot u^{\text{opal}} + 0.55 \cdot \left(\left(1 + \frac{T}{400}\right)^4 \cdot u^{\text{opal}}\right)^{9.25} \quad (3-16)$$

where R^{opal} is the dissolution rate of opal (in units of $\text{nmol s}^{-1} \text{g}^{-1}$) and T is the temperature ($^{\circ}\text{C}$). Although this function is wholly *ad hoc*, it is consistent with available data over a range in T and u^{opal} that spans typical abyssal conditions. It is also characterized by a Q_{10} of 2.3 consistent with Kamatani [1982] and can thus be expected to have useful predictive power over a much wider range of (temperature) conditions. A scaling factor $\eta_{(z)}^{\text{opal}}$ accounting for the relative change in dissolution rate due to deviations in ambient temperature from 0°C and zero silicic acid concentration (i.e., completely under-saturating) is derived by normalizing (3-16) to a value of unity at $T = 0^{\circ}\text{C}$ and $u_{(z)}^{\text{opal}} = 1$

$$\eta_{(z)}^{\text{opal}} = 0.225 \cdot \left(1 + \frac{T}{15}\right) \cdot u_{(z)}^{\text{opal}} + 0.775 \cdot \left(\left(1 + \frac{T}{400}\right)^4 \cdot u_{(z)}^{\text{opal}}\right)^{9.25} \quad (3-17)$$

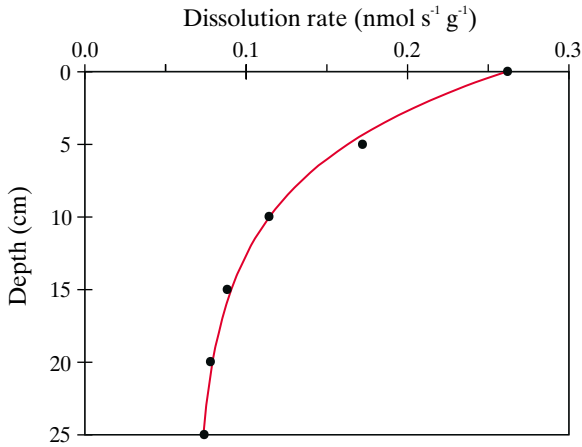


Figure 3-8 Down-core decrease in opal dissolution rate (at half-saturation). Observed data (filled circles) from *Van Cappellen and Qiu* [1997b] along with model fit (3-18).

Early diagenetic alteration of opal also appears to affect dissolution rates, with rate constants inversely correlated with depth in the sediment [*Van Cappellen and Qiu*, 1997b] (Figure 3-8). This can be approximated

$$R^{\text{opal}} = 0.068 + 0.194 \cdot e^{\left(\frac{-z}{7.0}\right)} \quad (3-18)$$

Normalizing to a value of unity at the sediment surface (i.e., before any additional diagenetic alteration has occurred) gives a second scaling factor

$$\eta_{2(z)}^{\text{opal}} = 0.26 + 0.74 \cdot e^{\left(\frac{-z}{7.0}\right)} \quad (3-19)$$

The introduction of this factor is analogous to the decrease in kinetic ‘constant’ with depth employed by *Rabouille et al.* [1997].

Diagenetic effects also appear to suppress solubility. *Van Bennekom et al.* [1988] found that low concentrations of Al markedly lower the solubility of biogenic and amorphous silica, with opal samples exhibiting a contraction of the lattice at relatively high Al/Si ratios suggesting a degree of substitution of Si by Al. This is supported by observations made by *Van Cappellen and Qiu* [1997a] regarding the asymptotic concentration of pore-water silicic acid ($[\text{H}_4\text{SiO}_4]_{\text{asym}}$) reached in the sediment. They noted that $[\text{H}_4\text{SiO}_4]_{\text{asym}}$ correlated with the mass ratio of detrital material to opal, suggesting that interstitial incorporation of Al into opal surface layers during a process of continuous dissolution/recrystallization might lead to decreasing solubility. Reduction in $[\text{H}_4\text{SiO}_4]_{\text{asym}}$ with the ratio of detrital to opal content [*Van Cappellen and Qiu*, 1997a] (Figure 3-9) can be approximated

$$[\text{H}_4\text{SiO}_4]_{\text{asym}} = 895 - \left(5528 \cdot \frac{c^{\text{detrital}}}{c^{\text{opal}}} \right)^{0.58} \quad (3-20)$$

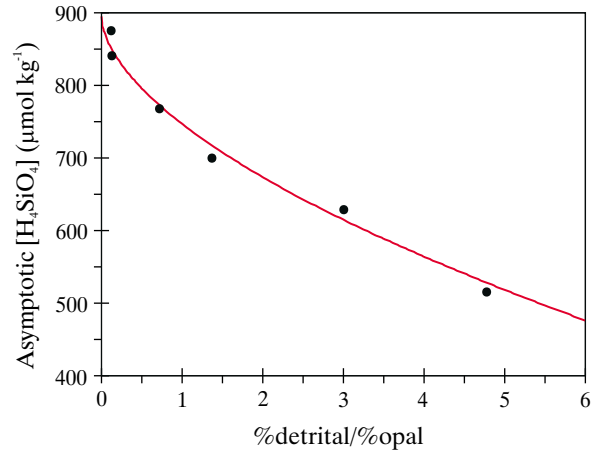


Figure 3-9 Dependence of $[\text{H}_4\text{SiO}_4]_{\text{asym}}$ on the ratio of detrital to opal sediment content; observed data (filled circles) from *Van Cappellen and Qiu* [1997a] along with model fit (3-20).

where c^{detrital} and c^{opal} are the fractions (wt%) of detrital material and opal in the sediment, respectively. Although the highest sediment core %detrital/%opal ratio considered by *Van Cappellen and Qiu* [1997a] was 4.8 (corresponding to a reduction in $[\text{H}_4\text{SiO}_4]_{\text{asym}}$ from ~880 to ~520 $\mu\text{mol kg}^{-1}$) values of $[\text{H}_4\text{SiO}_4]_{\text{asym}}$ as low as 150 to 300 $\mu\text{mol kg}^{-1}$ have been observed in opal-poor cores outside of the Southern Ocean [*Archer et al.*, 1993; *Martin et al.*, 1991; *McManus et al.*, 1995]. The observed relationship is therefore extrapolated to a maximum %detrital/%opal ratio of 15, producing a potential minimum $[\text{H}_4\text{SiO}_4]_{\text{asym}}$ value of around 180 $\mu\text{mol kg}^{-1}$ under typical abyssal temperatures. Despite the dependence of asymptotic silicic acid concentrations on sediment composition being accountable on a purely kinetic basis [*Rabouille et al.*, 1997], to reduce the degrees of freedom in the model the assumption is made that the equilibrium saturation state of opal is directly affected (i.e., $[\text{H}_4\text{SiO}_4]_{\text{eq}}^{\text{opal}}$). A reduction factor (γ_{Al}) accounting for Al-inhibition is then defined

$$\gamma_{\text{Al}} = 0.2 \quad \frac{c^{\text{detrital}}}{c^{\text{opal}}} > 15 \quad (3-21a)$$

$$\gamma_{\text{Al}} = 1.0 - \left(0.045 \cdot \frac{c^{\text{detrital}}}{c^{\text{opal}}} \right)^{0.58} \quad \frac{c^{\text{detrital}}}{c^{\text{opal}}} \leq 15 \quad (3-21b)$$

and used to modify $[\text{H}_4\text{SiO}_4]_{\text{eq}(z)}^{\text{opal}}$ (3-15), to give

$$[\text{H}_4\text{SiO}_4]_{\text{eq}(z)}^{\text{opal}} = \gamma_{\text{Al}} \cdot 10^{\left(\frac{6.44 - 968}{T(z)} \right)} \quad (3-22)$$

A full description for the dissolution rate of opal within the sediments can now be written

$$R_{(z)}^{\text{opal}} = \eta_{1(z)}^{\text{opal}} \cdot \eta_{2(z)}^{\text{opal}} \cdot k_0^{\text{opal}} \cdot \rho^{\text{opal}} \cdot [1 - \phi_{(z)}] \cdot c_{(z)}^{\text{opal}} \quad (3-23)$$

where k_0^{opal} is the dissolution rate constant (a^{-1}) for ‘fresh’ opal delivered to the sediment surface (i.e., in a diagenetically unaltered state) under conditions of complete under-saturation and at a temperature of 0°C . All that remains is then to determine a value for k_0^{opal} . Unfortunately, published estimates for the dissolution rate constant of opal vary widely. Model fitting of a series of Antarctic cores suggests a value at the sediment surface in the range 0.016 to 0.315 a^{-1} [Rabouille *et al.*, 1997]. Schink *et al.* [1975] adopted a value of 0.032 a^{-1} , but noted that experimental determinations often give much higher values than this, upwards of 0.063 - 0.252 a^{-1} . A further complication arises in that all these estimates are based on the assumption of linear kinetics.

The value of k_0^{opal} is therefore optimized to reproduce (under equivalent conditions) estimated opal dissolution fluxes across the sediment-water interface ($fdis^{\text{opal}}$) of each of a series of Southern Ocean cores [Rabouille *et al.*, 1997]. To achieve this, the model was run for each of the cores detailed in Table 3-4, taking opal and detrital content from observations and assuming a bottom-water H_4SiO_4 concentration of $145 \mu\text{mol kg}^{-1}$ typical of that area [Conkright *et al.*, 1994]. Since laboratory analyses on these cores were carried out at relatively elevated temperatures (2 to 4°C) compared to the abyssal Southern Ocean [Rabouille *et al.*, 1997] and there being a general likelihood of post-recovery distortion in $[\text{H}_4\text{SiO}_4]$ profile [Martin *et al.*, 1991; McManus *et al.*, 1995], the adoption of a temperature characteristic of the benthic location may not necessarily be appropriate. Instead, an effective temperature of 3.5°C is assumed, giving good agreement between observed values of $[\text{H}_4\text{SiO}_4]_{\text{asym}}$ [Rabouille *et al.*, 1997] and $[\text{H}_4\text{SiO}_4]_{\text{eq}}^{\text{opal}}$ predicted by (3-15). However, even accounting for all these factors the estimated value of k_0^{opal} still ranges from 0.07 to 0.3 a^{-1} . That these are all significantly lower than suggested by the kinetic experiments of Van Cappellen and Qiu [1997b] made on

samples taken from the same cores ($0.66 \text{ nmol s}^{-1} \text{ g}^{-1}$, equivalent to 1.25 a^{-1}) may be due to further differences between experimental and *in situ* conditions. It is likely that opal isolated from a sedimentary matrix behaves in a thermodynamically different manner from that still in the presence of detrital material, so that care must be taken in the interpretation of laboratory analyses.

On the basis that the presence of detrital material appears to exert an important control on asymptotic silicic acid concentrations (Figure 3-9) k_0^{opal} is made a function of the %detrital/%opal ratio. The relationship is defined consistent with the individually fitted core-specific dissolution rates (Table 3-4). An additional constraint is imposed of a value of 1.25 a^{-1} at a %detrital/%opal ratio of 0.0 , assuming that the kinetic experiments of Van Cappellen and Qiu [1997b] are representative of conditions where there is no detrital matter influence. This gives rise to the relationship (Figure 3-10)

$$k_0^{\text{opal}} = 0.05 + 0.055 \cdot \left(0.0164 + \frac{c^{\text{detrital}}}{c^{\text{opal}}} \right)^{-0.75} \quad (3-24)$$

3.2.5.2 Look-up table implementation

In an analogous manner to that for CaCO_3 , the sedimentary diagenesis of opal in SUE is represented via means of a look-up table. The spanning set of parameters utilized for this are shown in Table 3-5. As before, these represent something of a compromise between the dimensionality and resolution of the parameter space describing the processes, and considerations of computational resource availability.

A look-up table function is defined for the H_4SiO_4 flux density across the sediment-ocean interface resulting from opal dissolution within the sediment

$$fdis^{\text{H}_4\text{SiO}_4} = L(T, [\text{H}_4\text{SiO}_4], c^{\text{opal}}, c^{\text{detrital}}) \quad (3-25)$$

where T and $[\text{H}_4\text{SiO}_4]$ are the bottom-water temperature and silicic acid concentrations, respectively, while c^{opal} and

Table 3-4 Details of Sediment Core Observations Together With Fitted Model Dissolution Flux ($fdis^{\text{opal}}$)

Core ID	opal (wt%)	CaCO_3 (wt%)	detrital (wt%)	$\frac{\text{wt\%detrital}}{\text{wt\%opal}}$	$[\text{H}_4\text{SiO}_4]_{\text{asym}}^1$ ($\mu\text{mol kg}^{-1}$)	$fdis^{\text{opal } 1}$ ($\mu\text{mol cm}^{-2} \text{ a}^{-1}$)	$[\text{H}_4\text{SiO}_4]_{\text{asym}}^2$ ($\mu\text{mol kg}^{-1}$)	$fdis^{\text{opal } 2}$ ($\mu\text{mol cm}^{-2} \text{ a}^{-1}$)	$k_0^{\text{opal } 2}$ (a^{-1})
KTB05	75.5	12.8	9.2	0.12	875	132.0	835	146.3	0.293
KTB06	86.3	0.3	10.8	0.13	841	203.0	834	154.0	0.288
KTB11	36.7	33.8	26.5	0.72	768	66.0	761	65.4	0.119
KTB19	38.0	7.7	52.2	1.37	700	53.5 ³	709	55.7	0.093
KTB26	17.5	28.0	53.3	3.05	629	31.0	608	30.3	0.074
KTB28	15.8	7.7	75.5	4.78	515	24.0	526	23.9	0.067

¹ Rabouille *et al.* [1997]

² model fitted (present study)

³ estimated

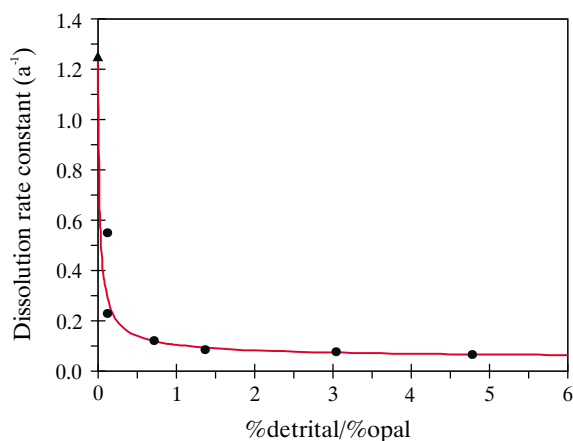


Figure 3-10 Dependence of k_0^{opal} on the ratio of detrital to opal sediment content. Model dissolution rates required to produce the estimated dissolution fluxes of *Rabouille et al.* [1997] are shown as filled circles, while the dissolution rate of free opal under ambient conditions of 0°C and complete under-saturation estimated from *Van Cappellen and Qiu* [1997b] is shown as a filled triangle.

c^{detrital} are the (mass) fractions of the opal and detrital material in the sediment surface layer, respectively.

3.2.5.3 Model validation

The opal diagenesis model has been constructed empirically on studies utilizing cores taken from a single transect located in the Southern Ocean. It is therefore essential to validate the model against data from geographically, and more importantly, biogeochemically different locations. Rather than focus on the specifics of any one particular site for validation, since the diagenesis model is to be used within a global framework where only mean regional behaviour is under consideration, it is more appropriate to analyse general trends of response. A database of parameters having direct equivalence with model output is constructed (detailed in Appendix III), taken from studies carried out on cores located mainly in the tropical and sub-tropical Pacific and sub-tropical Atlantic. Conditions in these regions generally deviate substantially from those in the Southern Ocean, often characterized by much higher CaCO_3 sediment content (especially in the Atlantic), lower opal rain rates, higher (Pacific) or lower (Atlantic) silicic acid concentrations, and slightly warmer temperatures. Such data is thus able to provide a robust test of the model parameterization.

Model data is generated with SUE configured with the simple box structure, ocean circulation, and biological export production of the PANDORA box model [*Broecker and Peng*, 1986]. Remineralization of POM, CaCO_3 , and opal takes place below the surface layer according to the schemes of *Archer et al.* [1998] for POM and CaCO_3 , and *Gnanadesikan* [1999] for opal, with sediment modules employed at 100 m depth intervals. The model was run for a total of 300 ka with inputs to the system of DIC, ALK, and

dissolved SiO_2 chosen to attain a steady-state consistent with the modern ocean [*Yamanaka and Tajika*, 1996]. It should be noted that since PANDORA considers only seven geographically distinct surface regions, reducing to as few as four at depth, spatial variability in actual ocean biogeochemical conditions is unlikely to be well represented. The exact correspondence between observed and model data must therefore be interpreted with some caution.

Model results are shown in Figure 3-11, demonstrating a number of trends in the ocean. Of particular importance is the clear non-linear increase of opal burial with rain flux (a). There are a number of obvious artefacts present, such as the apparent decrease in mean opal content (\bar{c}^{opal}) with increasing rain flux (b), and the decrease in dissolution flux ($f_{\text{dis}}^{\text{opal}}$) with increasing \bar{c}^{opal} (c). These are likely to be a consequence of unrealistic CaCO_3 sediment distributions produced by the overly-simple ocean configuration and biological schemes in PANDORA. Figure 3-12 shows the same model data, but now on an expanded scale and contrasted with observations. The main points that can be drawn from this exercise are;

- (1) The model successfully reproduces a number of observed trends, such as in \bar{c}^{opal} as a function of opal rain flux ($f_{\text{set}}^{\text{opal}}$) as shown in plot (b) and asymptotic silicic acid concentrations in the sediment ($[\text{H}_4\text{SiO}_4]_{\text{asym}}$) as a function of \bar{c}^{opal} (e). The correspondence between model predictions and the relationship deduced from observations relating $[\text{H}_4\text{SiO}_4]_{\text{asym}}$ with $f_{\text{set}}^{\text{opal}}$ [*Archer et al.*, 2000] is particularly good (d).
- (2) The model is much less successful in predicting opal dissolution fluxes across the sediment-water interface ($f_{\text{dis}}^{\text{opal}}$), which are generally overestimated, as demonstrated in plots (c) and (f).

Overall, considering that the opal diagenesis model was developed from core data taken solely from the Southern Ocean, many aspects of its performance under completely different conditions are in good agreement with observations. That dissolution fluxes at low- and mid-latitude regions tend to be overestimated is much less important in terms of the global mass balance of Si since the Southern Ocean dominates the global sink. However, it will be shown subsequently that the use of a more ‘realistic’ ocean representation greatly enhances the apparent success of the model (4.5.2).

Table 3-5 Opal Diagenesis Look-up Table Spanning Set

Parameter	range	step	units
Sedimentary opal content	2 to 100	2	%
Bottom-water $[\text{H}_4\text{SiO}_4]$	0 to 250	10	$\mu\text{mol kg}^{-1}$
Bottom-water temperature	270 to 280	1	K
Base dissolution rate, k_0^{opal}	0.01 to 1.00	0.01	a^{-1}
Sedimentary %detrital/%opal	0 to 10	1	n/a

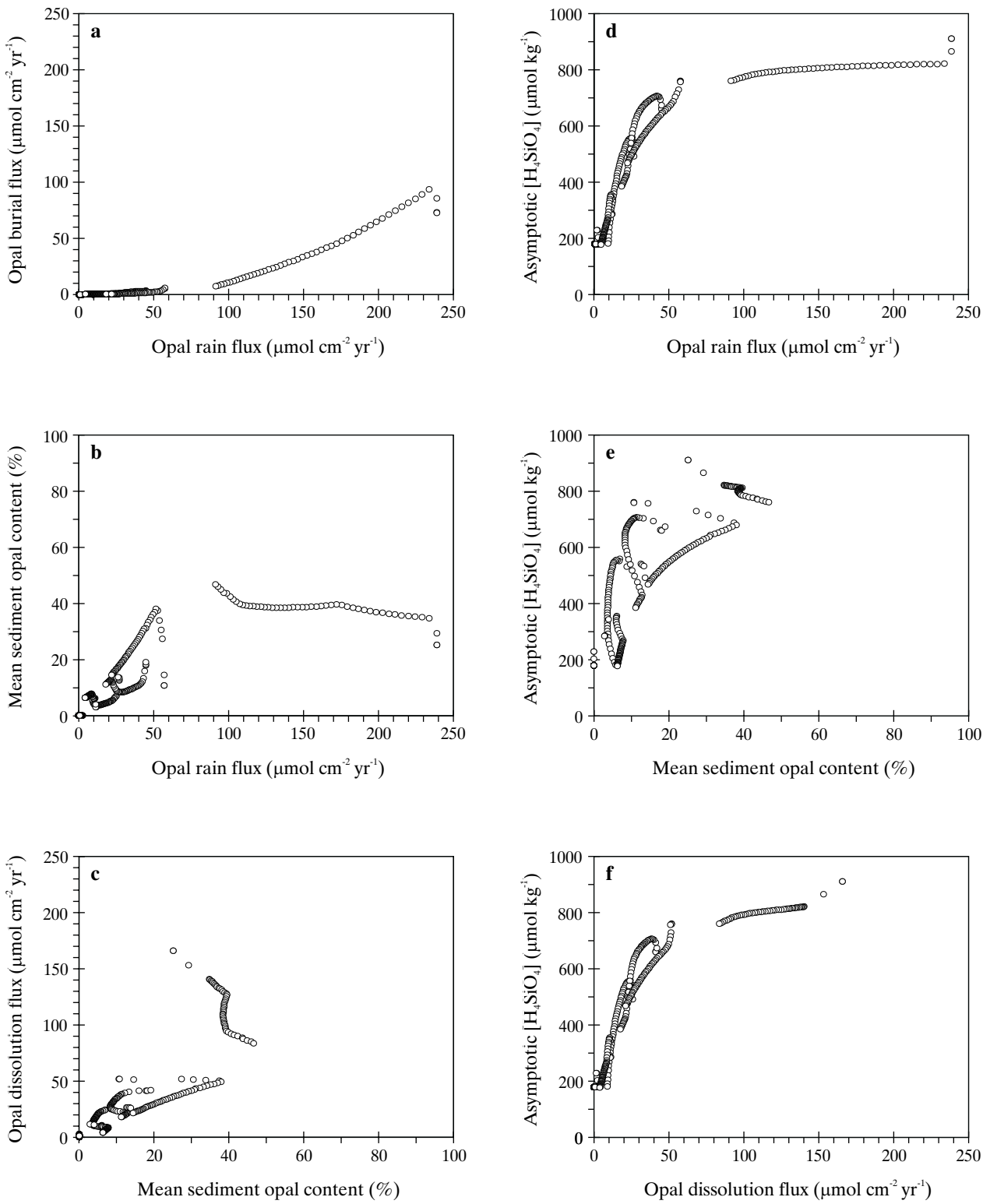


Figure 3-11 Combined response of the opal diagenesis model within SUE (configured following Broecker and Peng [1986]).

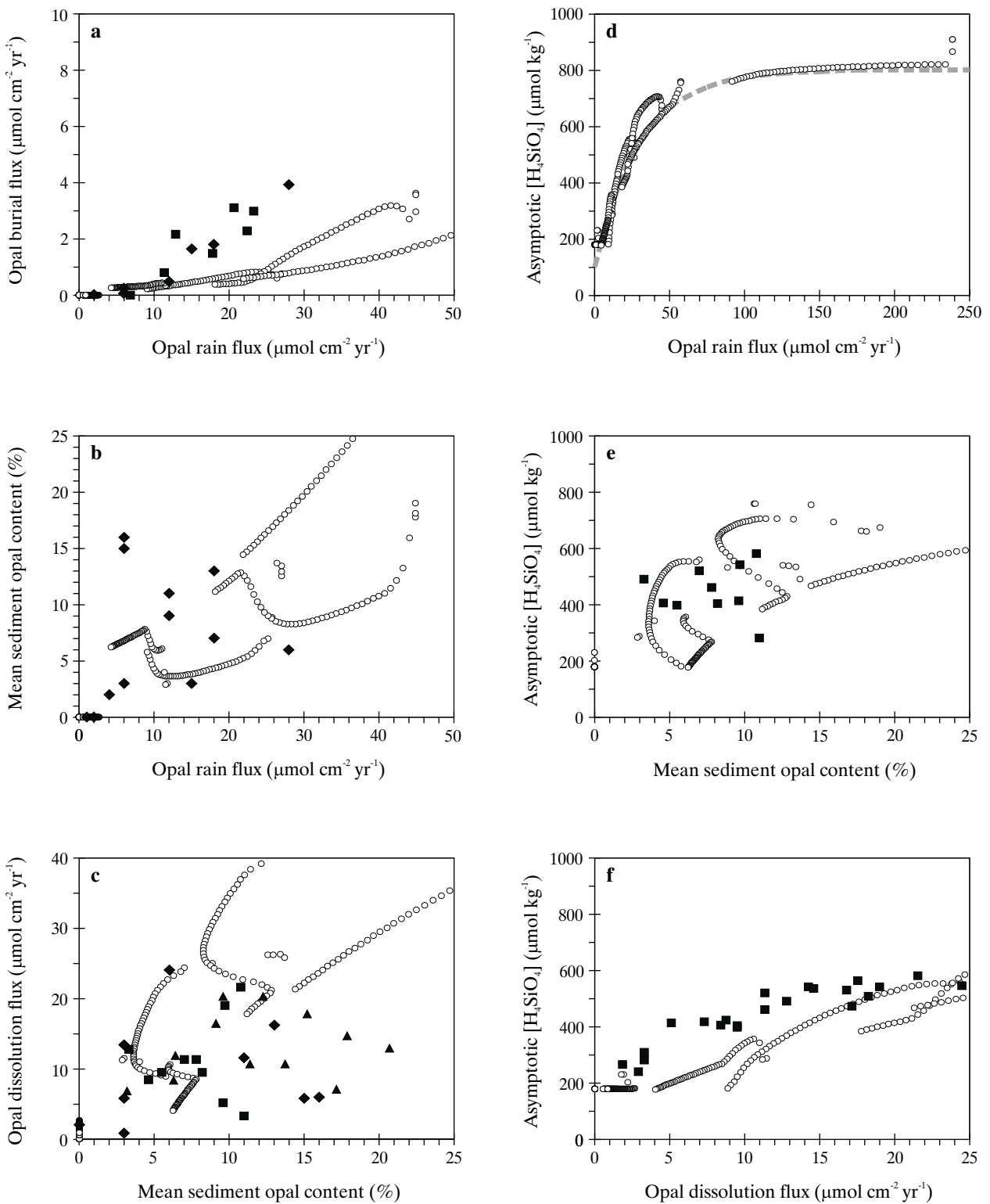


Figure 3-12 Combined response of the opal diagenesis model within SUE (small open circles) contrasted with the validation data, indicated by larger filled symbols; squares - *McManus et al.* [1995], diamonds - *Archer et al.* [1993], triangles - *Martin et al.* [1991]. The thick dashed grey line in (d) indicates the estimated trend of *Archer et al.* [2000].

3.3 Synthetic deep-sea sediment cores

Much of the available information regarding the glacial-interglacial cycles of the late Quaternary comes from sediment cores recovered from the benthic environment. Not only is there excellent global coverage afforded by such records but in addition they contain a large number of proxies relating to different aspects of the state and operation of the Earth system. However, to be of use in understanding glacial-interglacial change these proxies must be interpreted. This is often no easy matter, particularly where a number of separate nonlinear processes all contribute to the observed net change. It may then not be possible to unequivocally deduce the mechanism(s) responsible for this change.

An alternative but very much complementary approach to glacial-interglacial analysis is developed here - working forwards from a description of processes driving the change towards observations. The advantage of this methodology is that the processes operating are explicitly known, and as such can be isolated and fully characterized through sensitivity studies and similar analyses. The possibility of non-unique solutions remains; correctly simulating a paleoceanographic proxy can not prove unequivocally that the model processes involved were actually important. However, use of multiple paleoceanographic proxy indicators can provide powerful additional constraints to a chosen hypothesis.

3.3.1 Synthetic sediment core construction

The thickness of accumulating material that the sediment module can track is theoretically limitless. However, in the sediments integral to the model where there is one module associated with every depth interval at each of every ocean grid point, practicalities of data storage forces the maximum number of sub-layers represented to be restricted. Sub-layers at the bottom of the stack are now gradually 'lost' as sediment accumulates at the top of the stack. As long as the depth of sediment represented exceeds the maximum possible thickness that can be lost due to sediment erosion [Archer *et al.*, 1998] the dynamical response of the model will be unaffected.

A second set of sediment modules is introduced, distinct from the 'integral' modules. These are prescribed only at key and/or representative locations in the ocean. This gives a much more manageable number of cores such that enough sub-layers can be represented to enable the entire history of sediment accumulation over the course of the model run to be tracked. Although the representations of sediment deposition, diagenetic alteration, and bioturbation are identical to those acting in the integral modules, these additional core systems are assumed to be completely passive in that there is no exchange of mass with the ocean.

Age scales (i.e., age as a function of depth in the sediment) are provided for these synthetic cores in order to allow direct comparisons to be made with actual cores recovered from the deep sea. A number of different approaches for this are provided for.

Oxygen isotope stratigraphy

Age scales for sediment cores recovered from the deep-sea are typically generated by a rather complex procedure involving tuning measured foraminiferal $\delta^{18}\text{O}$ stratigraphy to an orbital template [Berger, 1994; Berger *et al.*, 1994, 1995, 1996; Imbrie *et al.*, 1984]. The foraminiferal $\delta^{18}\text{O}$ colour tracer in SUE provides the raw information to allow this procedure to be followed. However, constructing orbitally-tuned age scales for the huge number of synthetic sediment cores which can be generated from multiple model runs is likely to be very time-consuming. This approach is therefore not adopted for routine use with SUE.

Single stratigraphic marker

The simplest approach for down-core age assignment is to assume constant sediment accumulation rates. A single stratigraphic marker is generated by applying an impulse of a conservative colour tracer to the sediment surface at the end of model spin-up (identical to inert tracer profile simulations - 3.2.1.2). The level at which the peak concentration of colour tracer occurs in the core is identified and assumed to have an age equal to that at which the impulse event occurred. Linear interpolation between the age at this depth level and zero at the sediment surface thus defines the sediment age scale. This method is analogous to the use of linear interpolation from the magnetic reversal at the Brunhes-Matuyama boundary to core-top [Raymo, 1997], a relatively common technique, particularly in cores lacking a reliable $\delta^{18}\text{O}$ stratigraphy [Farrell and Prell, 1991]. However, many potential mechanisms for glacial-interglacial change in the global carbon cycle lead to significant variability in sediment accumulation rates. This methodology is thus only of use either with a sub-set of glacial-interglacial hypotheses or for cores located in environments inhibitive to the preservation of calcite (upon which other age scales depend).

Carbon-14

Calclitic ^{14}C in the sediments is continuously decayed allowing radiocarbon ages to be calculated. However, this is of limited practical use in contrasting extended model and observed core signals. Uncertainties in past cosmogenic production rates, and changes in reservoir capacity [Stocker and Wright, 1996], together with analytical considerations all act so as to restrict the age interval over which radiocarbon dating is reliable to within the last full glacial cycle.

Depositional age tracer

The advantage of synthetic sediments is that the precise time at which material is deposited to the sediment surface is known. A (calcite-tied) colour tracer representing the time of deposition can be used to provide a mean age for each sediment sub-layer. In light of the various drawbacks associated with the three methodologies outlined above this simple internal age scale is adopted for all further analysis of synthetic sediment cores in the present study.

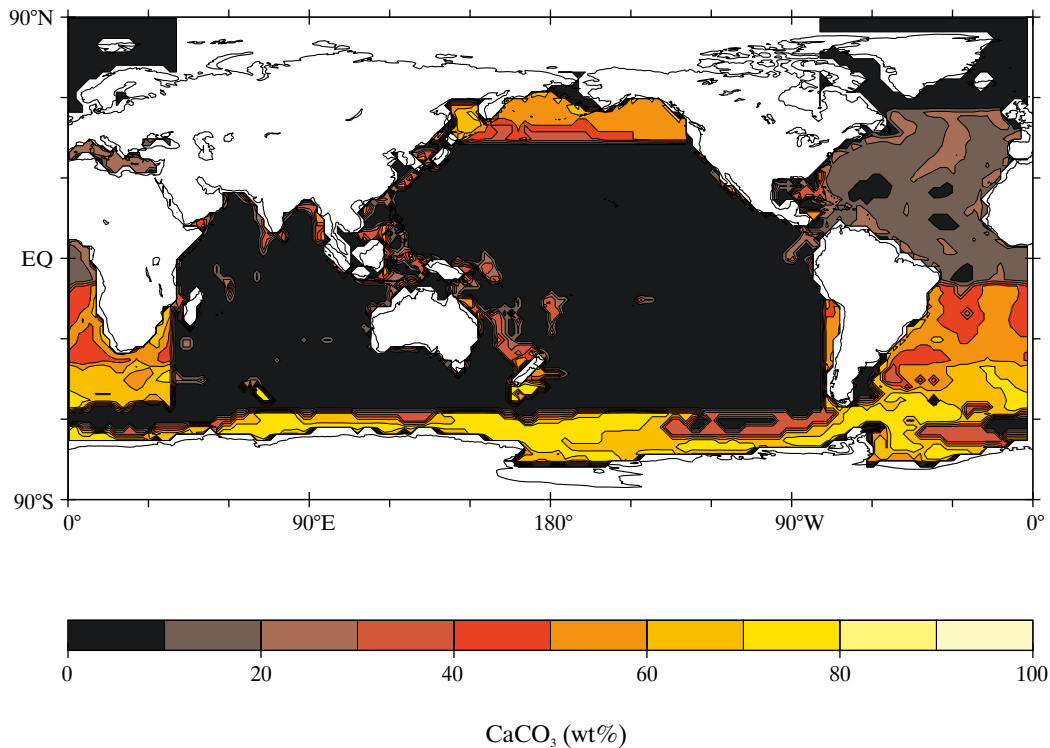


Figure 3-13 Global distribution of sediment surface CaCO_3 generated by SUE (configured after *Broecker and Peng* [1986]), and interpolated to a 2.5° by 2.5° grid.

3.3.2 The application of synthetic sediment cores to paleoclimatic analysis

Three primary areas for application of synthetic deep-sea sediment cores to glacial-interglacial paleoclimatic investigation are identified; analysis of the global distribution of sediment composition, general down-core variability within individual cores, and changes in the character of the CaCO_3 lysocline transition zone. In the following sections these are exemplified with the aid of the results of a simple carbon cycle model. SUE is run in a 'PANDORA'-type configuration (see 3.2.5.3) for a period of 500 ka following 50 ka of spin-up. The system is perturbed by varying the magnitude of the terrestrial carbon reservoir. The forcing signal for this is a square-wave; period 100 ka, amplitude 1000 GtC, and with a linear transfer of carbon between reservoirs taking place over an interval of 1 ka.

3.3.2.1 Sediment distribution analysis

Model-generated (core-top) sediment composition and isotopic signatures can be used to produce maps of global distributions. Contrasts with available data sets [*Archer, 1996b; Catubig et al., 1998; Henize et al., 1999*] can give essential diagnostics on the operation of the model carbon cycle and aid in the optimization of unconstrained parameter

values. This analysis need not be restricted to the present-day and can be extended back in time, with characteristics extracted from buried sediments for any required period. Comparisons with paleoceanographic observations can then yield important clues as to the past operation of the global carbon cycle. For example, the belt of maximum opal accumulation in the Southern Ocean appears to have migrated northwards at the time of the LGM compared to the present-day [*Anderson et al., 1998; Francois et al., 1997; Kumar et al., 1995*]; any complete solution for glacial-interglacial change should therefore be able to reproduce such a shift.

Mapping global sediment distributions from results produced by SUE is complicated by the absence of a single ocean floor depth associated with each grid point (as is the case in 3D OGCMs). Instead, each model region has a series of sediment modules which span discrete intervals over the maximum depth of the water column. Distributions are therefore produced for each ocean region in turn by mapping the sediment composition characterizing each sediment module onto all ocean floor lying within the depth interval spanned by that module as defined by observed ocean bathymetry [*ETOPO5, 1988*]. To illustrate this Figure 3-13 shows the global distribution of core-top CaCO_3 . While the prescribed export fluxes in PANDORA [*Broecker and*

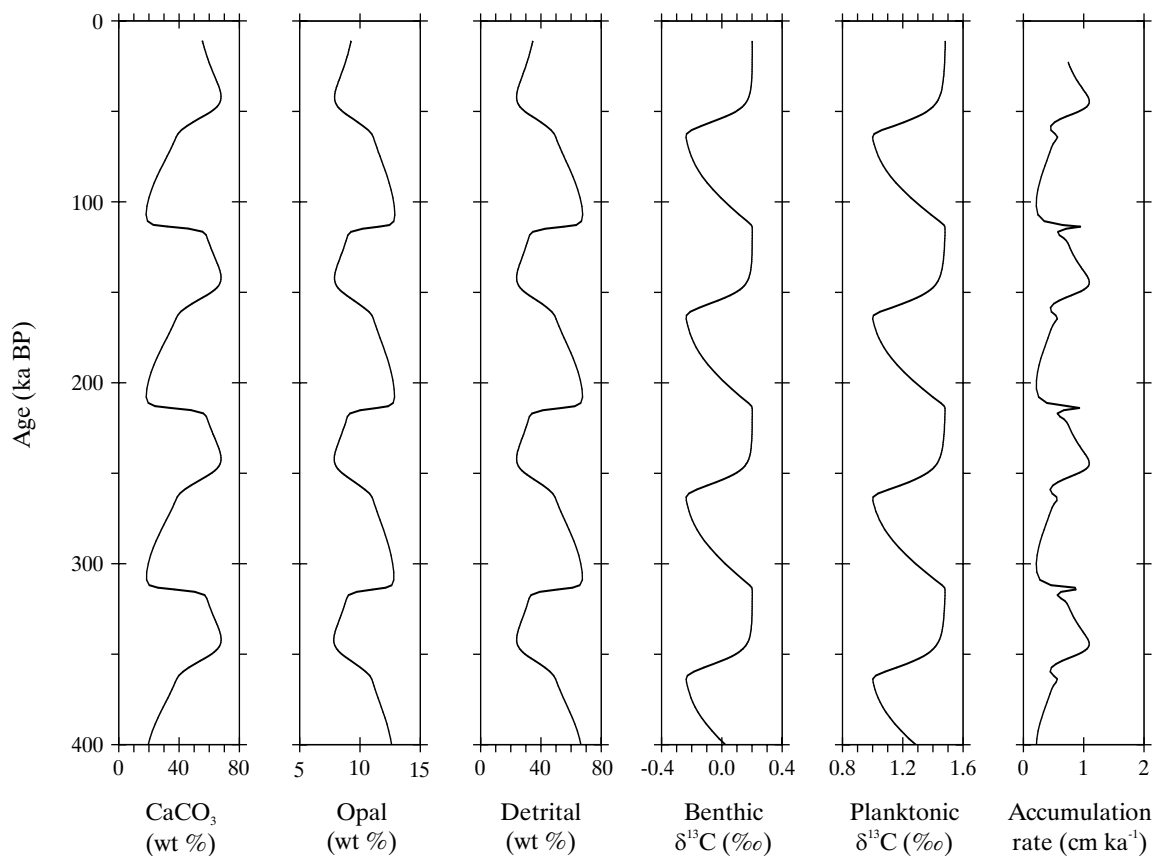


Figure 3-14 Down-core variability in major sediment solid components, isotopic foraminiferal ^{13}C tracers, and overall sediment accumulation rate in a synthetic sediment core located at an intermediate depth in the Southern Ocean. The model is forced by a simple cyclical (square-wave) change in terrestrial carbon storage.

Peng, 1986] clearly produce erroneously high CaCO_3 preservation in the Southern Ocean with little preservation in the northern Atlantic and Indo-Pacific, this exercise does highlight two important features. Firstly, the depth-dependence of CaCO_3 preservation (for instance, the topographic and therefore preservational high of the mid-Atlantic ridge can be picked out). Secondly, distinct regional differences in preservation arising from a combination of the specifics of ocean circulation and biological export can be generated. The boundaries differentiating between the various grid point regions can be seen as sharp linear transitions in $\% \text{CaCO}_3$, an artifact of the low spatial ocean resolution of PANDORA.

3.3.2.2 Single core analysis

Of particular interest in this present study of glacial-interglacial change are comparisons that can be made between variability in model and observed down-core sediment characteristics. Ideally, mismatches between model and observations should indicate deficiencies in the model representation of changes in the global carbon cycle. However, in practice such direct analysis is not possible. The

information contained in synthetic model sediment cores is determined by processes and environments representing large temporal and spatial means. In contrast, sediment cores recovered from the deep sea may be influenced by local processes such as up-welling [Bertrand *et al.*, 1996] and sediment redistribution by bottom currents [Bareille *et al.*, 1994; Seidov and Haupt, 1999]. Moreover, in order to maximize core resolution locations are often deliberately chosen where such local processes result in enhanced sedimentation rates. As a result, the degree of bioturbational filtering in down-core variability is likely to differ substantially between model-generated and observed signals. The respective amplitudes and mean values of such variability cannot therefore be expected to closely correlate. Random events can further increase the specificity of recovered cores, particularly through non-local mixing (such as through burrow formation) and core damage during recovery, but also from turbidity events. These can all result in depth intervals characterized by intense distortion and hiatuses in proxy signals, factors which cannot be prognostically generated by the model.

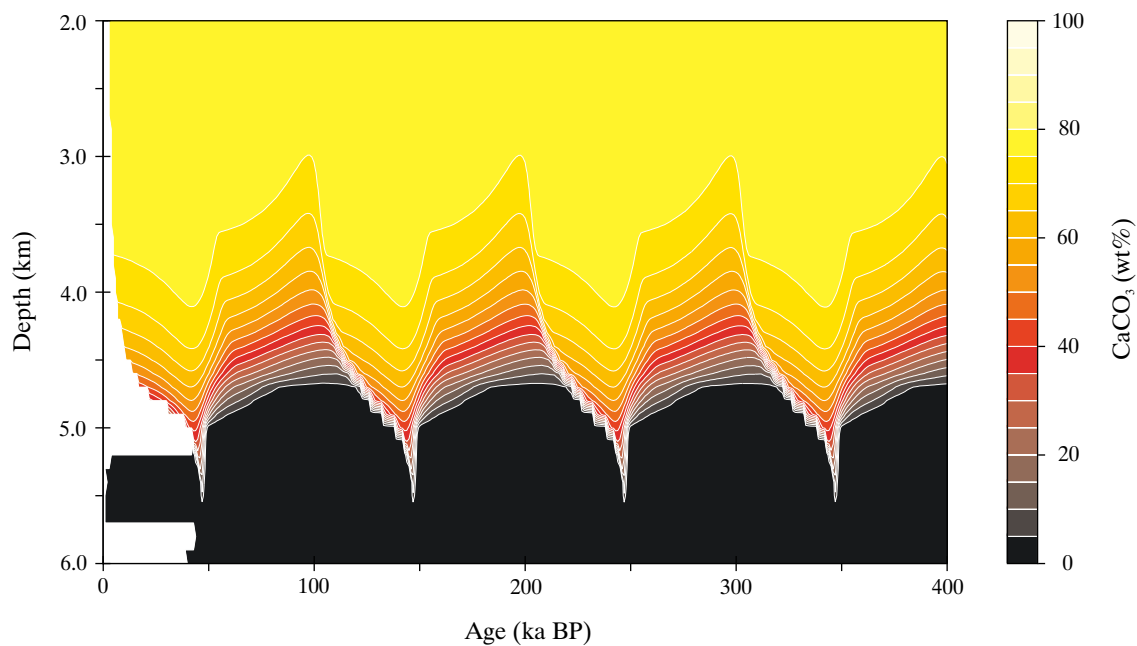


Figure 3-15 Variability in the shape of the CaCO_3 lysocline transition zone with time, as recorded by a series of synthetic sediment cores.

Although processes operating on smaller scales than those represented by the model exert an important control on the observed record there is no reason *a priori* why the timing and direction of change on glacial-interglacial time scales should not generally find a strong correspondence with synthetic proxies (that is where perturbations in the global carbon cycle are correctly represented in the first place). By contrasting the phase of model and observed signals information should be extractable regarding the mechanisms responsible for variability in the system. Visual inspection may often be sufficient for such analysis, although use of spectral methods can naturally provide a more quantitative assessment of the response (e.g., *Hagelberg et al.* [1991]; *Lau and Weng* [1995]; *Mann and Lees* [1996]).

Figure 3-14 shows a sub-set of the paleoceanographic proxy information extractable from a single synthetic sediment core generated by SUE. All are plotted as a function of sediment age for the past 400 ka (equivalent to a total core length of about 229 cm), defined according to the internal calcite-tied age tracer. The effect on the preservation of CaCO_3 resulting from changes in ocean chemistry as carbon is alternately removed from and added to the ocean can be clearly seen, with the relative proportions of the other major solid phase responding in anti-phase. In this particular model run ^{13}C fractionation in benthic and planktonic foraminifera is assumed to follow that for bulk calcite (2-61a), such that variability in $\delta^{13}\text{C}_{\text{foram}}$ reflects only changes in the mean isotopic composition of the ocean as a whole. Finally, pronounced changes in sediment accumulation rate are apparent. Use of an age scale derived from a single stratigraphic marker with the assumption of constant

accumulation rate (3.3.1) would obviously therefore produce a distorted picture were it to have been adopted in this example.

3.3.2.3 CaCO_3 lysocline transition zone

Although there is no precise definition, the location of the calcium carbonate (as either calcite or aragonite) lysocline is often taken to mark the depth in the ocean at which the presence of CaCO_3 starts to decline rapidly in surface sediments with increasing depth [*Berger*, 1968; *Balsam*, 1983; *Broecker and Takahashi*, 1978; *Farrell and Prell*, 1989]. A second characteristic feature of deep-sea sediment composition is the carbonate compensation depth. This is the point at which the CaCO_3 dissolution flux is exactly balanced by the rain rate and is usually taken to be the depth where CaCO_3 first disappears from the sediments [*Farrell and Prell*, 1989]. Between these lies the lysocline transition zone.

In any restricted region of the ocean, the depth and thickness of the lysocline transition zone will vary on glacial-interglacial time scales as a result of changes in ocean chemistry and/or particulate rain rates to the sediment surface. Analysis of past changes in this zone obtained by comparison of model simulation with observations can thus provide important information regarding the operation of the carbon cycle. Although a number of studies report past variability in the depth profiles of both calcite and aragonite sediment content [*Balsam*, 1983; *Berger*, 1977; *Farrell and Prell*, 1989, 1991; *Karlin et al.*, 1992] there has only been one modelling attempt to date [*Walker and Opdyke*, 1995].

To reconstruct glacial-interglacial variability in the depth and shape of the calcite and aragonite lysocline transition

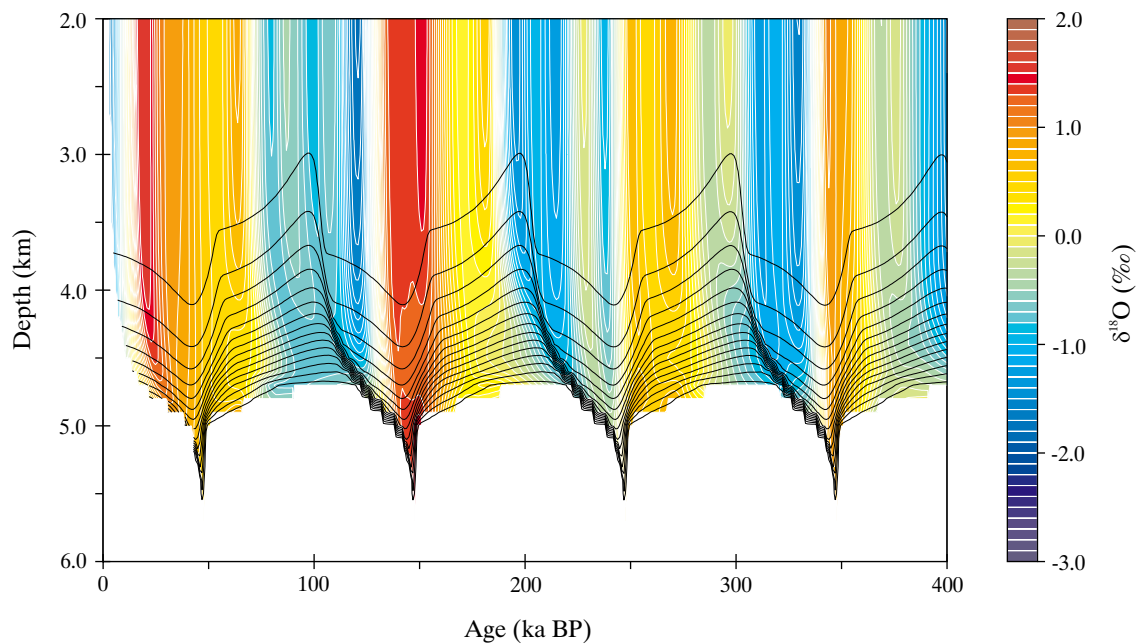


Figure 3-16 Variability in the synthetic foraminiferal $\delta^{18}\text{O}$ tracer over the CaCO_3 lysocline transition zone with time, together with contours of CaCO_3 content (see Figure 3-15).

zones a series of synthetic sediment cores are defined within the same grid point region and at closely spaced depths. Figure 3-15 shows how the shape of the CaCO_3 lysocline transition zone changes over the past 400 ka in response to the applied terrestrial carbon storage forcing. It can be seen that there is a pronounced cyclicity in both lysocline and carbonate compensation depths over this period, with a peak-to-peak amplitude of about 1 km. Pronounced preservation spikes during times of rapid carbon transfer out of the ocean-atmosphere system are also present.

Other sedimentary characteristics can be plotted in a similar manner. Figure 3-16 shows the distribution of the synthetic foraminiferal $\delta^{18}\text{O}$ tracer over the same depth and time range as before. In the absence of any explicit representation of ^{18}O fractionation within the system (2.2.1.2), sediment boundary conditions are provided by simply assuming an isotopic signature of settling CaCO_3 reaching the sediment surface equal to the equivalent value dictated by the SPECMAP $\delta^{18}\text{O}$ signal [Imbrie *et al.*, 1984] at the time of deposition. It should be noted that while use of SPECMAP gives a first-order representation of observed glacial-interglacial variability in $\delta^{18}\text{O}$, the mean and amplitude of this stacked record are somewhat artificial in value. That maxima and minima in $\delta^{18}\text{O}$ occur approximately simultaneously at all depths down through the water column suggests that even during episodes of intense erosion or preservation, the internal model age scale should be comparable to one derived via orbital tuning of the down-core $\delta^{18}\text{O}$ signal.

Modelling the pre-industrial state

4.1 Introduction

The biogeochemical processes previously outlined delineate what is essentially a framework for representing the global (oceanic) carbon cycle. However, before SUE can be employed to test potential mechanisms behind the observed glacial-interglacial variability in the concentration of atmospheric CO₂, model ocean structure and circulation must be prescribed. Furthermore, the existence of a number of unconstrained parameter values within certain process parameterizations dictates that a degree of model ‘optimization’ must be carried out. The end-product of this optimization will be a steady-state representation of the modern (pre-industrial) carbon cycle which can be used to critically evaluate the model’s performance against observational data.

Parameter optimization and model evaluation should ideally be undertaken within a rigorous statistical framework, with indicators of ‘goodness of fit’ defined and utilized in order to achieve some quantitatively optimal model solution. System characteristics such as atmospheric composition, fields of physical and chemical ocean properties, areal distributions of biological production and sediment composition are all important indicators of system operation and therefore need to be considered in constructing any hypothetical ‘goodness of fit’ statistic. However, in order to achieve this, weightings of relative importance to the overall system response of the carbon cycle must be assigned to all these individual components. Unfortunately it is not possible in the context of this present study for such an approach to be undertaken since these assignments cannot be made unobjectively. Furthermore, with the exception of a few predominantly global values such as the concentration of atmospheric CO₂ and its isotopic signature, there is a serious scale mismatch between the descriptors of model state and observational data. While model ocean properties are regional in character, typically representing zonal or even entire basin averages, much of available observational data is in the form of point measurements, for which system characteristics such as biological productivity (and to a lesser extent, sediment composition) are extremely patchy in their global coverage. Instead, a ‘reasonable’ model state is objectively judged through consideration of a basket of apparently important system characteristics. In any event, the modern ocean carbon cycle is likely to be far from steady state, even prior to the advent of the Industrial Revolution. The validity of an exact simile of the pre-industrial system obtained with a steady state model is thus questionable, particularly for subsequent application to long-term change.

4.2 Ocean structure and circulation

Historically, substantial progress in our understanding of the potential causes behind the relatively low concentration of atmospheric CO₂ ($x\text{CO}_2$) observed to have occurred during the Last Glacial Maximum (LGM) has been made with the use of global carbon cycle models where the representation of the world ocean is highly simplified. In some of the earliest of these models the ocean was partitioned into only two or three homogeneous volumes or ‘boxes’ with a prescribed ocean circulation (e.g., *Knox and McElroy* [1984], *Sarmiento and Toggweiler* [1984], *Siegenthaler and Wenk* [1984]), soon followed by slightly more complex ‘multi-box’ models utilizing up to a few dozen boxes (e.g., *Broecker and Peng* [1986], *Keir* [1988]). Despite their apparent oceanographic naivety they are advantaged by relative ease of interpretation and numerical efficiency [*Joos et al.*, 1997; *Sarmiento et al.*, 1988; *Siegenthaler and Joos*, 1992] which has led to them playing a central role in the development of many of the mechanisms for glacial-interglacial $x\text{CO}_2$ changes proposed to date. However, a number of problems in representing the ocean carbon cycle arise, particularly as a result of the low vertical and horizontal resolution inherent in ocean structures comprising no more than a few dozen distinct elements;

- The remineralization of particulate organic matter (POM), CaCO₃, and opal within the water column are unlikely to be adequately resolved. Vertical adjacency between boxes lying at the surface (where nutrients may be limiting to biological productivity) and at intermediate depths (where most POM remineralization and nutrient release occurs) can lead to ‘nutrient trapping’ problems (see 4.3.4).
- The scavenging of Fe from the water column is similarly likely to suffer from low vertical resolution. Low horizontal resolution may also distort the system, particularly where regions receiving high aeolian Fe supply incorrectly adjoin regions of low aeolian supply rather than being separated by a zone where scavenging can restrict Fe transfer.
- With relatively low (mainly horizontal) resolution model validation attempted between spatially-aggregated model descriptors and point observations taken from paleoceanographic sediment cores becomes difficult.
- Failure to resolve important regions of CO₂ ocean-atmosphere exchange (such as strong net out-gassing from equatorial up-welling zones) may distort the dynamical response of $x\text{CO}_2$ to perturbations, even if model tuning allows for a realistic pre-industrial value to be simulated at steady-state.
- Circulation fields generated by tuning to a single tracer such as radiocarbon (natural or bomb) may be in error when applied to other tracers [*Joos et al.*, 1997; *Kurz and Maier-Reimer*, 1993; *Siegenthaler and Joos*, 1992].

Increasing the number of boxes beyond a few dozen in an attempt to alleviate these problems makes it difficult to construct a self-consistent and realistic ocean circulation. An alternative way of increasing vertical resolution is to use a diffusive box model [*Oeschger et al.*, 1975; *Shaffer*, 1989, 1993,

1996; *Shaffer and Sarmiento*, 1995]. However, where there is no analytical solution, this improvement is achieved at the expense of computational efficiency and issues related to horizontal resolution still remain. A final possible trick is to sub-divide vertically and/or horizontally boxes in an existing box model whilst retaining the original advective field [*Klepper et al.*, 1994].

In contrast to box models, Ocean General Circulation Models (OGCMs) represent the global ocean on a three-dimensional grid, with a typical horizontal resolution of order 3° and with upwards of 15-30 separate vertical levels resolved. Ocean circulation is calculated by consideration of forces generated through surface wind stress and ocean density contrasts (driven by heat and salinity gradients) [*McGuffie and Henderson-Seller*, 1996], with surface boundary conditions prescribed from observations or calculated through coupling with an (Atmospheric) General Circulation Model (GCM or AGCM). Although their grid spacing enables most major ocean biogeochemical provinces to be adequately resolved, the sheer number of cells in the 3D structure results in a considerable computation requirement, even when run ‘off-line’ (i.e., utilizing a pre-calculated circulation [*Bacastow and Maier-Reimer*, 1990]). The simulation of entire glacial-interglacial cycles is therefore currently beyond the practical application of most OGCMs, particularly where extensive sensitivity analyses might be required. In addition, despite having an apparently strong semblance of reality about them OGCMs are far from perfect, for instance often exhibiting serious deficiencies in equatorial circulation which are highlighted when biogeochemical cycling is incorporated [*Najjar et al.*, 1992]. Although such problems can be corrected with the use of a sufficiently fine grid spacing [*Aumont et al.*, 1999], this adds further to the computational costs of running the model.

There is, however, something of a ‘third way’. Zonally-averaged OGCMs (also known as ‘2D’ or ‘2.5D’ models, but referred to as ‘ZOGCM’s hereafter) divide the ocean meridionally into a number of latitudinal bands with a typical resolution of 5-15°. The ocean is therefore zonally averaged although each basin is represented separately. The number of vertical levels is comparable to that of full (3D) OGCMs. As with OGCMs, ocean circulation is calculated from basic fluid physics, albeit in a more highly parameterized form [*Wright and Stocker*, 1992]. While they cannot represent sub-zonal features such as boundary currents they are successful in reproducing the global and basin-scale features such as the Atlantic thermohaline circulation [*Hovine and Fichefet*, 1994; *Wright and Stocker*, 1992]. Indeed, simple single-basin models have been successfully employed in investigating modes of variability in overturning circulation [*Drbohlav and Jin*, 1998; *Yang and Huang*, 1996; *Yang and Neelin*, 1993]. The relatively short integration times of ZOGCMs achieved through zonal averaging (compared to that possible with a true 3D grid) together with their ability to produce an interactive ocean circulation (as opposed to the fixed prescribed circulation of box models) has made them ideal candidates for integrating into complete Earth System Models (ESMs) [*Ganopouloski et al.*, 1998a,b; *Sakai and Peltier*, 1997, 1998].

The flexibility in physical ocean structure enabled by SUE allows for implementation of a ZOGCM-type configuration as an alternative to a simple multi-box model format. While a number of different zonally-averaged global ocean circulation models have been developed (e.g., *Fichefet et al.* [1994], *Hovine and Fichefet* [1994], *Sakai and Peltier* [1996, 1997, 1998]), as an initial step the Bern 2D model is utilized [*Stocker et al.*, 1992; *Stocker and Wright*, 1991a, 1996; *Wright and Stocker*, 1991, 1992]. This has an ocean structure slightly simpler than possible alternatives, consisting of three zonally-averaged ocean basins (Atlantic, Indian, and Pacific) with a variable meridional resolution of between 7.5 and 15.0° (Figure 4-1). The three basins are linked by a Southern Ocean component with meridional but no zonal structure. 14 ocean levels are considered in the vertical. It also has the advantage of arguably the longest application pedigree, having been previously used in contexts such as ocean thermohaline circulation sensitivity [*Stocker and Wright*, 1991b], anthropogenic CO₂ uptake [*Stocker et al.*, 1994] and future feedbacks [*Joos et al.*, 1999], deglacial changes in the ocean ¹⁴C reservoir [*Stocker and Wright*, 1996] and factors affecting surface ocean δ¹³C distributions [*Lynch-Stieglitz et al.*, 1995]. Of obvious relevance to this present study is the fact that with the addition of a comprehensive carbon cycle [*Marchal et al.*, 1998b] the Bern 2D model has been previously employed in exploring the influence of changes in ocean circulation on xCO₂ [*Marchal et al.*, 1998a,b, 1999].

Although ocean circulation in the version of the Bern 2D model considered for application in SUE is annual [*Stocker and Wright*, 1996], important variability in the actual ocean system occurs seasonally. In particular, physical properties such as sea ice extent and mixed layer depth change markedly over the course of the year at high latitudes, leading to profound biogeochemical changes. The relatively sensitivity of CO₂ fugacity (*f*CO₂) with respect to ocean-atmosphere exchange CO₂ in a surface ocean layer thickness of ~50 m dictates that for numerical stability, carbon transfer across the air-sea interface in SUE must operate with a time step of order one month as opposed to annually. Taking advantage of this, an extremely crude pseudo-seasonality for high latitude processes is introduced in conjunction with a calculated annual insolation cycle (Appendix II). Firstly, fractional sea ice coverage is varied at the monthly time step according to relative changes in insolation levels. Although the cryosphere actually tends to lag changes insolation maximum sea ice extent is assumed to coincide with the winter insolation minimum, while minimum sea ice extent coincides with the summer maximum

$$A_{(t)}^{\text{ice}} = A_{\text{min}}^{\text{ice}} \cdot \left(A_{\text{max}}^{\text{ice}} - A_{\text{min}}^{\text{ice}} \right) \cdot \frac{I_{\text{max}} - I_{(t)}}{I_{\text{max}} - I_{\text{min}}} \quad (4-1)$$

where for each grid point, $A_{(t)}^{\text{ice}}$ is the sea ice-covered area at time t , $A_{\text{max}}^{\text{ice}}$ and $A_{\text{min}}^{\text{ice}}$ are the maximum and minimum sea ice-covered areas, respectively, with insolation (I) variables, similarly designated. Secondly, a ‘winter’ season is defined (used subsequently in the representation of seasonal convection – see 4.2.3.1) at a particular grid point on the basis of mean monthly insolation falling below a prescribed

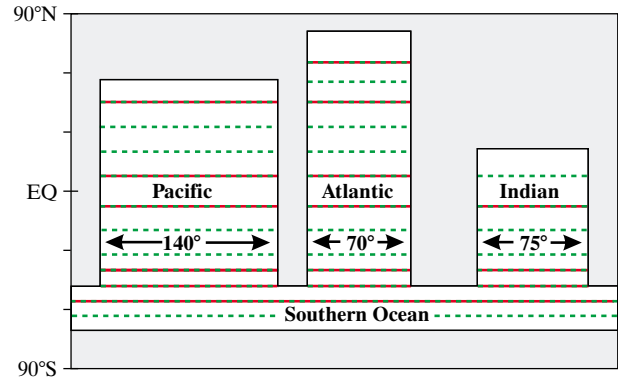


Figure 4-1 Configuration of the grid point regions in SUE1608 together with the location of boundaries of the parent Bern 2D ZOGCM [*Stocker and Wright*, 1996]. Meridional boundaries in SUE1608 are shown in red, whilst those of the Bern 2D model in green.

threshold. This threshold is arbitrarily set at a value of $I = 0.225$, giving a plausible ‘winter’ season of length 4-6 months south of ~55°S.

For carbon cycle work, OGCMs are typically run in an ‘off-line’ mode where a previously calculated advective field is imposed on the ocean biogeochemistry [*Archer et al.*, 2000; *Bacastow and Maier-Reimer*, 1990]. Such a configuration could virtually be considered a box model, albeit one with a huge number of boxes (in the range 10^3 - 10^5). By defining a structure of meta cells in the ocean, each of which encompassing multiple cells of the original ocean model, and by integrating fluxes across each of the meta cells boundaries, a new model structure can be obtained [*Michel et al.*, 1995]. While this ‘child’ structure will be characterized by lower vertical and/or horizontal resolution, ocean circulation should retain the basic characteristics of the ‘parent’ OGCM. Depending on to what extent resolution is degraded, a hierarchy of child models is possible based upon the same parent.

A new ‘pseudo-box’ model of the ocean carbon cycle for use over glacial-interglacial time scales is presented here (shown schematically in Figure 4-2) based upon the ocean configuration and circulation of the Bern 2D ZOGCM [*Stocker and Wright*, 1996]. Since its physical structure comprises 16 grid points horizontally with 8 levels in the vertical, it will hereafter be referred to as “SUE1608”.

4.2.1 Derivation of basic ocean structure

Ocean zonation results in a relatively uncomplicated model circulation field, with mass flow often in the same direction across a series of adjacent cell boundaries. This allows horizontal and vertical resolution to be degraded without any serious distortion of the overall circulation pattern. Grid points in the Bern 2D model are therefore amalgamated in

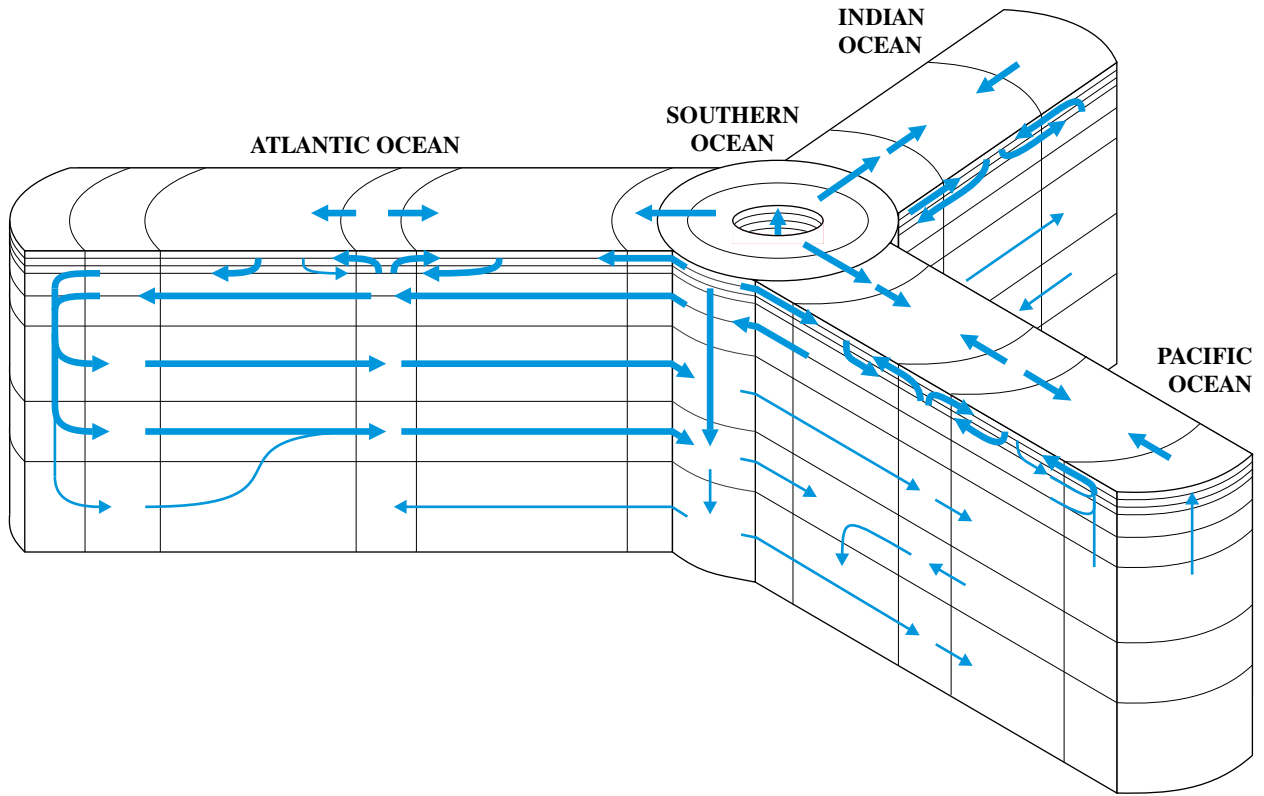


Figure 4-2 Ocean structure and schematic advective field of 'SUE1608'.

such a way that primary biogeochemically distinct surface regions and water masses are retained, the aim being to produce a minimum 'reasonable' representation of the ocean within the context of glacial-interglacial change and within constraints dictated by computational practicalities.

Taking the Bern 2D model, latitudinal boundaries are removed as indicated in Figure 4-1. A single grid point now represents the entire mid-latitude gyre zone (one for each hemisphere and for each of the ocean basins), the sub-polar zone of the Atlantic is enlarged, and both zones lying south of 50°S (the boundary which can be crudely taken to represent the location of the Antarctic Polar Front) in the Southern Ocean are merged. Since the spatial and seasonal complexity in Indian Ocean circulation north of 7.5°S is not reproduced in the parent model, both these regions are also amalgamated with little loss in realism. This leaves a total of 16 geographically distinct ocean regions.

In the vertical, the 50 m near-surface resolution is retained down as far as 150m, with layers amalgamated thereafter according to the apparent delineation of major water masses. A total of 8 vertical levels with lower boundaries at depths of 50, 100, 150, 500, 1000, 2500, 3500, and 4000 m are therefore retained. The overall reduction in the total number of cells by factor ~3 in SUE1608 results in a more than doubling in computational speed compared to that of the Bern 2D parent.

4.2.2 Physical boundary conditions

Physical ocean configuration in the Bern 2D model is highly idealized, assuming uniform zonal widths for each basin and with the longitudinal locations of the basin boundaries not specified in absolute terms [Stocker and Wright, 1996]. Regions associated with each model grid point are therefore prescribed as shown in Figure 4-3 for the purpose of deriving surface forcing data from observational fields. Forcing values for each region are then

$$b_{\text{mean}}^x = \frac{\sum_{\text{lat}} \sum_{\text{lon}} H(D_{(\text{lat}, \text{lon})}) \cdot A_{(\text{lat}, \text{lon})} \cdot b_{(\text{lat}, \text{lon})}^x}{\sum_{\text{lat}} \sum_{\text{lon}} H(D_{(\text{lat}, \text{lon})}) \cdot A_{(\text{lat}, \text{lon})}} \quad (4-2)$$

where D is the depth of the ocean floor (m) taken from ETOPO5 [1988], A is the ocean surface area associated with each ETOPO5 5' × 5' pixel, H is the Heaviside operator (acting to exclude terrestrial regions as defined by topography lying above sea level) and $b_{(\text{lat}, \text{lon})}^x$ is the observed value of surface property x . The physical boundary condition fields utilized are;

- Sea-surface temperature (SST) - from Levitus *et al.* [1994c] (taken at 30 m depth).
- Sea-surface salinity (SSS) - from Levitus *et al.* [1994b] (taken at 30 m depth), but modified in the southernmost grid cell (i.e., south of 55°S) to enable observed

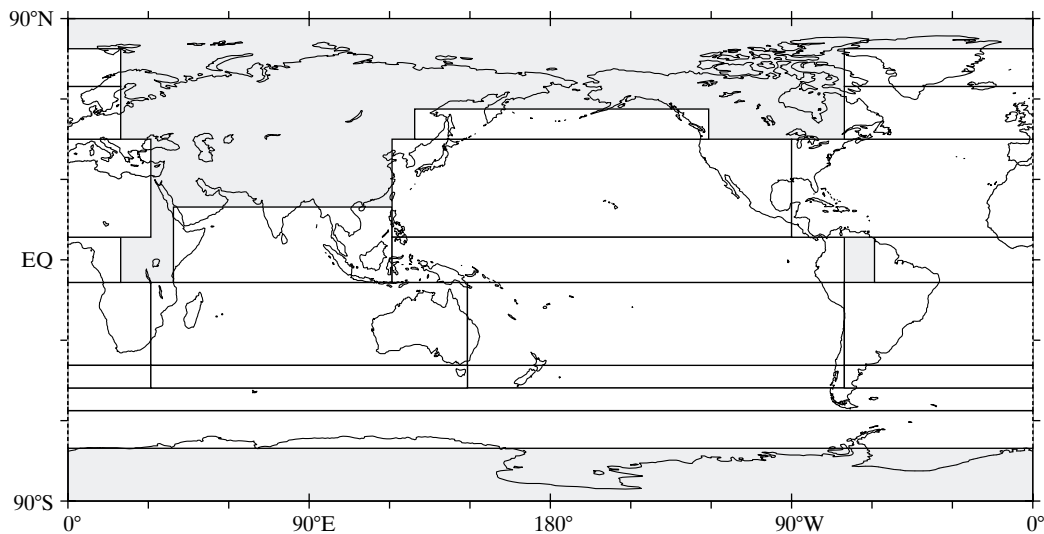


Figure 4-3 Prescribed ocean grid point regions in SUE1608.

deep-water values to be reproduced in that region [Stocker and Wright, 1996].

- Annual wind speed - calculated as an annual mean from individual monthly values [Trenberth *et al.*, 1989].
- Maximum sea ice coverage - set equal to the maximum (winter) monthly value [CLIMAP, 1984].
- Minimum sea ice coverage - set equal to the minimum (summer) monthly value [CLIMAP, 1984].
- Maximum mixed-layer depth - set equal to the deepest mean monthly depth of the mixed layer [Levitus *et al.*, 1994b,c].

Insolation is treated slightly differently, taking a value for each grid point region simply calculated at its mid-latitude (see Appendix II).

Unlike the meridional boundaries of each surface forcing region which have an exact correspondence with the physical ocean model, the longitudinal boundaries of the forcing regions are constrained in order to approximate actual basin topology. They therefore differ from those in the physical model. The resulting difference in area between the forcing and physical model grid point regions is a potential source of bias in terms of magnitude of mean global boundary conditions. However, even for surface properties that vary strongly with latitude such as SST, the area-weighted global mean surface temperature of the model is not significantly different ($\sim 0.1^\circ\text{C}$) from that derived directly from observations [Levitus *et al.*, 1994c].

4.2.3 Derivation of basic ocean circulation

Ocean circulation is taken from the modern (pre-industrial) annual velocity field of the Bern 2D ZOGCM [Marchal *et al.*, 1998a]. Meridional and vertical components of velocity are converted to an equivalent mass flow before any cell amalgamation takes place. Both net advection and exchange

(mixing) across each of the internal physical ocean boundaries in SUE1608 are calculated.

4.2.3.1 Convective processes

While the derivation of a new advective field is relatively straightforward, the limited spatial and temporal resolution of the Bern 2D model makes representation of non-advective circulation, such as (high latitude) convective processes extremely problematic. While convection in the actual ocean is a seasonal process operating on relatively fine spatial scales and occurring heterogeneously within a zonal region, in contrast, the Bern 2D model has no true seasonality and is characterized by extensive homogeneous zonal regions. SUE1608 suffers from an additional deficiency with regard to convective processes in that it lacks any thermodynamic consideration of sea ice formation. As a result, application of commonly-used algorithms for convective adjustment in regions of water column density instability (identified according to the equation of state polynomial approximation of Winton and Sarachik [1993]) produces an overly-ventilated and homogenized deep high latitude ocean [Stocker and Wright, 1996]. This situation is exacerbated if Levitus SSSs [Levitus *et al.*, 1994b] are adjusted in order to produce more realistic deep-water salinities [Stocker and Wright, 1996]. Where water column instabilities do not extend all the way down to the ocean floor, pronounced hiatuses in temperature (T), salinity (S), and nutrient distributions can arise. Three highly parameterized processes are therefore introduced into the model in an attempt to capture (to a first order) observed high latitude behaviour – one for each of; seasonal mixed layer deepening, the formation of deep water masses characterized by low temperature, high salinity, and high dissolved O_2 concentrations, and generally enhanced vertical

mixing in the water column arising through convective and other sub-grid scale processes.

Mixed-layer dynamics

There is a pronounced seasonal cycle apparent at high latitudes. Summer months are characterized by high insolation levels and a stratification of the surface ocean, providing physical conditions suitable for rapid phytoplankton growth. In contrast, during winter months biological activity is suppressed by restricted light availability due to a combination of lower insolation levels incident at the surface ocean together with the presence of a relatively deep mixed layer. During winter, previously depleted surface nutrients are replenished through the entrainment of nutrient-rich deeper waters. This cycle is approximated by allowing deepening of the surface ocean mixed layer during the 'winter' season in SUE (as defined by mean monthly insolation being less than a prescribed threshold) with biological export effectively prohibited. If the water column becomes convectively unstable during this period, convective adjustments are made by pair-wise homogenization of cells down through the water column [Wright and Stocker, 1992]. To prevent excessive ventilation of the deep ocean occurring via this route, mixing depth is restricted according to the maximum observed mean mixed-layer depth (4.2.2).

'Deep water' formation

Realistic deep ocean T, S, and dissolved O₂ distributions are reproduced by transporting surface properties to depth via a conceptual sinking plume. Each 'winter' season, a water mass equal to that of the surface cell is allowed to sink until it reaches a cell with higher potential density (or the ocean bottom, whichever occurs first). T, S, and [O₂] properties are incorporated into the intervening cells in proportion to the mass of each cell as a fraction of the total mass contained within the vertical interval over which the plume sinks. In order to further improve deep-water properties, the temperature of the sinking plume is reduced 4°C below mean annual SST (4.2.2) down to a minimum of -1°C.

Enhanced Southern Ocean mixing

Although between them the seasonal mixed-layer deepening and plume-generation go some way towards reproducing observed pelagic and benthic tracer fields, distributions at mesopelagic depths in the Southern Ocean, particularly of nutrients, are extremely poor. Lack of explicit vertical mixing in the ocean interior in this region due to convective and other sub-grid scale processes is counteracted by prescribing a mass exchange flux between layers lying at or below the maximum mixed-layer depth. This mixing is equivalent to a volumetric exchange of 50 Sv at 62.5°S and 10 Sv at 51.25°S.

4.2.3.2 Eddy diffusivity

The strength of vertical eddy diffusivity is varied down through the water column following Weaver and Sarachik [1991]. Use of a value for horizontal eddy diffusivity consistent with OGCMs and observational estimates of $1 \times 10^3 \text{ m}^2 \text{ s}^{-1}$ [Wright and Stocker, 1992] is found to result in overly-steep meridional gradients in T, [PO₄], [H₄SiO₄], and

[O₂] tending to develop in the Pacific and Indian Ocean basins. In order to improve these tracer fields a coefficient of $1 \times 10^4 \text{ m}^2 \text{ s}^{-1}$ is adopted, comparable to values used in some ZOGCM [Hovine and Fichefet, 1994] and box models [Archer *et al.*, in press; Rich *et al.*, 1999]. This higher value can be justified on the basis that the effective diffusivity at a zonal scale is unlikely to be comparable to local rates [Marchal *et al.*, 1998b] and will need to account for the large-scale meridional mixing processes not represented, such as through gyre circulation [Stocker *et al.*, 1994].

4.2.4 The addition of deep-sea sediments

The Bern 2D model assumes a uniform ocean depth of 4000 m. However, in order to correctly represent the interaction between the ocean and deep-sea sediments a more realistic bathymetry must be prescribed [Keir, 1995]. As an initial step a mean global bathymetric profile (made on the basis of ETOPO5 [1988] topography) is applied to each of the 16 grid points, imposing a maximum depth of 6000 m. Alteration of bathymetry in this way results in a slight reduction in total global ocean volume compared to the original model. In order to avoid biasing the residence time of water in each cell, global ocean volume is corrected by increasing the width of each ocean basin by ~9% and altering the depth of the base of each ocean layer. The lower boundary depths of the 8 vertical levels are now 47, 95, 144, 496, 1013, 2652, 3986, and 6000 m.

The depth resolution of the sediment modules employed to span the entire 6000 m depth of the ocean is chosen to maximize overall computational efficiency. Sensitivity analyses suggest that a depth interval of up to 500 m can be used with little distortion in the overall response of the global carbon cycle system to applied perturbations. However, since ocean layer thicknesses decrease and sedimenting fluxes increase as the ocean surface is approached, this resolution is progressively increased above 500 m depth in the ocean, to a minimum interval of 50 m.

4.3 Biogeochemical configuration

Final configuration of the global carbon cycle in SUE1608 requires the prescription of certain geochemical boundary conditions. In addition, there exist several unconstrained parameters associated with various biogeochemical processes that require a degree of optimization, with values chosen on the basis of achieving balanced model simulation 'success', as measured against a basket of present-day observational data. Such considered constraints include oceanic fields of [PO₄], [H₄SiO₄], and [Fe], particulate fluxes of POC, CaCO₃, and opal (and in particular the CaCO₃:POC rain ratio), and core-top CaCO₃ and opal sediment contents.

4.3.1 Geochemical boundary conditions

Since there is no explicit representation in SUE of processes lying outside of the atmosphere-ocean-sediment system (such

as terrestrial weathering) a number of geochemical boundary conditions need to be evaluated. Suitable values can be estimated on the basis of present-day observations, paleoclimate reconstructions, model simulations, or chosen simply to achieve a required system steady-state on an appropriate time scale.

4.3.1.1 Dissolved chemical input to the ocean

Coastal and continental shelf environments provide an important interface between terrestrial processes and the open ocean. In the absence of any explicit representation of these in SUE, dissolved chemical input to the ocean is simply applied directly to the surface ocean grid points in proportion to their relative surface area. Dissolved chemical inputs to SUE1608 are;

- Carbon and alkalinity (from Ca^{2+}) following Walker and Opdyke [1995]; some 20 and 40 Tmol a^{-1} for DIC and ALK, respectively.
- The ^{13}C isotopic signature of DIC is chosen in order to bring the system to a steady state characterized by an estimated pre-industrial mean oceanic $\delta^{13}\text{C}^{\text{DIC}}$ of -0.4‰ [Yamanaka and Tajika, 1996] over the long-term (>100 ka). A value for $\delta^{13}\text{C}^{\text{DIC}}$ of around -3.1‰ will achieve this.
- Global input of silicic acid arising from a combination of riverine influx, hydrothermal sources, and sea floor weathering (excluding the dissolution of biogenic opal) is taken to be 5.5 Tmol Si a^{-1} following Tréguer *et al.* [1995]. There is little difference between the delivery of aeolian-derived dissolved Si (assumed to be some 0.5 Tmol Si a^{-1} [Tréguer *et al.*, 1995]) in proportion to dust deposition fluxes or simply in proportion to surface ocean area. All (externally-derived) dissolved Si added to the ocean, a total of 6.0 Tmol Si a^{-1} therefore follows the other dissolved inputs in being delivered in proportion to surface area.

4.3.1.2 The delivery of aeolian material to the ocean

Supply of iron to the world ocean is thought to be dominated by riverine input [Duce and Tindale, 1991]. However, most of this iron is likely to be removed from the water column and sedimented in the neritic environment through a combination of low Fe utilization efficiency by coastal phytoplankton [Sunda and Huntsman, 1995] and high coastal productivity (with proportionally rapid scavenging). Indeed, the length scale of Fe penetration into the open ocean from coastal shelf areas has been estimated to be only ~ 16 km [Johnson *et al.*, 1997]. Iron input to the (open) ocean in the model is therefore assumed to be derived exclusively from aeolian dust deposited to the ocean surface.

Dust deposition rates are taken from the coupled GCM tracer advection and terrestrial ecosystem model simulations of Mahowald *et al.* [1999]. Fluxes to each grid point are derived from gridded GCM depositional fields in a similar manner to that used for deriving the physical surface forcings (4.2.2). However, on the basis that Fe originating from elevated near-shore dust deposition will suffer a similar fate to that of riverine Fe, coastal areas are masked out [Fung *et*

al., 2000]. Mean dust deposition fluxes ($f_{(\text{lat},\text{lon})}^{\text{dust}}$) to each grid point region in the model are thus given by

$$f_{(\text{lat},\text{lon})}^{\text{dust}} = \frac{\sum_{\text{lat}} \sum_{\text{lon}} H(D_{(\text{lat},\text{lon})} - 250) \cdot A_{(\text{lat},\text{lon})} \cdot f_{(\text{lat},\text{lon})}^{\text{dust}}}{\sum_{\text{lat}} \sum_{\text{lon}} H(D_{(\text{lat},\text{lon})} - 250) \cdot A_{(\text{lat},\text{lon})}} \quad (4-3)$$

where the Heavyside function H excludes shelf areas defined by ocean depth <250 m.

Dust deposition tends to be a highly episodic process with a substantial proportion of the annual total being delivered in only a few individual events [Jickells and Spokes, in press; Rea, 1990, 1994]. However, the simple biological export scheme used in SUE is unlikely to gain much benefit from increased realism in this respect. Mean annual dust fluxes are therefore used.

Detrital input to deep-sea sediments derived only from the overlying surface aeolian flux can cause CaCO_3 and opal preservation to be underestimated in regions of very low dust supply (particularly the Southern Ocean and much of the Pacific). Additional material derived from continental shelves and slopes and reworked by bottom currents [Bareille *et al.*, 1994; Seidov and Haupt, 1999] may therefore play a significant role in such regions. To qualitatively account for these sources, neither of which are explicitly represented in SUE, detrital fluxes to deep-sea sediments are enhanced by $1.8 \text{ g m}^{-2} \text{ a}^{-1}$ [Archer *et al.*, 1998].

4.3.1.3 Neritic sediment accumulation

Calcium carbonate in coral reefs has been estimated to have been accumulating at 7-10 Tmol C a^{-1} over the last few thousand years [Milliman, 1993; Munhoven and Francois, 1996]. CaCO_3 is also deposited in non-reefal sediments within the neritic environment at a similar rate (~ 7.5 Tmol C a^{-1} [Milliman, 1993]). During glacial periods, low sea level stands resulted in extensive exposure of continental shelves. Intuitively, it would therefore seem highly likely that total global CaCO_3 accumulation rates were lower during the LGM than at present [Berger, 1982a; Kleypas, 1997; Munhoven and Francois, 1994, 1996; Walker and Opdyke, 1995]. This presents a problem in constructing a modern simulation, since CaCO_3 in benthic sediments, with an adjustment time upwards of ~ 9 ka [Archer *et al.*, 1998] are likely to be far from steady state following the recent deglacial transition centred around 12 ka BP. This is supported by the observations of anomalous ^{14}C profiles in Pacific sediments [Berelson *et al.*, 1997; Broecker *et al.*, 1999b; Keir and Michel, 1993; Oxburgh, 1998; Stephens and Kadko, 1997]. For the purpose of generating a baseline simulation for parameter optimization, the carbonate system is assumed to be at steady state with respect to two thirds of the total estimated increase in CaCO_3 accumulation rate since the LGM, a net neritic sink of ~ 10 Tmol C a^{-1} . This is justified on the basis that following the rapid deglacial rise, sea level has been relatively stable for a period roughly equivalent to the e -folding time of the carbonate system.

An analogous situation might be expected to arise with respect to opal accumulation. That the global Si budget does not appear to balance at present, with an excess of loss

through deposition over dissolved inputs [Tréguer *et al.*, 1995] supports this hypothesis. However, since processes controlling neritic opal accumulation are much more poorly understood than for CaCO_3 no significant increase in opal accumulation rate since the LGM is taken into account in the construction of the baseline scenario.

4.3.2 Biological productivity

With a time step for biological uptake set at 1 day, unconstrained parameter values for export production are adjusted both in isolation and in concert in the search for an ‘optimal’ solution. The rate of net PO_4 uptake by (nutrient replete) siliceous phytoplankton ($u_{0,SP}^{\text{PO}_4}$) is set sufficiently high so as to enable realistic seasonal nutrient draw-down in the Southern Ocean. The value for net PO_4 uptake by (nutrient-replete) non-siliceous phytoplankton ($u_{0,NSP}^{\text{PO}_4}$) is then chosen in conjunction with the CaCO_3 :POC export rain ratio ($r_{NSP}^{\text{CaCO}_3:\text{POC}}$) both to obtain a reasonable global rain ratio field and to balance the ocean DIC and ALK budgets over the long-term. Organic matter production is assumed to be entirely in particulate form with no DOM formation. The opal:POC export ratio from siliceous phytoplankton under iron replete conditions ($r_{0,SP}^{\text{opal:POC}}$) is chosen in order to obtain an oceanic inventory of dissolved Si consistent with Tréguer *et al.* [1995] and to produce a reasonable seasonal cycle in $[\text{H}_4\text{SiO}_4]$. Final optimized parameter values are summarized in Table 4-1. A degree of differential recycling is expected between opal and POC [Dugdale and Wilkerson, 1998] such that Si:C uptake ratios might be expected to be significantly different from the ultimate export ratio. However, the magnitude of this differential is highly dependent on assumptions made regarding grazing pressure, and can approach unity under conditions of low grazing intensity [Dugdale *et al.*, 1995]. The value for $r_{0,SP}^{\text{opal:POC}}$ is therefore reasonably consistent with Si:C uptake ratios reported under Fe-enriched conditions in the Southern Ocean [Watson *et al.*, 2000] and from incubation studies [Hutchins and Bruland, 1998] (Table 2-2).

Table 4-1 Parameter Values Resulting from Model Optimization

Parameter	Value
$u_{0,SP}^{\text{PO}_4}$	$5.00 \mu\text{mol kg}^{-1} \text{a}^{-1}$
$u_{0,NSP}^{\text{PO}_4}$	$0.25 \mu\text{mol kg}^{-1} \text{a}^{-1}$
$r_{0,SP}^{\text{opal:POC}}$	0.175
$r_{NSP}^{\text{CaCO}_3:\text{POC}}$	0.300
λ_{SP}	1.0
λ_{NSP}	1.0
$k_{scav}_{dust}^{\text{Fe}}$	$0.0750 \text{a}^{-1} (\text{mol C m}^{-2} \text{a}^{-1})^{-1}$
$k_{scav}_{POC}^{\text{Fe}}$	$0.0025 \text{a}^{-1} (\text{mol C m}^{-2} \text{a}^{-1})^{-1}$

4.3.3 Fe biogeochemical cycling

Initial constraints can be imposed upon basic aeolian Fe solubility in the surface ocean ($Fesol^{\text{dust}}$) through consideration of global dust input and estimated oceanic Fe residence times [Jickells and Spokes, in press]. Values for ‘self-scavenging’ and biogenic particulate scavenging rates ($k_{scav}_{dust}^{\text{Fe}}$ and $k_{scav}_x^{\text{Fe}}$, respectively) are adjusted in order to obtain a reasonable [Fe] field and produce surface ocean macro-nutrient concentrations (i.e., PO_4 and H_4SiO_4) approximately in line with observations. In the absence of any quantitative information regarding differential scavenging characteristics of the various materials comprising biogenic particulate matter, it is assumed that Fe is scavenged by POM, calcite, aragonite, and opal, in a 10:1:1:1 ratio (by molar flux density). Optimized values for Fe scavenging rate constants are summarized in Table 4-1. Aeolian Fe solubilities range from 1% in regions proximal to dust source areas such as low and mid latitudes in the Atlantic and Indian Oceans, to 3% in remote high southern latitudes and much of the Pacific Ocean, giving a mean global solubility of 1.17%. The influence of ‘self-scavenging’ reduces effective solubilities by up to ~70% under the highest dust deposition fluxes and surface dissolved Fe concentrations. The effective global mean solubility is therefore reduced to 0.69%, slightly lower than the range 0.8-2.1% estimated by Jickells and Spokes [in press].

4.3.4 “Nutrient trapping”

A common problem afflicting carbon cycle models is that of ‘nutrient trapping’ [Najjar *et al.*, 1992] – a positive feedback mechanism whereby nutrients released through the remineralization of particulate matter beneath highly productive up-welling regions are rapidly advected back to the surface, fuelling further productivity. This can lead to excessive nutrient concentrations and near-anoxic conditions at mesopelagic depths in such affected regions [Maier-Reimer, 1993; Marchal *et al.*, 1998b; Najjar *et al.*, 1992; Yamanaka and Tajika, 1996]. Distorted rain rates can also result in insufficient CaCO_3 preservation in the underlying sediments [Heinze and Crowley, 1997; Heinze *et al.*, 1999].

A number of different solutions to this highly undesirable feature have been proposed. The most common of these being to partition a substantial fraction of new production into the form of dissolved organic matter (DOM), allowing nutrients to advectively ‘leak’ out of the up-welling system. This fraction can be either explicitly prescribed [Marchal *et al.*, 1998b; Najjar *et al.*, 1992; Paillard *et al.*, 1993; Sarmiento *et al.*, 1988; Yamanaka and Tajika, 1997] or derived internally as a result of grazing and cell lysis within a multi-trophic mechanistic biological scheme [Six and Maier-Reimer, 1996]. However, the DOM export fraction required in order to largely alleviate this problem is substantial, typically being more than 50% (Table 4-2).

Although biogeochemical ‘fixes’ have tended to be chosen in order to remove nutrient trapping from equatorial up-welling systems, it has been suspected that it is the representation of ocean circulation that is at fault [Yamanka

and Tajika, 1996]. *Aumont et al.* [1999] found that increasing meridional resolution in the Pacific can vastly improve the simulation of nutrient transport by the equatorial undercurrent (EUC) into the region of equatorial divergence and up-welling and result in very little nutrient trapping. Application of a numerical scheme with relatively low diapycnal diffusivity has also been found to lessen nutrient trapping in the equatorial Atlantic [*Oschlies and Garcon*, 1999]. There must be serious concerns regarding attempts made to correct for local problems in the representation of the physical ocean through what is effectively the distortion of global biogeochemical cycling. In any case, there is scant observational evidence to support the magnitude of the required DOM fraction, with some model results suggesting that DOC is unlikely to constitute more than 10% of the total organic carbon transport out of the equatorial Pacific [*Aumont et al.*, 1999].

Nutrient trapping is muted in the Equatorial Pacific because the EUC (the primary source of up-welled nutrients) is tightly confined in the vertical so that the proportion of settling POM remineralized within it is low. Instead, nutrients are predominantly released at depths below the EUC and are thus prevented from feeding directly back into the equatorial divergence and up-welling. On this basis, an oceanographic topological ‘fix’ is employed in SUE1608. In this, the depth at which remineralization begins is artificially deepened; 400 m in the equatorial Atlantic and Pacific with 200 m in the equatorial Indian Ocean.

4.4 The ‘present-day’ in SUE1608

A modern (pre-industrial) baseline simulation is generated by running SUE1608 for 500 ka following an initial 50 ka spin-up, sufficient to bring even the slowest adjusting part of the system approximately into equilibrium (ocean ^{13}C with an

e -folding time of order 100 ka). Final model state is characterized by an atmospheric CO_2 concentration of 269 ppmv, slightly lower than pre-industrial estimates of 278 ppmv [*IPCC*, 1990], with a ^{13}C isotopic signature of -6.2‰ , some $\sim 0.3\text{‰}$ too high [*Smith et al.*, 1999]. The reasons for the discrepancies in atmospheric composition probably lie mainly in a combination of the simplistic partitioning of biological export between just two phytoplankton groups, the representation of convective regimes at high latitudes, and lack of true seasonality. Since the primary focus of this study is on the dynamical behaviour of the system over an extended time period there is little to be gained from over-tuning model steady-state. Indeed, it would be detrimental to the ability of SUE1608 to produce a realistic glacial-interglacial response if deficiencies in physical ocean representation were to be entirely compensated for through the alteration of biogeochemical processes. Mean ocean DIC, ALK, PO_4 , and H_4SiO_4 concentrations of 2234, 2370, 2.1, and $74.5 \mu\text{mol kg}^{-1}$, respectively, are all in line with pre-industrial estimates [*Tréguer et al.*, 1995; *Yamanka and Tajika*, 1996], as is a mean ocean $\delta^{13}\text{C}^{\text{DIC}}$ of 0.37‰ [*Yamanka and Tajika*, 1996]. Total POC export out of the euphotic zone is 8.8 GtC a^{-1} , similar to current model estimates of $7.5\text{--}10.0 \text{ GtC a}^{-1}$ as summarized in Table 4-2. CaCO_3 export is 1.3 GtC a^{-1} , giving a mean ocean $\text{CaCO}_3\text{:POC}$ export rain ratio of 0.14, again consistent with estimates lying in the range 0.08-0.25. Global opal export is 137 Tmol a^{-1} , somewhat lower than previous model-derived estimates of $170\text{--}275 \text{ Tmol a}^{-1}$ but close to the value of $\sim 120 \text{ Tmol a}^{-1}$ obtained by *Tréguer et al.* [1995] from mass balance considerations. Model parameter values are summarized in Appendix IV.

The degree of ‘success’ of this simulation in reproducing the characteristics of the modern state of the global ocean carbon cycle is now evaluated in more detail against a variety of ocean tracer, biogenic flux, and sediment compositional fields.

Table 4-2 Global New Production Estimates from Global Carbon Cycle Models

Model class	F_{np}^{POC} (GtC a^{-1})	F_{np}^{DOC} (GtC a^{-1})	F_{np}^{TOC} (GtC a^{-1})	$r^{\text{DOC:TOC}}$	$F_{np}^{\text{CaCO}_3}$ (GtC a^{-1})	$r^{\text{CaCO}_3\text{:POC}}$	F_{np}^{opal} (Tmol a^{-1})	Reference
3D OGCM	10	0	10	0.00	0.80	0.08	n/a	<i>Yamanka and Tajika</i> [1996]
3D OGCM	8	3	11	0.27	-	-	n/a	<i>Yamanka and Tajika</i> [1997]
3D OGCM	9.4	1.7	11.1	0.15	-	-	n/a	<i>Six and Maier-Reimer</i> [1996]
3D OGCM	8.9	0.0	8.9	0.00	1.80	0.20	170	<i>Heinze et al.</i> [1999]
3D OGCM	-	-	-	0.12	-	-	n/a	<i>Aumont et al.</i> [1999]
3D OGCM	7.5	0.0	7.5	0.00	1.65	0.22	n/a	<i>Archer et al.</i> [1998]
3D OGCM	-	-	12-15	0.80	-	-	n/a	<i>Najjar et al.</i> [1992]
3D OGCM	11.0	0.0	11.0	0.00	2.18	0.20	275	<i>Archer et al.</i> [2000]
ZOGCM	-	-	6.3-10.8	0.50	0.38-0.65	0.06	n/a	<i>Marchal et al.</i> [1998b]
Box (SUE)	8.5 8.8	0.0 0.0	8.5 8.8	0.00 0.00	- 1.3	- 0.14	n/a 137	<i>Rich et al.</i> [1999] This study

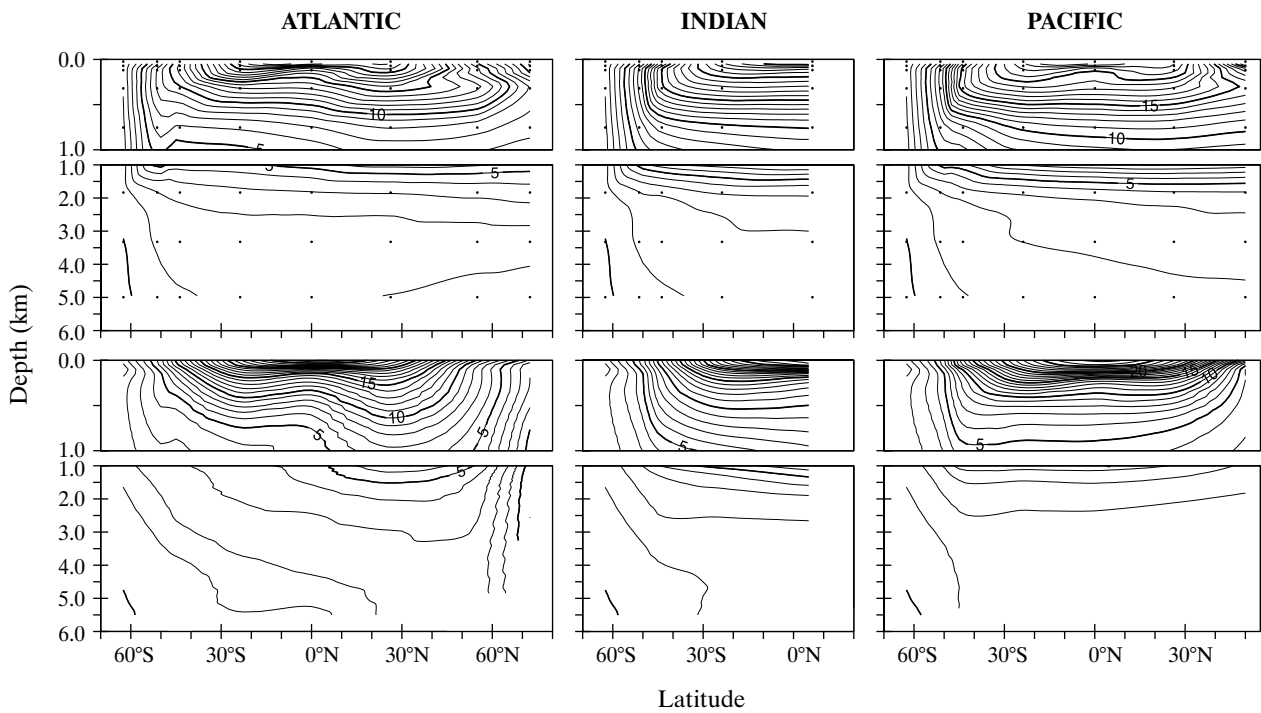


Figure 4-4 Ocean temperature field ($^{\circ}\text{C}$); model results (top) compared with observations [Levitus *et al.*, 1994c] (bottom).

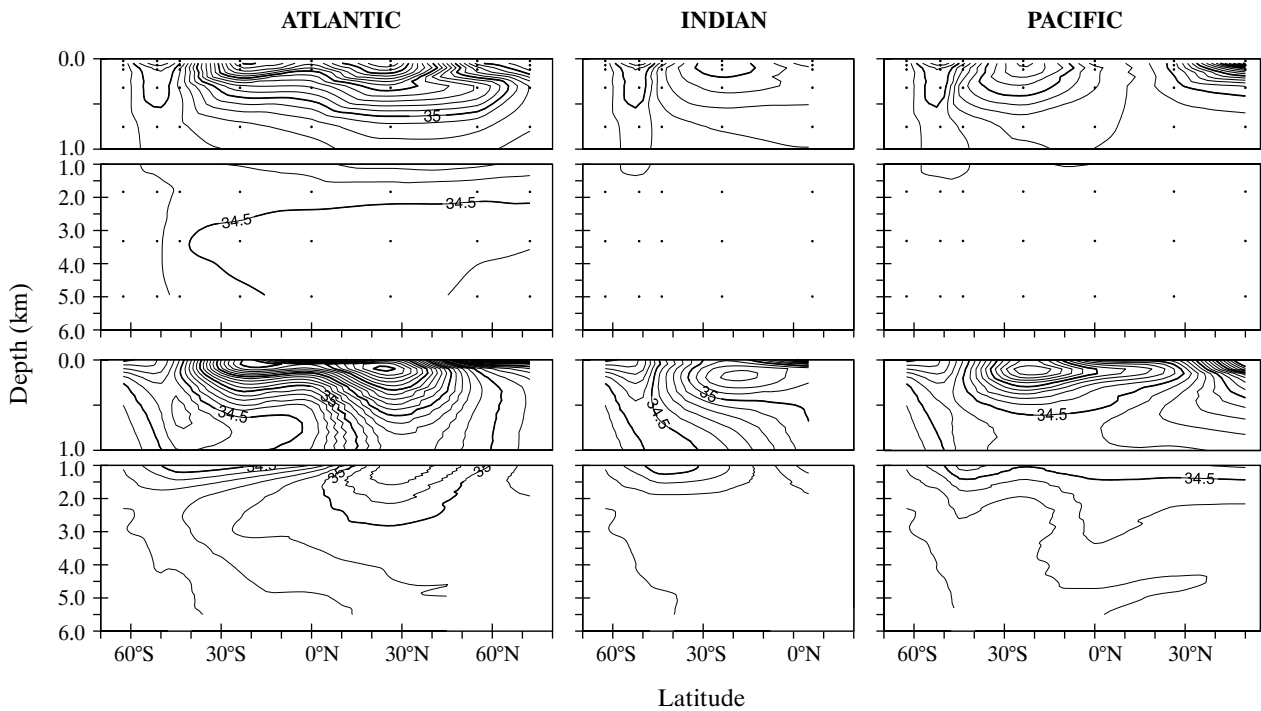


Figure 4-5 Ocean salinity field (‰); model results (top) compared with observations [Levitus *et al.*, 1994b] (bottom).

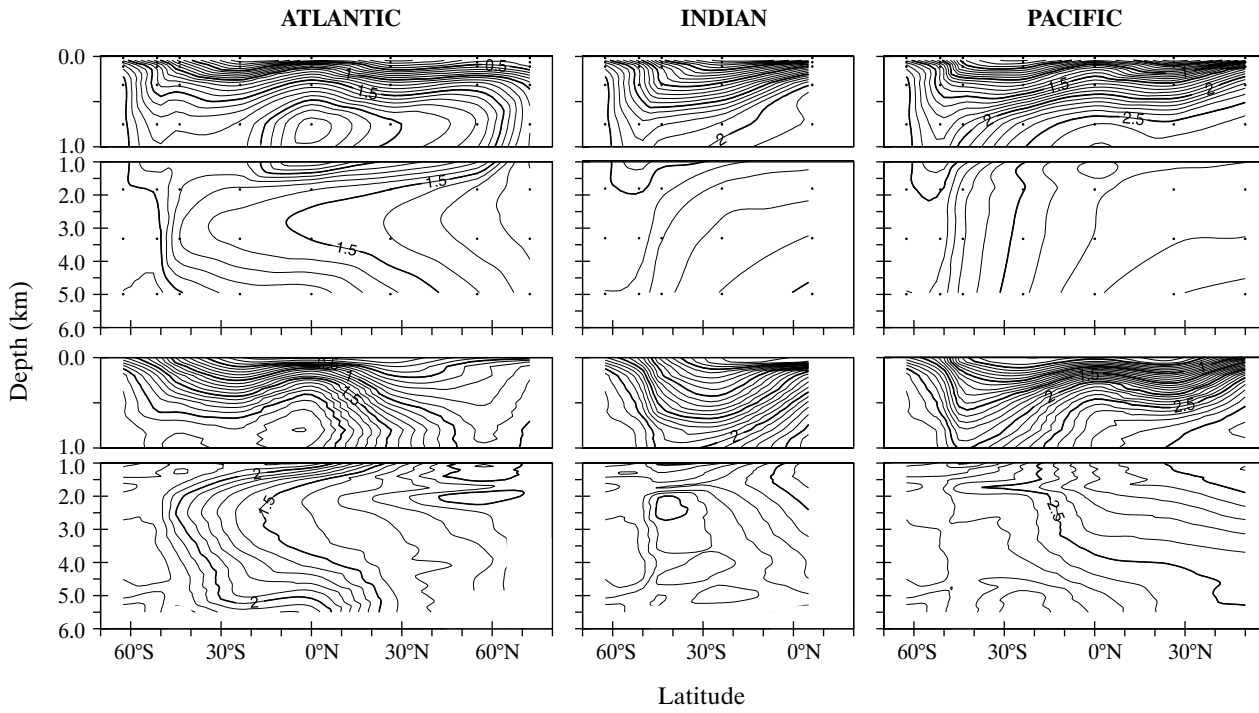


Figure 4-6 Ocean PO_4 field ($\mu\text{mol kg}^{-1}$); model results (top) compared with observations [Conkright *et al.*, 1994] (bottom).

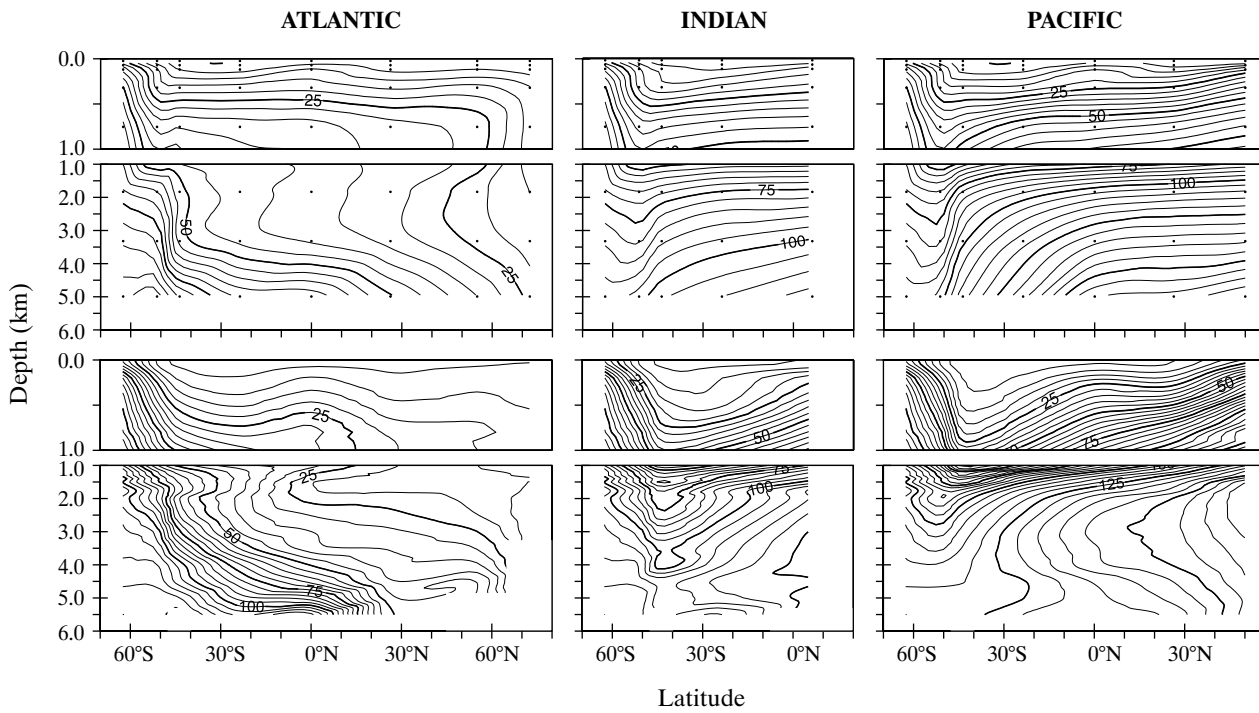


Figure 4-7 Ocean H_4SiO_4 field ($\mu\text{mol kg}^{-1}$); model results (top) compared with observations [Conkright *et al.*, 1994] (bottom).

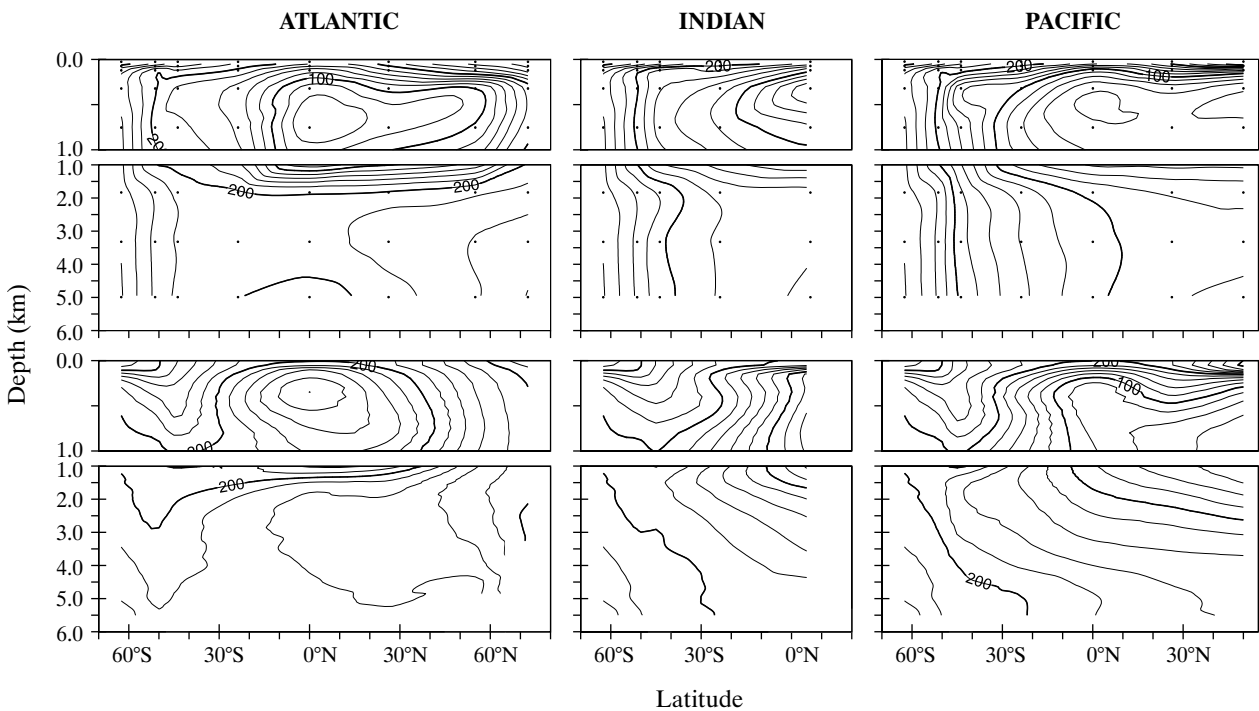


Figure 4-8 Ocean dissolved O_2 field ($\mu\text{mol kg}^{-1}$); model results (top) compared with observations [Levitus *et al.*, 1994a] (bottom).

4.4.1 Ocean tracer fields

4.4.1.1 Temperature and salinity

The annual mean temperature field in the model (Figure 4-4) is generally quite realistic. However, there are several obvious deficiencies; the thermocline in all three ocean basins is too weak and high latitude temperature distributions tend to be poorly reproduced, particularly in the north Atlantic (associated with the formation of North Atlantic Deep Water (NADW)) and in the north Pacific where there appears to be inadequate up-welling and/or wintertime convective overturning. The weak thermocline structure may exacerbate nutrient trapping problems in the model, as a temperature overestimate of $\sim 5^\circ\text{C}$ (typical of much of the mesopelagic zone) will result in an overestimate in the dissolution rate of settling opal of $\sim 50\%$ (assuming a Q_{10} of 2.3).

Salinity fields (Figure 4-5) are much more poorly reproduced than those for temperature, with obvious problems associated with the formation and transport of NADW and Antarctic Intermediate Waters. Fortunately, with prescribed ocean circulation, salinity plays little part in controlling the global carbon cycle. Even where aqueous carbonate chemistry is moderately sensitive to salinity such as its influence on CO_2 fugacity in the surface ocean, salinity values are restored to and thus always follow observations.

4.4.1.2 Phosphate

The ocean phosphate field is generally fairly well reproduced by the model (Figure 4-6) particularly in the upper water column (< 1000 m), although there is still some distortion of equatorial Pacific profiles associated with residual nutrient trapping. As with temperature, circulation-related problems occur at high latitudes although to a lesser degree, since remineralization processes within the water column dominate over advection in controlling vertical PO_4 distributions. Contrary to observations there are no distinct mid-depth nutrient maxima in either the northern Indian or Pacific basins, suggesting potential deficiencies with the scheme used for POM remineralization. Lack of any explicit representation of the diagenetic alteration of particulate organic matter in deep-sea sediments may also play a role.

4.4.1.3 Silicic acid

As with phosphate, the model is reasonably successful in reproducing general trends in the H_4SiO_4 field (Figure 4-7). However, again there is a failure to reproduce observed ocean interior nutrient maxima in both the Pacific and Indian basins. In addition, the degree of opal remineralization appears to be slightly too extensive in surface layers (above ~ 500 m), possibly associated with the weak thermocline structure as noted previously. The model also underestimates the gradient of the deep H_4SiO_4 nutricline centred on the $75 \mu\text{mol kg}^{-1}$ contour. That the

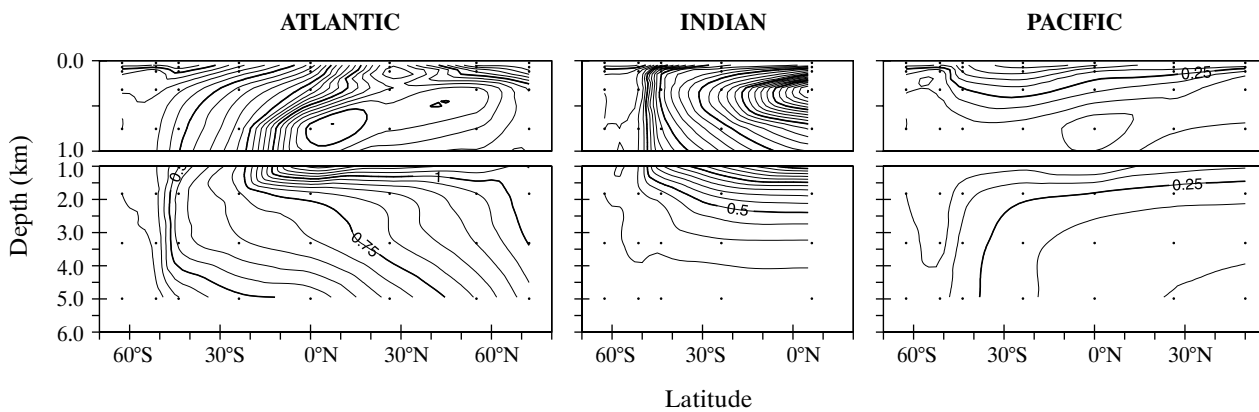


Figure 4-9 Ocean total dissolved Fe field (nmol kg^{-1}); model results only.

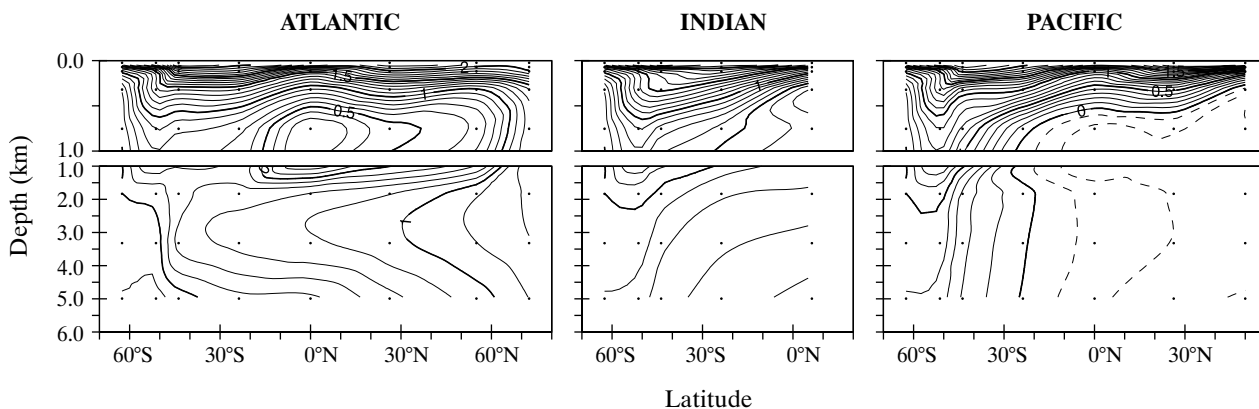


Figure 4-10 Ocean $\delta^{13}\text{C}_{\text{DIC}}$ field (‰); model results only.

remineralsation of POM and opal are represented and controlled in very different ways within SUE supports the notion that it is ocean structure and/or circulation that is predominantly to blame for such failures.

4.4.1.4 Dissolved oxygen

The dissolved oxygen field (Figure 4-8) is arguably the least successfully reproduced. That this should be so is perhaps not entirely surprising considering that its distribution is highly dependent on seasonal high latitude processes to delivering O_2 to the ocean interior, processes that are poorly-represented in the model. Despite this, $[\text{O}_2]$ minima beneath the equatorial Atlantic and at intermediate depths in the northern Indian Ocean are simulated, although the northern Pacific minima is clearly too shallow and weak.

4.4.1.5 Total dissolved iron

Figure 4-9 shows the model field of total dissolved iron. Unlike other chemical ocean properties which have been

routinely analysed for many years, measurements of $[\text{Fe}]$ are a relatively recent innovation with the result that there is no comparable global data set available. The following comparisons can still be drawn between predicted and observed $[\text{Fe}]$, although care must be taken since model values represent zonal and depth-averaged annual means while measurements are discrete in space and time;

- Fe concentrations appear to be over-estimated in the north Atlantic with the existence of a prominent mesopelagic maximum ($>1.0 \text{ nmol kg}^{-1}$) whereas JGOFS data suggests a more steady increase down through the water column and not reaching a maximum ($\sim 0.7 \text{ nmol kg}^{-1}$) until a depth of 2000 - 3000 m [Martin *et al.*, 1993].
- Relatively high Fe concentrations observed in the northeast Pacific [Martin and Gordon, 1988; Martin *et al.*, 1989; Johnson *et al.*, 1997] are not captured by the model with deep-water concentrations being too low. The existence of a mesopelagic maximum is predicted, however.

- The model matches observations at depths shallower than ~500 m in the equatorial Pacific [Coale *et al.*, 1996; Gordon *et al.*, 1997], although deeper concentrations are again underestimated.
- In the Southern Ocean there is generally good agreement between model and observed Fe concentrations at shallow and intermediate depths (< 1500 m) in the Drake Passage [Martin *et al.*, 1990], the SE Pacific sector [de Baar *et al.*, 1999], and the Australian sector [Sohrin *et al.*, 2000]. However, once more, values in the deep ocean tend to be underestimated.

It is likely that SUE1608 fails to reproduce the enhanced Fe concentrations observed in the deep ocean due to the lack of any representation of the return to the ocean of dissolved Fe derived from material deposited to the sediments. This diagenetically-released Fe may be largely restricted to the deep ocean due to a constant downward scavenging pressure. If so, this omission may not significantly affect Fe supply to the surface ocean (a critical factor in controlling biological productivity).

4.4.1.6 $\delta^{13}\text{C}^{\text{DIC}}$

Figure 4-10 shows the field for the ^{13}C isotopic signature of total dissolved inorganic carbon ($\delta^{13}\text{C}^{\text{DIC}}$). In the Atlantic basin model $\delta^{13}\text{C}^{\text{DIC}}$ distributions are reasonably similar to observations (not shown) [Yamanaka and Tajika, 1996]. However, surface values are generally too high across all three basins (responsible for the over-prediction in atmospheric $\delta^{13}\text{C}$). The strength of mid-depth minima underlying the equatorial Atlantic and northern Pacific are also incorrectly predicted.

4.4.2 The biological pump

Meridional distributions of annual mean nutrient concentrations and biological fluxes are shown in Figure 4-11 for each of the three ocean basins. It can be seen that observed zonally averaged surface ocean PO_4 concentrations are reasonably reproduced, albeit slight too low. Observed trends in H_4SiO_4 concentrations with deplete conditions in much of the low- and mid-latitude world ocean but rising steeply south of the Antarctic Polar Front are also correctly predicted, although again there is a general slight under-prediction in concentrations. However, there is a complete failure to capture high $[\text{H}_4\text{SiO}_4]$ values observed in the north Pacific, suggesting serious deficiencies in ocean circulation and/or biological representation in this region. The control that silicic acid availability exerts on the partitioning of POC between siliceous and non-siliceous phytoplankton in the biological model is exemplified by the export rain ratio of $\text{CaCO}_3:\text{POC}$. For instance, in the Southern Ocean where H_4SiO_4 is not limiting to siliceous phytoplankton, export by this class dominates the biological system and net $\text{CaCO}_3:\text{POC}$ is extremely low.

The availability of iron exerts a number of different controls on export production. Excess PO_4 remaining in the equatorial Pacific up-welling zone is a result of the high degree of Fe limitation there, while a combination of summertime Fe limitation and wintertime deep mixing act to

limit annual production in the Southern Ocean and north Pacific. High concentrations of Fe present in surface waters in the mid and northern latitude Atlantic and Indian Oceans are due to their relative proximity to dust source regions, with concentrations declining sharply towards the south as the remote Southern Ocean is approached. Low dust deposition rates to the low- and mid-latitude Pacific restricts Fe availability preventing the complete utilization of PO_4 advected from the equator and high latitudes. Iron also plays an important role in determining the efficiency with which H_4SiO_4 is utilized by siliceous phytoplankton per unit carbon fixed (2.2.3.3). For instance, while POC export derived from siliceous phytoplankton is slightly greater at the equator in the Atlantic compared to that in the Pacific, greater Atlantic Fe availability allows increased H_4SiO_4 utilization efficiency resulting in opal export being suppressed.

The meridional profile of (total) $\delta^{13}\text{C}^{\text{POC}}$ in each of the three basins is very similar, with a relatively constant degree of ^{13}C fractionation in exported POC between -19 and -21‰ over mid and low latitudes. South of around 30°S, however, the isotopic signature decreases sharply to a value of around -28‰ by 60°S, while a less steep decrease with latitude is apparent north of 30°N, reaching a minimum of only about -25‰. These model distributions are consistent with measurements made on suspended particulate organic matter recovered from along meridional transects (not shown) [Bentaleb *et al.*, 1998; Goericke and Fry, 1994; Hofmann *et al.*, 1999; Popp *et al.*, 1999], sharing remarkably similar features and values. Differences do arise in the location and slope of the transition zone lying either side of the low- and mid-latitude $\delta^{13}\text{C}^{\text{POC}}$ 'plateau'. This is probably simply an artifact of the low meridional resolution of SUE1608 rather than reflecting anything more fundamental regarding biological export or ^{13}C fractionation. However, observed data do exhibit a significant degree of scatter with extreme values lying up to $\pm 5\%$ from the general trend. While this may be partly due to the high degree of spatial averaging inherent in the model it may also reflect variability in ecosystem assemblage and the physiological state of individual cells [Burkhardt *et al.*, 1999; Hinga *et al.*, 1994], both of which are poorly accounted for in the biological scheme employed in SUE.

There is a reasonable similarity between model-generated settling fluxes of POC and CaCO_3 and observational data [Tsunogai and Noriki, 1991] (not shown). Water-column profiles of CaCO_3 are well reproduced with little dissolution occurring in the water column below 500-1000 m, although observations indicate a greater degree of POC remineralization at depth than predicted by the model. Inter-regional contrasts are generally correctly simulated, with lowest POC fluxes in the ocean associated with mid-latitude gyre regions. However, problems in the representation of the equatorial Pacific up-welling zone results in a significant overestimation of POC fluxes. As CaCO_3 fluxes here are of the correct magnitude, the $\text{CaCO}_3:\text{POC}$ rain ratio is then distorted.

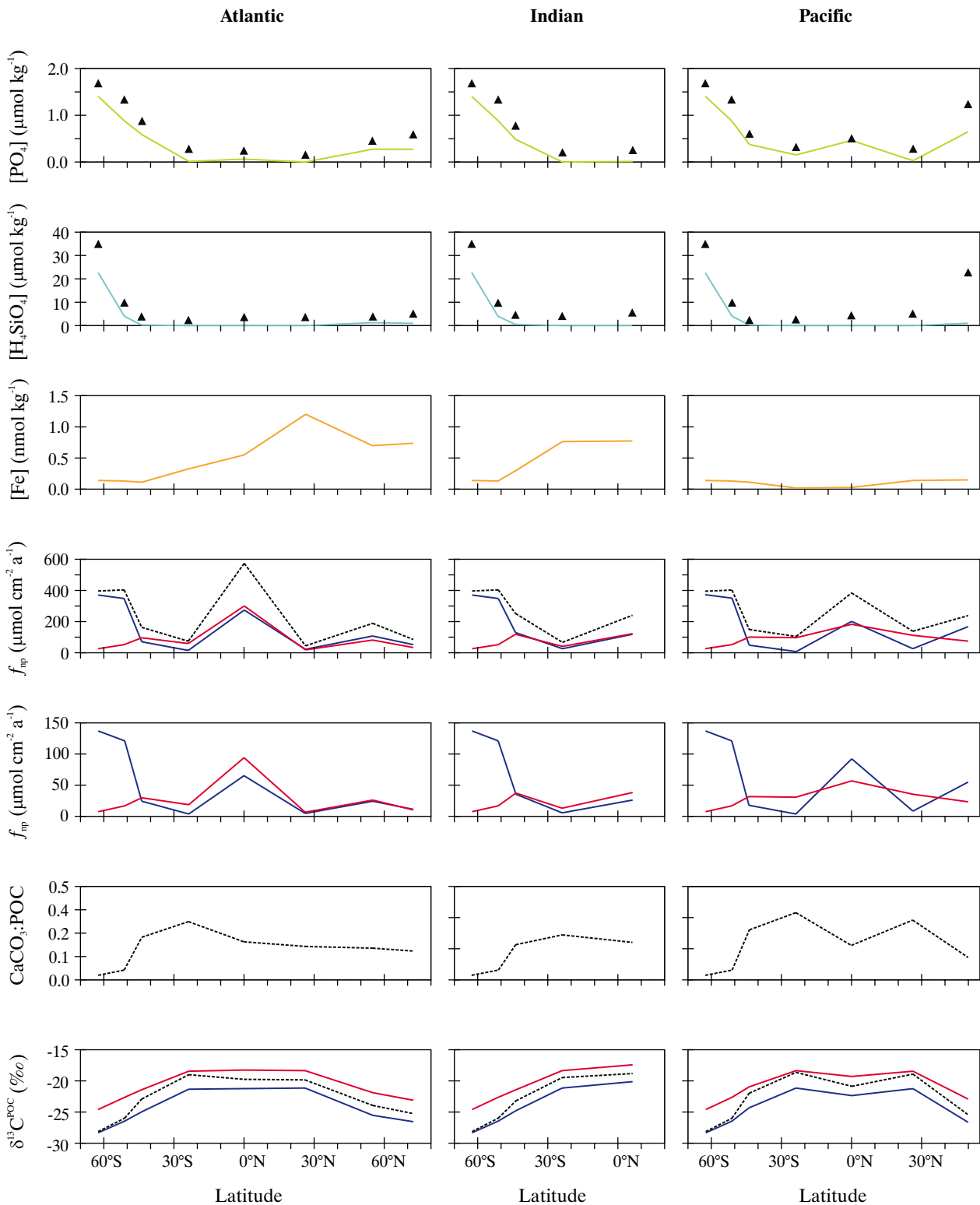


Figure 4-11 Meridional profiles of ocean surface characteristic in each ocean basin in SUE1608. Shown (from top to bottom) are; mean annual PO_4 concentrations (model values in green, observations (at 30 m depth) [Conkright *et al.*, 1994] marked as filled triangles); mean annual H_4SiO_4 concentrations (model values in light blue, observations (at 30 m depth) [Conkright *et al.*, 1994] marked as filled triangles); mean annual Fe concentrations (orange); POC export fluxes from siliceous phytoplankton (dark blue), non-siliceous phytoplankton (red), together with the total flux (black dotted); opal export (dark blue) and $CaCO_3$ export (red) fluxes; $CaCO_3:POC$ rain ratio (black dotted); and $\delta^{13}C^{POC}$ of siliceous phytoplankton (dark blue), non-siliceous phytoplankton (red), together with the total flux (black dotted).

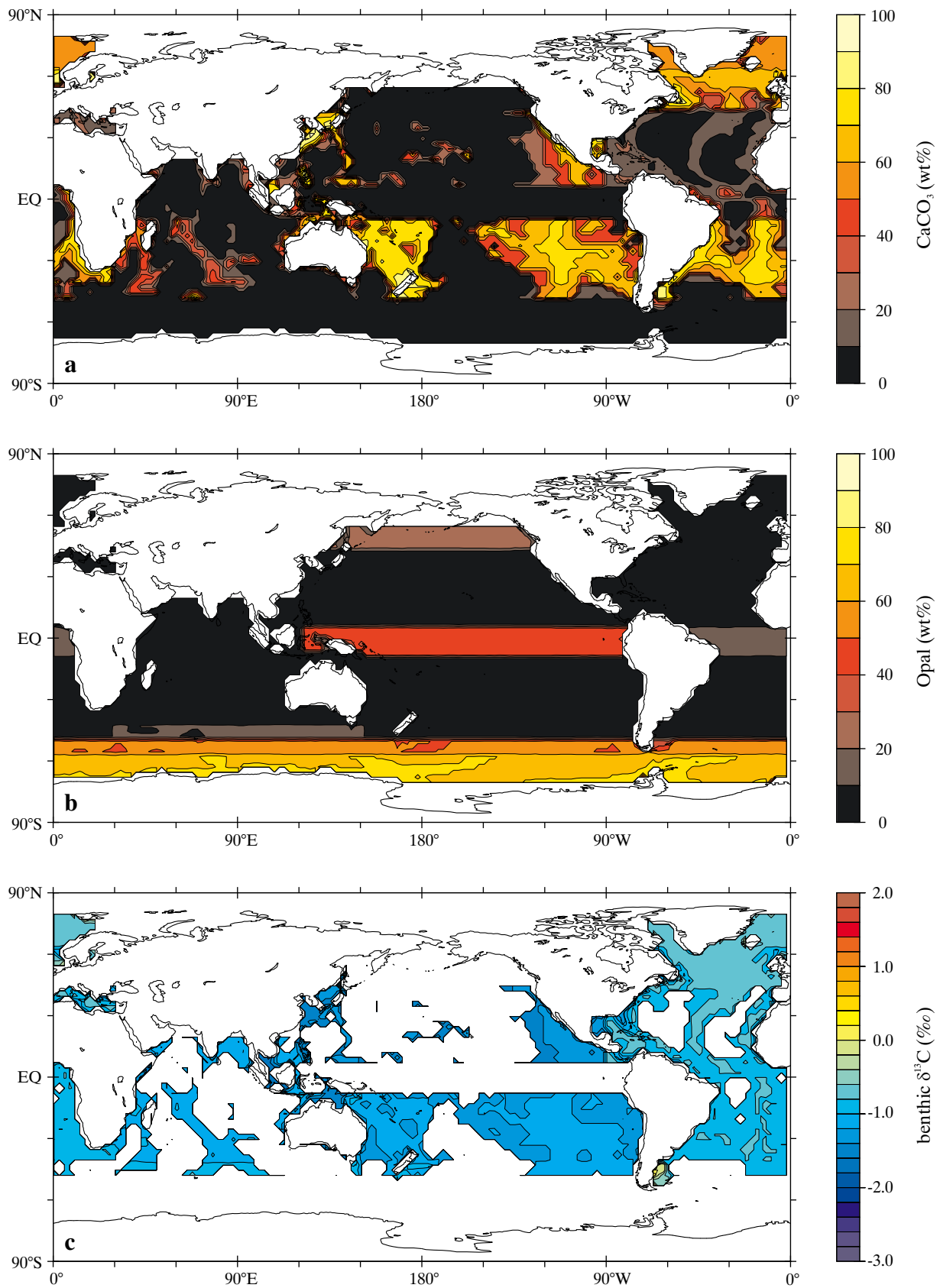


Figure 4-12 Modern steady-state distributions of surface sediment characteristics generated by SUE1608; wt% CaCO_3 (top), wt% opal (middle), and benthic foraminiferal $\delta^{13}\text{C}$ (bottom) assuming the *Globigerina bulloides* ^{13}C fractionation relationship (2-63). Spatial resolution is gridded at $2.5^\circ \times 2.5^\circ$.

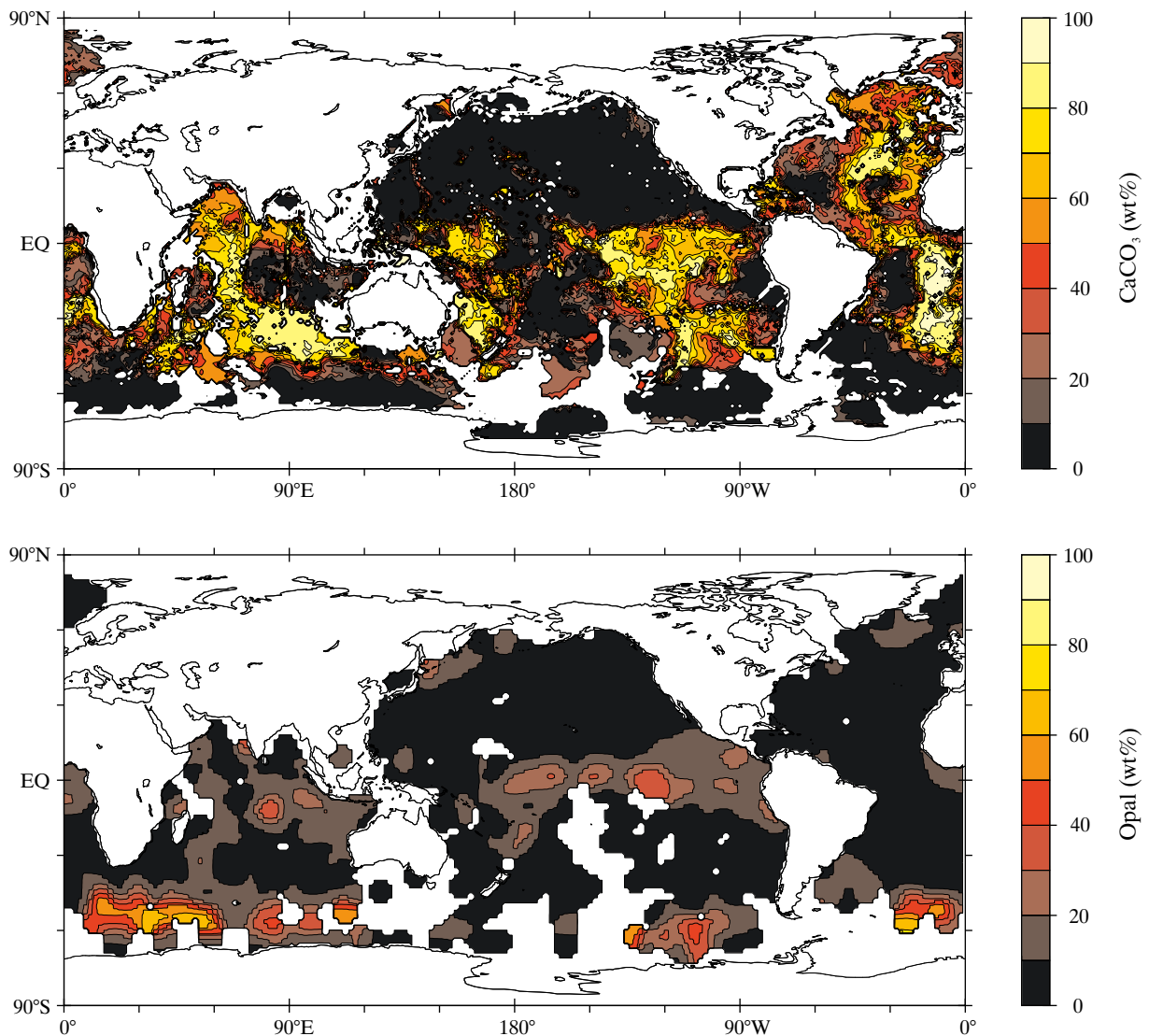


Figure 4-13 Observed core-top sediment composition distributions; wt% CaCO_3 (top) [Archer, 1996b], and wt% opal (middle) [Archer, pers com].

4.4.3 Sediment composition

The composition of deep-sea sediments is controlled by a combination of benthic environmental conditions (physical and chemical) and particulate matter rain rates (in turn affected by a combination of ocean properties throughout the water column and surface ocean biological productivity). Since surface sediment properties effectively reflect an integrated state of ocean biogeochemical cycling, their global distribution can be used as a powerful diagnostic of model operation. Figure 4-12 shows predicted distributions of surface sediment CaCO_3 (as calcite) and opal content, together with benthic foraminiferal $\delta^{13}\text{C}$. Equivalent observational data (where available) is shown in Figure 4-13.

It can be seen that there is a good correspondence between predicted CaCO_3 contents and observations for many regions of the world ocean. In particular, the apparent depth of the calcite lysocline appears to be extremely well reproduced in the south Atlantic and south Pacific. However, there are a number of notable problem areas. Firstly, there is too little CaCO_3 preservation in the equatorial Pacific. This is most likely a result of an under-predicted CaCO_3 :POC rain ratio, since the poor representation of biogeochemical cycling in this region produces excessive POC export which in turn drives enhanced CaCO_3 dissolution in the underlying sediments. This problem is not specific to SUE1608 and is apparent in 3D OGCM carbon cycle models [Heinze and Crowley, 1997; Heinze et al., 1999], although nutrient trapping tends to be much more localized in these. Similar arguments

apply to the equatorial Atlantic. The other major areas of concern are the Indian Ocean and northern mid latitude Atlantic where the zonally-averaged nature of ocean circulation tends to overly-restrict nutrient supply and thus potential CaCO_3 export. That these two regions are both characterized by high dust deposition fluxes suggests that the influence of Fe availability on H_4SiO_4 utilization efficiency (2.2.3.3) may potentially be overstated, distorting the POC partitioning between the two phytoplankton groups and with it the net CaCO_3 :POC rain ratio. The aragonite lysocline is predicted to lie at a depth of around 2000-3000 m in the Atlantic and <1000 m in the Pacific, both consistent with observations [Balsam, 1983; Berger, 1977].

Global distributions of core-top opal content are also generally reasonable. However, little opal accumulation is predicted for the Indian Ocean contrary to observations, whereas opal contents in the equatorial Atlantic and north Pacific are slightly over-estimated. The only other area of significant mismatch concerns the Southern Ocean, where a maximum in opal content occurs in the southernmost grid point region (centred on 62.5°S) in contrast to observations of a relatively tightly constrained circumpolar 'belt' of maximum opal accumulation further to the north at around ~55°S. This is likely to be primarily an artifact of the low meridional resolution in this region employed in the model.

The distribution of the benthic foraminiferal calcite isotopic signature ($\delta^{13}\text{C}^{\text{foram}}$) in the model is also shown (Figure 4-12c). A trend is visible across the ocean with maximum values of -0.6 ‰ in the north Atlantic, through -1.1 ‰ in the sub-polar Antarctic, to less than -1.5 ‰ in parts of the northwestern Pacific. This oceanic trend is comparable to that reconstructed from the analysis of deep-sea sediment cores [Matsumoto and Lynch-Stieglitz, 1999; Michel et al., 1995], although a few tenths of a per mill less in the total range spanned. It should be noted that due to vital differences between species used for observational analysis and those represented in the model, absolute values are not directly comparable.

4.5 An improved representation of the Southern Ocean and global Si cycling

One of the most noticeable deficiencies resulting from the ocean configuration adopted in SUE1608 was in the inability of the model to resolve the circumpolar opal maximum observed in the Southern Ocean. There is a danger that any significant failure in correctly representing what is the primary opal sink in the world ocean might distort the dynamics of the global silica cycle in the model and thereby degrade the applicability of SUE1608 to many of the mechanisms for glacial-interglacial CO_2 variability. In addition, use of a single grid point region covering the entire polar Southern Ocean makes any attempt in a realistic representation of variability in sea ice extent (thought to be a key mechanism driving CO_2 changes [Stephens and Keeling, 2000]) problematic. An alternative configuration is therefore

introduced to allow more detailed analysis of the global silica cycle and of mechanisms for glacial-interglacial change located in the Southern Ocean.

The ocean configuration of the improved model is derived from Bern 2D ZOGCM [Marchal et al., 1998a; Stocker and Wright, 1996] as previously for SUE1608 (4.2.1). However, rather than amalgamating the two zonal regions in the parent model south of 55°S these are now kept discrete. Meridional resolution is further enhanced by sub-dividing these two 7.5° zones into sub-zones of width 2.5°. Ocean circulation in these regions is derived by assuming that each of the sub-zones is characterized by the same vertical velocity as its parent zone. Meridional velocities across the boundaries separating the sub-zones are obtained by linearly interpolating between velocities at 55°S and 62.5°S in the Bern 2D circulation, and extrapolating south of 62.5°S. A total of six zonal regions now replaces the single zone south of 55°S in SUE1608 – with a total of 21 grid points the new model is designated 'SUE2108'. The same parameter values as optimized for SUE1608 (4.3.2) are adopted, resulting in a similar baseline model state.

4.5.1 Sedimentary opal distributions

Figure 4-14a shows the global distribution of surface sediment opal content in SUE2108. It can be seen that a distinct circumpolar belt of maximum opal content is now resolved. The meridional location of this feature is centred on ~60°S with maximum opal contents reaching around 75 wt%, both reasonably consistent with observations [Archer, pers com; Broecker and Peng, 1982]. Preservation efficiencies in these high opal content sediments have been recently estimated at some 6.8% [DeMaster, 2000], comparable to model predictions of 7-9% (Figure 4-14c). There is an apparent southerly offset (~3-4°) in the latitude of maximum opal content relative to the location of peak surface ocean biogenic opal export rates (not shown). This is a result of the trend of increasing H_4SiO_4 concentrations at intermediate and shallow depths (< 4000 m) with southerly latitude (Figure 4-7), producing a similar trend in the preservation efficiency within the water column (Figure 4-14b) and displacing southwards peak opal fluxes reaching the sediment surface. Near to the Antarctic continental shelf, model sediment preservation efficiencies of 5-7% are also comparable to observational-based estimates in the Ross Sea of around 6% [DeMaster, 2000]. A consequence of the improved representation of the Southern Ocean silica cycle is a slight reduction in equatorial and north Pacific opal contents, bringing them more in line with observations. Primary observed variability in sedimentary opal distributions not captured by the model is now intra-zonal, beyond the ability of a zonally-averaged model to prognostically generate.

4.5.2 Re-evaluation of the opal diagenesis module

Previously, the opal diagenesis module was validated with the aid of a simple box model (3.2.3.5). Re-validation of this

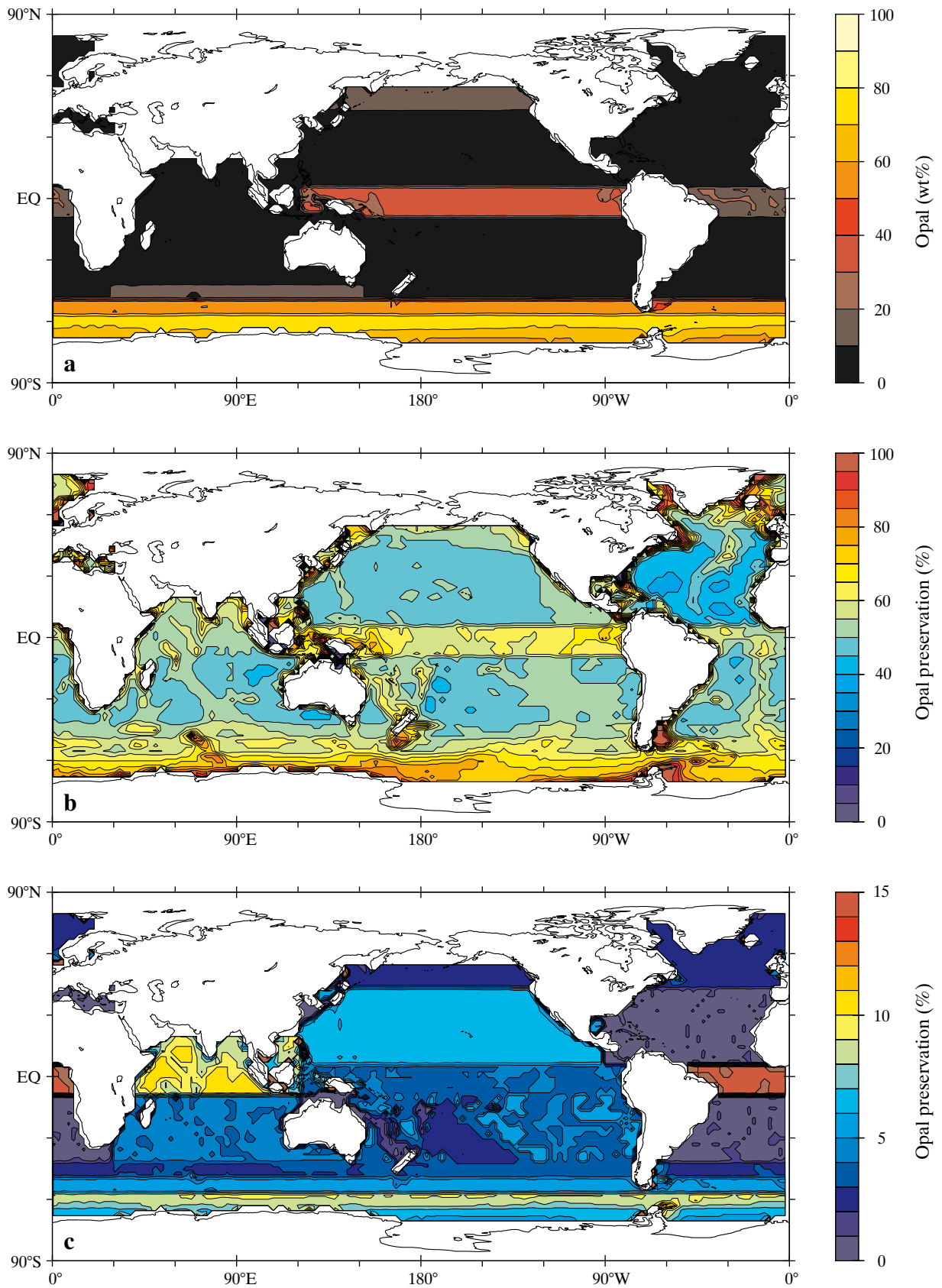


Figure 4-14 Modern steady-state distributions generated by SUE2108 of; (a) sediment surface wt% opal, (b) opal preservation efficiency within the water column, and (c) opal preservation efficiency within the sediments. Spatial resolution is gridded at 2.5°×2.5°.

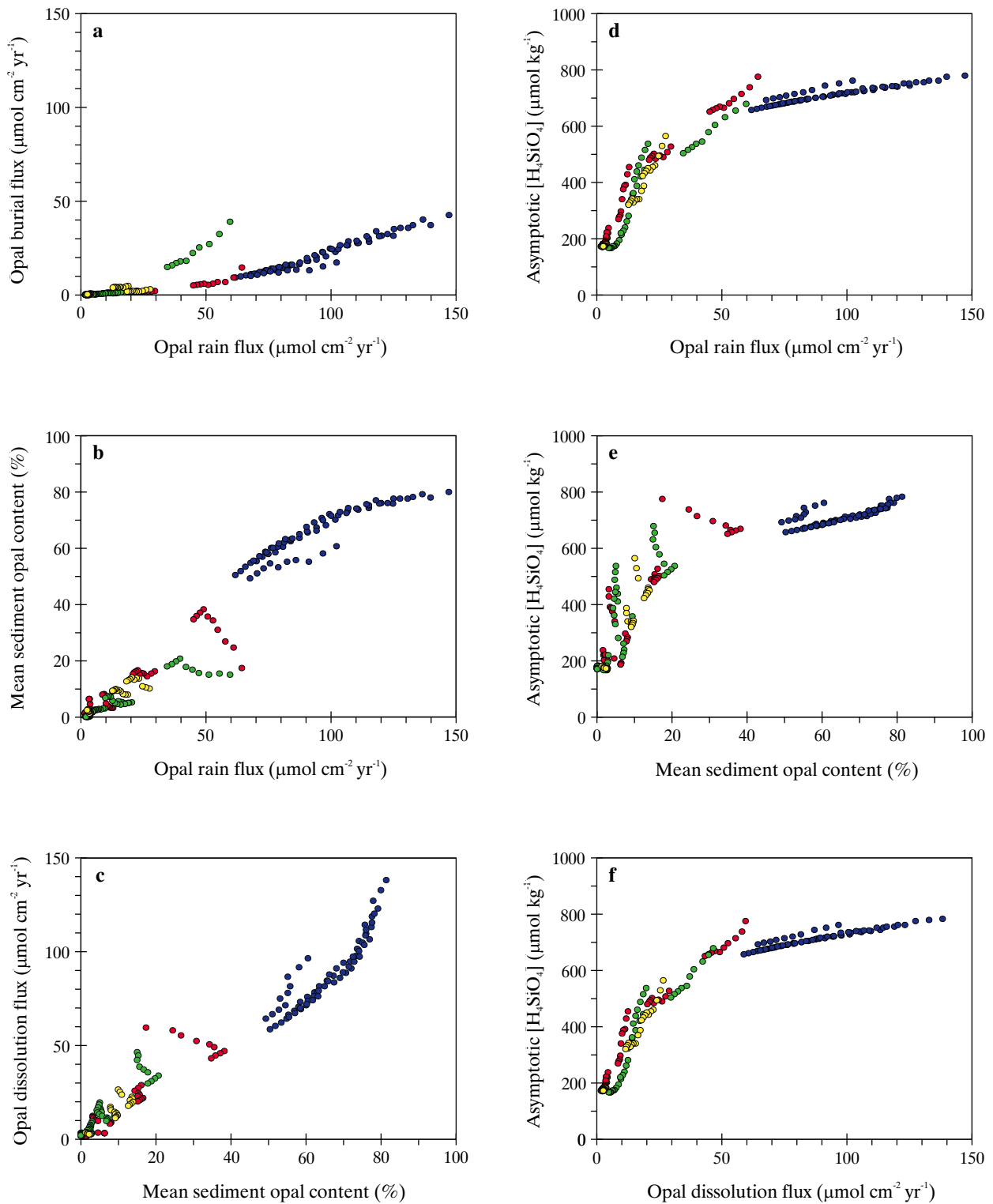


Figure 4-16 Combined response of the opal diagenesis model within SUE2108, shown by small filled circles colour-coded by ocean region; Southern Ocean (blue), Atlantic Ocean (green), Indian Ocean (yellow), Pacific Ocean (red). Sediments lying at depths shallower than 1000 m are excluded.

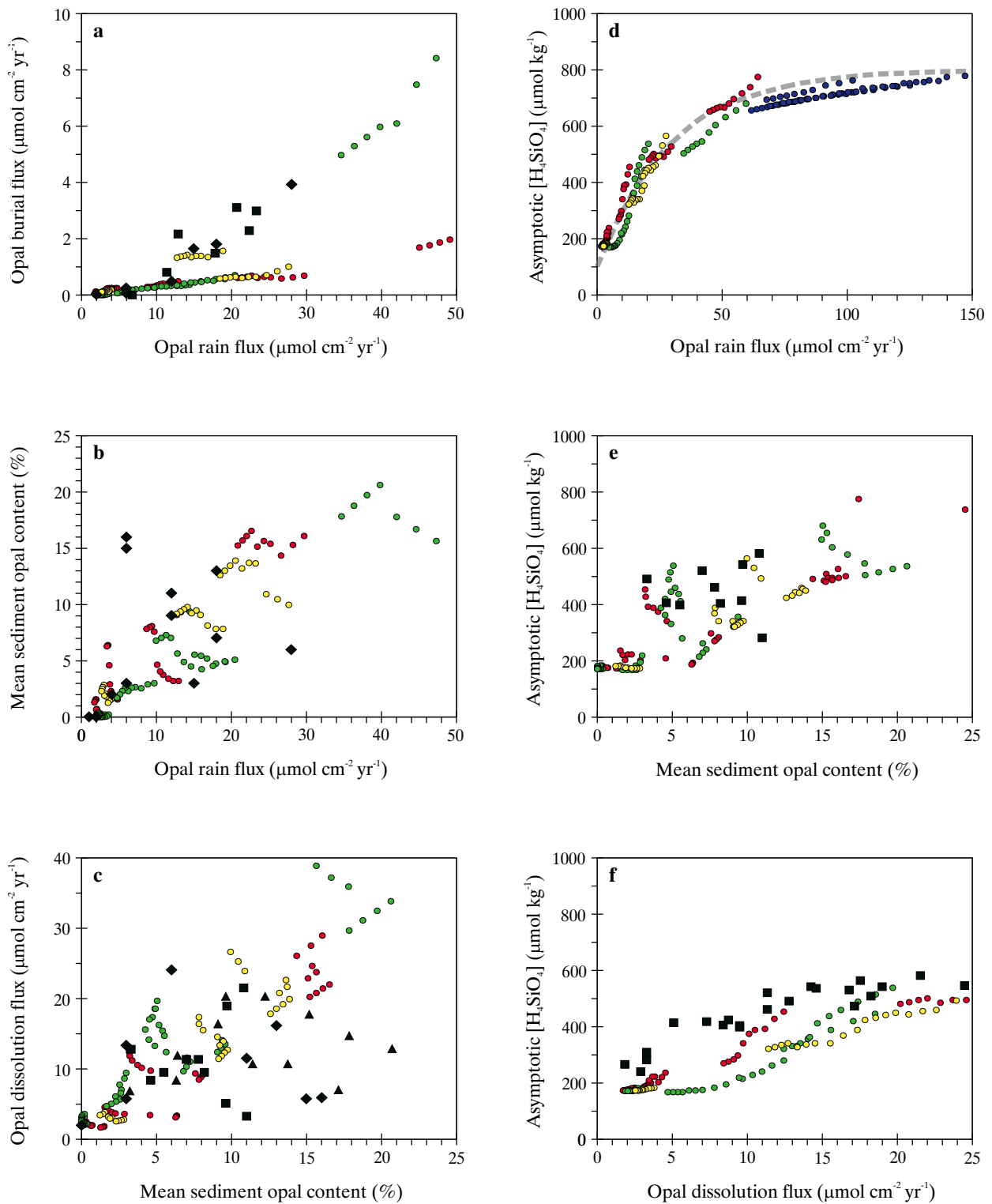


Figure 4-17 Combined response of the opal diagenesis model within SUE2108 shown by small filled circles colour-coded by ocean region; Southern Ocean (blue), Atlantic Ocean (green), Indian Ocean (yellow), Pacific Ocean (red). Sediments lying at depths shallower than 1000 m are excluded. Also shown is the validation data, indicated by larger filled symbols; squares - *McManus et al.* [1995], diamonds - *Archer et al.* [1993], triangles - *Martin et al.* [1991]. The thick dashed grey line in (d) indicates the estimated trend of *Archer et al.* [2000].

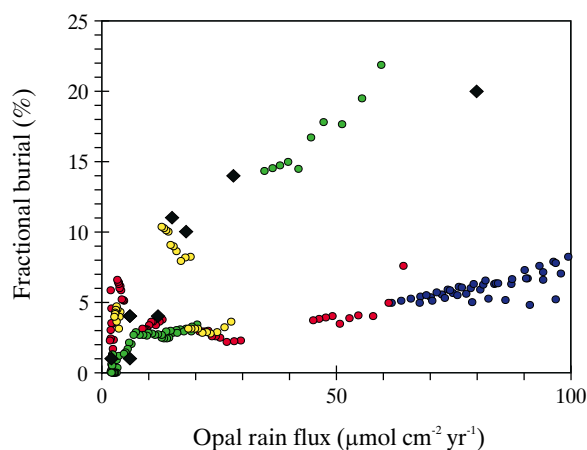


Figure 4-18 Combined response of the opal diagenesis model within SUE2108 shown by small filled circles colour-coded by ocean region; Southern Ocean (blue), Atlantic Ocean (green), Indian Ocean (yellow), Pacific Ocean (red). Sediments lying at depths shallower than 1000 m are excluded. Also shown is the validation data, indicated by larger filled diamonds [Archer *et al.*, 1993].

biogeochemically critical module is now carried out with SUE2108. Global functional (steady-state) relationships exhibited by the opal diagenesis module are displayed in Figure 4-16, with results from the four distinct ocean basins now differentiated. General trends are similar to before (3-11), although increased spatial resolution leads to trends being slightly better constrained with fewer prominent hiatuses. However, when model output is contrasted with the validation data set (Figure 4-17) the performance of the opal diagenesis module appears to be significantly better than suggested by the original analysis (3.2.3.5). Most striking is that the observed trend of opal burial flux with rain flux (a) is now extremely well reproduced whereas before, the slope was underestimated by a factor of >2 . Interestingly, although the observational data delineating this trend is derived from cores mainly located in the eastern equatorial and temperate northeast Pacific [Archer *et al.*, 1993; McManus *et al.*, 1995], the matching model results come from equatorial Atlantic and Indian Ocean grid points. In the model both these regions are characterized by relatively high aeolian detrital fluxes to the sediments with low CaCO_3 contents. Such conditions are similar to those found at the core locations in the eastern and northeast Pacific [Archer *et al.*, 1993; McManus *et al.*, 1995]. Thus, while there is a poor geographical correspondence between model regions and core locations, there is a much closer match on the basis of prevailing biogeochemical conditions (which the diagenesis module appears to be correctly responding to). Observed relationships between both opal content and asymptotic $[\text{H}_4\text{SiO}_4]$ with rain flux ((b) and (d), respectively), and also asymptotic $[\text{H}_4\text{SiO}_4]$ with opal content (e) are well reproduced as before. Although the observed trend of asymptotic $[\text{H}_4\text{SiO}_4]$ with dissolution flux (f) is slightly

improved, it is obvious both from this and from the trends of dissolution flux with opal content (c) that dissolution fluxes are still somewhat over-predicted. Despite the continued existence of apparent deficiencies in several of the functional relationships characterizing opal diagenesis, behaviour critical to the global silica cycle such as the degree of fractional burial as a function of the flux of biogenic opal is still captured (Figure 4-18).

4.6 Summary

It is clear that significant deficiencies in the representation of global biogeochemical cycles arise out of zonalization of ocean circulation and structure. However, in spite of this SUE1608 is generally successful in capturing the characteristics of most of the key distinct biogeochemical provinces in the world ocean. Furthermore, SUE is designed to capture the dynamics of the carbon cycle on glacial-interglacial time scales, for which failure to accurately simulate the modern state is not necessarily a strict pre-requisite. Indeed, for long-term dynamical realism it is probably better to retain deficiencies arising from problems in the physical ocean representation rather than compensate for them by distorting biogeochemical cycling.

Perturbations to the system

5.1 Introduction

Ice core records reveal that the concentration of CO₂ in the Earth's atmosphere ($x\text{CO}_2$) has undergone substantial fluctuations over the course of the late Quaternary [Petit *et al.*, 1999]. That the climatic system in general has undergone parallel excursions, with glacial periods characterized by extensive northern hemisphere ice sheets occurring contemporaneously with low $x\text{CO}_2$ suggests that there is a fundamental causal link between the two. Should changes in $x\text{CO}_2$ be at least partly responsible for driving the global climate system there would be obvious repercussions for our predictions for the coming decades of the radiative forcing effects due to anthropogenic CO₂ emissions. Even if over the glacial-interglacial cycles atmospheric composition responded in a predominantly passive manner, then elucidation of the mechanisms involved is still vital to our understanding of key feedbacks operating in the present-day Earth system [Falkowski *et al.*, 2000].

The sheer diversity and biogeochemical scope of mechanisms purporting to explain low glacial levels of CO₂ has made any comparative assessment within a single framework problematic, with models often customized around a single process. Hypotheses range from relatively simple changes in surface ocean biological productivity [Knox and McElroy, 1984; Martin, 1990; Rich *et al.*, 1999; Sarmiento and Toggweiler, 1984], ocean circulation [Keir, 1988; Siegenthaler and Wenk, 1984; Toggweiler, 1999], and changes in the storage on continental shelves of nutrients and CaCO₃ [Berger, 1982a; Broecker, 1982; Opdyke and Walker, 1992; Shaffer, 1990], through subtle effects on deep-sea sediments exerted by changes in the particulate composition of biogenic material exported out of the euphotic zone [Archer and Maier-Reimer, 1994], to more exotic mechanisms such as transients in ocean pH driven by rapid manganese depositional events [Mangini *et al.*, 1991] and CH₄ out-gassing [Loehle, 1993]. However, of the mechanisms forwarded to date, when taken in isolation all fall short of simultaneously meeting constraints dictated by the various marine, terrestrial, and ice core paleoclimatic records [Broecker and Henderson, 1998; Holligan and Robertson, 1995]. It is thus becoming increasingly obvious that in spite of the perhaps aesthetic desirability of a single mechanism yet to be discovered and able to completely solve the mystery, the solution to the observed glacial-interglacial variability in $x\text{CO}_2$ almost certainly lies in a combination of processes operating during the late Quaternary. The problem then lies in determining the important mechanisms involved and constraining their relative overall contribution to the dynamics of the system. A series of potentially important mechanisms will therefore be characterized in isolation within the same model framework (SUE) and then combined together in a 'best guess' scenario. Although a number of comparative studies have been carried out in the past, these all have shared a common approach, of contrasting two steady states of the system: one characterized by modern (pre-industrial) boundary conditions and the other by those thought to be representative of the Last Glacial Maximum (LGM). Partly as a consequence of this, many of these studies (particularly those based around simple box model representations of the ocean) have concluded that permutations which give rise to a simile of glacial atmospheric and ocean chemistry are relatively easy to construct [Hausman and McElroy, 1999; Keir, 1988; Marino *et al.*, 1992; Toggweiler, 1999]. However, recent work based around a comprehensive OGCM-based global carbon cycle model has suggested that we are still far from solving the problem [Archer *et al.*, 2000]. In an attempt to increase the utilization efficiency of information available from both ice cores and the paleoceanographic record in constraining the operation of the global carbon cycle, mechanisms are tested on a dynamical (i.e., time-stepping) basis. Changes in the boundary conditions of the global carbon cycle are reconstructed for multiple glacial-interglacial cycles so that the dynamical evolution of the system may be followed over that entire period. Special emphasis will be placed on the role of the Southern Ocean, particularly with respect to the inception of deglacial transitions in the system.

5.2 Evidence for glacial-interglacial variability of the global carbon cycle

The primary records of past change in the global carbon cycle over the course of the late Quaternary comes from ice cores. Material (both solid and gaseous) contained within the crystalline structure of accumulating ice in both low latitude glaciers [Thompson *et al.*, 1995] and high latitude ice caps [Edwards *et al.*, 1998; Jouzel *et al.*, 1995; Petit *et al.*, 1999; Smith *et al.*, 1999] present us with a proxy record of past climate. While cores located in low latitude glaciers rarely extend back even as far as the LGM, the greater ice thickness afforded by high latitude ice caps generally allows a much longer record to be obtained, with records obtained to date spanning almost 250 ka in Greenland [Johnsen *et al.*, 1997], but back as far as 420 ka BP in Antarctica [Petit *et al.*, 1997, 1999]. With respect to the past state of the global carbon cycle the most important single indicator is the concentration of CO₂ held within bubbles trapped within the ice. Such bubbles start to form in the firn relatively near the surface, effectively recording a snapshot of atmospheric composition at the time of occlusion [Oeschger *et al.*, 1984]. However, Greenland ice contains high concentrations of aeolian carbonate-rich dust, which can chemically denature over time thereby contaminating trapped air samples with CO₂ produced *in situ* [Indermühle *et al.*, 1999; Smith *et al.*, 1997]. Therefore they cannot be relied upon as indicators of a changing carbon cycle. In contrast, the low carbonate content of Antarctic ice suggests that cores recovered there will record past CO₂ concentrations with much greater fidelity [Smith *et al.*, 1997]. The ice core record from Vostok (78°S, 106°E, elevation 3,488 m) covering the last ~400 ka [Petit *et al.*, 1999] will be used to provide the model target for glacial-interglacial variability in $x\text{CO}_2$.

A second property of atmospheric composition recorded in ice cores and of direct relevance to the state of the global carbon cycle at any point in time is the stable isotopic composition of CO₂ ($\delta^{13}\text{C}^{\text{CO}_2}$). The ~27 ka long record from Taylor Dome [Smith *et al.*, 1999] will be used to provide the model target for variability in this. Visual inspection suggests that the age scales constructed for the Vostok and Taylor Dome cores do not exactly correspond. A simple linear age transformation (reduction in gas age of 7.5%) is therefore made to the Taylor Dome CO₂ record so that it matches that at Vostok over the most recent deglacial transition (Figure 5-1a). As a result of considerable analytical difficulties inherent in measuring isotopic composition of ice core $\delta^{13}\text{C}^{\text{CO}_2}$ [Leuenberger *et al.*, 1992; Smith *et al.*, 1999] there is a considerable degree of uncertainty in the values obtained. Confidence in many of the major features of this record can be improved, however, through reference to estimates of past (atmospheric) isotopic composition made by an entirely independent method, based on preserved samples of the shrub *Atriplex confertifolia* [Marino *et al.*, 1992]. The ¹⁴C-derived age scale for *A. confertifolia* is adjusted so that major transitions are in phase with recorded events at Taylor Dome, as shown in Figure 5-1b. It can be seen that while the magnitude of some of the events disagree, many of the

general features are held in common between the two records. In particular, there is a pronounced negative $\delta^{13}\text{C}^{\text{CO}_2}$ anomaly during the initial stages of Termination I, with a second one around the time of the Younger Dryas (~12.8 ka BP [Blunier *et al.*, 1997]). The presence of this first anomaly is also supported by planktonic foraminiferal $\delta^{13}\text{C}$ records which exhibit contemporaneous features, similar in magnitude to cores located between the Antarctic polar and subtropical fronts in the Southern Ocean [Ninnemann and Charles, 1999] but slightly more muted than cores from the eastern tropical Pacific and tropical Atlantic [Curry and Crowley, 1987; Shackleton *et al.*, 1983].

Another effective integrator of the state of the global carbon cycle for which there is extensive (paleoceanographic) information available concerns the CaCO₃ lysocline transition zone. The CaCO₃ content of benthic sediments is primarily a function of deep ocean pH together with particulate matter rain rates. Changes in the shape and depth of the CaCO₃ lysocline transition zone, therefore, represents a powerful constraint upon the operation of the majority of mechanisms forwarded to explain the observed variability in $x\text{CO}_2$. Sediment cores located in the Pacific Ocean indicate that CaCO₃ was more abundant during glacial than interglacial times there; LGM time-slice reconstructions show a slightly greater areal extent of CaCO₃-rich sediments [Catubig *et al.*, 1998] while lysocline sections detail glacial age lysoclines lying of order 500 m deeper [Berger, 1978, 1982b; Farrell and Prell, 1989, 1991; Karin *et al.*, 1992]. In contrast, distribution patterns of sediments in the Atlantic basin exhibit significantly lower CaCO₃ abundances than during glacial periods [Balsam and McCoy, 1987; Catubig *et al.*, 1998]. This is supported by estimates made of the location of the calcite lysocline during glacial periods which suggest it was some 200-700 m deeper [Berger, 1968; Crowley, 1983], although some estimates put this shoaling as large as 1500 m or more in the western north Atlantic [Balsam, 1983]. Variability in the depth of the carbonate compensation depth (CCD) appears to be generally much more muted when compared to the response of the lysocline in either basin [Balsam, 1983; Farrell and Prell, 1989]. Thus, not only the depth of the lysocline but the shape of the entire transition zone must be altering in response to perturbations of the global carbon cycle. That some mechanisms (such as whole-ocean changes in pH) will tend to alter the depth of both the lysocline and CCD to a similar extent while others (such as changes in the CaCO₃:POC rain ratio [Archer and Maier-Reimer, 1994]) tend to shift lysocline depth whilst leaving the location of the CCD relatively invariant, may further aid in the elucidation of the key mechanisms involved.

There is a cornucopia of other paleoceanographic proxies reflecting changes in the earth system; for instance, in the relative abundance of solid sediment constituents (calcite, aragonite, opal, detrital material, organic matter), the isotopic ($\delta^{11}\text{B}$, $\delta^{13}\text{C}$, $\delta^{14}\text{C}$, $\delta^{15}\text{N}$, $\delta^{18}\text{O}$, $\delta^{30}\text{Si}$, $^{87}\text{Sr}/^{86}\text{Sr}$, $^{231}\text{Pa}/^{230}\text{Th}$) and chemical (Cd/Ca, Ge/Si, and Mg/Ca ratios) composition of these solid components, together with phytoplankton and zooplankton species abundance, marine and terrestrial biomarkers, the degree of shell fragmentation,

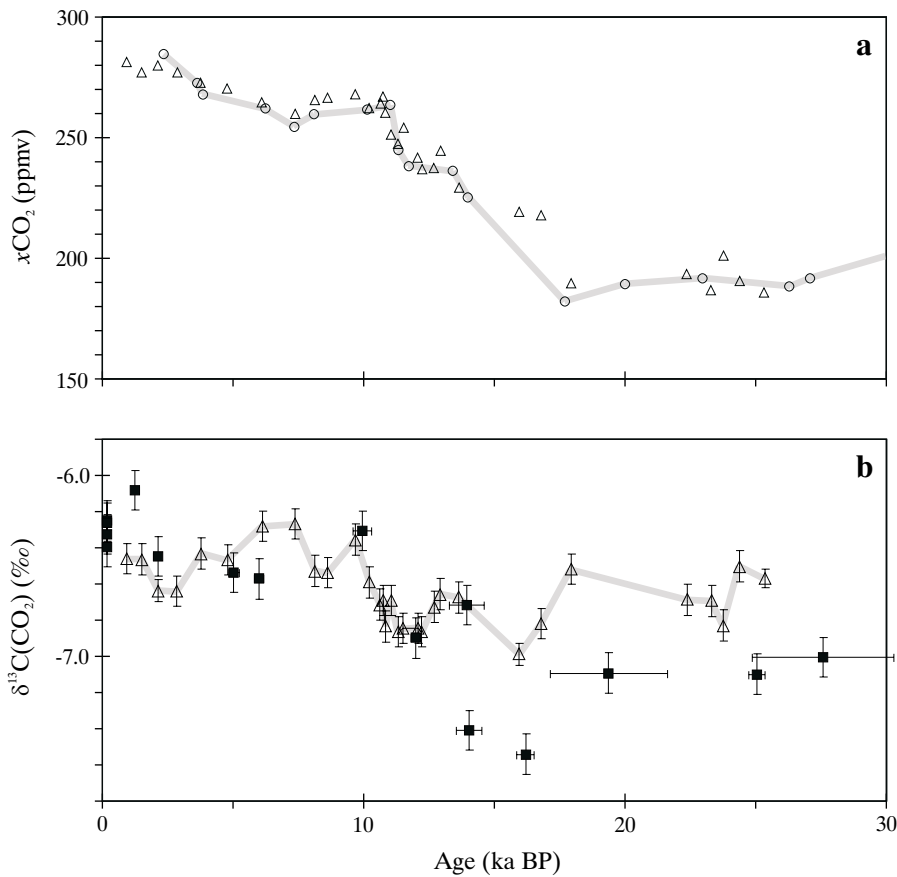


Figure 5-1 Comparisons between; (a) the CO₂ ice core records from Vostok (empty circles) [Petit *et al.*, 1999] and Taylor Dome (empty triangles) [Smith *et al.*, 1999] and transformed onto the Vostok age scale, (b) δ¹³C(CO₂) record from the Taylor dome ice core (empty triangles) and reconstructed from plant organic matter (filled squares) [Marino *et al.*, 1992], both on the Vostok age scale.

and varied burial fluxes (³He, Ba, Fe, Al, Zn, authigenic U). However, many of these depend on individual processes operating with the ocean not accounted for in the model and can be more localized in scope than the resolution of SUE1608 reasonably allows for. The implications of such proxies for this present study will therefore only be discussed where especially relevant to a particular mechanism or region of glacial-interglacial change.

for the relative importance of low vs high latitude regions in controlling xCO₂ indicate a fundamental divide separating box models from OGCMs [Archer *et al.*, in press; Broecker *et al.*, 1999a]. It is important to establish what class of response the models developed from use in this present study fall into, before either SUE1608 or SUE2108 can be wholly relied upon to critically assess mechanisms for glacial-interglacial change.

5.3 Uncertainties in model response to perturbations of the carbon cycle

Recent studies have questioned whether certain types of model can be relied upon to correctly predict the response of atmospheric composition to a perturbation applied to the system. In particular, attention has focussed on whether simple box-type models might over-estimate the sensitivity of xCO₂ to physical and biological changes located at high latitudes. The results of two independently-developed indices

5.3.1 The ‘Harvardton Bear Equilibrium Index’

Using an index (the ‘Harvardton Bear Equilibrium Index’, or ‘HBEI’) first devised by Bacastow [1996], Broecker *et al.* [1999a] found that global carbon cycle models based around a box-type representation of the ocean scored considerably lower (~0.11 for 2- and 3-box models and around 0.2 for ‘multi-box’ models) than those based around 3D OGCMs (up to 0.32). In this index (the ‘Warm Surface’ variant), higher values represent a greater relative equilibrium response of xCO₂ to a perturbation of the low latitude surface ocean. It was concluded from this that box models significantly overestimate the importance of high latitude

regions; the implication being that the results of early studies based upon such models, which suggested that low glacial $x\text{CO}_2$ is explicable through changes in Southern Ocean circulation and/or biological productivity, might be in error [Broecker *et al.*, 1999a]. Somewhat worryingly, the parent model from which both SUE1608 and SUE2108 derive their ocean structure and circulation, the Bern 2D ZOGCM [Stocker and Wright, 1996], scored an HBEI value of just 0.14, putting its response into a similar class to (and in fact below) the box models. Rather surprisingly, however, SUE1608 gives an HBEI score of just under 0.39, making atmospheric composition slightly less sensitive to high latitude perturbations even than in OGCM-based models. This apparently anomalous behaviour of the Bern 2D model is now investigated.

A new baseline model is constructed (designated 'SUE1608'), taking the same physical structure and advective field as SUE1608 (outlined in 4.2) but otherwise configured following Marchal *et al.* [1998b], the main features being: 18 time steps of 20 days each with no seasonality, CO_2 air-sea gas exchange with a uniform transfer rate of $0.067 \text{ mol m}^{-2} \text{ a}^{-1} \text{ ppmv}^{-1}$, no sea ice cover, new production derived by restoring ocean surface $[\text{PO}_4]$ towards observations at 30 m depth [Conkright *et al.*, 1994] on a time scale of 100 days with export production split 50:50 between DOM and POM phases, uniform vertical and horizontal eddy diffusivities of $0.2 \text{ cm}^2 \text{ s}^{-1}$ and $10 \times 10^6 \text{ cm}^2 \text{ s}^{-1}$, respectively, and with the system run entirely 'closed' (i.e., no sediment burial or weathering inputs). The HBEI value so obtained is 0.21, a little higher than that reported by Broecker *et al.* [1999a] for the full Bern 2D model, probably largely a result of

remaining differences in model resolution and biogeochemical schemes. With total export production fixed, a number of changes are made to the details of ocean mixing in SUE1608' and the HBEI value recalculated. These are summarized in Table 5-1.

From this sensitivity analysis it can be seen that the details of vertical and horizontal diffusivity have a relatively minor effect on the HBEI score (± 0.04). However, there is a strong dependence on the details of high latitude convection, with the introduction of just 5% mixing to a stratified high latitude ocean surface almost halving the HBEI score. This suggests that much of the variability in values reported by Broecker *et al.* [1999a] might be attributed to differences in the representation of convective mixing. Indeed, whether mixing takes place seasonally or uniformly all year around (for the same mean annual rate) can account for much of the difference between the seasonal Hamburg [Maier-Reimer, 1993] and the annual circulation Princeton [Murnane *et al.*, 1999] 3D OGCMs. Furthermore, the low HBEI value of the 'PANDORA' box model [Broecker and Peng, 1986] can be almost entirely explained by the relatively thick surface layer (~450 m) used. Other factors (not shown) such as the introduction of a wind speed dependency on air-sea CO_2 gas exchange, the presence of sea ice cover, and the absence of DOM production (equivalent to exacerbating nutrient trapping in equatorial up-welling regions) have relatively little effect.

Table 5-1 Sensitivity to Ocean Mixing of HBEI Value Scored by the Re-configured Baseline Model SUE1608'

Model details	HBEI value
SUE1608' (default)	0.21
SUE1608' - enhanced vertical diffusivity ¹	0.24
SUE1608' - enhanced ($200 \times 10^6 \text{ cm}^2 \text{ s}^{-1}$ at depth) horizontal eddy diffusivity	0.17
SUE1608' - 100% intensity convective adjustment (default)	0.21
SUE1608' - 50% intensity convective adjustment	0.22
SUE1608' - 25% intensity convective adjustment	0.23
SUE1608' - 10% intensity convective adjustment	0.26
SUE1608' - 5% intensity convective adjustment	0.30
SUE1608' - 0% intensity convective adjustment	0.49
SUE1608' - depth of all convective adjustment unrestricted (default)	0.21
SUE1608' - depth of all convective adjustment restricted to upper 1000 m (equivalent to the uppermost 5 layers)	0.22
SUE1608' - depth of all convective adjustment restricted to upper 500 m (equivalent to the uppermost 4 layers)	0.23
SUE1608' - depth of all convective adjustment restricted to upper 150 m (equivalent to the uppermost 3 layers)	0.35
SUE1608' - depth of all convective adjustment restricted to upper 100 m (equivalent to the uppermost 2 layers)	0.41
SUE1608' - depth of all convective adjustment completely restricted (i.e., none)	0.49

¹ Following Weaver and Sarachik [1991]

5.3.2 The ‘Archer Abiotic xCO₂’ test

In a contemporary study, David Archer investigated the potential bias that simpler ocean models might exhibit [Archer *et al.*, in press] in the relative strength of regional control on atmospheric composition. Various global carbon cycle models were run in an ‘abiotic’ mode and the steady state concentration of CO₂ in the atmosphere noted. A similar trend was apparent to that found by Broecker *et al.* [1999a], whereby 3-box and ‘multi-box’ models tended to cluster at one end of the scale with an abiotic xCO₂ value in the range ~220-230 ppmv, while most 3D OGCMs exhibited high values in the range 250-290 ppmv. Archer *et al.* [in press] deduced that it was low latitude vertical diffusivity in 3D OGCMs (not present in box models) that went towards overcoming the control exerted by deep water formation at high latitudes. They therefore concluded, similarly to Broecker *et al.* [1999a], that the importance of high latitudes in glacial xCO₂ draw-down (such as through Southern Ocean Fe fertilization) deduced from box models has been overstated. However, contrary to the results of the HBEI test, abiotic xCO₂ exhibited by the Bern 2D model (289 ppmv) places it firmly into the same group as the 3D OGCMs, supported by tests made with SUE1608 (287 ppmv). The factors controlling the value of this second index are also further investigated.

SUE was configured following a number of different published configurations, detailed in Table 5-2. The results of the abiotic xCO₂ test closely follow those of Archer *et al.* [in press]. Small (≤ 7 ppmv) differences do arise, possibly due to differences in the choices made for the carbonate dissociation constants. With the exception of the 3-box model (whose representation of only two surface boxes is a little too crude to translate to the real world), latitudinal and longitudinal boundaries are now assigned to each surface ocean region, chosen in order to both retain the surface areas of the original model and to be generally consistent with regional descriptions given of the surface boxes. SSTs are derived from Levitus *et al.* [1994c] using these boundaries (see 4.2.2) and the tests re-run. It can be seen (Table 5-2) that use of more realistic SSTs has a dramatic effect on multi-box model abiotic xCO₂ values, with that of ‘PANDORA’ now comparable to most (depth-coordinate) OGCMs, while ‘CYCLOPS’ only just falls short of isopycnic OGCMs [Archer *et al.*, in press]. This suggests that the apparent divide between box and OGCM-based carbon cycle

models dictated by this test may be partly an artefact of unrealistically low mean SSTs adopted in the original model definitions.

5.3.3 Implications for this present study

Under both the ‘HBEI’ and ‘Abiotic xCO₂’ tests of relative inter-regional control on atmospheric composition SUE1608 (as does SUE2108) scores similarly to carbon cycle models based upon 3D OGCMs. That the HBEI score is slightly on the high side suggests that the response of xCO₂ to perturbations occurring at high latitudes in SUE1608 may, if anything, be underestimated. There is thus little danger of seriously overstating the importance of high latitudes in this present study. In light of the strong control exerted by convective mixing regime on the sensitivity of the system to perturbations, it is important that convective adjustments are prevented from co-varying in order that the response of the atmosphere to specific mechanisms for low glacial xCO₂ might be isolated.

5.4 Model evaluation of mechanisms for glacial-interglacial xCO₂ variability

A variety of mechanisms purporting to explain the observed glacial-interglacial variability in the concentration of atmospheric CO₂ are now evaluated. However, there are several aspects of the operation of the global carbon cycle over the late Quaternary for which SUE1608 is not entirely suited for investigating. Changes in the balance between nitrogen supply (through its fixation from the atmosphere) and losses (through denitrification) are suspected to play an important role [McElroy, 1983; Shaffer, 1990]. However, the lack of explicit representation of the oceanic nitrogen cycle in SUE precludes such analysis. In addition, with the exception of the Atlantic overturning circulation, changes in ocean circulation will not be considered further in any detail.

One of the aims of the approach taken here is to consider the dynamical evolution of the global carbon cycle over the entirety of several glacial-interglacial cycles. For assessment of system response, the Vostok ice core provides a target record of fluctuations in the concentration of atmospheric CO₂ over the last ~400 ka [Petit *et al.*, 1999]. However, in

Table 5-2 ‘Abiotic xCO₂’ Values Exhibited by Various Configurations of SUE, and as a Function of SST Prescription

Model	Number of boxes - original configuration	SUE configuration - (as columns×layers)	xCO ₂ (ppmv); original SSTs	xCO ₂ (ppmv); adjusted SSTs	Reference
3-box	3	2×2	218	n/a	Sarmiento and Toggweiler [1984]
PANDORA	10	8×3	224	279	Broecker and Peng [1986]
CYCLOPS	13	6×3	230	249	Keir [1988]
Bern 2D ZOGCM	406	29×14	285	288	Stocker and Wright [1996]

order to generate a synthetic atmospheric record the model must be informed of changes in boundary conditions (e.g., physical ocean surface conditions, dissolved chemical or aeolian inputs) over a comparable period, i.e., the model must be continuously ‘forced’ for the duration of the simulation run. With the possible exception of the use of benthic oxygen isotopes as a proxy for sea level change, there is no continuous 400 ka record fully describing any suspected forcing of the system. Indeed, for many glacial-interglacial changes in boundary conditions such as SST, terrestrial carbon storage, or sea ice extent, there exist paleoclimatic reconstructions for only isolated periods (‘time slices’) [Adams *et al.*, 1990; CLIMAP, 1984]. Even then, the magnitude of regional change is often highly controversial [Crosta *et al.*, 1998b; Crowley, 1995, 2000]. Forcings (externally imposed changes in boundary condition) are therefore devised with the aid of continuous records spanning at least the last 400 ka which can taken to be first-order proxies for the timing and rate of forcing variability over this period. The absolute magnitude of change spanning the last deglacial transition (i.e., 19→0 ka BP) is taken directly from time slices reconstructed for modern (pre-industrial) and glacial (LGM) conditions. Model forcing over the complete 400 ka interval is then derived by linearly transforming the proxy signal so that its magnitude at 0 and 19 ka BP corresponds to the respective values given by the two time slices. Forcing signals are applied to the model at a resolution of 1 ka but subsequently (internally) linearly interpolated to an annual time step. As a consequence, SUE is not particularly suited for detailed investigation of millennial-scale changes such as Dansgaard-Oeschger [Dansgaard *et al.*, 1982] and Heinrich [Bond *et al.*, 1992] events, which will not be considered further in this study. In light of the phase differences exhibited by climatic changes as deduced from ice cores taken from Greenland and Antarctica [Blunier *et al.*, 1997, 1998; Broecker and Henderson, 1998; Kim *et al.*, 1998; Sowers *et al.*, 1991], it may not always be appropriate to use the same forcing template for both hemispheres. In such situations different proxy templates are assigned to each polar region. The relative influence of these signals is then diminished away from each pole according to a pair of weighting functions

$$\gamma_{(lat)}^N = \left(\cos\left(\frac{90 - lat}{2}\right) \right)^2 \quad (5-1 a)$$

$$\gamma_{(lat)}^S = \left(\cos\left(\frac{90 + lat}{2}\right) \right)^2 \quad (5-1 b)$$

where $\gamma_{(lat)}^N$ and $\gamma_{(lat)}^S$ are the weighting factors for changes in boundary conditions of the Northern Hemisphere (NH) and Southern Hemisphere (SH), respectively, both as a function of (northern) latitude (*lat*).

In the model investigations that follow, following a spin-up of 50 ka (sufficient to bring the sediment system largely into steady state), SUE1608 is run for a total of 500 ka, a period over which it is informed by a variable boundary condition (the model ‘forcing’). Although the Vostok CO₂ record

extends back only just beyond 400 ka BP [Petit *et al.*, 1999], the model is forced over the entire 500 ka run length. This allows the initial 100 ka of model run to be treated as an additional spin-up period, the aim of which is to allow the model to relax towards a quasi-steady state (the long-term mean about which the system oscillates over the course of the glacial-interglacial cycles). Indeed, it is probably prudent to regard about half of the entire model run in this manner (i.e., up until 250 ka BP), leaving the response to 3 individual deglacial transitions and 2 glacial inception available for comparison with observations. To avoid contaminating the direct effects of the mechanisms being tested through secondary perturbations arising through changes in non-advective ocean circulation to which the system is apparently extremely sensitive (see 5.3.3), convective regimes produced by the steady-state baseline model are applied and held invariant.

As a first-order assessment, four key indicators of the state of the global carbon cycle will be considered: the concentration of atmospheric CO₂ together with its ¹³C isotopic signature and the shape evolution of the calcite lysocline in both the Atlantic and Pacific basins. All these records are presented for the last 400 ka (with the exception of $\delta^{13}\text{C}^{\text{CO}_2}$, for which observational data is currently only available back to ~25 ka BP [Smith *et al.*, 1999]). The calcite lysoclines are reconstructed with the aid of a series of synthetic sediment cores separated in ocean depth by 100 m (see 3.3.2.3); one set located in the south Atlantic and the other in the south Pacific Ocean (both centred on 23.75°S).

5.4.1 Sea level

In response to the waxing and waning of ice sheets over the course of the late Quaternary there was significant associated variability in sea level height. Of all the processes suspected to exert any significant perturbatory effect on the global carbon cycle over this period, only past changes in sea level can be reconstructed with any accuracy. However, while these changes are reliably recorded by proxy indicators such as coral terraces [Adkins *et al.*, 1998; Fairbanks, 1989; Lambeck and Nakada, 1992; Stein *et al.*, 1993] and transgressions of shallow marine environments [Yokoyama *et al.*, 2000], these are only primarily available for events surrounding the two most recent glacial terminations. As an alternative, changes in the oxygen isotopic composition of benthic foraminiferal calcite has often been used as a proxy for global ice volume and thus for sea level [Munhoven and Francois, 1994, 1996; Walker and Opydyke, 1995].

There are three distinct effects on the (oceanic) global carbon cycle arising from sea level change;

- Since the solubility ratio of CaCO₃ is a sensitive function of pressure (Appendix I), glacial reduction in the ambient hydrostatic pressure at the surface of deep-sea sediments will drive enhanced CaCO₃ preservation and thus lead to the removal of DIC and ALK from the ocean in a 1:2 ratio, driving $x\text{CO}_2$ higher.
- During glacial periods of lower ocean volume, dissolved species such as DIC, ALK, and nutrients will all become more concentrated in the ocean. Increasing DIC and

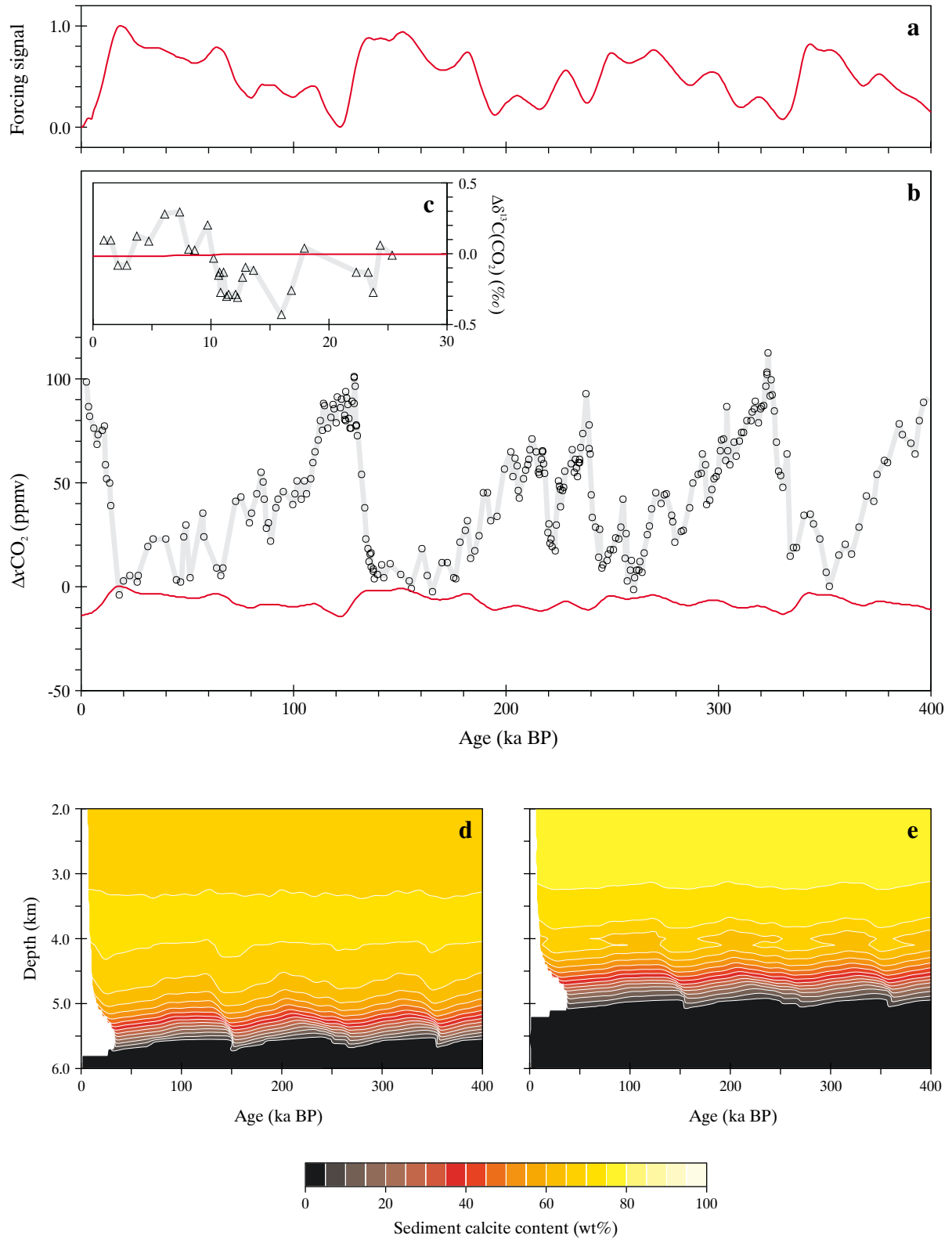


Figure 5-2 Effects on the global carbon cycle of glacial-interglacial variability in sea level. Shown are; (a) the forcing signal (normalized to a value of unity at the LGM); (b) model $x\text{CO}_2$ response (red line) compared to the Vostok ice core record [Petit *et al.*, 1999] (grey line with data points); (c) model $\delta^{13}\text{C}^{\text{CO}_2}$ response (red line) compared to the Taylor Dome ice core record [Smith *et al.*, 1999] (grey line with data points); (d) and (e) the response of the calcite lysocline in the (south) Atlantic and (south) Pacific basins, respectively.

ALK in a 1:1 ratio has the effect of driving $x\text{CO}_2$ up. However, complicating this response are further influences on $x\text{CO}_2$ related to increased export production and sedimentary opal preservation during glacial periods, both driven by the increased nutrient availability.

- Lastly, there is the effect of generally higher ocean salinity during glacials. This manifests itself (at least in terms of atmospheric composition) almost entirely through its influence on aqueous carbonate equilibria in the surface ocean, with an increase in salinity of 1‰ producing a typical increase in CO_2 fugacity ($f\text{CO}_2$) of order 10 ppmv.

The control that glacial-interglacial changes in sea level may have exerted on atmospheric composition is now tested. The SPECMAP stacked $\delta^{18}\text{O}$ record [Imbrie *et al.*, 1984] is used as a signal template for the reconstruction of sea level change over the last 400 ka. The magnitude of this signal is scaled by assuming that sea level just prior to Termination I was 117 m lower than at present [Fairbanks, 1989]. Since ocean volume is calculated directly from prescribed sea level in SUE and dissolved constituents in the ocean are considered inherently in mass unit terms, changes in oceanic tracer concentrations are automatically accounted for. Sea surface salinity (SSS) values are simply varied linearly with changes in sea level, resulting in a typical glacial enhancement in SSSs of $\sim 1\%$.

The results of this exercise are summarized in Figure 5-2. Deglacial sea level rise produces a decrease in $x\text{CO}_2$ of some 13.8 ppmv over the period 19→0 ka BP. This compares favourably with previous estimates for the magnitude of this effect of around 14 ppmv [Broecker and Peng, 1986]. Of the total change, decreasing SSSs are responsible for just under 50% via control exerted on surface ocean $f\text{CO}_2$, while the remaining processes tied to sea level change account for the rest. There is virtually no influence of sea level on $\delta^{13}\text{C}^{\text{CO}_2}$ ($<0.02\%$ over 19→0 ka BP). Perturbations in the lysocline transition zones in both Atlantic and Pacific basins is relatively modest (Figure 5-2d,e), with glacial deepening of ~ 300 and ~ 100 m, respectively. Around half of the Atlantic lysocline response and virtually the entirety of the Pacific response can be accounted for purely by changes in hydrostatic pressure. Although the sign of the change in the Atlantic basin is inconsistent with observations, the magnitude of the change is relatively small and thus could be easily masked by the operation of one or more additional mechanisms.

5.4.2 Ocean surface temperatures

Paleoclimatic reconstruction of the Earth's climate at the time of the LGM suggests that sea surface temperatures (SSTs) were significantly lower than today [CLIMAP, 1984]. Since temperature exerts a strong control on both the fugacity of CO_2 in ocean surface waters and on the degree of ^{13}C fractionation during air-sea gas exchange, it has been suggested that rising SSTs over the course of a deglacial transition could potentially account for much of the observed increase in both $x\text{CO}_2$ and $\delta^{13}\text{C}^{\text{CO}_2}$ [Bacastow, 1996;

Hofmann *et al.*, 1999; Stephens and Keeling, 2000]. As an initial test of the role that glacial-interglacial changes in SSTs may have played in altering atmospheric composition, spatially uniform changes in temperature are applied to the ocean surface taking LGM SSTs to be some 1.7°C lower than at present, consistent with estimates of mean global change [Broecker and Peng, 1986; Guilerson *et al.*, 1994]. Different signal templates are used to represent the differential climatic variability characterizing the two hemispheres. Northern latitudes are simply weighted via the SPECMAP curve [Imbrie *et al.*, 1984], while southern latitudes take information regarding the timing and rate of change of events from the Vostok δD record [Petit *et al.*, 1999] on the basis that changes in local (air) temperatures in continental Antarctica are strongly coupled with Southern Ocean SSTs [Sowers *et al.*, 1993].

The results of this exercise are summarized in Figure 5-3. The magnitude of the response of $x\text{CO}_2$ to the two separate forcings is comparable, with a 19→0 ka BP increase of 9.5 ppmv for SH-weighted SST changes and 7.2 ppmv weighted towards the NH. Differences between these arise only as a result of the shapes of the respective forcing signals, and due to the imbalance in the distribution of ocean surface area between the hemispheres. The combined $x\text{CO}_2$ deglacial rise is thus some 16.5 ppmv, a value which falls comfortably within the range 14-21 ppmv estimated from box models and 3D OGCMs for a similar global temperature change [Broecker and Peng, 1986, 1989; Heinze *et al.*, 1991]. Isotopic composition (Figure 5-3c) exhibits a 0.11% (19→0 ka BP) increase associated with SST changes weighted towards the SH and 0.08% to the north. The net deglacial increase in $\delta^{13}\text{C}^{\text{CO}_2}$ is then 0.19% . There is virtually no change in deep-sea sedimentary CaCO_3 (Figure 5-3d,e).

Glacial cooling at high latitudes was actually much more pronounced than nearer to the equator [CLIMAP, 1984]. A more realistic test of the effect of glacial-interglacial variability in SSTs on the global carbon cycle would be to consider inherent spatial heterogeneity in this change. The CLIMAP [CLIMAP, 1984] reconstructions of modern (pre-industrial) and LGM Earth surface conditions can be used to define this. However, recent studies based on paleoclimatic evidence from low latitudes such as from coral paleothermometers [Guilerson *et al.*, 1994] and high altitude air temperatures [Thompson *et al.*, 1995] suggest that the CLIMAP reconstruction may significantly underestimate glacial cooling in the tropics, although the precise degree of regional underestimation is highly controversial [Crowley, 2000]. A series of sensitivity tests are therefore carried out following Archer *et al.* [2000], with low latitude glacial SSTs progressively modified from their CLIMAP values. Three model runs are carried out. The first takes present-day and LGM ocean temperature distributions directly from CLIMAP. The second assumes tropical cooling at the time of the LGM was $\sim 2^\circ$ greater than suggested by CLIMAP, implemented in SUE1608 by reducing temperatures in each equatorial grid point by 2°C , with a 1°C reduction in the adjoining mid-latitude gyre regions (designated 'CLIMAP-2'). The third is similarly modified, but represents an end-member scenario of maximum likely change, with a

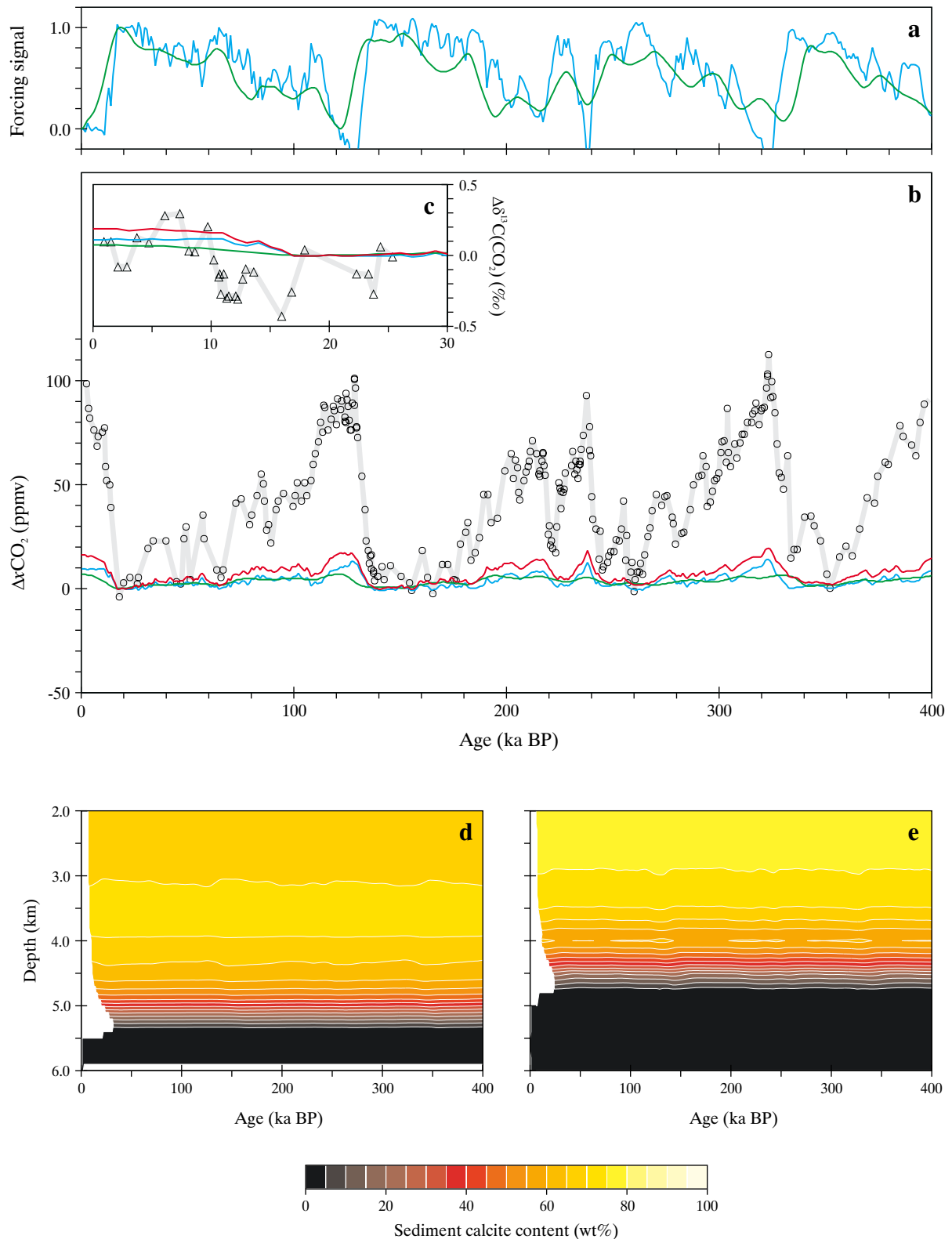


Figure 5-3 Effects on the global carbon cycle of glacial-interglacial variability in SST. Shown are; (a) the NH-weighted (green) and SH-weighted (blue) forcing signals; (b) model NH-weighted (green), SH-weighted (blue) and net (red) $\Delta x\text{CO}_2$ response compared to the Vostok ice core record [Petit et al., 1999] (grey line with data points); (c) model NH-weighted (green), SH-weighted (blue) and net (red) $\delta^{13}\text{C}^{\text{CO}_2}$ response compared to the Taylor Dome ice core record [Smüh et al., 1999] (grey line with data points); (d) and (e) the net response of the calcite lysocline in the (south) Atlantic and (south) Pacific basins, respectively.

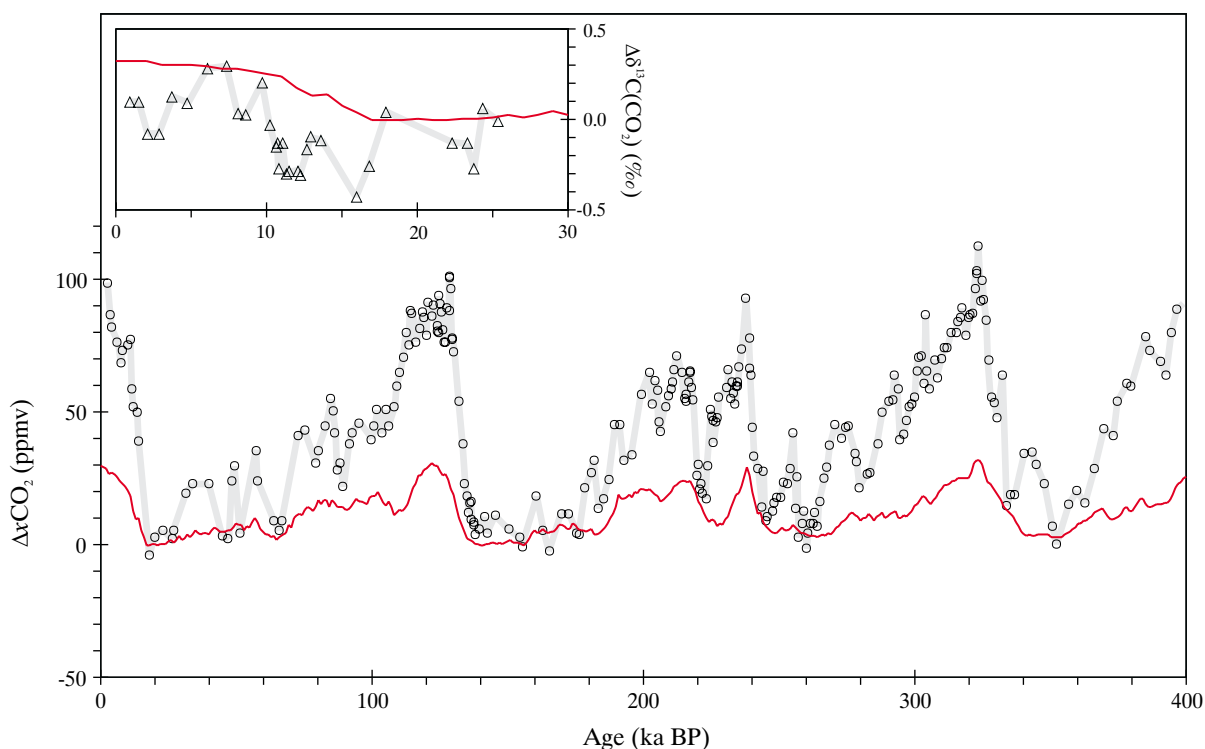


Figure 5-4 Effects on the global carbon cycle of glacial-interglacial variability in SST. Shown is the model $x\text{CO}_2$ response (red line) compared to the Vostok ice core record [Petit *et al.*, 1999] (grey line with data points) with inset – model $\delta^{13}\text{C}^{\text{CO}_2}$ response (red line) compared to the Taylor Dome ice core record [Smith *et al.*, 1999] (grey line with data points).

4°C tropical cooling and 2°C in the sub-tropics (designated ‘CLIMAP-4’).

The difference between the three CLIMAP-based scenarios is relatively small, with the model exhibiting a sensitivity to tropical SST changes of ~ 2 ppmv $^{\circ}\text{C}^{-1}$. This is slightly greater than the ~ 1 ppmv $^{\circ}\text{C}^{-1}$ reported by Archer *et al.* [2000], which might reflect differences between the respective model sensitivities to low latitude surface perturbations as highlighted by respective ‘HBEI’ scores (5.3.1). Alternatively, it may simply be an artefact arising from differences in model resolution with respect to how additional cooling is prescribed adjacent to the equatorial zones.

A glacial SST scenario similar to ‘CLIMAP-2’ is consistent both with recent oxygen isotope analyses and coupled ocean-atmosphere modelling studies, which suggest that glacial temperatures in the tropics were likely to have been intermediate between that as reconstructed by CLIMAP and suggested by corals and snow lines [Crowley, 2000; Spero *et al.*, 1997; Wolff *et al.*, 1998]. The ‘CLIMAP-2’ scenario for glacial-interglacial SST change is therefore adopted as default. The results of this are summarized in Figure 5-4. The amplitude of $x\text{CO}_2$ variability is now much greater, with a 19→0 ka BP increase of 29.6 ppmv. The associated increase in $\delta^{13}\text{C}^{\text{CO}_2}$ is similarly enhanced at some 0.33‰.

5.4.3 Wind speed driven air-sea gas transfer

Variability in the air-sea gas transfer coefficient driven by changes in wind speed has been proposed as being an important control on atmospheric composition [Erickson, 1989; Keir, 1993a], with a simple box model being able to account for around 50 ppmv of the observed deglacial increase in atmospheric CO_2 [Keir, 1993b]. As a first-order test of the potential influence of glacial-interglacial changes in surface ocean wind speeds, the LGM climate is assumed to be characterized by mean annual wind speeds 50% higher than at present. Different forcing signals are used to characterize assumed differential variability between the two hemispheres. Northern latitudes are weighted using the SPECMAP curve [Imbrie *et al.*, 1984], while southern latitudes take information regarding the timing and rates of change from the Na concentration record contained within the Vostok ice core [Petit *et al.*, 1999], a proxy for wind speeds in Southern Ocean source areas of marine aerosol production [De Angelis *et al.*, 1987; Petit *et al.*, 1981].

The results of this exercise are summarized in Figure 5-5. Differences in the nature of the response between the two hemispheres are evident; while decreasing wind speeds weighted towards NH latitudes produce a noticeable increase in $x\text{CO}_2$ (3.6 ppmv over 19→0 ka BP), SH latitudes appear to have little influence (< 0.9 ppmv over 19→0 ka BP). In contrast, it is only SH wind speeds that exert any significant

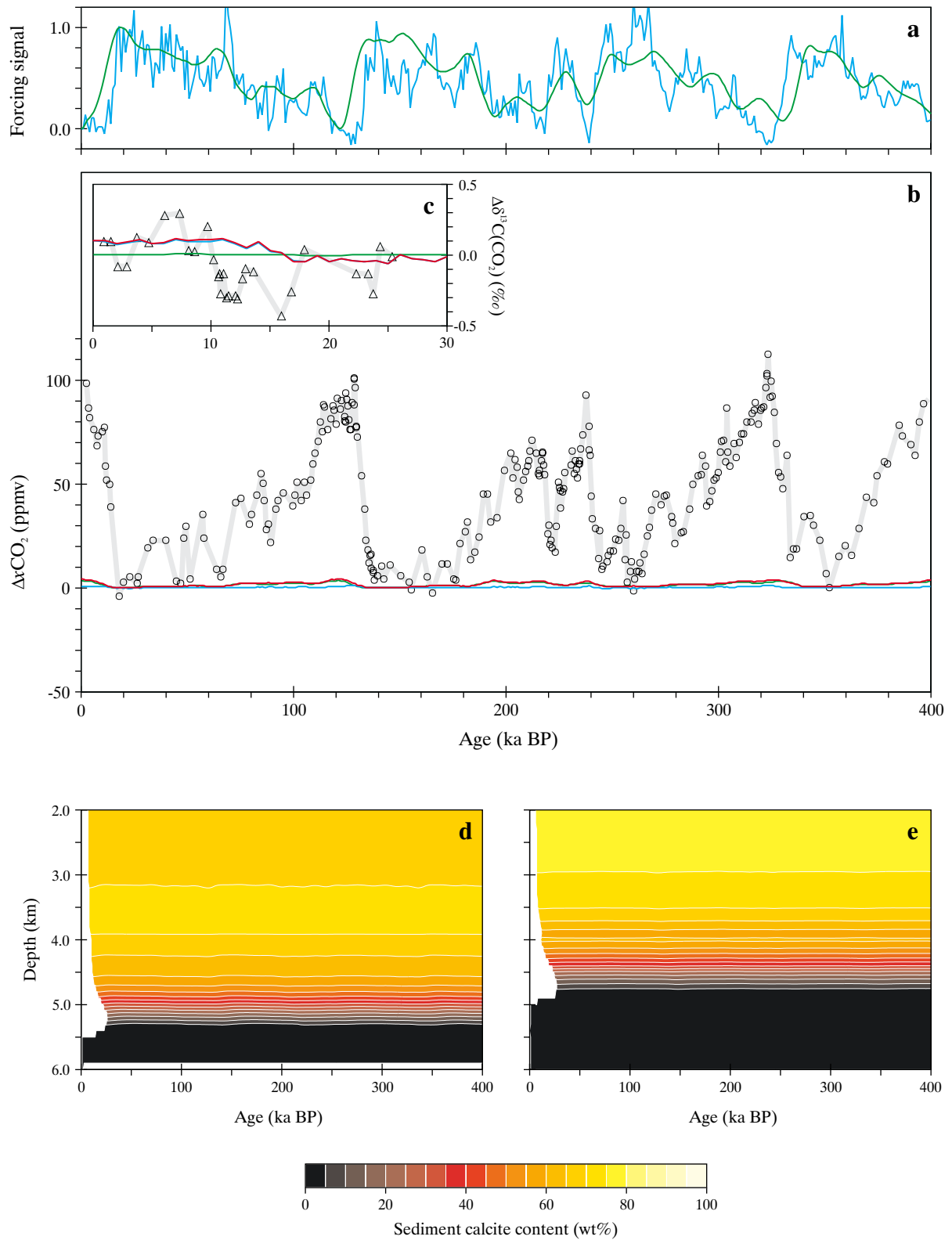


Figure 5-5 Effects on the global carbon cycle of glacial-interglacial variability in surface ocean wind speed. Shown are; (a) the NH-weighted (green) and SH-weighted (blue) forcing signals; (b) model NH-weighted (green), SH-weighted (blue) and net (red) $\Delta x\text{CO}_2$ response compared to the Vostok ice core record [Petit *et al.*, 1999] (grey line with data points); (c) model NH-weighted (green), SH-weighted (blue) and net (red) $\delta^{13}\text{C}^{\text{CO}_2}$ response compared to the Taylor Dome ice core record [Smith *et al.*, 1999] (grey line with data points); (d) and (e) the net response of the calcite lysocline in the (south) Atlantic and (south) Pacific basins, respectively.

control on $\delta^{13}\text{C}^{\text{CO}_2}$ – a deglacial increase of some $\sim 0.15\%$. Global reduction in wind speed consequently produces a net rise in $x\text{CO}_2$ and $\delta^{13}\text{C}^{\text{CO}_2}$ of 4.4 ppmv and 0.16% , respectively. Since only the rates of gas transfer across the air-sea interface are being modified through this test it comes as little surprise that there is virtually no detectable response in the shape and depth of the calcite lysocline (Figure 5-5d,e).

This subdued response in $x\text{CO}_2$ is at odds with previous box model results [Keir, 1993b]. One contributing factor is that a glacial enhancement in wind speed of only 50% is assumed (at the lower end of estimates derived from Antarctic ice cores [Petit *et al.*, 1981]), substantially less than the 80-150% increase considered by Keir [1993]. However, the greatest difference is probably due to the global change applied in this present study where concurrent changes in gas transfer rates in warm low latitude regions will tend to offset the influence on $x\text{CO}_2$ of changes occurring at higher colder latitudes, although both will constructively combine in terms of the net $\delta^{13}\text{C}^{\text{CO}_2}$ response. Keir [1993b] restricted changes to a single high latitude box in a class of model ocean representation strongly suspected of significantly over-estimating the effect of high latitude perturbations [Archer *et al.*, in press; Broecker *et al.*, 1999a]. The results obtained with SUE1608, with relatively little response in the atmospheric CO_2 inventory but much greater change in isotopic composition are consistent with those obtained with 3D OGCMs [Sarmiento *et al.*, 1992].

5.4.4 Sea ice extent

Reconstructions of the cryosphere at the time of the LGM suggest that seasonal sea ice cover was much more extensive than today, particularly during the summer months [CLIMAP, 1984]. A recent modelling study found that glacial-interglacial variability in Southern Ocean sea ice coverage had a profound effect on both the concentration of CO_2 in the atmosphere and on its isotopic composition [Stephens and Keeling, 2000]. To test this hypothesis, maximum (wintertime) and minimum (summertime) sea ice extent are varied, with the fractional coverage in each grid point region of the model taken from CLIMAP [1984]. Different forcing signals are used to represent the differential climatic variability characterizing the two hemispheres; northern latitudes are weighted using the SPECMAP curve [Imbrie *et al.*, 1984] while Southern latitudes take information regarding the timing and rate of change of events from the Vostok δD record [Petit *et al.*, 1999] (assuming a first-order correspondence between sea ice cover and local air temperature).

The results of this exercise are summarized in Figure 5-6. While the response of $x\text{CO}_2$ to changes in sea ice cover weighted towards either hemisphere are of a similar magnitude, the signs of glacial-interglacial change are opposite. At high northern latitudes, increased sea ice cover acts so as to effectively 'cap' what is a strong CO_2 sink region, with its deglacial retreat driving $x\text{CO}_2$ down by 11.9 ppmv over 19→0 ka BP. This can be taken as a maximum likely response, since circulation patterns in the north Atlantic

would have shifted further south during glacial periods in parallel with expanded sea ice cover. In the Southern Ocean, mean model annual surface ocean CO_2 fugacity is much more neutral with respect to atmospheric composition during interglacials such that capping this region has little direct effect. However, the overall response of the system to changes in Southern Ocean sea ice cover is more complicated than this. Increased sea ice cover suppresses biological productivity, resulting in an increased northwards advective transport of nutrients. These fuel increased export production and thus additional surface ocean CO_2 draw-down at lower latitudes, with the net effect of a deglacial reduction in sea ice cover being a 7.5 ppmv increase in $x\text{CO}_2$ over 19→0 ka. In contrast, Stephens and Keeling [2000] reported an increase of over 45 ppmv associated with a reduction of sea ice coverage of surface ocean boxes lying south of the Antarctic Polar Front (APF) in their model. Much of this inter-model contrast is probably due to the more highly idealized nature of their box model, where only 5 surface zones are resolved. A direct consequence of the lack of any representation of distinct equatorial up-welling zones (regions of intense CO_2 out-gassing in the modern ocean [Tans *et al.*, 1990]) is that only the Southern Ocean is a significant source of CO_2 to the (modern) atmosphere. The strong response of $x\text{CO}_2$ to changes in Southern Ocean sea ice cover found by Stephens and Keeling [2000] could, therefore, largely be an artefact of an initially unrealistic distribution of surface ocean $f\text{CO}_2$. Indeed, with a reduction of ice-free area by a factor of 3 in the Southern Ocean of their 'PANDORA' multi-box model, Broecker and Peng [1986] reported a reduction in $x\text{CO}_2$ of only 2 ppmv. In SUE1608, the antagonistic influences of the two hemispheres produces a relatively small net response, with a 19→0 ka BP decrease in $x\text{CO}_2$ of just 4.9 ppmv.

As with CO_2 concentrations, the response of isotopic composition is also highly hemisphere-dependent with the NH playing little role in controlling $\delta^{13}\text{C}^{\text{CO}_2}$ (a 19→0 ka BP decrease of only 0.07%). The degree of exposure of the atmosphere to the Southern Ocean has a much greater effect (primarily due to its larger surface area) with a 19→0 ka BP decrease of 0.30% , virtually identical to that reported by Broecker and Peng [1986]. The net effect of global deglacial sea ice retreat is then 0.41% . The magnitude of this change is comparable to the substantial transient excursion observed in $\delta^{13}\text{C}^{\text{CO}_2}$ at the onset of Termination I [Smith *et al.*, 1999], supporting suggestions that it is sea ice retreat that is primarily responsible for this feature [Stephens and Keeling, 2000].

The re-organization of ocean nutrient cycles driven by changes in sea ice cover results in deepening in the calcite lysoclines of ~ 400 and ~ 300 m in the Atlantic and Pacific basins, respectively (Figure 5-6d,e). Re-organization is most significant in the ocean Si cycle, with rain ratios and thus CaCO_3 dissolution distorted. Greatest CaCO_3 preservation occurs during interglacial periods when the oceanic H_4SiO_4 inventory is depleted.

Recent Southern Ocean reconstructions based upon the Modern Analogue Technique and applied to core-top and LGM diatom assemblages suggest that although the position

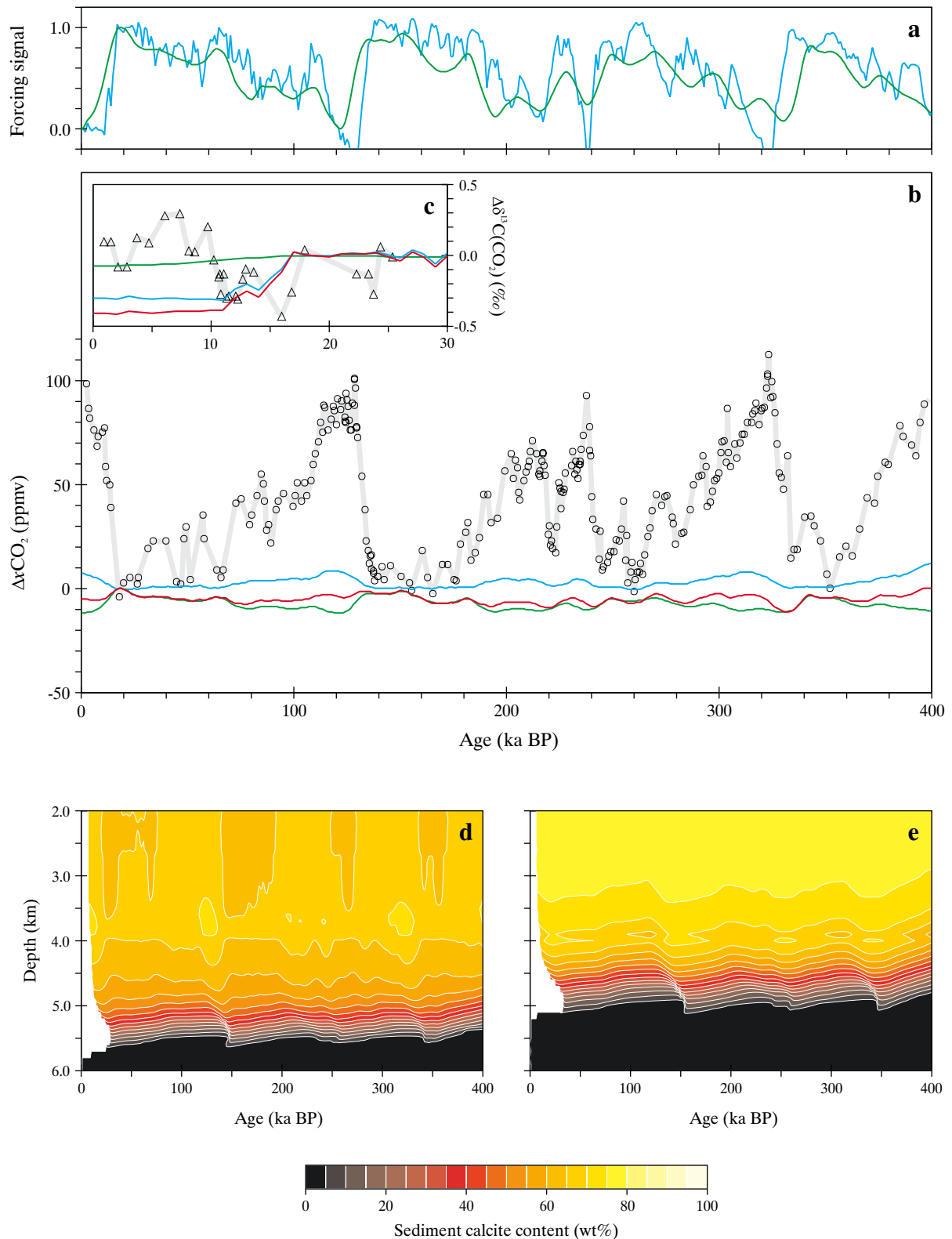


Figure 5-6 Effects on the global carbon cycle of glacial-interglacial variability in fractional sea ice cover. Shown are; (a) the NH-weighted (green) and SH-weighted (blue) forcing signals; (b) model NH-weighted (green), SH-weighted (blue) and net (red) $x\text{CO}_2$ response compared to the Vostok ice core record [Petit *et al.*, 1999] (grey line with data points); (c) model NH-weighted (green), SH-weighted (blue) and net (red) $\delta^{13}\text{C}^{\text{CO}_2}$ response compared to the Taylor Dome ice core record [Smith *et al.*, 1999] (grey line with data points); (d) and (e) the net response of the calcite lysocline in the (south) Atlantic and (south) Pacific basins, respectively.

of maximum (winter-time) sea ice extent was shifted much further to the north during glacial times [Crosta *et al.*, 1998a,b] in reasonable agreement with CLIMAP [1984], the position of minimum (summer-time) sea ice extent may have been little changed [Crosta *et al.*, 1998b]. The rather crude representation of sea ice extent in SUE, where a fractional coverage is applied to a zonally homogeneous ocean region, makes quantitative assessment of alternative LGM sea ice regimes difficult. Even so, summer sea ice extent appears to have a substantial effect on model $\delta^{13}\text{C}^{\text{CO}_2}$, with the assumption of constant summer sea ice extent reducing the amplitude of glacial-interglacial isotopic variability by over 50%. This sensitivity suggests that ice core records of $\delta^{13}\text{C}^{\text{CO}_2}$ could potentially help in providing additional constraints on reconstructions of past sea ice extent.

5.4.5 Ocean circulation

Changes in ocean circulation have often been invoked as a key driving force behind glacial-interglacial variations in atmospheric composition. In particular, changes in the supply of nutrients together with DIC and ALK to the surface Southern Ocean, both through variability in convective regime and advective up-welling have been suspected to produce profound changes in $x\text{CO}_2$ through the solubility and biological pumps in this region [Knox and McElroy, 1984; Martin, 1990; Sarmiento and Toggweiler, 1984]. In particular, increased surface stratification has been proposed as the single most important driver of low glacial $x\text{CO}_2$ [Francois *et al.*, 1997; Sigman *et al.*, 1999a,b]. Variations in the solubility and biological pumps arising through changes in the strength and depth of the Atlantic thermohaline circulation and through wind-driven enhancement of equatorial up-welling rates could also have played important roles [Howard and Prell, 1994; Oeschger *et al.*, 1984; Rich *et al.*, 1999; Siegenthaler and Wenk, 1984; Toggweiler, 1999].

There are few unambiguous constraints on glacial ocean circulation, particularly with respect to the details of convective and advective regimes in the Southern Ocean. This present study is also limited in scope by the requirement of a prescribed advective field. While the baseline ocean configuration of SUE1608 is derived from a modern-type ocean simulation of the Bern 2D ZOGCM [Marchal *et al.*, 1998b], there is currently no equivalent simulation available for the LGM. However, a glacial-type Atlantic circulation field is available, produced in an identical way to that for modern conditions with the exception that surface salinity in the northernmost Atlantic grid box (65°N-80°N) was restored to 34.2‰ [Marchal, pers comm]. This leads to a maximum stream function in the Atlantic, approximately half that obtained in the modern simulation and with shallower NADW, allowing increased penetration of AABW into the north Atlantic in accordance with observations [Marchal *et al.*, 1998a; Peltier and Marshall, 1995].

As a simple test of the influence of variability in Atlantic overturning circulation, the model is forced by a hybrid of modern and glacial circulations. A continuous 400 ka record is constructed assuming that the advective field at any point in time can be described as a linear combination of the two

end-member advective fields, weighted via the SPECMAP curve [Imbrie *et al.*, 1984].

The results of this exercise are summarized in Figure 5-7. There is a small 19→0 ka BP deglacial increase in $x\text{CO}_2$ of 6.3 ppmv accompanied by almost no change in $\delta^{13}\text{C}^{\text{CO}_2}$ (<0.03‰). However, altering the Atlantic thermohaline circulation produces a more substantial influence on the calcite lysocline transition zone. In the Atlantic basin, increased northwards penetration of AABW (characterized by lower carbonate ion concentrations thus being more caustic to CaCO_3) during glacial periods clearly leads to decreased CaCO_3 preservation as compared with during interglacials [Broecker *et al.*, 1993], resulting in a 600-700 m shoaling of the calcite lysocline. Ocean chemistry is balanced on a global scale through antagonistic changes occurring in the Pacific, where glacial preservation is slightly enhanced with a lysocline some ~200 m deeper. The respective sign of glacial-interglacial change in both basins is in agreement with paleoceanographic observations [Balsam, 1983; Catubig *et al.*, 1998; Farrell and Prell, 1989; Howard and Prell, 1994; Karlin *et al.*, 1992].

5.4.6 Terrestrial carbon storage

Shackleton [1977] first proposed that glacial-interglacial changes in foraminiferal $\delta^{13}\text{C}$ might indicate that transfers of carbon had occurred between the ocean (and atmosphere) and terrestrial biosphere. From measurements made on deep-sea sediment cores which suggested ambient glacial $\delta^{13}\text{C}$ conditions around 0.7‰ lighter than during the Holocene, Shackleton [1977] estimated that some 10^{18} g of carbon (1000 GtC) must have been removed from the ocean since the LGM. This was consistent with what was suspected at that time regarding a deglacial increase in carbon stored in terrestrial ecosystems through the expansion of tropical rainforests and afforestation of high northern latitudes. Should a significant quantity of carbon have been removed from the ocean and atmosphere upon deglaciation, this would effectively increase the gross deglacial CO_2 rise that other mechanisms must together explain [Berger and Wefer, 1991; Maslin, 1995]. The magnitude of the change in carbon storage is therefore of primary importance in accounting for glacial-interglacial change.

From an extensive survey of deep-sea sediment cores, Curry *et al.* [1988] concluded that an increase in mean ocean $\delta^{13}\text{C}^{\text{DIC}}$ of 0.46‰ had taken place during the last deglacial transition (19→0 ka BP), although this was subsequently reduced to 0.32‰ [Duplessy *et al.*, 1988]. Further re-analysis of benthic $\delta^{13}\text{C}$ data now suggests a mean oceanic $\delta^{13}\text{C}$ increase intermediate between the two, perhaps ~0.40‰ [Crowley, 1995]. To translate this into an equivalent shift in terrestrial biospheric carbon requires an estimate to be made of the mean isotopic composition of terrestrial organic carbon. This lies in the range -22 to -25‰ for the pre-industrial biosphere [Bird *et al.*, 1994]. However, the mean isotopic composition of land biota cannot be guaranteed to have remained invariant over the course of the late Quaternary, with a shift in the dominance of C_4 over C_3 species suspected to have occurred since the LGM [Crowley,

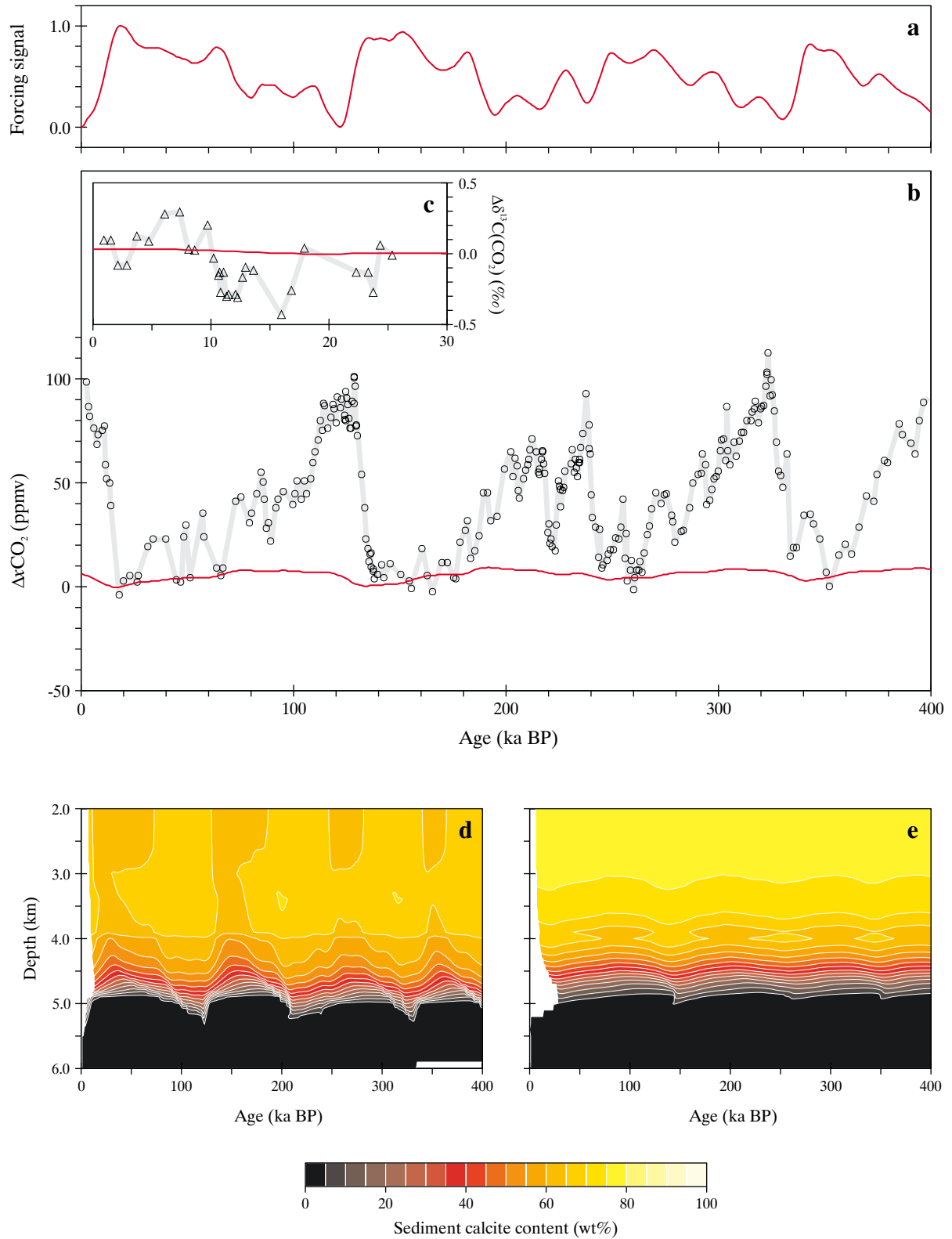


Figure 5-7 Effects on the global carbon cycle of glacial-interglacial variability in Atlantic overturning circulation. Shown are; (a) the forcing signal (normalized to a value of unity at the LGM); (b) model $x\text{CO}_2$ response (red line) compared to the Vostok ice core record [Petit *et al.*, 1999] (grey line with data points); (c) model $\delta^{13}\text{C}^{\text{CO}_2}$ response (red line) compared to the Taylor Dome ice core record [Smith *et al.*, 1999] (grey line with data points); (d) and (e) the response of the calcite lysocline in the (south) Atlantic and (south) Pacific basins, respectively.

1991, 1995; Maslin *et al.*, 1995]. Further complications arise as a result of recent culture studies, which have found a dependence on ambient carbonate ion concentrations ($[\text{CO}_3^{2-}]$) of the degree of calcitic ^{13}C fractionation in several planktonic foraminiferal species [Spero *et al.*, 1997]. If benthic species were to behave in a comparable manner then changes in deep sea $[\text{CO}_3^{2-}]$ might act to either amplify or diminish apparent variations in $\delta^{13}\text{C}^{\text{DIC}}$ recorded by foraminiferal tests [Russell and Spero, 2000]. Changes in foraminiferal $\delta^{13}\text{C}$ would therefore need to be interpreted in light of glacial-interglacial perturbations in oceanic DIC and ALK inventories, both of which are poorly constrained.

There are independent methods available for quantifying the deglacial change in carbon stored in the terrestrial biosphere, primarily through the reconstruction of terrestrial ecosystems (and their associated soils) both for LGM and modern (pre-industrial) conditions. This can be done either directly from terrestrial proxy evidence [Adams *et al.*, 1990; Adams and Faure, 1998; Crowley, 1995; Faure *et al.*, 1996; Maslin *et al.*, 1995] or by means of climate-vegetation models [Esser and Lautenschlager, 1994; Francois *et al.*, 1998, 1999; Friedlingstein *et al.*, 1992; Peng *et al.*, 1998; Prentice and Fung, 1990; Van Campo *et al.*, 1993]. Estimates made by these two methods often do not entirely agree, however, either amongst themselves or when compared with estimates based on oceanic $\delta^{13}\text{C}^{\text{DIC}}$ changes [Bird *et al.*, 1994; Crowley, 1991, 1995; Maslin *et al.*, 1995] as summarized in Table 5-3. That reconstructions suggest increases ranging from -100 GtC to 1900 GtC puts a high degree of uncertainty on the

importance to observed glacial-interglacial variability in atmospheric composition of the transfer of carbon between the terrestrial biosphere and ocean and atmosphere.

The perturbing effect that changes in terrestrial vegetation might have had on the global carbon cycle is now investigated by varying the magnitude of the terrestrial carbon reservoir. As an initial test, 500 GtC is assumed to have been removed from the atmosphere following the LGM; a value chosen to be consistent with the mid-point of the range of estimates made from observed foraminiferal $\delta^{13}\text{C}$ change and climate-vegetation models. The SPECMAP $\delta^{18}\text{O}$ stack [Imbrie *et al.*, 1984] is taken as a first-order proxy for glacial-interglacial variability in the terrestrial reservoir.

The results of this exercise are summarized in Figure 5-8. It can be seen that the effect of an expansion of the terrestrial biosphere is to reduce $x\text{CO}_2$ by a total of 24.7 ppmv for the interval 19→0 ka BP, contrary to the sign of the observed change. The magnitude of this decrease is greater than suggested by other models that predict change in the range 12 to 17 ppmv [Archer *et al.*, 2000; Broecker and Peng, 1986]. However, these all assume that a steady state with respect to deep-sea CaCO_3 has been reached (i.e., through 'carbonate compensation'). This process occurs with an e -folding time of ~9 ka such that if the main transfer of carbon were to be centred around ~10 ka BP then the reduction in oceanic DIC inventory will be far from having been fully compensated for. Indeed, Archer *et al.* [2000] reported that the uncompensated change in $x\text{CO}_2$ in response to a 500 GtC perturbation is almost 40 ppmv. Thus not only is the absolute magnitude of the change in terrestrial carbon storage of fundamental importance to the response of the system but so too is the rate of this change. Associated with the deglacial reduction in $x\text{CO}_2$ is a gradual increase in $\delta^{13}\text{C}^{\text{CO}_2}$ of ~0.31‰.

The response of the calcite lysocline in both the Atlantic and Pacific basins is very similar, with weak preservational spikes characterized by a 200-300 m deepening, synchronous with the deglacial transitions. These transients of enhanced preservation are slightly greater in depth for the aragonite lysocline (not shown) than for calcite, and are consistent with observations of CaCO_3 preservation between the end of the LGM and early Holocene [Berger, 1977; Broecker *et al.*, 1993, 1999b].

5.4.7 Neritic sediment storage

A number of hypotheses to explain glacial-interglacial variations in atmospheric CO_2 concentrations have been based upon the extraction from the ocean (during interglacial periods of high sea level) and temporary storage in continental shelf sediments of materials whose presence would otherwise tend to exert a negative pressure on $x\text{CO}_2$. The earliest of such schemes was the 'Phosphate Extraction Model', in which the removal of organic phosphate from the ocean resulted in the limiting of ocean productivity and thus higher $x\text{CO}_2$. During glacial times, PO_4 returned to the ocean through shelf sediment erosion fuels ocean productivity, leading to lower $x\text{CO}_2$ [Broecker, 1982; Broecker and Peng, 1982]. However, as a sole explanation for the magnitude of

Table 5-3 Estimates of the Increase in Carbon Stored in Terrestrial Ecosystems Since the LGM (ΔC)

ΔC (GtC)	Reference
foraminiferal $\delta^{13}\text{C}$ changes	
700	Curry <i>et al.</i> [1988]
490	Duplessy <i>et al.</i> [1988]
1070	Shackleton [1977]
610	Crowley [1995]
paleovegetation reconstructions	
1351	Adams <i>et al.</i> [1990], Faure <i>et al.</i> [1996]
900 to 1900	Adams and Faure [1998]
1100	Maslin <i>et al.</i> [1995]
760 to 1040	Crowley [1995]
coupled climate-vegetation models	
134 ¹ to 606	Francois <i>et al.</i> [1998]
-460 ¹ to 213	Esser and Lautenschlager [1994]
-70 to 710	Francois <i>et al.</i> [1999]
-30	Prentice and Fung [1990]
300	Friedlingstein <i>et al.</i> [1992]

¹ Assuming no CO_2 fertilization effect on net primary productivity

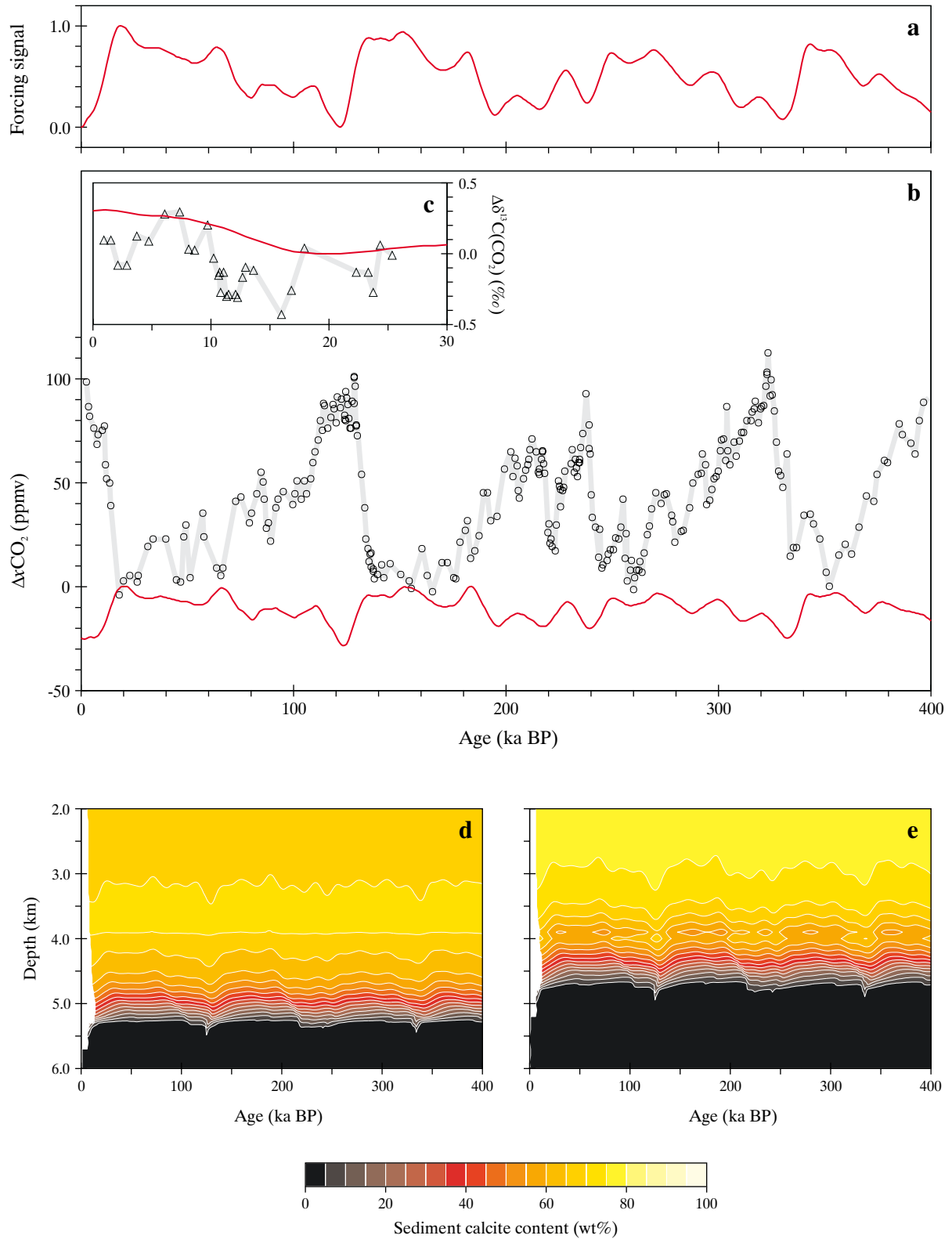


Figure 5-8 Effects on the global carbon cycle of glacial-interglacial variability in terrestrial carbon storage. Shown are; (a) the forcing signal (normalized to a value of unity at the LGM); (b) model $\Delta x\text{CO}_2$ response (red line) compared to the Vostok ice core record [Petit et al., 1999] (grey line with data points); (c) model $\delta^{13}\text{C}^{\text{CO}_2}$ response (red line) compared to the Taylor Dome ice core record [Smith et al., 1999] (grey line with data points); (d) and (e) the response of the calcite lysocline in the (south) Atlantic and (south) Pacific basins, respectively.

glacial-interglacial change it fell foul of considerations such as observed changes in oceanic $\delta^{13}\text{C}$ [Keir and Berger, 1983; Knox and McElroy, 1984], Cd/Ca ratios [Boyle, 1988; Shaffer, 1990], dissolved oxygen concentrations [Knox and McElroy, 1984], and the tendency for $x\text{CO}_2$ rise to lag sea level change contrary to the observed sequence of events surrounding glacial terminations [Barnola *et al.*, 1987; Sowers *et al.*, 1991].

5.4.7.1 The 'Coral Reef Hypothesis'

A variant on the phosphate extraction model that avoids many of the above-mentioned proxy violations considers the deposition of CaCO_3 in shelf sediments. This envisages that glacial-interglacial changes in the rate of accumulation of CaCO_3 in the neritic environment driven by sea level change would perturb global ocean chemistry and thus atmospheric composition [Berger, 1982a,b; Keir and Berger, 1983, 1985; Opdyke and Walker, 1992]. This is known as the 'Coral Reef Hypothesis' [Berger, 1982a], although accumulation of CaCO_3 can take place as both reefal (coral-derived) and non-reefal (unconsolidated sediments) components. Simple logic supports the notion that there must have been a significant degree of variability in CaCO_3 accumulation rates over the late Quaternary; reduced submerged continental shelf area during glacial periods would result in a lower global rate of CaCO_3 accumulation compared to interglacials. Indeed, erosion of carbonate-rich sediments from exposed shelves may even have produced a net transfer of CaCO_3 back during times of low sea level stand. Although deep-sea sediments will eventually counteract any perturbation in the magnitude of shelf accumulation rates via transient changes in the depth of the lysocline, this only occurs with an e -folding time of the order of 10 ka. Changes in sea level (and thus neritic accumulation rates) will therefore produce a degree of disequilibrium between benthic sediments and ocean chemistry. It is this disequilibrium that allows the oceanic inventories of DIC and ALK to be perturbed, affecting $x\text{CO}_2$ [Berger, 1982b]. As with the phosphate extraction model, such atmospheric changes will, at best, lag sea level change, invalidating the coral reef hypothesis as a sole explanation for the observed deglacial $x\text{CO}_2$ rise [Broecker and Henderson, 1998]. However, it might play an important role in the later part of the deglacial transition, for instance in counteracting the downward forcing pressure upon $x\text{CO}_2$ due to the buildup of carbon in the terrestrial biosphere (5.4.6) [Berger, 1982b; Broecker and Peng, 1993; Maslin *et al.*, 1995].

Accurate estimation of the magnitude of glacial-interglacial change in neritic CaCO_3 accumulation is far from straightforward. Areal accumulation rates have previously been derived from estimates made of neritic CaCO_3 build-up over the course of the late Holocene [Mundhoven and Francois, 1996; Walker and Opdyke, 1995], taken to be 7×10^{12} and 7.5×10^{12} mol $\text{CaCO}_3 \text{ a}^{-1}$, for reefal and non-reefal components, respectively [Milliman, 1993]. For reefal accumulation this figure is independently corroborated by process-based global models of coral reef growth [Kleypas, 1997]. Erosion rates are especially hard to quantify, with values previously either adapted from observed terrestrial weathering rates [Mundhoven and Francois, 1996] or simply

treated as a model tuning parameter [Opdyke and Walker, 1992]. As an initial test of the potential role of this mechanism, the parameterization of Mundhoven and Francois [1996] is adopted. Sea level history is the same as assumed previously (5.4.1).

The results of this exercise are summarized in Figure 5-9. It can be seen that the coral reef hypothesis as formulated by Mundhoven and Francois [1996] has a very substantial influence on $x\text{CO}_2$, with a total 19→0 ka BP increase of 45.9 ppmv. This is despite the concurrent effect of sea level change alone (i.e., excluding SSS changes) being some 7.7 ppmv in the opposite direction. Changes in the oceanic inventory of DIC and ALK in the ocean therefore drive a total deglacial increase of 53.6 ppmv, almost two thirds of the observed increase [Petit *et al.*, 1999] and consistent with comparable models [Mundhoven and Francois, 1994, 1996; Opdyke and Walker, 1992; Walker and Opdyke, 1996]. There is virtually no associated change in atmospheric $\delta^{13}\text{C}^{\text{CO}_2}$ (<0.02‰).

Although this appears to offer a simple means of explaining much of the observed amplitude of glacial-interglacial change in $x\text{CO}_2$ there appears to be a serious problem with the magnitude of the perturbation in deep-sea sediments which it drives (Figure 5-9d,e). Both basins exhibit glacial deepening in the depth of the calcite lysocline of between 1 and 2 km. Changes of this order in the Pacific are not supported by available data [Berger, 1978, 1982b; Farrell and Prell, 1989, 1991; Karin *et al.*, 1992]. Furthermore, observed Atlantic changes are opposite in sign to that predicted by the model [Balsam, 1983; Berger, 1968; Crowley, 1983; Gardner, 1975]. It is unlikely that additional mechanisms might act so as to correct excess CaCO_3 preservation of this degree. Either the magnitude of changes in neritic CaCO_3 storage must have then been over-estimated, or deficiencies in the model CaCO_3 cycle artificially magnify the response of the system. In the latter case, the apparent under-estimation of CaCO_3 content in the equatorial zones of the ocean as well as in several mid-latitude regions (4.4.3) might reduce the overall buffering capacity of the deep-sea sediment system with respect to changes in neritic CaCO_3 accumulation rates. Variability in CaCO_3 preservation in other regions of the world ocean (coincidentally the locations the synthetic sediments cores used for reconstructing the two lysocline sections) would thus be intensified.

A more plausible response of the CaCO_3 lysocline can be obtained by reducing the rate of neritic build-up and erosion (both reefal and non-reefal components) by 50%. This results in a maximum glacial-interglacial difference in deposition rates of $\sim 7 \times 10^{12}$ mol $\text{CaCO}_3 \text{ a}^{-1}$. To re-balance ocean DIC and ALK inventories over the long term, the influence of CaCO_3 dissolution through the oxidation of organic carbon within the sediments (3.2.4) is reduced by 50%, thereby increasing deep-sea CaCO_3 preservation and making up the neritic shortfall. This has the desirable side-effect of generally improving the global distribution of CaCO_3 -rich sediments in the model (not shown), with sedimentary CaCO_3 distributions much closer to

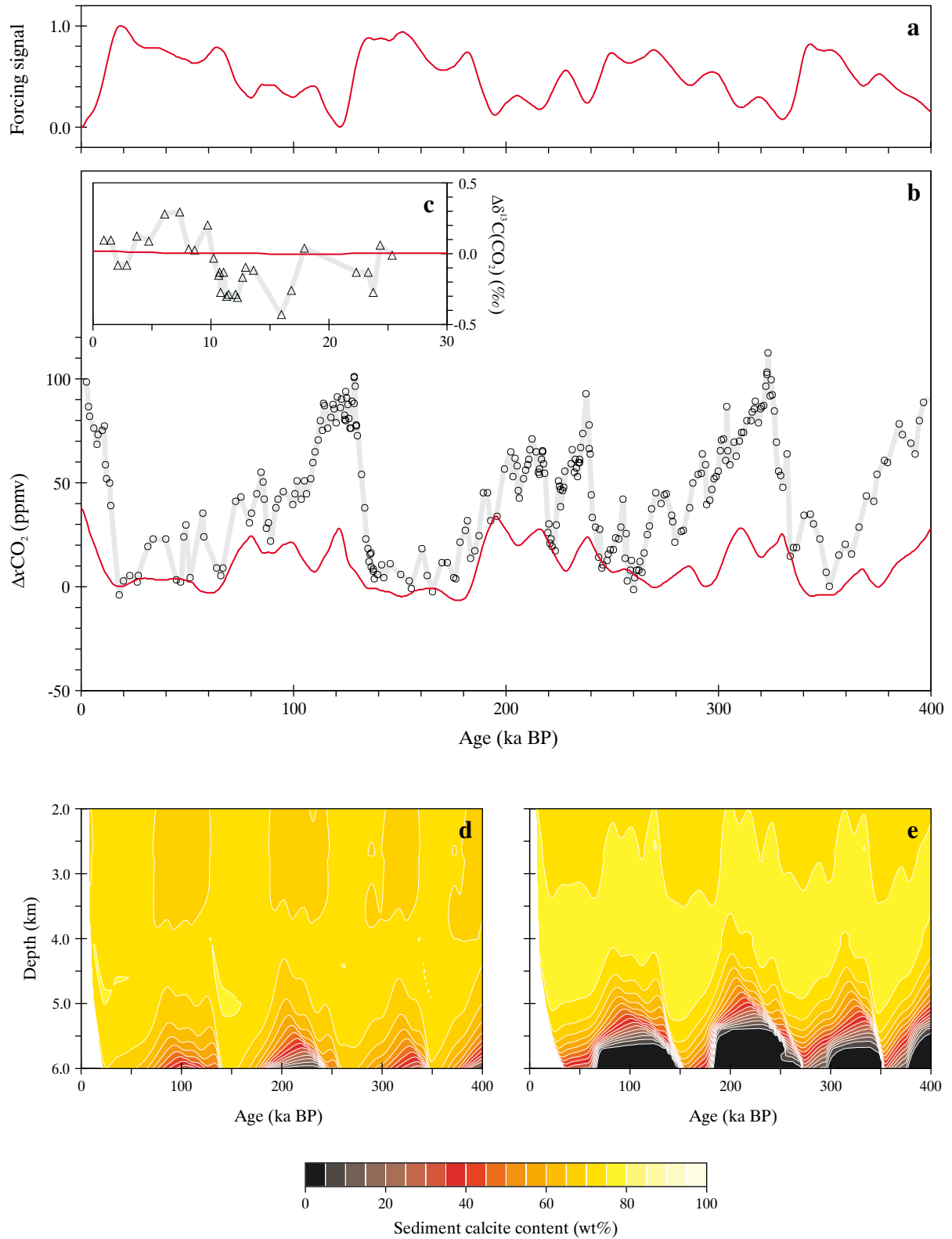


Figure 5-9 Effects on the global carbon cycle of glacial-interglacial variability in neritic CaCO₃ storage. Shown are; (a) the forcing signal (normalized to a value of unity at the LGM); (b) model $\Delta x\text{CO}_2$ response (red line) compared to the Vostok ice core record [Petit *et al.*, 1999] (grey line with data points); (c) model $\delta^{13}\text{C}^{\text{CO}_2}$ response (red line) compared to the Taylor Dome ice core record [Smith *et al.*, 1999] (grey line with data points); (d) and (e) the response of the calcite lysocline in the (south) Atlantic and (south) Pacific basins, respectively.

observations in the equatorial Atlantic and Pacific zones and in the Indian Ocean.

The peak-to-peak amplitude in $x\text{CO}_2$ variability is now almost exactly 50% of that obtained before, with a rise of 22.5 ppmv over the interval 19→0 ka BP. Importantly, changes in lysocline depth are much more modest. While Atlantic change is still in a direction opposite to that observed, it is no longer overwhelmingly so (~900 m). A glacial-interglacial amplitude of 400-600 m in the Pacific is consistent with observations.

5.4.7.2 Introducing the 'Opal Extraction Model'

An analogue to the phosphate extraction model can be found in the limiting nutrient silicic acid, with variable accumulation rates of biogenic opal deposited on continental shelves in response to changes in sea level likely. Indeed, the potential significance of this mechanism to the global carbon cycle is highlighted by estimates made of the present-day ocean sink of H_4SiO_4 in neritic sediments equivalent to ~20% of the entire abyssal ocean sink ($5.9 \text{ Tmol Si a}^{-1}$) [Treguer *et al.*, 1995]. While the effect of glacial-interglacial variability in H_4SiO_4 may not significantly alter the absolute strength of the biological pump, the favouring of siliceous phytoplankton over non-siliceous species will alter the CaCO_3 :POC rain ratio, driving changes in ocean chemistry and thus $x\text{CO}_2$ [Archer and Maier-Reimer, 1994; Harrison, 2000].

To test this hypothesis, a simple model is constructed based directly upon the neritic (non-reefal component) CaCO_3 sediment accumulation model of Mundhoven and Francois [1996]. Specific opal accumulation rates are chosen to reproduce estimated mean global neritic buildup during the late Holocene ($1.2 \text{ Tmol Si a}^{-1}$) [Treguer *et al.*, 1995]. Since little is known regarding possible rates of erosion of previously-deposited material, no erosional term is included. A variable oceanic sink for H_4SiO_4 of between 0.36 and $1.21 \text{ Tmol Si a}^{-1}$ thus arises as a function of sea level.

The action of this mechanism is to produce a small deglacial (19→0 ka BP) decrease in $x\text{CO}_2$ of 5.4 ppmv with virtually no associated effect on $\delta^{13}\text{C}^{\text{CO}_2}$. These results, together with the interglacial shoaling of the calcite lysocline (some ~300 m in the Atlantic basin), are practically indistinguishable from the effects of sea level change alone, suggesting that this mechanism has little influence on the global carbon cycle (at least in isolation).

5.4.8 Dissolved silica supply to the ocean

Interest has recently been stimulated in the role that changes in the dissolved Si input to the ocean may have had on glacial-interglacial $x\text{CO}_2$ variability. This has arisen out of the potential for the ocean Si cycle, with a residence time for dissolved Si of ~15 ka, to account for the lag of up to 8 ka that occurs between the start of dust decline towards the end of Stages 2 and 6, and the initial CO_2 rise that follows in each core [Broecker and Henderson, 1998]. On this basis, Harrison [2000] proposed a 'Silica Hypothesis', whereby increased glacial aeolian Si supply to the surface ocean enhances diatom productivity at the expense of calcium carbonate

shell-forming species, thus affecting $x\text{CO}_2$ via the 'rain ratio hypothesis' [Archer and Maier-Reimer, 1994]. Harrison [2000] went further to suggest the entire glacial-interglacial $x\text{CO}_2$ difference might be explained in this way. Increases in dissolved Si supply to the oceans driven by changes in the weathering rate of continental (silicate) rock might further enhance this effect [Treguer and Pondaven, 2000]. The potential role of these mechanisms in perturbing the global carbon cycle are now individually assessed.

5.4.8.1 Aeolian flux

To test the hypothesis that glacial-interglacial changes in dissolved Si supply derived from aeolian silicates exert a strong control over atmospheric CO_2 levels, dust deposition to the surface ocean is varied. Modern dust deposition to the model ocean surface is some $6.85 \times 10^{14} \text{ g a}^{-1}$ [Mahowald *et al.*, 1999]. Assuming that SiO_2 comprises 66 wt% of dust (mean upper continental crustal abundance [Taylor and McLennan, 1985]) gives a solid input of some $4.52 \times 10^{14} \text{ g SiO}_2 \text{ a}^{-1}$, equivalent to $7.54 \text{ Tmol Si a}^{-1}$. To achieve a value for total aeolian dissolved Si input $0.5 \text{ Tmol Si a}^{-1}$ consistent with Treguer *et al.* [1995] therefore requires a solubility of ~6.6%, in line with experimental estimates [Wollast and Chou, 1985]. Dissolved (riverine) Si supply is reduced by an equivalent amount in the model in order to balance the (modern) ocean budget. For the LGM, the equivalent global dust deposition flux is $2.29 \times 10^{14} \text{ g a}^{-1}$ [Mahowald *et al.*, 1999] giving a peak glacial aeolian dissolved Si flux of $1.67 \text{ Tmol Si a}^{-1}$, more than 3 times greater than at present. The temporal variability in the Vostok dust concentration record [Petit *et al.*, 1999] is used as a proxy for relative changes in global dust deposition fluxes in order to reconstruct a record for the last 400 ka. Aeolian iron supply is held constant for the purpose of this experiment.

The results of this exercise are summarized in Figure 5-10. It can be seen that there is a rather minimal response in $x\text{CO}_2$ to this forcing with a glacial-interglacial amplitude of less than 2.2 ppmv and virtually no detectable change in $\delta^{13}\text{C}^{\text{CO}_2}$. Similarly, sedimentary CaCO_3 contents in both Atlantic and Pacific basins are little affected. Sensitivity analyses suggest that even by assuming a solubility for aeolian SiO_2 as high as 14.2% (sufficient to produce a 50% increase in total dissolved Si supply at the LGM over present-day rates) the 19→0 ka BP deglacial increase in $x\text{CO}_2$ is proportionally increased only to ~6 ppmv.

5.4.8.2 Riverine fluxes

To test the secondary hypothesis, that glacial-interglacial changes in riverine dissolved Si supply might have produced a significant effect on $x\text{CO}_2$, the riverine input to the ocean is varied. Glacial rates of supply were set some $1.0 \text{ Tmol Si a}^{-1}$ higher than at present, comparable in peak amplitude to the aeolian experiment (5.4.8.1). However, the SPECMAP $\delta^{18}\text{O}$ stack [Imbrie *et al.*, 1984] is now used as a proxy for relative changes in weathering-derived fluxes in order to reconstruct a forcing record for the last 400 ka.

As with aeolian Si supply, the response of atmospheric composition to the forcing is small, with a 19→0 ka BP increase in $x\text{CO}_2$ of 2.4 ppmv and no detectable change in

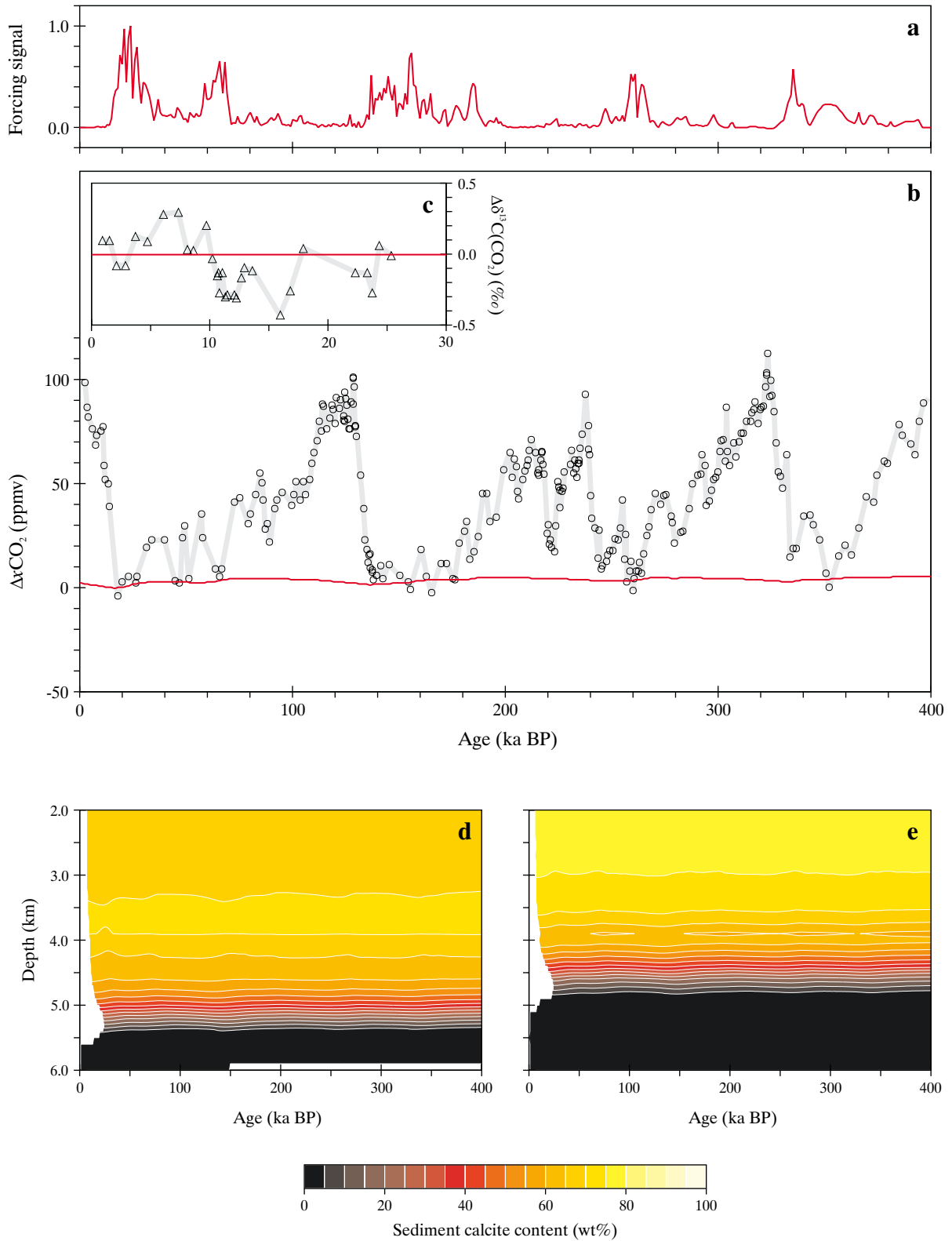


Figure 5-10 Effects on the global carbon cycle of glacial-interglacial variability in aeolian Si supply. Shown are; (a) the forcing signal (normalized to a value of unity at the LGM); (b) model $x\text{CO}_2$ response (red line) compared to the Vostok ice core record [Petit et al., 1999] (grey line with data points); (c) model $\delta^{13}\text{C}^{\text{CO}_2}$ response (red line) compared to the Taylor Dome ice core record [Smith et al., 1999] (grey line with data points); (d) and (e) the response of the calcite lysocline in the (south) Atlantic and (south) Pacific basins, respectively.

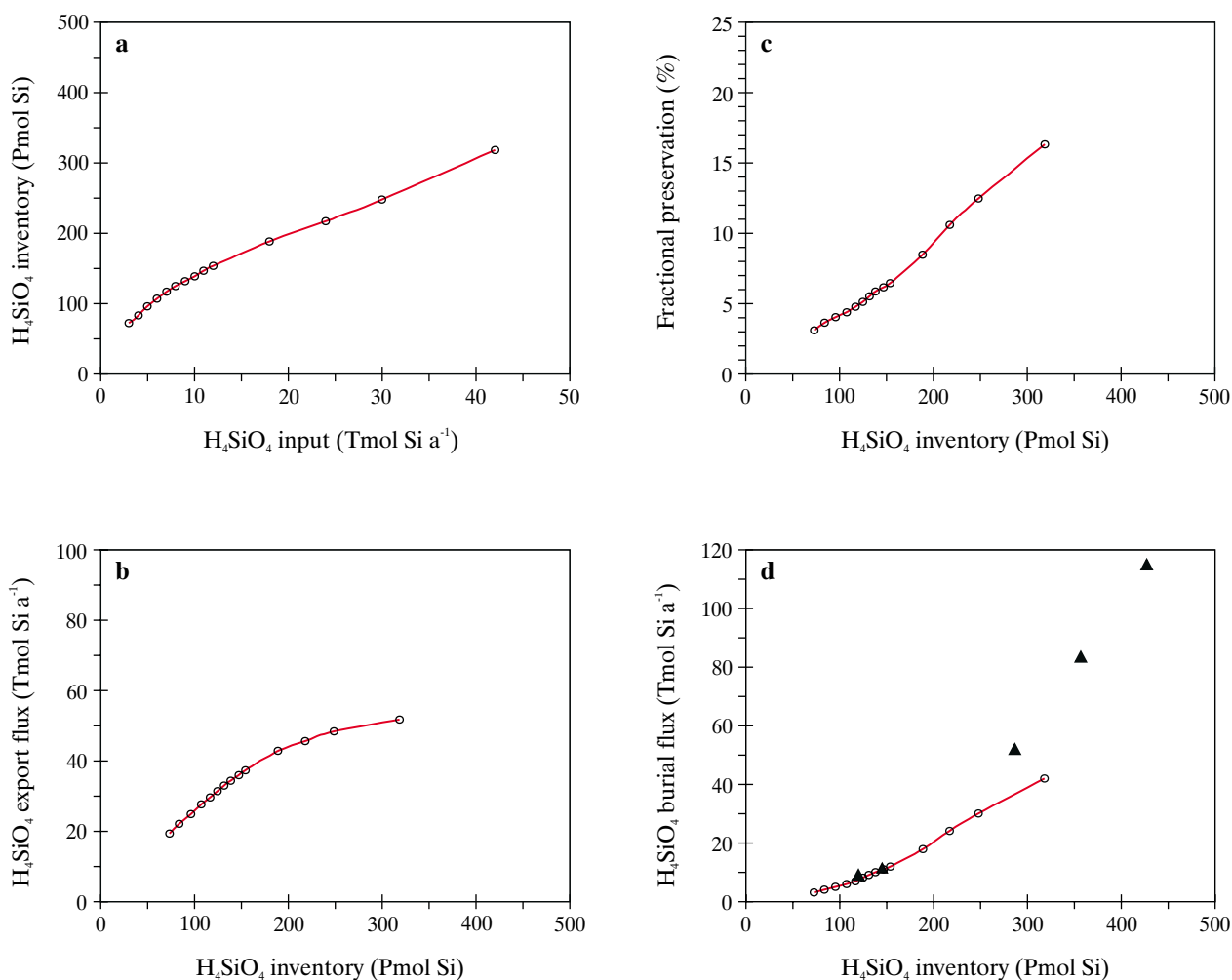


Figure 5-11 Relationships within the ocean Si cycle in response to changing dissolved Si supply.

$\delta^{13}\text{C}^{\text{CO}_2}$. Despite substantial differences in the shape and integrated area of the forcing signal used for weathering rate change compared to that in the aeolian deposition experiment, the overall effect on the global carbon cycle is similar. There is slightly greater variability in the depth of the calcite lysocline, although a glacial shoaling of ~ 100 m is still relatively minor. Sensitivity analyses again suggest that enhancing the strength of the forcing produces a proportional (but still small) atmospheric response.

5.4.8.3 Oceanic Si cycling and the ‘Silica Hypothesis’

Contrary to conceptual schemes purporting to explain glacial-interglacial change in atmospheric composition via increased dissolved Si supply to the world ocean during glacial times [Harrison, 2000; Treguer and Pondaven, 2000], the results of a mechanistic ocean silica cycle model suggest that there is little effect. This present study supports the conclusions of Archer *et al.* [2000] that attempting to change the oceanic inventory of H₄SiO₄ is a relatively ineffective way

of altering $x\text{CO}_2$. However, it is an interesting question as to what processes operating within the system are responsible for the surprisingly damped response to what appear quite substantial perturbations in the supply of this key nutrient.

One contributing factor relates to the time-varying nature of the perturbations employed in this study. Some of the more prominent features in the Vostok dust concentration [Petit *et al.*, 1999] and SPECMAP $\delta^{18}\text{O}$ [Imbrie *et al.*, 1984] forcing signals (such as deglacial transitions) are characterized by time scales of only 2-5 ka. This is short compared to the residence time of H₄SiO₄ in the ocean which in SUE1608 is about 16 ka (consistent with estimates of 10-20 ka derived from modelling and mass balance considerations [Archer *et al.*, 2000; Treguer *et al.*, 1995]). Furthermore, when interactions between CaCO₃ and silica cycles within the carbon cycle as a whole are taken into account, the e -folding time of changes in atmospheric composition with respect to perturbations in dissolved Si supply is even longer, some ~ 23 ka. Variability in the $x\text{CO}_2$

response to changes in dissolved Si input are therefore highly damped. This is in contrast to that expected by *Harrison* [2000] and *Treguer and Pondaven* [2000] who implicitly assume a system at steady-state.

An equally important contributor to overall system response involves the dynamics of Si burial, with *Archer et al.* [2000] finding that since Si burial appeared to rise with the second power of H_4SiO_4 inventory it would be extremely difficult to significantly change the H_4SiO_4 inventory through increased Si supply in the first place. Results of sensitivity analyses carried out with SUE1608 and driven by (total) dissolved Si inputs to the ocean of between 3 and 42 Tmol Si a^{-1} are shown in Figure 5-11. For this test, following a spin-up period, a step increase in dissolved Si input is applied and the system allowed to adjust for a further 50 ka (thus achieving ~95% of true steady state). The resulting model state is then compared to a control run forced continuously with the baseline dissolved Si input (6 Tmol Si a^{-1}). From this it can be seen that the oceanic H_4SiO_4 inventory is relatively insensitive to the dissolved Si input; a 14-fold increase in input is required to produce just over a 4-fold increase in inventory (Figure 5-11a). Export production of biogenic opal appears to be linear with H_4SiO_4 inventory over a range spanning plausible dissolved Si input rates to the ocean (3-12 Tmol Si a^{-1}) above which there is a rapid decline in slope with further increases in H_4SiO_4 availability (probably due to a maximum shift in species composition towards siliceous phytoplankton having been approached). These effects, together with a scaling of sedimentary opal preservation efficiency with H_4SiO_4 inventory (Figure 5-11c) combine to produce a non-linear response of burial flux with H_4SiO_4 inventory (Figure 5-11d). This final relationship is consistent with results from 3D OGCM carbon cycle modelling work suggesting an approximately parabolic relationship [*Archer et al.*, 2000]. However, in SUE1608 this relationship breaks down at an inventory of around 225 Pmol Si as a result of the saturation in export flux (Figure 5-11b).

The apparent failure of the 'Silica Hypothesis' in the model employed here can now be assessed in light of these two factors. In order to explain low glacial levels of CO_2 an increase in the oceanic H_4SiO_4 inventory of between about 10% and 67% (depending upon assumptions made regarding ecosystem composition and interaction) was suggested to be sufficient [*Harrison*, 2000]. Taking the absolute minimum requirement, a 10% increase in H_4SiO_4 inventory requires a 32% increase in dissolved Si input (Figure 5-11a), equivalent to an additional ~1.9 Tmol Si a^{-1} . This could be achieved with a solubility for aeolian silicates of about 11%, higher than available estimates allow for [*Wollast and Chou*, 1985] (but not unreasonably so). Given that the full width at half maximum (FWHM) of the Stage 2 dust peak in the Vostok core is only of order 10 ka, the 16 ka oceanic Si residence time suggests that solubility would have to be substantially greater in order to have attained the required increase in H_4SiO_4 inventory by the end of the LGM. Indeed, a peak aeolian influx of over 4.4 Tmol Si a^{-1} corresponding to a solubility of SiO_2 of ~25% is required in SUE1608 to produce such an inventory. Solubilities of this order are highly unlikely. A further problem with this hypothesis

concerns the uniform global distribution assumed of phytoplankton species abundance and thus of export ratio [*Harrison*, 2000]. With the exception of equatorial up-welling regions, most deep-sea sediment CaCO_3 accumulation tends to occur beneath regions where diatoms are responsible for a relatively minor proportion of POC export. In such regimes, a 10% increase in the POC export from siliceous species would result in much less than a 10% decrease in non-siliceous POC export and thus less than a 10% decline in CaCO_3 flux. The minimum increase needed in H_4SiO_4 inventory to achieve the required reduction in CaCO_3 export by *Harrison* [2000] would therefore be greater, further adding to the aeolian SiO_2 solubility requirement.

By similar arguments, the solubility requirement of an ocean nutrient cycle model [*Tyrrell*, 1999] used in the variation of the hypothesis put forward by *Treguer and Pondaven* [2000] proves to be even worse. In this, model glacial $x\text{CO}_2$ levels are explained by a 48% increase in biogenic opal export. If a similar increase in H_4SiO_4 inventory is required as an absolute minimum, an additional dissolved Si input of 6.6 Tmol Si a^{-1} is needed at steady state. The solubility requirement is now already 16% – this is before either the transitory nature of the input forcing or spatial heterogeneity in species composition have been taken into account.

Additional model experiments suggest that even a combination of aeolian supply and riverine influx fall far short of being able to account for the magnitude of observed $x\text{CO}_2$ changes. Indeed, with an assumption of 10% aeolian SiO_2 solubility together with a 50% LGM enhancement in riverine input, $x\text{CO}_2$ increases by only ~9 ppmv (19→0 ka BP). The response time of the system with respect to changes in dissolved supply is too long for any significant role to be played in the initial observed rapid rise in atmospheric CO_2 levels, with just ~2 ppmv occurring before Termination I is substantially complete by 10 ka BP. Despite this, changes in the global Si cycle may yet be important in driving declining $x\text{CO}_2$ as glaciations deepen, being responsible in this test for as much as 18 ppmv of the overall trend apparent between Stages 5a and 2.

5.4.9 The 'Iron Hypothesis'

One of the great puzzles in oceanography has been the reason for the existence of certain areas of the world ocean, particularly the Southern Ocean together with the equatorial and north Pacific, where there is an abundance of unused macro-nutrients [*de Baar and Boyd*, 2000]. Although physical (solar insolation and ocean surface mixing) and grazing regimes must play a part in controlling phytoplankton standing stocks in these so-called 'High-Nitrate Low-Chlorophyll' (HNLC) regions, John Martin suggested that growth limitation through insufficient availability of the micro-nutrient iron (Fe) might also exert an important control [*Martin and Fitzwater*, 1988]. He furthermore proposed that stimulation of biological productivity through increased aeolian Fe delivery to the Southern Ocean at the height of the last ice age might have led to the concurrently low levels observed of atmospheric CO_2 [*Martin*, 1990]. The

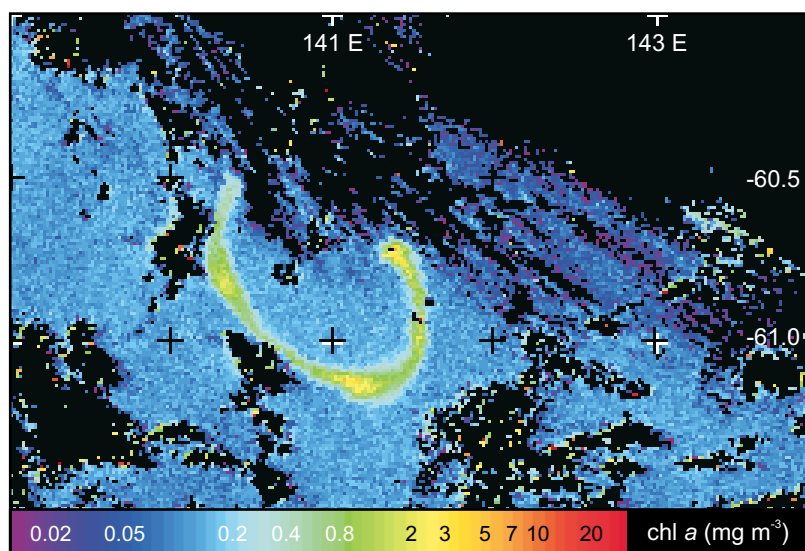


Figure 5-12 Image of the SOIREE bloom in the Southern Ocean in the region of 141°E 61°S, taken from the SeaWiFS ocean colour satellite on 23rd March 1999, some 6 weeks following initial Fe release [Abraham *et al.*, 2000]. The SeaWiFS data, provided by the NASA DAAC/GSFC and copyright of Orbital Imaging Corps and the NASA SeaWiFS project, was processed at CCMS-PML.

‘IronEx II’ open ocean Fe fertilization experiment demonstrated unequivocally the role that iron played in limiting phytoplankton growth (particularly of larger diatoms) in the equatorial Pacific [Coale *et al.*, 1996a,b]. More recently, a similar experiment (‘SOIREE’) was carried out in the Southern Ocean. Here too, an unambiguous response of the phytoplankton standing stock to the addition of Fe was observed [Boyd *et al.*, 2000].

To test the ‘Iron Hypothesis’ for low glacial $x\text{CO}_2$ it should be sufficient to increase aeolian deposition rates in the model and record the results. However, there is a caveat to the use of SUE in predicting the atmospheric response to Fe fertilization. This concerns the nature of the scheme for biological productivity in which export production is estimated directly from ambient nutrient concentrations with the aid of Michaelis-Menten kinetics (2.2.3). A response of POC export upon relief of Fe limitation is, therefore, implicitly assumed. Although increased export production was indeed reported in the equatorial Pacific as a result of Fe fertilization [Coale *et al.*, 1996b], there was no evidence during the 14-day course of SOIREE that POC export was similarly enhanced in the Southern Ocean [Boyd *et al.*, 2000; Charette and Buesseler, 2000] in spite of a significant draw-down in surface ocean $f\text{CO}_2$ having occurred [Boyd *et al.*, 2000; Watson *et al.*, 2000]. Furthermore, the apparent persistence of the bloom (on the basis of remotely-sensed elevated surface chlorophyll concentrations, as shown in Figure 5-12) for several months after the end of the experiment [Abraham *et al.*, 2000] implies that losses of Fe must have been relatively restricted over this entire period and thus export constrained to be modest. A very different response, though, might be expected from a continuous

enhancement of aeolian Fe supply over a period of thousands of years and across the entire Southern Ocean, as opposed to that obtained under the temporal and spatially-limited experimental conditions of SOIREE [Ridgwell, 2000]. Regardless of the specifics of Southern Ocean ecosystem dynamics, a more general response of the system to changes in aeolian Fe supply is to be expected. Accumulation rates of aeolian mineral material in deep-sea sediments around the world are generally higher during glacial periods than at present [Balsam *et al.*, 1995; deMenocal, 1995; deMenocal *et al.*, 1993; Pye, 1989; Rea *et al.*, 1986; Ruddiman, 1997]. This is supported by AGCM modelling studies, which predict that in the drier, colder, and windier glacial climate, dust transport from terrestrial sources to the open ocean is more efficient [Andersen *et al.*, 1998; Genthon, 1992; Mahowald *et al.*, 1999; Joussaume, 1993]. Furthermore, concurrent expansion of arid dust source areas [Adams *et al.*, 1990; Iriondo, 2000] would act so as to further enhance the flux of material to the ocean [Andersen and Ditlevsen, 1998; Mahowald *et al.*, 1999; Reader *et al.*, 1999]. Although the primary impact of increased aeolian Fe supply is on the enhancement of productivity (in HNLC regions) there are more subtle secondary effects that may be equally important in affecting $x\text{CO}_2$ over the longer term. Fe-replete conditions have been demonstrated to favour (predominantly larger) diatoms over pico- and nano-plankton [Boyd *et al.*, 2000; Coale *et al.*, 1996b; Watson *et al.*, 2000]. Since CaCO_3 is only produced by smaller phytoplankton (coccolithophorids), such a shift in species composition will reduce the CaCO_3 :POC rain ratio [Harrison, 2000; Watson and Lefèvre, 1999], driving enhanced

CaCO₃ dissolution in deep-sea sediments and thus lower $x\text{CO}_2$ [Archer and Maier-Reimer, 1994].

To test the hypothesis that glacial-interglacial changes in aeolian Fe supply to the ocean exerted a strong control over atmospheric composition, dust deposition fluxes to the ocean surface were altered. Present-day and LGM distributions of dust flux were taken from Mahowald *et al.* [1999]. The Vostok dust concentration record [Petit *et al.*, 1999] is used as a proxy for the timing and rate of change of deposition in order to reconstruct a record for the last 400 ka. Use of a signal template of dust deposition rates at Vostok (reconstructed using estimated snow accumulation rates [Petit, pers com]) as opposed to the dust concentration record makes very little difference.

The results of this exercise are summarized in Figure 5-13. The response of $x\text{CO}_2$ to this forcing is pronounced, with a 19→0 ka BP increase of 52.4 ppmv. There are several components that contribute to this: a fast response via the direct effects of changes in iron availability on export production (accounting for perhaps three quarters of the deglacial increase) together with a slower one, arising through adjustment of the deep-sea sediment system [Watson *et al.*, 2000]. The first component is associated with total POC export during the LGM being some ~10% higher than at present. There is also a shift in species composition with siliceous phytoplankton favoured (via increased Fe-driven efficiency in H₄SiO₄ utilization), suppressing CaCO₃ export by 24%. The second component involves a reduction in the CaCO₃ inventory of deep-sea surface sediments driven by a lower CaCO₃:POC rain ratio [Archer and Maier-Reimer, 1994]. This takes place more gradually with an adjustment time scale of ~9 ka. There is also a third component, although this is only apparent in the response of the system to an artificial stepped transition in dust supply. This involves a gradual depletion in oceanic H₄SiO₄ inventory under the influence of enhanced biogenic opal export. This acts so as to partly reverse the influence on atmospheric composition of the first two components, taking place with an *e*-folding time of ~25 ka (characteristic of direct perturbations made to the global Si cycle – see 5.4.8.3).

In addition to the model explaining slightly more than half the entire deglacial rise, there is an obvious marked similarity in shape between the time evolution of model and observed CO₂ concentrations. In particular, the model can explain virtually all the variability associated with full glacial periods (e.g., Stages 4 through 2). $\delta^{13}\text{C}^{\text{CO}_2}$ also exhibits a response consistent with early observed deglacial change, with a fall of some 0.19‰ over the interval 19→0 ka BP. However, an extremely marked response is exhibited by the calcite lysoclines (Figure 5-13d,e). Associated with episodes of high dust deposition is intense dissolution and dilution (by increased detrital input) of calcite virtually throughout the depth of the water column, both in the Atlantic and Pacific basins. A perturbation of sedimentary composition of this magnitude is greater than can be supported by available paleoceanographic evidence, at least for the Pacific. There are a number of possible explanations for this mismatch:

- Glacial dust supply might be over-estimated.

- The simplistic zonally-averaged ocean circulation might lead to variability in mid-latitude export production being over-sensitive to changes in global Fe availability.
- The biological export scheme might be producing an unrealistic response of the CaCO₃:POC rain ratio to changes in Fe availability.
- The component of sedimentary CaCO₃ dissolution driven by the respiration of POC might be over-estimated.
- General deficiencies in the global CaCO₃ cycle, with insufficient burial of CaCO₃ in the benthic environment.

In light of these uncertainties the effect on atmospheric composition of whole-ocean changes in dust deposition should be considered as an upper limit of possible response.

5.4.10 The nitrogen hypothesis

Although it can't be directly assessed in SUE, the oceanic nitrogen cycle has been suggested to be a potentially significant element in the dynamical evolution of the global carbon cycle over the late Quaternary. Various hypotheses have been forwarded to explain the observed glacial-interglacial variability in atmospheric composition, all envisioning in some way or other an oceanic NO₃ inventory higher during glacial periods than interglacials. Comparisons made between the predictions of ocean N cycle models and paleoceanographic $\delta^{15}\text{N}$ proxy data go some way to supporting this assertion [Altabet and Curry, 1989].

Hypotheses forwarded for the rapid rise in $x\text{CO}_2$ at deglacial inception require the existence of a critical threshold within the oceanic nitrogen cycle. In this, during the descent into full glacial climate, dissolved O₂ concentrations in the ocean gradually fall until at some point widespread denitrification rapidly proceeds. Since the oceanic residence time of NO₃ is relatively short (3-10 ka [Codispoti, 1995]) the oceanic nitrate inventory could be quickly depleted, resulting in decreased biological productivity and thus a steep rise in atmospheric CO₂ [Knox and McElroy, 1984; Shaffer, 1990]. Declining [O₂] could be driven by increased productivity fuelled by nutrients (PO₄ and/or NO₃) eroded from shelf sediments exposed as sea level falls [McElroy, 1983; Shaffer, 1990].

A second hypothesis draws its basis from the likelihood that the modern ocean nitrogen cycle is far from steady state, with nitrogen losses from the ocean through denitrification (particularly on continental shelves) exceeding the combined input from rivers, atmosphere, and nitrogen fixation in the surface ocean [Berger and Vincent, 1986; Codispoti, 1995; McElroy, 1983]. With sea level fall, denitrification within neritic sediments ceases on the newly exposed shelf area. This leads to an increase in the oceanic N inventory, which fuels greater productivity leading to CO₂ draw-down [Altabet and Curry, 1989; Berger and Vincent, 1986; Codispoti, 1995; Ganeshram *et al.*, 1995]. Although this mechanism can correctly generate CO₂ draw-down as glaciations intensify, deglacial CO₂ rise will lag sea level change contrary to observed temporal relationships, barring it from being a stand-alone explanation.

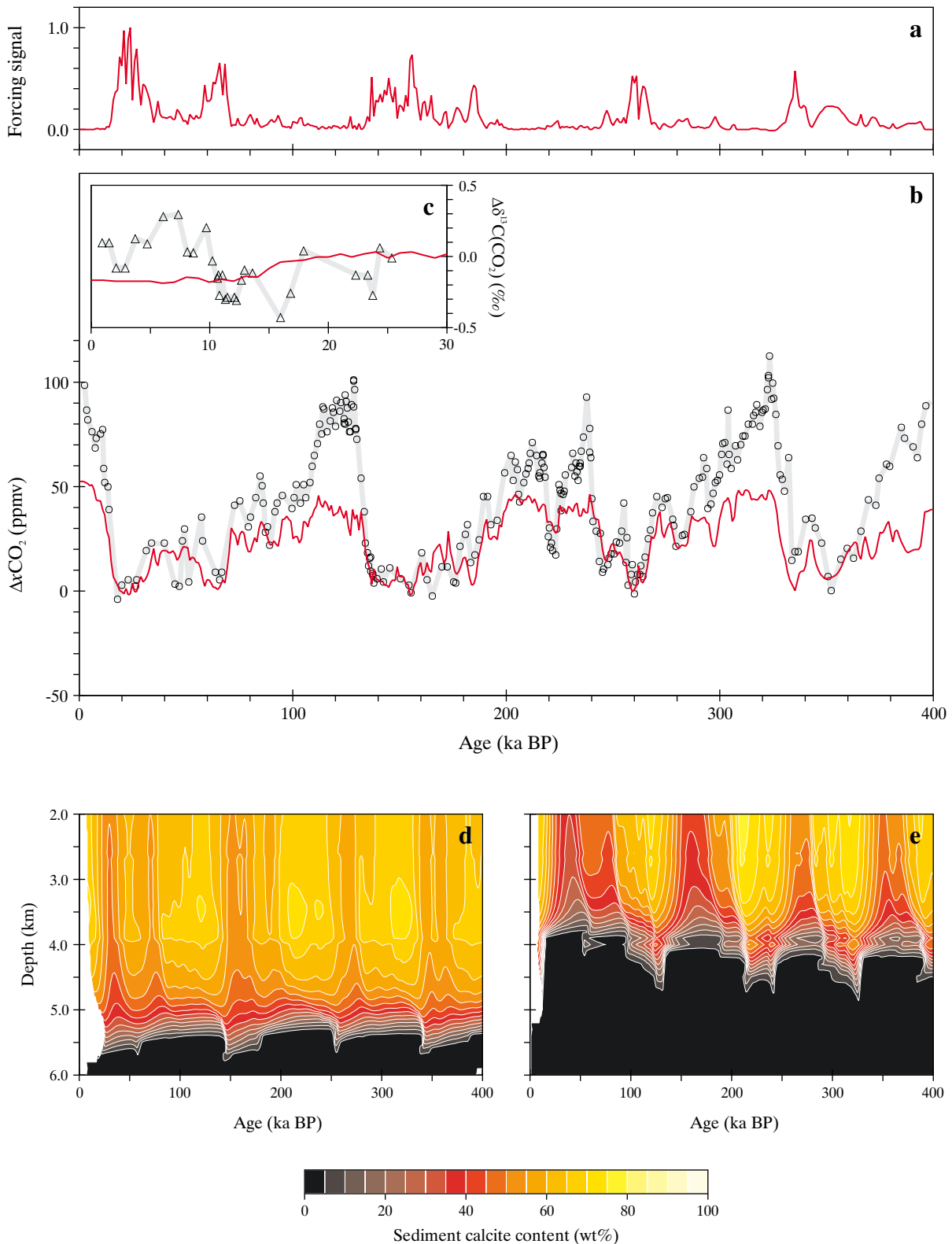


Figure 5-13 Effects on the global carbon cycle of glacial-interglacial variability in dust deposition to the world ocean. Shown are; (a) the forcing signal (normalized to a value of unity at the LGM); (b) model $\Delta x\text{CO}_2$ response (red line) compared to the Vostok ice core record [Petit *et al.*, 1999] (grey line with data points); (c) model $\delta^{13}\text{C}^{\text{CO}_2}$ response (red line) compared to the Taylor Dome ice core record [Smith *et al.*, 1999] (grey line with data points); (d) and (e) the response of the calcite lysocline in the (south) Atlantic and (south) Pacific basins, respectively.

Recently, a third variant has been suggested whereby increased Fe availability arising from aeolian dust deposition simulates the activity of diazotrophs such as *Trichodesmium* spp. in the surface ocean, thereby increasing the rate of N₂ fixation [Broecker and Henderson, 1998; Falkowski, 1997]. As a consequence, biological productivity and thus CO₂ draw-down follow (lagged) changes in aeolian dust supply, in general agreement with ice core records.

All these require as a minimum a detailed representation of the oceanic nitrogen cycle. However, this is still relatively poorly understood, particularly in terms of the rates and locations of nitrogen fixation and denitrification in the ocean. These in turn are critically dependent on seasonal and transient [O₂] and [Fe] distributions in the ocean, both of which are beyond the capability of the model configurations developed in the present study to reproduce sufficiently well for this purpose.

5.5 The role of the Southern Ocean

The Southern Ocean has long been regarded as a pivotal region for glacial-interglacial change in the global carbon cycle, with mechanisms relating to increased biological productivity [Knox and McElroy, 1984; Martin, 1990; Sarmiento and Toggweiler, 1984], decreased vertical mixing rates [Francois et al., 1997; Sigman et al., 1999a,b], increased wind speed [Keir, 1993a,b], and greater sea ice cover [Broecker and Peng, 1986; Moore et al., 2000; Stephens and Keeling, 2000] all having been proposed as playing important roles. The Southern Ocean achieves its climatic status both biochemically, as a result of the pool of excess nutrients found there [de Baar and Boyd, 2000], and through its physical oceanographic characteristics as a pathway of relatively low resistance linking the carbon reservoirs of the atmosphere and deep ocean [Sarmiento and Toggweiler, 1984]. Mechanisms influencing the carbon cycle relating to changes in biological productivity and sea ice extent in this region are now investigated in more detail with the aid of the higher resolution model implementation, SUE2108 (4.5), and constrained through consideration of additional paleoceanographic proxies.

5.5.1 Glacial-interglacial variability in dust deposition

John Martin's glacial Fe fertilization hypothesis [Martin, 1990], formulated specifically with regards to the Southern Ocean is now tested. For this, dust deposition is only varied within the Southern Ocean, defined as ocean area south of 47.5°S (Figure 4-1). Restricting Fe fertilization in this way avoids many of the possible biases suspected to arise from whole-ocean dust forcing (5.4.9). Variability in atmospheric composition thereby obtained will now represent a minimum likely effect of whole-ocean change in dust deposition, particularly since the HBEI score of the model suggests that the role of the Southern Ocean in controlling $x\text{CO}_2$ may be underestimated (5.3.1). As before, the magnitudes of

deposition flux under modern and LGM conditions is taken from Mahowald et al. [1999] with the forcing signal following Vostok dust concentrations [Petit et al., 1999].

The results of this exercise are summarized in Figure 5-14. The response of $x\text{CO}_2$ to declining dust fluxes in the Southern Ocean is an increase of 21.9 ppmv over the interval 19→0 ka BP with an associated decrease in $\delta^{13}\text{C}^{\text{CO}_2}$ of 0.15‰. Glacial draw-down in $x\text{CO}_2$ is a consequence of POC export being enhanced by ~100% south of about 54°S driven by increased Fe-availability. Although export from siliceous phytoplankton dominates this response (>95%), opal export increases by no more than ~35% due to greater Si utilization efficiency (enabled by higher ambient dissolved Fe levels). As a result of greater macro-nutrient utilization in the Southern Ocean there is decreased advective nutrient supply to the north, reducing POC export at lower latitudes. This slightly offsets $x\text{CO}_2$ draw-down driven by the Southern Ocean alone. In contrast to the significant response obtained in this study, box models of ocean Fe cycling have predicted that an increase in dust supply of order 1000 is required to produce a comparable decrease in $x\text{CO}_2$ [Lefèvre and Watson, 1999]. However, boundary conditions for this were taken from the Duce et al. [1991] dust deposition field such that the supply of Fe to the modern surface Southern Ocean was almost entirely from below (~99%). Although adoption of a similar depositional field might diminish the response in SUE1608, aeolian Fe solubilities assumed here are relatively low and could be substantially increased (countering lower dust fluxes) without degrading the plausibility of model assumptions. This present study also differs from results obtained from a coupled ecological and ocean box model which suggested that a realistic lifting of Fe limitation in the Southern Ocean would produce a draw-down in $x\text{CO}_2$ of only 12 ppmv [Popova et al., 2000]. However, this draw-down resulted from an increase in global new production of 1.7 GtC a⁻¹. That an increase in new production only slightly higher (2.2 GtC a⁻¹) obtained upon the lifting of physical constraints on productivity in the Southern Ocean in a 3D OGCM produced a draw-down of 34 ppmv [Kurz and Maier-Reimer, 1993] suggests that the relatively simple ocean model of Popova et al. [2000] may be overly insensitive to high latitude perturbations.

The general shape of the response of atmospheric composition over the course of the late Quaternary is noticeably different from that arising from whole ocean changes in dust flux (Figure 5-13). In particular, peak Holocene $x\text{CO}_2$ appears to be centred on ~7 ka BP. Since Fe-fertilization now takes place away from ocean regions overlying CaCO₃-rich sediments, there can be relatively little direct control exerted on CaCO₃ dissolution, with only modest changes in lysocline depth occurring (Figure 14d,e). The effect of the gradual recovery in oceanic H₄SiO₄ inventory following its previous glacial draw-down is now revealed – increasing H₄SiO₄ availability over the course of the Holocene shifts species composition towards siliceous phytoplankton which in turn produces a negative pressure on $x\text{CO}_2$, dominating the atmospheric response once the decline in dust flux has virtually ceased. The poor reproduction of the general trend observed in $x\text{CO}_2$ from Stage 5e through 2

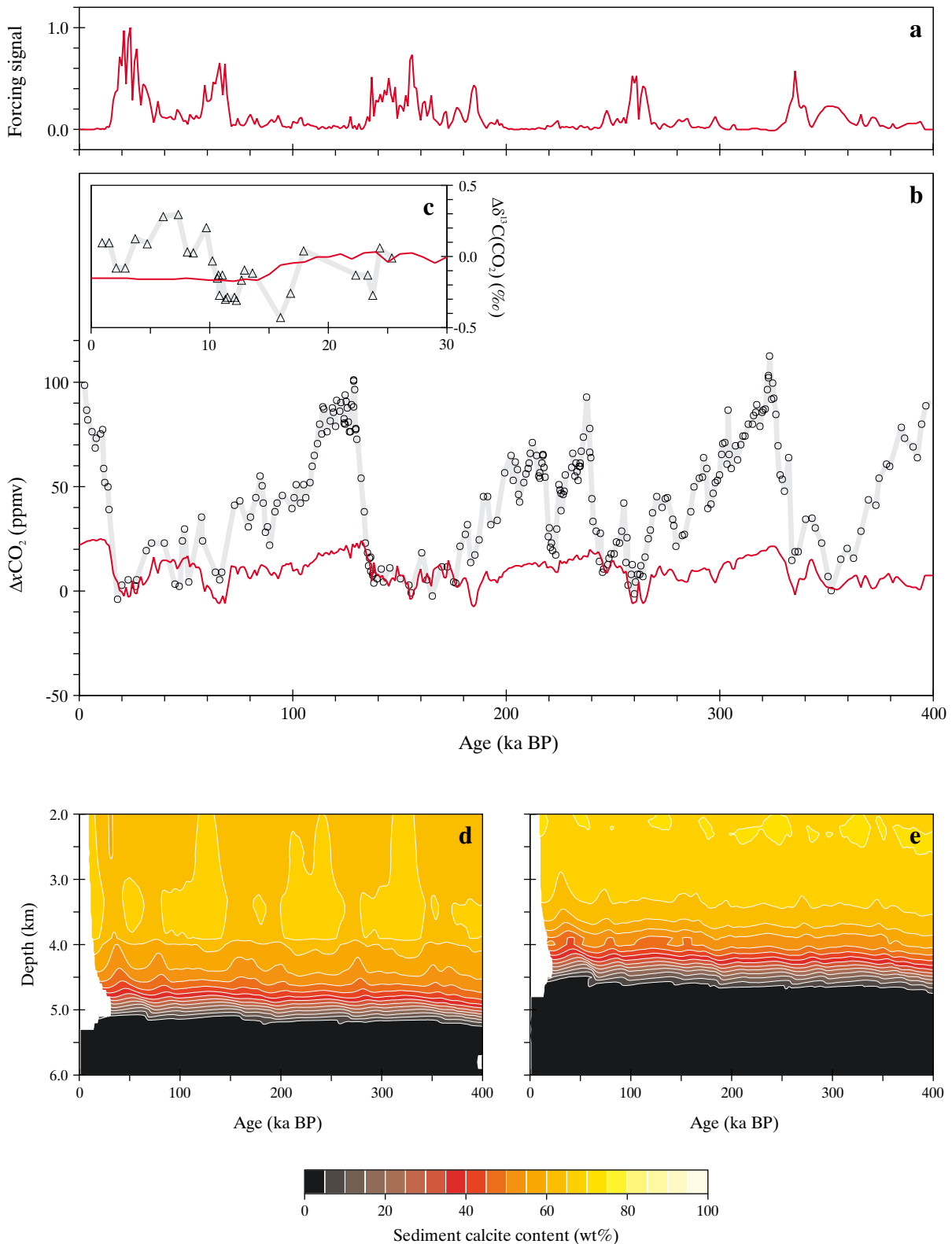


Figure 5-14 Effects on the global carbon cycle of glacial-interglacial variability in dust supply to the Southern Ocean. Shown are; (a) the forcing signal (normalized to a value of unity at the LGM); (b) model $\Delta x\text{CO}_2$ response (red line) compared to the Vostok ice core record [Petit *et al.*, 1999] (grey line with data points); (c) model $\delta^{13}\text{C}(\text{CO}_2)$ response (red line) compared to the Taylor Dome ice core record [Smith *et al.*, 1999] (grey line with data points); (d) and (e) the response of the calcite lysocline in the (south) Atlantic and (south) Pacific basins, respectively.

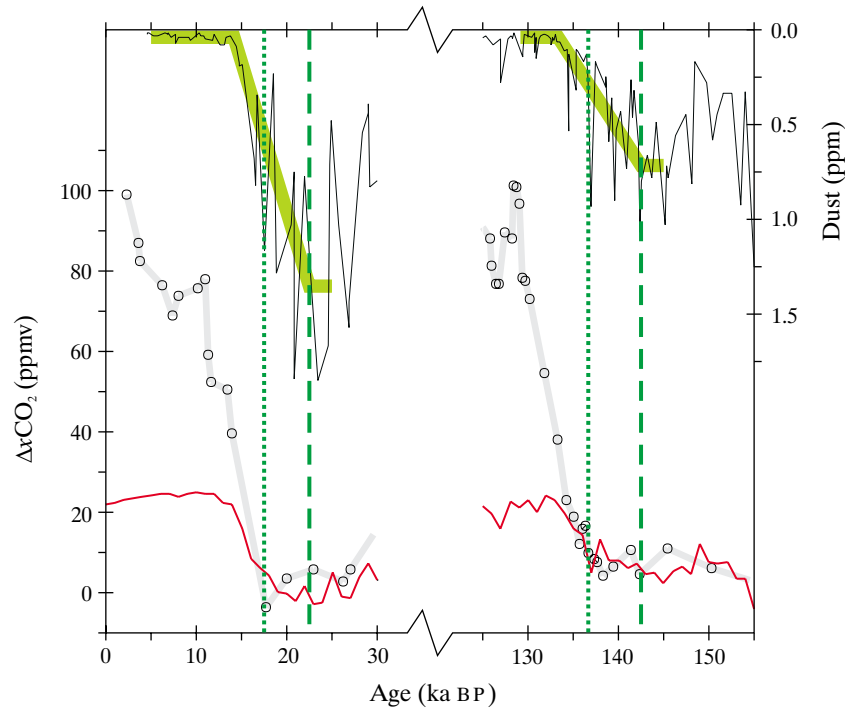


Figure 5-15 Temporal relationships surrounding glacial Terminations I and II between observed dust (thin black line, inverted at top) and CO₂ concentrations contained within the Vostok ice core (thick grey line with data points) [Petit *et al.*, 1999] and model xCO₂ (red line). The general decreasing trend in dust concentrations associated with the deglacial transition is highlighted in green, with the start of this dust decline marked by a dashed line, and the start of CO₂ rise by a dotted line.

is partly due to the same effect, whereby a gradually decreasing H₄SiO₄ inventory works against CO₂ draw-down driven by increasing Fe availability in the Southern Ocean. The maximum glacial-interglacial contrast associated with Termination I is therefore some 27.7 ppmv (over 23→7 ka BP) with 0.19‰ in δ¹³C^{CO₂}.

Probably the most compelling aspect of the model atmospheric CO₂ response to dust variability concerns the timing of the major perturbations [Watson *et al.*, 2000]. Figure 5-15 shows the events surrounding the last two glacial terminations on an expanded time scale. It can be seen that there is an excellent temporal match (within ~1 ka) between the onset of periods of rapid xCO₂ rise in both modelled and observed signals. This is despite dust deposition fluxes having begun to decline at least 5 ka before this point, with little associated increase in xCO₂. This lag has previously been interpreted by Broecker and Henderson [1998] as a powerful argument against John Martin's hypothesis. That a system as complex as the global carbon cycle should be highly non-linear in this respect should hardly be surprising. Non-linearities arise in the model through a number of factors:

- Onset of (summer-time) H₄SiO₄ limitation in the more northerly reaches of the Southern Ocean.
- Through Michaelis Menten saturation kinetics in the biological export model, whereby further increases in export start to tail off rapidly with increasing Fe

availability once half saturation concentrations have been surpassed.

- Increasing loss of Fe from the surface ocean through both 'self-scavenging' (2.2.5) and decreasing efficiency of Fe use by phytoplankton (i.e., increasing organic matter Fe:C ratios - see Figure 2-2).

These combine to produce the observed behaviour with POC export declining rapidly (and thus increasing xCO₂) once dust deposition fluxes start to drop below a critical level. A degree of variability can still be observed even during peak glacial times. However, because the amplitude of the response during this time is highly dampened, an apparent lag is produced between the start of dust decline and significant CO₂ rise as observed by Broecker and Henderson [1988].

Paleoceanographic evidence from the Southern Ocean reveals a fundamental meridional divide, with glacial-interglacial changes in the opal content of deep-sea sediments either side of the position of the present-day Antarctic Polar Front (APF) being virtually opposite in sign. To the south, glacial-age sediments are characterized by a lower opal content than during interglacial periods, while to the north, it is interglacial sediments that are the more opal-rich [Anderson *et al.*, 1998; Charles *et al.*, 1991; De La Rocha *et al.*, 1998; Francois *et al.*, 1997; Kumar *et al.*, 1995; Mortlock *et al.*, 1991]. Although changes in preservation efficiency, sediment focussing, and the physiological effects

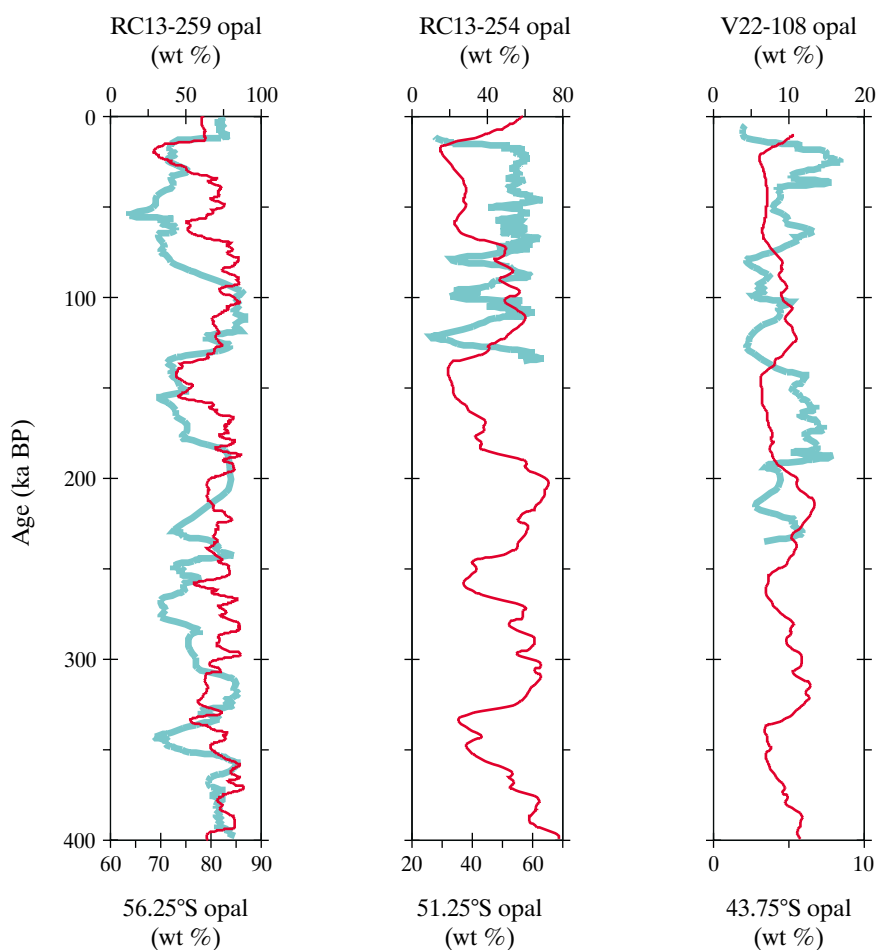


Figure 5-16 Observed variability in sedimentary opal content from a transect spanning the approximate location of the modern Antarctic Polar Front in the Atlantic sector of the Southern Ocean [Mortlock *et al.*, 1991] (blue) compared to synthetic model sediment core results (red) generated by SUE2108 and forced by glacial-interglacial variability in dust deposition to the Southern Ocean.

of Fe availability on diatoms can all complicate the interpretation of this [Anderson *et al.*, 1998; Boyle, 1998; Francois *et al.*, 1997; Takeda, 1998], indicators of H_4SiO_4 utilization in the surface ocean such as opal Ge/Si ratios [Froelich *et al.*, 1989; Mortlock *et al.*, 1991] and $\delta^{30}\text{Si}$ [De La Rocha *et al.*, 1998] are consistent at least with the sign of the observed change in opal content. This coupled antagonistic response presents us with an important validation target for proposed carbon cycle mechanisms operating in the Southern Ocean.

Figure 5-16 shows down-core variability in opal content in three cores spanning the APF in the Atlantic sector of the Southern Ocean [Mortlock *et al.*, 1991]. Core RC13-259 (53°53'S) is located to the south of the APF while RC13-254 (48°34'S) and V22-108 (43°11'S) both come from further to the north. Also shown are records of down-core opal content contained within synthetic sediments cores located at the nearest equivalent model grid points. It can be seen that while deglacial increases in %opal are reproduced by the model for Terminations I and II in RC13-259 there is little

other correspondence with this core. For the two cores located to the north of the APF the situation is far worse, with the model exhibiting a distinct anti-phase relationship with paleoceanographic observations. Low glacial opal content in these two synthetic cores is a direct consequence of local nutrient limitation, as macro-nutrients previously advected northwards across the APF are depleted under the influence of Fe-fertilization to the south. Clearly, either the effect of Fe fertilization in the Southern Ocean is being substantially overstated in the model, or one or more mechanisms important to the paleoceanographic record in the Southern Ocean have not been accounted for.

5.5.2 The role of changes in seasonal sea ice extent

It was shown earlier that, in isolation, changes in the maximum seasonal limits of sea ice extent in the Southern Ocean have little direct impact on the concentration of atmospheric CO_2 . However, such changes might be critical in

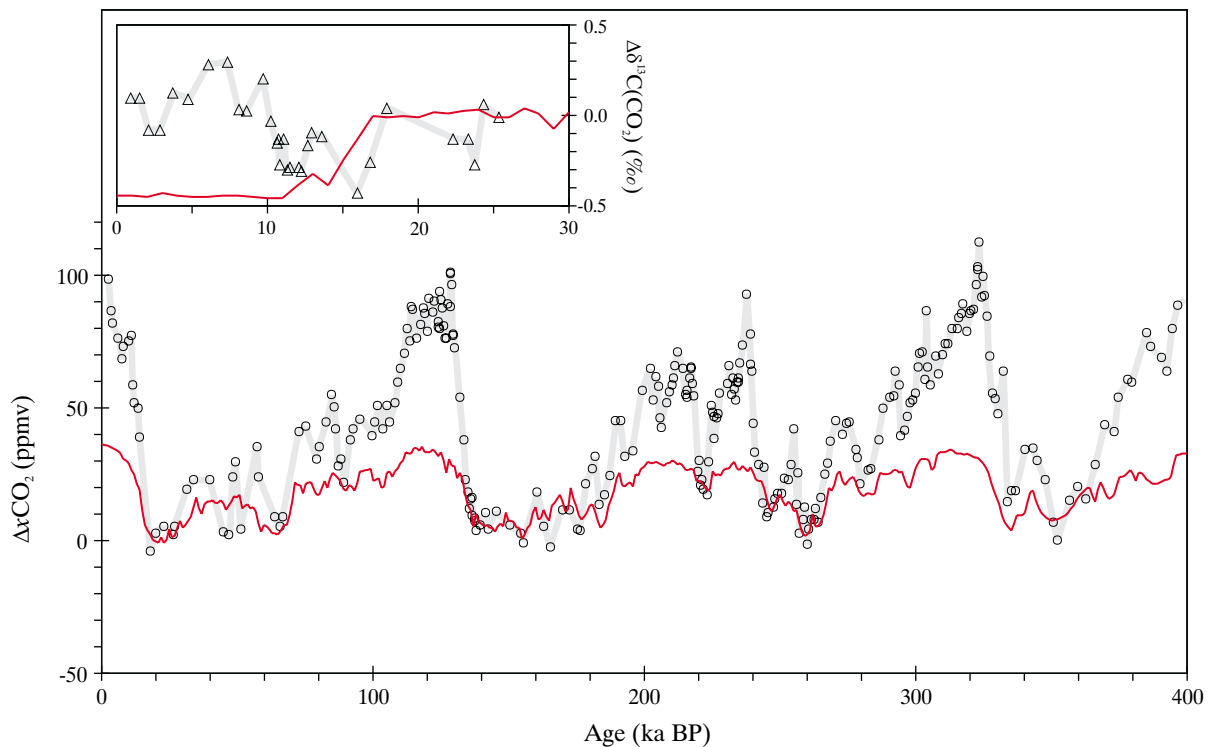


Figure 5-17 Effects on the global carbon cycle of glacial-interglacial variability in both dust deposition to the Southern Ocean and sea ice extent. Shown is the model $x\text{CO}_2$ response (red line) compared to the Vostok ice core record [Petit et al., 1999] (grey line with data points) with inset – model $\delta^{13}\text{C}^{\text{CO}_2}$ response (red line) compared to the Taylor Dome ice core record [Smith et al., 1999] (grey line with data points).

explaining some of the observed paleoceanographic features of this region [Charles et al., 1991]. Fractional sea ice cover is, therefore, now varied in addition to changes in dust deposition. A record of sea ice cover is reconstructed for the past 400 ka as before (5.4.4), taking maximum (winter-time) and minimum (summer-time) coverage for each grid point region from the CLIMAP [1984] and taking Vostok δD [Petit et al., 1999] as a signal template.

The response of atmospheric composition to this combined forcing is shown in Figure 5-17. During glacial periods, the presence of increased seasonal sea ice cover south of the APF results in much lower POC export, with a complete cessation south of about 62.5°S. Importantly, sea ice cover prevents escape of CO_2 to the atmosphere during non-productive winter months. Previously utilized macro-nutrients are advected northwards, fuelling much greater (>100%) POC export just to the north of the APF in conjunction with higher Fe availability. The combination of these factors helps to enhance the glacial-interglacial contrast in $x\text{CO}_2$ to 36.3 ppmv (19→0 ka BP). The overall form of the model $x\text{CO}_2$ signal now bears a noticeably closer resemblance to the Vostok record than through Fe fertilization alone, particularly in the relative levels along the sequence of transitions Stage 5e through Stage 2. The full ~0.4‰ decrease observed in $\delta^{13}\text{C}^{\text{CO}_2}$ associated with deglacial inception can also now be accounted for.

The addition of varying sea ice extent brings about a remarkable change in the synthetic opal sediment records (Figure 5-18), with most of the major transitions in opal content reproduced extremely well (even the characteristic antagonistic variability either side of the APF). Although there is a substantial mismatch between model and observations during Stages 3 and 4 in RC13-259, this core has a known hiatus around this level [Anderson, pers comm], which could easily account for this. The correspondence in the timing of the changes are all the more surprising considering that the synthetic model age scale and that derived on the basis of $\delta^{18}\text{O}$ stratigraphy in the observed records are unlikely to be equivalent. Indeed, by eye, RC13-254 appears to share an even greater similarity in opal variability with the paired synthetic model record than it does with core V29-105, located only 0°29' further to the north [Mortlock et al., 1991]. Absolute values of opal content do not correspond nearly so well, particularly for core RC13-254. However, this is not entirely unexpected since model sediments represent zonal means whilst individual deep-sea sediment cores record local conditions.

With regard to other paleoceanographic proxy evidence from the Southern Ocean, the model predicts generally lower glacial POM export well to the south of the APF compared to at present but becomes largely invariant with respect to the deglacial transition as the APF is approached.

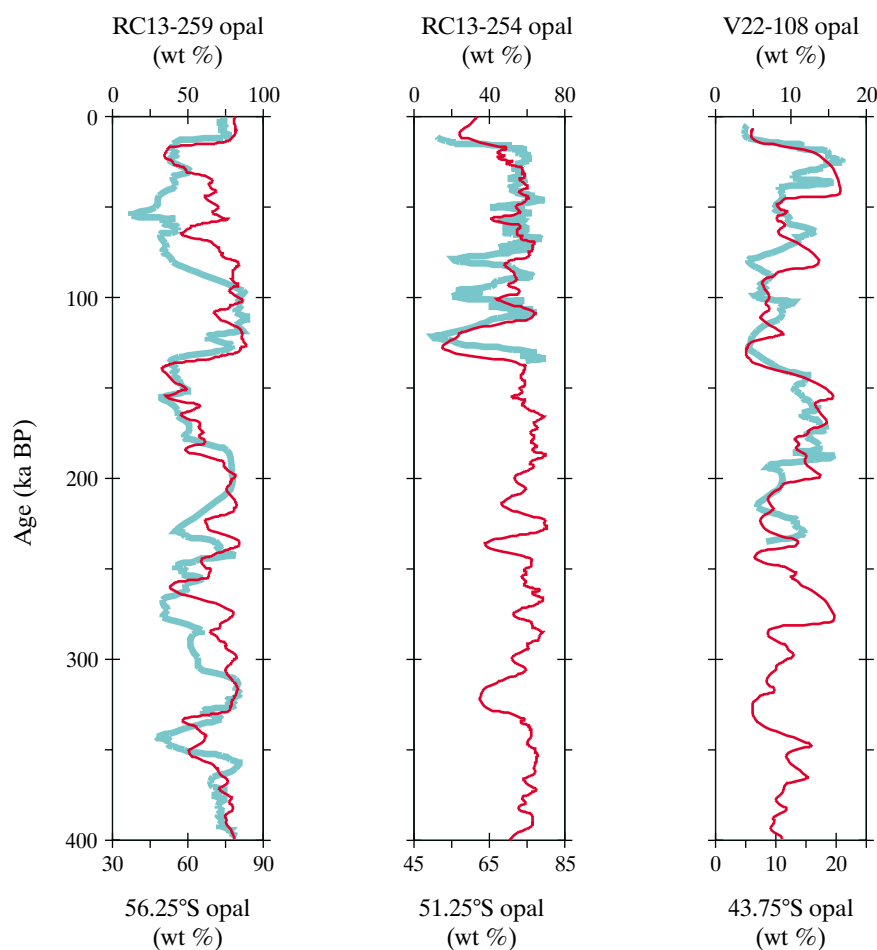


Figure 5-18 Observed variability in sedimentary opal content from a transect spanning the approximate location of the modern Antarctic Polar Front in the Atlantic sector of the Southern Ocean [Mortlock *et al.*, 1991] (blue) compared to synthetic model sediment core results (red) generated by SUE2108 and forced by glacial-interglacial variability in both dust deposition to the Southern Ocean and sea ice extent.

This is consistent with organic matter export proxies such as $^{231}\text{Pa}/^{230}\text{Th}$ and $^{10}\text{Be}/^{230}\text{Th}$ ratios, authigenic U production, and Ba accumulation fluxes [Anderson *et al.*, 1998; Francois *et al.*, 1997; Kumar *et al.*, 1995]. As a result, annual mean PO_4 concentrations are at their highest levels during the LGM, in line with lower PO_4 utilization suggested by Cd/Ca ratios [Elderfield and Rickaby, 2000; Rickaby and Elderfield, 1999]. In addition, the synthetic sediment record exhibits a deglacial (19→0 ka BP) rise in planktonic foraminiferal $\delta^{13}\text{C}$ of $\sim 1.0\text{‰}$ at 56.25°S (not shown), virtually identical to the change recorded in RC13-259 [Mortlock *et al.*, 1991].

To the north of the APF the model also performs well against additional observational indicators. Substantially higher glacial POM export is again consistent with $^{231}\text{Pa}/^{230}\text{Th}$, $^{10}\text{Be}/^{230}\text{Th}$, authigenic U production, and Ba accumulation records, as well as with phytoplankton biomarkers [Anderson *et al.*, 1998; Francois *et al.*, 1997; Ikehara *et al.*, 2000; Kumar *et al.*, 1995]. Although temperature-corrected changes in sub-Antarctic Cd/Ca ratios have been interpreted as indicating a fairly minimal change

in surface ocean PO_4 concentrations [Elderfield and Rickaby, 2000], uncertainties in this proxy allow for a reduction during the LGM of up to $0.5 \mu\text{mol kg}^{-1}$, agreeing with a mean annual glacial draw-down in the model at 51.25°S and 43.75°S of ~ 0.4 and $\sim 0.3 \mu\text{mol kg}^{-1}$, respectively.

However, there is one further paleoceanographic indicator conspicuous by its absence in the discussion so far. Changes in the ^{15}N isotopic composition of organic matter, a proxy for surface ocean nitrate utilization, is difficult to reconcile with the interpretation of other nutrient and export proxies in this region. Indeed, $\delta^{15}\text{N}$ suggests almost the complete opposite, with increased glacial nutrient utilization south of the APF and decreased or unchanged utilization to the north [Francois *et al.*, 1997; Sigman *et al.*, 1999a,b]. Factors controlling productivity proxies are therefore probably much less well understood than was previously assumed [Cullen *et al.*, 1999; Sigman and Boyle, 2000]. In the case of $\delta^{15}\text{N}$ it is possible that the observed variability may be significantly affected by factors other than the degree of nitrate utilization. For instance, increased export production due to

prymnesiophytes such as *Phaeocystis antarctica* might radically alter N/P uptake ratios and thus decouple nitrate utilization from POC export, while the different ^{15}N fractionation regime associated with sea ice algal communities might distort the mean $\delta^{15}\text{N}$ signal [Elderfield and Rickaby, 2000].

5.6 Towards the complete picture

It is apparent, at least for the hypotheses tested in this present study that no single mechanisms can simultaneously fulfill the constraints dictated even by the limited paleoclimatic evidence considered so far. The explanation for the observed glacial-interglacial variability in the concentration of atmospheric CO_2 must therefore lie in a combination of processes at work together over the course of the late Quaternary. Indeed, it has already been shown that through combining changes in sea ice extent with dust deposition in the Southern Ocean it is possible to correctly account for a number of key paleoatmospheric and paleoceanographic features. Although in this case the influence on $x\text{CO}_2$ of sea ice in isolation is limited, its addition to dust deposition forcing is evidently non-linear, producing a marked improvement in the amplitude and overall character of the resulting $x\text{CO}_2$ signal. Mechanisms that in isolation appear to have little impact may therefore actually play an essential role as a component of wider change in the global carbon cycle. It is therefore important that even effects that are superficially ‘unhelpful’ in reproducing the observed atmospheric signal, such as CO_2 draw-down forced by deglacial increases in terrestrial carbon storage, must be included in order to build up a complete picture of the evolution of the system. All the separate mechanisms tested so far are now combined.

SUE2108 is run with the ocean carbon cycle forced by the following perturbations:

- sea level change (117 m 19→0 ka BP rise with a 1.05‰ decrease in ocean salinity) and following SPECMAP
- ocean surface temperature changes (19→0 ka BP difference taken from CLIMAP, but with LGM tropical temperatures cooler by an additional 2°C), with the NH weighted according to SPECMAP and the SH to Vostok δD .
- wind speed changes in the SH only, weighted to Vostok Na concentrations
- variability in sea ice extent (19→0 ka BP difference taken from CLIMAP) in the SH only, weighted to Vostok δD
- changes in Atlantic overturning circulation (19→0 ka BP difference taken from the two alternative circulations of the Bern 2D ZOGCM [Marchal, pers comm]) and following SPECMAP
- changes in terrestrial carbon storage (500 GtC 19→0 ka BP increase) following SPECMAP
- changes in neritic CaCO_3 storage (50% strength of the parameterization of Munhoven and Francois [1996])
- 6.6% solubility of SiO_2 (present at 66 wt%) in aeolian dust deposited to the ocean surface, and a variable sink

in neritic opal accumulation rate (19→0 ka BP increase of $\sim 0.8 \text{ Tmol Si a}^{-1}$)

- variability in aeolian Fe deposition to the Southern Ocean (19→0 ka BP decrease from Mahowald *et al.* [1999]) and following Vostok dust concentration changes.

In order to account for the fact that by simply ‘poisoning’ NADW formation (in order to produce the alternative circulation in the Bern 2D model) north Atlantic circulation does not shift southwards, sea ice extent is not extended in this composite scenario. To prevent overall glacial gas transfer rates in this region from then being overestimated wind speeds are also held invariant. The ocean carbon cycle is configured with a reduced POC-driven dissolution component to deep-sea sediment CaCO_3 diagenesis (5.4.7.1).

The results of this exercise are summarized in Figure 5-19. It can be seen that when combined these mechanisms can explain around two thirds of the observed variability in $x\text{CO}_2$, with a deglacial (19→0 ka BP) increase of some 61.1 ppmv. However, there are a number of specific areas where the model noticeably falls short with respect to the Vostok record. In particular, the initial rapid deglacial increase in $x\text{CO}_2$ surrounding Terminations I through III is significantly underestimated, there is too little intra-glacial variability (e.g., Stages 4 through 2), and the magnitude of the overall decline from interglacial to full glacial is lacking. A deglacial minimum in $\delta^{13}\text{C}^{\text{CO}_2}$ around ~ 15 ka BP is successfully predicted by the model, although it is less than half of the observed magnitude.

What are the reasons for the model-observation mismatches? Dealing with deglacial inception first, a critical aspect of combining together different model forcings which has not yet been fully considered is the relative phase between them [Henderson and Slowey, 2000]. The temporal evolution of boundary conditions of the northern hemisphere have, up until now, been assumed to mirror changes in the SPECMAP $\delta^{18}\text{O}$ stack [Imbrie *et al.*, 1984]. However, this record is a composite of mainly planktonic foraminifera and is not corrected for changes in ocean temperature. Rates of change predicted by this record and the timing of the mid-point of the deglacial transition, while sufficient for the investigation of the magnitude of glacial-interglacial change and to define long-term trends arising from single mechanisms, is unlikely to be adequate in a composite environment. Of particular concern in this regard is when (and how rapidly) increases in carbon stored in terrestrial ecosystems occur, since this acts so as to oppose the general trend of deglacial CO_2 increase. Indeed, it is noticeable that the model is more successful in predicting observed $x\text{CO}_2$ variability further back than ~ 250 ka BP, a period when the SPECMAP and Vostok time scales appear to be significantly out of sync.

An improved temporal framework for forcing the composite scenario over the course of Termination I can be devised by deriving signal templates for NH-weighted change from proxy signals taken from the GRIP Greenland ice core in lieu of SPECMAP. Following Blunier *et al.* [1997], the GRIP ice core is placed onto the same age scale as the Vostok CO_2 target by matching changes in CH_4 concentrations surrounding the Younger Dryas event as

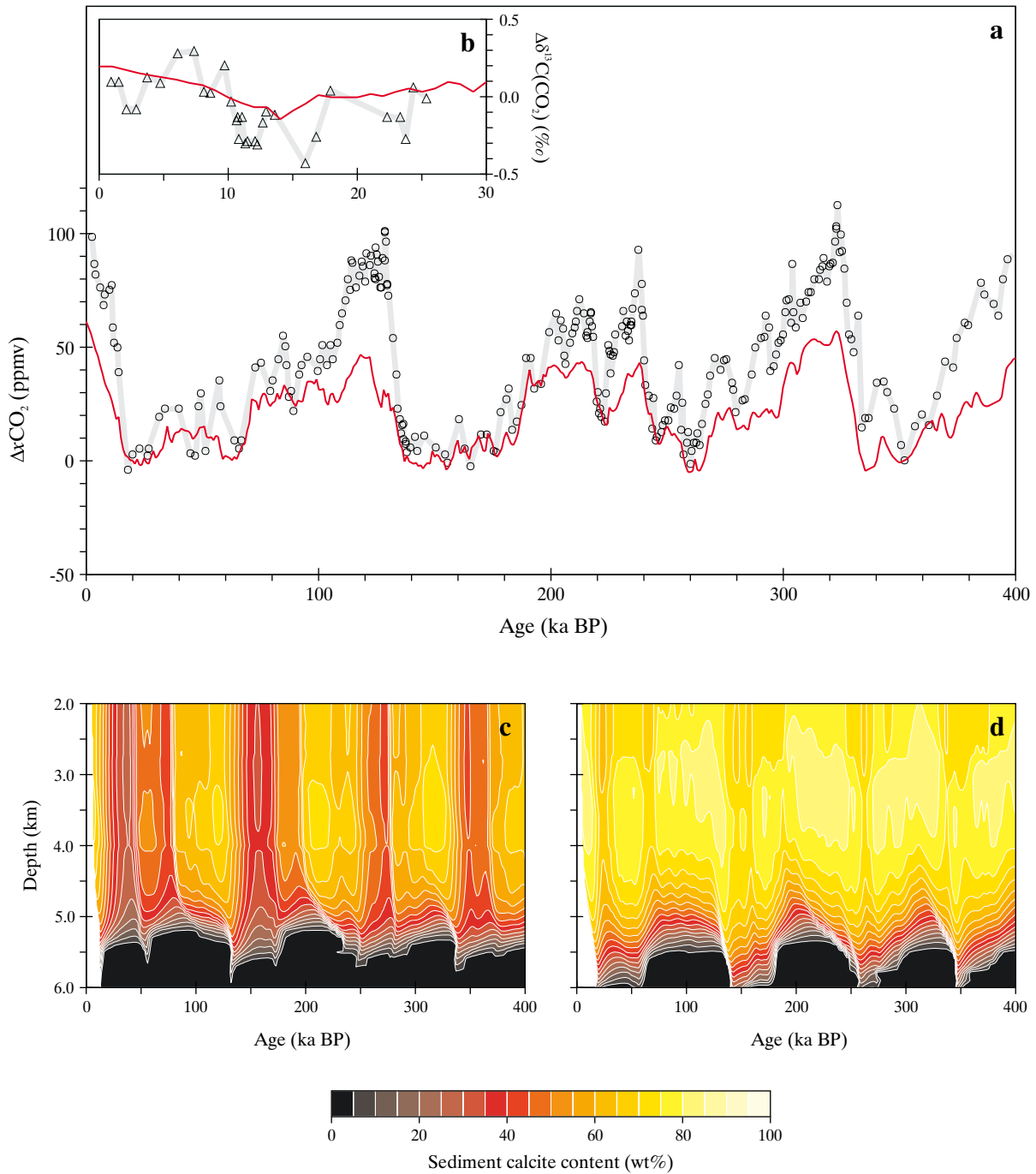


Figure 5-19 Effects on the global carbon cycle of a composite scenario for glacial-interglacial change. Shown are; (a) model $x\text{CO}_2$ response (red line) compared to the Vostok ice core record [Petit *et al.*, 1999] (grey line with data points); (b) model $\delta^{13}\text{C}(\text{CO}_2)$ response (red line) compared to the Taylor Dome ice core record [Smith *et al.*, 1999] (grey line with data points); (c) and (d) the response of the calcite lysocline in the (south) Atlantic and (south) Pacific basins, respectively.

recorded in these two cores. The $\delta^{18}\text{O}^{\text{ice}}$ record [Johnsen *et al.*, 1997], a proxy for local (air) temperature, is adopted to describe the evolution of NH-weighted SSTs over the last 20 ka together with changes in the Atlantic overturning circulation. The deglacial evolution of sea level is taken from Fairbanks [1989] and placed onto a common chronology with the other forcing records by linearly transforming ^{14}C ages so that the period separating meltwater pulses 1A and 1B corresponds with the Younger Dryas, as defined by GRIP $\delta^{18}\text{O}^{\text{ice}}$. Estimating the past history of changes in the size of the terrestrial biosphere carbon reservoir is much more difficult. While variations in atmospheric CH_4 concentrations relate to changes in terrestrial ecosystems, much of the magnitude of $x\text{CH}_4$ variability over the deglacial transition is thought to relate to changes in low latitude wetland extent [Blunier *et al.*, 1995] and thus predominantly reflect rapid changes occurring in local (tropical) hydrological regime rather than global biomass. Sea level rise (Fairbanks [1989]) is instead taken as a proxy for global biospheric state, but lagged with an *e*-folding time of 2 ka to account for the time taken for climax ecosystems to develop and soil carbon levels to stabilize. The maximum deglacial (19→0 ka BP) change is scaled to 500 GtC as before (5.4.6).

The effect on atmospheric composition of the new Termination I forcing chronologies is shown in Figure 5-20. It can be seen that the model now explains slightly more of the initial rapid increase in $x\text{CO}_2$ with the hiatus in CO_2 rise surrounding the Younger Dryas reproduced. However, even with this improved inter-hemispheric chronology the model still only accounts for almost 50% of CO_2 rise surrounding deglacial inception. With respect to $\delta^{13}\text{C}^{\text{CO}_2}$ the improvement is also partial. Again, the hiatus of the Younger Dryas period is reproduced but the initial transient is shallower than observed. It is likely that the relative chronologies of the forcings may still not reflect the real sequence of events. In particular, it is possible that collapse in sea ice extent was either slightly earlier or much more rapid than changes recorded by local temperature (as indicated by Vostok δD). This would enable a much more pronounced early minimum in $\delta^{13}\text{C}^{\text{CO}_2}$. Changes in convective regime, particularly if resulting in a greater degree of exposure of the atmosphere to the deep ocean would also enhance the respective responses in both $x\text{CO}_2$ and $\delta^{13}\text{C}^{\text{CO}_2}$. In addition, buildup in carbon stored in the terrestrial biosphere might be more sluggish still.

A second aspect of apparent deficiencies in predicted $x\text{CO}_2$ concerns the inherent sensitivity of model response. It has already been seen that according to indices of inter-regional control of levels of $x\text{CO}_2$ (5.3), SUE2108 has a tendency to under-estimate the importance of that high latitude regions of the world ocean. At least part of the missing response at deglacial inception and in intra-glacial variability (especially Stages 4 through 2) might then be due to an underestimation of mechanisms such as Fe fertilization in the Southern Ocean. Likewise, the model may be too insensitive to changes in fractional sea ice cover, particularly should the Southern Ocean actually be a stronger source of CO_2 to the atmosphere under interglacial conditions than it predicts. There is also the question of the real effect of whole ocean

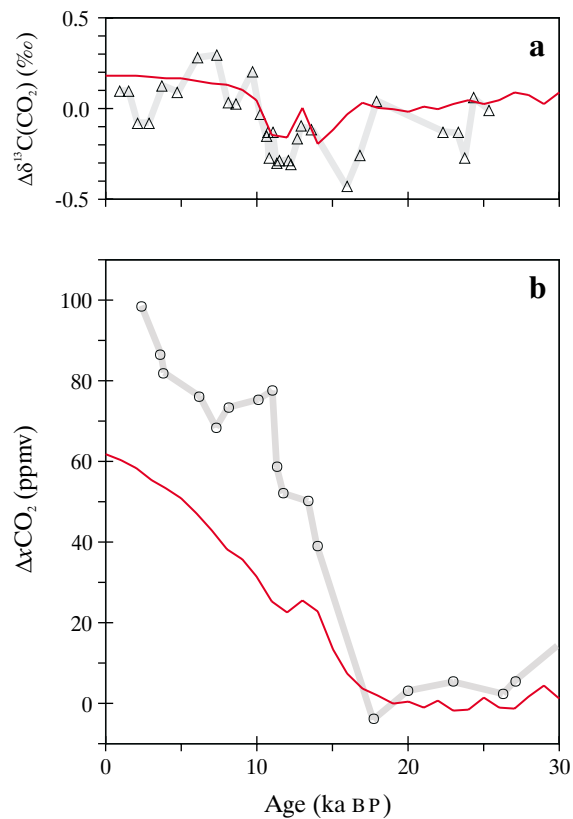


Figure 5-20 Evolution of atmospheric composition surrounding Termination I as a result of the composite scenario with improved temporal relationships of northern hemisphere forcing with respect to change in the southern hemisphere; (a) model $\delta^{13}\text{C}^{\text{CO}_2}$ (red line) with observations from the Taylor Dome ice core record [Smith *et al.*, 1999] (grey line with data points), (b) model $x\text{CO}_2$ (red line) with observations from the Vostok ice core record [Petit *et al.*, 1999] (grey line with data points).

aeolian deposition as opposed to the minimum case (i.e., Southern Ocean only) imposed in the composite scenario. It would not be unreasonable to assume that Fe fertilization could account for the missing intra-glacial variability in $x\text{CO}_2$, particularly since no other potential forcings share a similar pattern over this period. This would imply an additional ~15 ppmv at deglacial inception taking the initial rise to around 40 ppmv (only 10 ppmv short of that observed). The deficit in total CO_2 increase since the LGM would then be reduced to ~15 ppmv. Aside from model sensitivity to Fe availability, the temporal evolution of the global silica cycle also plays a role. Since the onset of H_4SiO_4 limitation in parts of the Southern ocean appears to be a key factor in the degree of CO_2 draw-down obtained, if the ocean inventory of dissolved Si is incorrectly predicted at the LGM then the magnitude of the effect of Fe fertilization may also be in error. Unfortunately, there are no reliable quantitative constraints available as to the state of the global silica cycle over the late Quaternary, leaving this as an unknown factor.

Perhaps more problematic to the composite scenario is the response of deep-sea sedimentary CaCO_3 . Preservation of CaCO_3 during glacial periods is over-predicted in the Pacific with a deepening of the calcite lysocline of ~ 1 km. Increased aeolian detrital supply to the deep ocean during glacial periods (e.g., Stages 2, 4, and 6) has a significant diluting effect on CaCO_3 content, indicated by a sharp shoaling of the depth of the lysocline. That this feature is not apparent in the lysocline evolution reconstruction of *Farrell and Prell* [1989] (if not an artefact of their relatively low core resolution and interpolation algorithm) may be a consequence of zonal averaging in the model. Mean detrital deposition to ocean zones in the model will be biased by a component of elevated dust fluxes near ocean margins, and thus will not be representative of the more remote location of many of the sediment cores used in lysocline reconstructions. Similarly, accepting some of the glacial lysocline shoaling as an artefact of model resolution places reconstructed sedimentary CaCO_3 changes in the Atlantic in first-order agreement with observations. The comparatively muted response of the CCD in both Atlantic and Pacific basins is in accordance with observations.

Interestingly, periods of peak detrital input aside, the thickness of the lysocline transition zone in the Pacific appears to be relatively invariant compared to that in the Atlantic. This suggests that Pacific CaCO_3 sediments are responding primarily to changes in ocean $p\text{H}$ rather than being controlled by changes in the CaCO_3 :POC rain ratio. The excessive excursions in lysocline depth in the Pacific together with over-estimated glacial CaCO_3 preservation thus indicates too great a change in deep ocean $p\text{H}$, which at the equator is some ~ 0.12 $p\text{H}$ units higher (3300 depth) during glacial times. This is in contrast to the increase of ~ 0.3 $p\text{H}$ units deduced via the $\delta^{11}\text{B}$ 'paleo-acidity' proxy in this region [*Sanyal et al.*, 1995, 1997]. If this proxy were to be correct then an even greater excursion in lysocline depth than that predicted would be expected. This apparent contradiction between evidence for glacial-interglacial changes in ocean chemistry deduced from sedimentary CaCO_3 and from boron isotopes has been a considerable puzzle in paleoceanography [*Archer et al.*, 2000; *Sanyal et al.*, 1995; *Sigman et al.*, 1998]. However, there is a substantial inter-specific vital influence on ^{11}B fractionation upon calcite deposition [*Sanyal et al.*, 1996; *Vengosh et al.*, 1991]. Benthic foraminiferal $\delta^{11}\text{B}$ measurements are made on mixed assemblages because of the analytical requirements of this method [*Sanyal et al.*, 1996, 1997]. Therefore, there is no guarantee that changes in bulk $\delta^{11}\text{B}$ represent changes in ambient ocean $p\text{H}$ as opposed to changes in species composition or even of the sedimentary environment [*Berger and Vincent*, 1986; *Mackensen et al.*, 1993; *Palmer et al.*, 1998]. If, for the sake of argument, the interpretation of $\delta^{11}\text{B}$ is taken to be correct, then deep waters in the Pacific during the last glacial were characterized by a carbonate ion content some $\sim 100 \mu\text{mol kg}^{-1}$ higher than at present [*Sanyal et al.*, 1995]. However, applying the least $[\text{CO}_3^{2-}]$ -sensitive dependence of foraminiferal ^{13}C fractionation observed by [*Spero et al.*, 1997] (2.2.6.4) would suggest that glacial ocean $\delta^{13}\text{C}^{\text{DIC}}$ was actually some $\sim 0.6\%$ higher than observed,

giving a net deglacial decrease in $\delta^{13}\text{C}^{\text{DIC}}$ of $\sim 0.3\%$. This completely contradicts all that is currently accepted regarding increased storage of carbon in the terrestrial biosphere since the LGM (5.4.6). Given that both proxies extrapolate planktonic fractionation behaviour to the benthic environment [*Spero et al.*, 1997], it would be difficult to entirely accept one whilst disregarding the other. It is, therefore, concluded that the $\delta^{11}\text{B}$ paleo-acidity proxy may well overestimate the magnitude of glacial-interglacial $p\text{H}$ change, perhaps by a factor of three. $[\text{CO}_3^{2-}]$ -dependent ^{13}C fractionation may be similarly overstated for the benthic environment.

In light of its poorly quantified envelope of operation, it is tempting to remove the 'coral reef hypothesis' from the composite scenario in order to meet criteria laid down by the paleoceanographic CaCO_3 record. Indeed, without this mechanism both modern and LGM-age CaCO_3 distributions in the model are consistent with reconstructions (not shown). However, intuitively it seems unlikely that rates of neritic CaCO_3 accumulation should have been largely invariant with respect to substantial changes in sea level and shelf area. However, it is possible that these effects were offset by decreased riverine supply of DIC and ALK (derived via continental weathering) during glacial periods. Although the 'coral reef hypothesis' produces a lagged response in $x\text{CO}_2$ at deglaciation, it is an important component in setting the overall sawtooth form of the glacial-interglacial cycles. It would therefore appear that a mechanism is required that enhances the underlying decline of $x\text{CO}_2$ as glacials deepen but does not drive deep ocean $p\text{H}$ overly high. Such a solution might lie in the long-overlooked phosphate extraction model. As an explanation for the entire magnitude of glacial-interglacial change this fell foul of timing issues together with considerations of oceanic $\delta^{13}\text{C}^{\text{DIC}}$ and dissolved oxygen changes [*Keir and Berger*, 1983; *Knox and McElroy*, 1984; *Shaffer*, 1990]. However, none of these need be violated if only a proportion of the total CO_2 draw-down is required. In the absence of parallel changes in the dissolved Si inventory of the ocean, only non-siliceous phytoplankton might generally be expected to be able to take advantage of increased PO_4 availability. This would lead to increased CaCO_3 export and thus the removal of DIC and ALK from the ocean, exerting a negative pressure on $p\text{H}$. Unfortunately, little is currently quantitatively understood with regards to deposition in the neritic environment and less still reliably known about the fate of interglacial-age sediments deposited there when sea level falls.

Finally, considering the problems discussed above regarding adherence to ocean chemical constraints, even in order to achieve only two thirds of the observed amplitude of glacial-interglacial $x\text{CO}_2$ variability, it is difficult to envisage a substantially larger change in terrestrial carbon inventory than the 500GtC considered so far, as has been proposed by some authors [*Adams et al.*, 1990; *Adams and Faure*, 1998; *Maslin et al.*, 1995].

5.7 The sequence of events surrounding Termination I

In light of the results from both the individual mechanisms tested and from the composite scenario, a conceptual sequence of events perturbing the global carbon cycle at deglaciation is proposed. Termination I is chosen for illustration. A sequence of transitional stages between the end of the LGM and the present-day (pre-industrial) is defined on the basis of identifiable paired trends in both $x\text{CO}_2$ and $\delta^{13}\text{C}^{\text{CO}_2}$ with additional constraints taken from the timing of The Antarctic Cold Reversal (ACR) and Younger Dryas (as delineated by observed variations in Vostok and GRIP CH_4 concentrations [Blunier *et al.*, 1997], and from the recent results presented from DOME C by Monnin *et al.* [2001]). Marine Isotope Stage 1 is subdivided for illustration, something akin to that for Stage 5. The proposed sequence of events surrounding Termination I is as follows (Figure 5-21):

Stage 2. Full glacial conditions. High rates of dust supply to the Southern Ocean (although already starting to decline towards the end of this period). Generally iron replete conditions with a dominance of siliceous phytoplankton in the determination of POC export production. Low levels of $x\text{CO}_2$ and intermediate $\delta^{13}\text{C}^{\text{CO}_2}$.

Stage 1g. Dust deposition to the Southern Ocean decline rapidly and iron starts to limit export production leading to a rise in $x\text{CO}_2$. A combination of decreased productivity together with a shift in ecosystem composition towards non-siliceous species (which fractionate ^{13}C in organic matter less strongly) results in a drop in $\delta^{13}\text{C}^{\text{CO}_2}$ concurrent to the $x\text{CO}_2$ rise. The negative trend in atmospheric isotopic signature is exacerbated by a collapse of the maximum seasonal limits of sea ice extent in the Southern Ocean, perhaps driven by a combination of increasing local temperature and relatively high austral summer insolation levels at 65°S at this time [Jouzel *et al.*, 1987, 1995; Laskar *et al.*, 1993]. Slightly offsetting the negative excursion in $\delta^{13}\text{C}^{\text{CO}_2}$ but enforcing the $x\text{CO}_2$ rise during this stage are increasing SSTs in the southern hemisphere.

Stage 1f. Dust decline is virtually complete, with Southern Ocean productivity at near-interglacial levels. There is a much slower rise in CO_2 levels, perhaps due to increases in carbon stored in the terrestrial biosphere, particularly in the tropics and in the SH offsetting the effect of increasing SSTs. Together these two effects constructively interfere to force $\delta^{13}\text{C}^{\text{CO}_2}$ to start to rise.

Stage 1e. Bölling/Alleröd. The northern hemisphere now starts to deglaciate, with substantial ice sheet collapse. Rapidly rising SSTs in the NH together with an intensification of the Atlantic overturning circulation drive CO_2 levels higher. This is later compensated for by lower SH SSTs during the ACR [Blunier *et al.*, 1997; Smith *et al.*, 1999] producing a slight decline towards the end of this stage. Initial continuing increases in $\delta^{13}\text{C}^{\text{CO}_2}$ also reflect the sudden change in NH climate and

increases in terrestrial biome carbon storage (although it is not immediately obvious what might subsequently produce the slight decline observed).

Stage 1d. Younger Dryas. Return to near-LGM conditions in the North Atlantic region. Atmospheric CO_2 concentrations increase again following the end of the ACR event. Reductions in carbon stored in the terrestrial biosphere could produce further increases in $x\text{CO}_2$ while reducing $\delta^{13}\text{C}^{\text{CO}_2}$, as observed.

Stage 1c. Deglaciation restarts. Similar initial forcings on the system as per Stage 1e. Global climate attains typical interglacial conditions. Further increases in $\delta^{13}\text{C}^{\text{CO}_2}$ throughout this stage driven by higher SSTs in both hemispheres together with greater terrestrial biome carbon storage. After the initial rise there is a gradual reduction in $x\text{CO}_2$ possibly a result of the continued expansion of terrestrial ecosystems, particularly in northern subtropical regions [Brovkin *et al.*, 1998; Claussen and Gayler, 1997; Indermühle *et al.*, 1999].

Stage 1b. Collapse of sub-tropical ecosystems with a slight cooling in climate, leading to a significant fall in $\delta^{13}\text{C}^{\text{CO}_2}$ over the course of this stage, with reduced terrestrial biomass dominating over SST effects to bring about an increase in $x\text{CO}_2$ [Indermühle *et al.*, 1999].

Stage 1a. Slight decrease in $x\text{CO}_2$ with an increase in $\delta^{13}\text{C}^{\text{CO}_2}$ despite no significant climatic change occurring during this interval, perhaps as a result of the expansion of northern hemisphere peatlands [Klinger *et al.*, 1996].

Changes in the oceanic CaCO_3 system (i.e., ‘carbonate compensation’ and neritic CaCO_3 storage) and dissolved Si cycles have not been discussed in the above. While these have time constants of change too long for them to be directly involved in some of the observed rapid variations in the sign of change of atmospheric composition, they will be important in determining the overall deglacial trend.

Supporting the causal linkage between dust supply and $\delta^{13}\text{C}^{\text{CO}_2}$ suggested to account for part of the Stage 1g anomaly are records presented by Ninnemann and Charles [1999] of planktonic foraminiferal $\delta^{13}\text{C}$ from the Southern Ocean. Not only do these exhibit a prominent negative excursion consistent with the Taylor Dome record [Smith *et al.*, 1999] following the dust decline at the end of Stage 2, but also a (slightly smaller) negative excursion at around 60 ka BP, apparently synchronous with the earlier substantive drop-off in dust deposition (as recorded in the Vostok core [Petit *et al.*, 1999]). Additional paleoceanographic evidence that changes in productivity drive at least part of the Stage 1g $\delta^{13}\text{C}^{\text{CO}_2}$ excursion comes from benthic foraminiferal $\delta^{13}\text{C}$ records from the South Atlantic [Charles *et al.*, 1996]. These show prominent negative anomalies, synchronous both with initial rise in local SST (itself synchronous with Vostok δD) and again, also with the Stage 3/4 boundary.

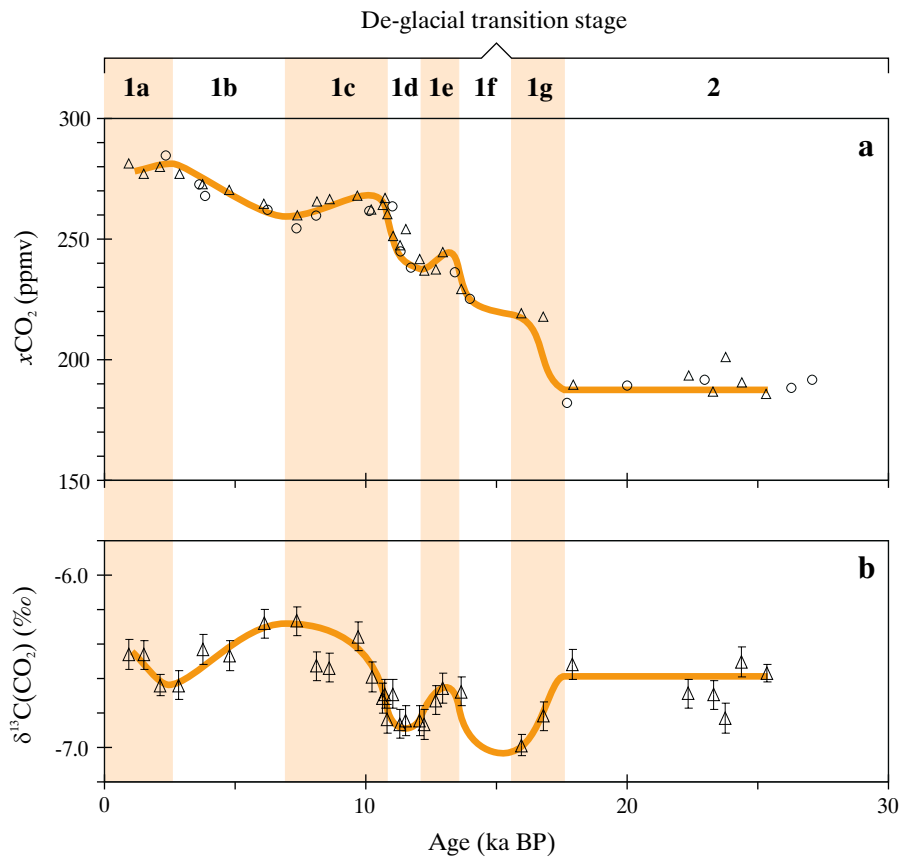


Figure 5-21 Conceptual transition stages in the global carbon cycle surrounding Termination I; (a) observed atmospheric CO₂ concentration records from the Vostok [Petit *et al.*, 1999] (circles) and Taylor Dome [Smith *et al.*, 1999] (triangles) ice cores placed on the Vostok chronology as described previously (5.2), with suggested general trends indicated by the orange line, (b) observed δ¹³C^{CO₂} record from the Taylor Dome [Smith *et al.*, 1999] (triangles) ice core, with suggested general trends again indicated.

5.8 What ultimately drives the deglacial rise in atmospheric CO₂?

Should the onset of Fe limitation in the Southern Ocean brought about by a decline in dust deposition to this region be the primary driving force behind the initial deglacial increase in atmospheric CO₂ levels, what might cause dust to decline in the first place? The mechanisms driving dust variability are especially intriguing since at each glacial termination the decline appears to precede significant changes in other indicators of southern hemisphere climate (such as ice core δD and $x\text{CO}_2$) by some ~5 ka. The interval is as great as 10 ka with respect to northern hemisphere ice sheet collapse [Broecker and Henderson, 1998]. A clue comes from the apparent correlation between periods of rapid sea level fall and peak dust deposition fluxes (Figure 5-22), at least over the last ~250 ka (before which the SPECMAP and Vostok time scales diverge). Furthermore, dust starts to decline slightly prior to the stabilization of sea level at local minima.

Mineralogical and isotopic analysis suggest that the primary source area for dust deposited at Vostok during the LGM was Patagonia [Grousset *et al.*, 1992]. The effective land area of this region would have been substantially enhanced during glacial periods of low sea level stand through the exposure of the adjoining continental shelves [Iriando, 2000]. Unconsolidated shelf sediments could have been easily deflated and transported by the prevailing winds out across the Southern Ocean [Iriando, 2000]. The simplest explanation for the apparent relationship between sea level and Vostok dust fluxes would then be that dust supply is directly related to exposed shelf area. However, assuming dust fluxes in proportion to this area (derived from mean ocean bathymetry lying between 20°S and 70°S [ETOPO5, 1988], encompassing the Patagonian region [Basile *et al.*, 1997]) produces a response that bears little resemblance to the Vostok record. On the basis that dust source regions have a finite lifetime after which they become effectively completely deflated [Pye, 1989; Rea, 1994], the source strength of each portion of shelf newly exposed is relaxed. With a characteristic decay rate of 0.1 ka⁻¹, a series of sharp peaks is obtained lying atop of a background (not shown).

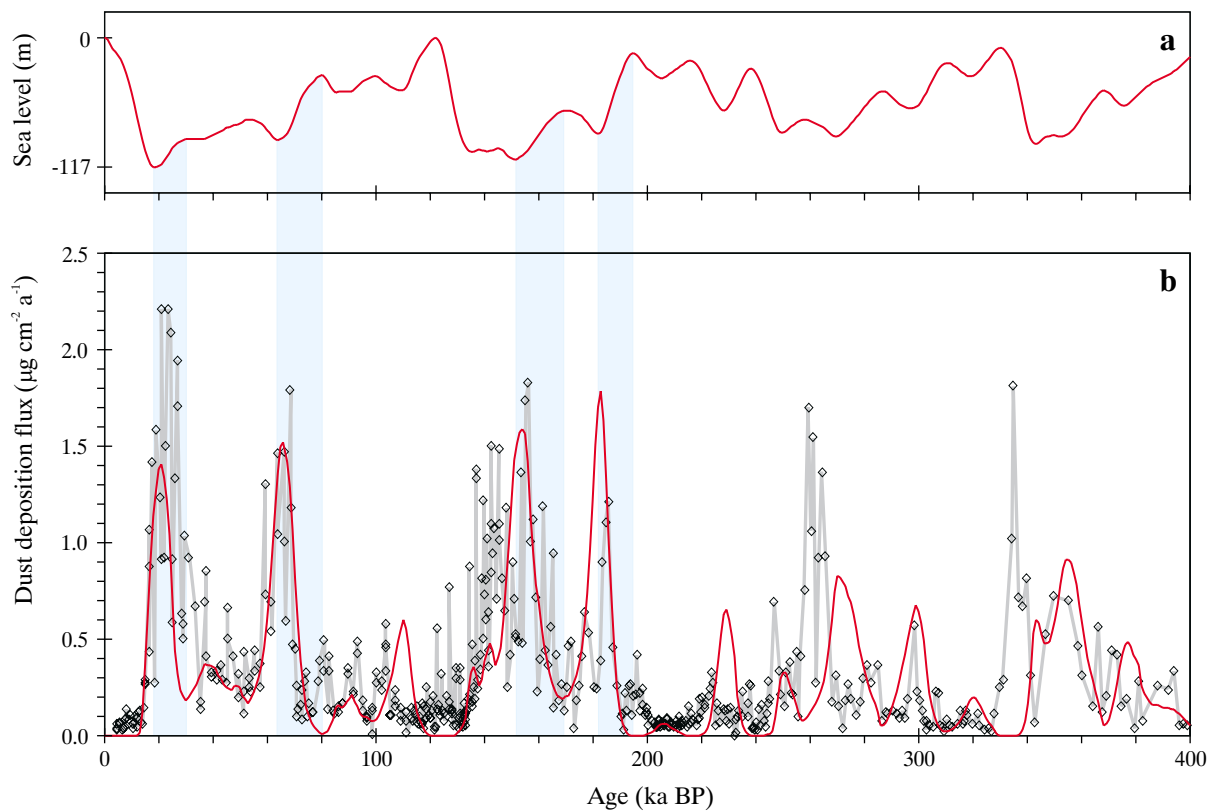


Figure 5-22 Idealized dust flux model based on changes in exposed shelf area in the mid and high southern hemisphere latitudes. Shown are (a) sea level history reconstructed from the SPECMAP $\delta^{18}\text{O}$ stack [Imbrie *et al.*, 1984] and assuming a 117 m rise rise the LGM [Fairbanks, 1989], (b) the Vostok dust deposition flux record [Petit *et al.*, pers comm] (grey line with data points) together with model results (red line). Periods of rapid sea level fall of particular interest are highlighted.

Although the timing of these peaks is in excellent agreement with Vostok, since their heights relate directly to the rate and overall magnitude of each fall in sea level, the strongest dust peak is predicted to occur with the Stage5e/5d transition, contrary to the Vostok record. One final adjustment is now made to the model: since a warm wet climate is conducive to vegetation cover and will hinder atmospheric dust transport [Yung *et al.*, 1996], account must be taken of the gradual climatic transition into cold dry glacial conditions. Model dust fluxes are therefore arbitrarily weighted by the square of SPECMAP (normalized to a value of unity at 19 ka BP). The result of this final model is shown in Figure 5-22. It can be seen that not only can the relative heights and timing of the major dust peaks be reproduced, so can background trends. For the Stage 4 and 2 dust peaks in particular, the respective phases of declining dust fluxes between model and observations correspond to within ~ 1 ka.

Despite the surprising success of such a simple model, recent studies of the provenance of dust deposited in Antarctic ice casts some doubt on this shelf dust source hypothesis. Detailed geochemical analyses based on the Rb-Sr and Sm-Nd isotopic systems put the primary source regions of dust deposited in East Antarctica as Patagonian

loess rather than sediments lying on the Argentine continental shelf [Basile *et al.*, 1997]. Although this suggests that sea level fall cannot directly control dust sources through shelf exposure, the apparent linkage between periods of rapid change as delineated by the SPECMAP $\delta^{18}\text{O}$ record [Imbrie *et al.*, 1984] and peak dust concentrations still requires an explanation. A second hypothesis is therefore advanced, in that during periods of ice sheet advance the supply of glacially-eroded material (particularly fines such as rock flour) fuels the overall rate of dust deflation from Patagonia. In such a scenario, supply falls off as active erosion of new regions ceases with the stabilization of ice extent, with the result that dust fluxes start to decline just as peak glacial conditions are attained, as observed.

Sudden increases in the concentration of atmospheric CO_2 in the atmosphere could thus be a consequence of glaciological dynamics. That deglaciation occurs following Stage 2 rather than Stage 4 may be due to a critical glacial extent having been attained in Patagonia, analogous to the ‘excess ice’ hypothesis [Paillard, 1998; Raymo, 1997; Ridgwell *et al.*, 1999], with the catastrophic collapse of dust supply at the end of Stage 2 perhaps occurring as glaciers reach the ocean margin or extend beyond regions rich in erodible

material. Whatever the ultimate cause of dust variability, declining deposition rates to the Southern Ocean is the only mechanism that clearly precedes $x\text{CO}_2$ rise, strongly implicating it in the initial deglacial perturbation of the global carbon cycle and thus in the dynamics of the 100 ka ice age cycles of the late Quaternary.

Conclusions

The following main conclusions can be drawn from the study presented herein;

(i) simulation of the modern carbon cycle

The framework for biogeochemical cycling developed here, when used in conjunction with a zonally-averaged representation of ocean circulation enables a reasonable simile of the modern ocean carbon cycle to be produced. However, a number of apparent deficiencies arise as a result of the simplified two dimensional circulation, particularly that of 'nutrient trapping' in equatorial up-welling zones. There are also associated problems manifested 'down-stream'; as a consequence of the strong control on total nutrient supply to mid-latitude gyre regions exerted by the equatorial zones, biogeochemical changes at the equator (such as through iron fertilization) are amplified to produce unrealistically large changes in biological productivity at higher latitudes. To retain model biogeochemical integrity, a simple topological fix is employed to lessen the degree of nutrient trapping. This has the advantage of avoiding any serious distortion of global nutrient cycles, such as might occur through the prescription of an excessive dissolved organic matter component to export production.

Despite the obvious first-order importance of the depth at which nutrients are released back into the ocean, the remineralization of biogenic particulates within the water column has been a relatively neglected area of model development. In particular, only recently has account been taken of important influences on opal remineralization such as that of ambient temperature. A new scheme for the remineralization of biogenic opal within the water column developed here, when contrasted with available opal sediment trap data, is demonstrated to offer a significant improvement on previous schemes. However, serious deficiencies in the reproduction of some observations remain, suggesting that further progress will require additional sediment trap observations to be made and the dissolution of biogenic opal more fully (experimentally) characterized. The development and inclusion of mechanistic schemes able to take into account factors determining particulate matter settling rates (including the representation of rapid export events such as those associated with phytoplankton blooms in the surface ocean) would be likely to result in a substantial improvement in overall model realism.

While indices of differential regional control exerted on atmospheric composition are difficult to interpret in terms of the underlying processes responsible, the wide range of sensitivities exhibited to perturbation in key regions (such as the Southern Ocean) amongst different models suggests that more care needs to be taken in model interpretation.

Generation of a standard 'benchmark' of response, perhaps obtained through the one-off use of a state-of-the-art model could form the basis for subsequent quantitative assessment of predictions made by different model formulations.

(ii) simulation of the dynamic evolution of the system

The use of a representation of world ocean circulation derived from a zonally-averaged ocean general circulation model has important computational advantages over its three-dimensional counterpart, enabling easy access to multi-millennial time scales. Fully dynamic (i.e., 'time-stepping') model simulations made over multiple glacial-interglacial cycles provides a means for more fully utilizing the information contained within ice core records. Consideration of both the phase and amplitude of observed variability provides an important constraint on the underlying mechanisms. Ideally, model assessment would be made quantitatively via statistical and spectral methodologies, with system forcings taking into account spatial heterogeneity in the timing and magnitude of changes in boundary conditions. However, full global reconstructions are currently available only for discrete time-slices. An alternative might be to generate continuous time series of spatially-explicit boundary conditions from within a suitable Earth System Model. Forcings on the carbon cycle produced by such a model would have the advantage of being internally consistent, in contrast to paleoclimatic reconstructions made from sediment and ice cores for which there is no precise common chronology. As demonstrated here, even on a simple visual basis, it is still possible to make better use of the Vostok record, with the likely type of mechanism(s) missing from a composite scenario deduced through consideration of the timing of periods of greatest model-observation mismatch.

There is considerable interplay between the various biogeochemical cycles on glacial-interglacial time scales. Central to these is that of the ocean silicic acid cycle, which exerts important controls upon atmospheric and sediment composition through its influence upon biological productivity (particularly in determining the export ratio of calcium carbonate (CaCO_3) to organic carbon). With an adjustment time of order ~ 15 ka for the oceanic silicic acid inventory and ~ 9 ka for the calcite lysocline, it is not necessarily safe to rely upon steady-states when considering glacial-interglacial change. Indeed, the interaction between these two cycles produces an even slower response in the atmospheric concentration of carbon dioxide ($x\text{CO}_2$) with respect to perturbations of the global silicic acid cycle in the model, characterized by an e-folding time of ~ 23 ka. The traditional methodology of contrasting pairs of time slices made at steady state either side of the last deglacial transition (an interval of less than 18 ka) may, therefore, result in an

erroneous assessment of the magnitude of the predicted change in $x\text{CO}_2$.

(iii) simulation of paleoceanographic proxies

Comparisons made between synthetic sediment cores and paleoceanographic proxy records can provide important additional constraints in the elucidation of the processes involved in glacial-interglacial change. For example, although in isolation, reduced aeolian iron supply to the Southern Ocean could explain a significant fraction of the initial observed deglacial increase in $x\text{CO}_2$, the paleoceanographic proxy record in this region clearly indicated an important omission. The anti-phase relationship exhibited by glacial-interglacial changes in sedimentary opal content in cores located either side of the Antarctic Polar Front suggested the presence of contrasting meridional variability in boundary conditions. The substantial glacial expansion of seasonal sea ice limits south of the Antarctic Polar Front, with little change to the north, represents such a contrast. The generation of synthetic sediment records driven by this additional forcing does indeed confirm sea ice extent as a vital element of glacial-interglacial change in this region.

(iv) the role of the neritic environment in the global carbon cycle

Changes in the neritic environment have the potential to account for much of the amplitude of observed $x\text{CO}_2$ variability, particularly through changes in the accumulation rate of CaCO_3 and of organic matter (including its associated nutrients). There is, therefore, a compelling need to understand the role that the coastal system plays in the global carbon cycle. Mechanistic descriptions need to be developed for this environment and coupled with existing carbon cycle models (which tend to represent just the open ocean system).

(v) the role of the Southern Ocean in the global carbon cycle

Results from this study suggest that changes in the surface boundary conditions of the Southern Ocean played a key role in perturbing the global carbon cycle, at least at the time of deglacial inception. Rapid reductions in aeolian iron supply and in maximum seasonal sea ice extents can, between them, explain much of the initial rise in $x\text{CO}_2$ together with the concurrent decrease in its stable isotopic signature. In addition, these two processes produce a response in the ocean surface consistent with the bulk of paleoceanographic observations made in this region. Crucially, even the apparently antagonistic response of the system either side of the Antarctic Polar Front can be accounted for. It is likely that changes in convective regime in the Southern Ocean (not tested here) will have enhanced the effect on the atmosphere.

(vi) glacial-interglacial perturbations in the global carbon cycle

None of the mechanisms considered in this study when considered in isolation are able to simultaneously meet all the constraints dictated by the paleoclimatic record. With the mechanisms applied in concert, though, over two thirds of the amplitude of $x\text{CO}_2$ variability can be explained. However, the component of $x\text{CO}_2$ change due to the 'Coral Reef

Hypothesis' may be overstated (on the basis of deficiencies in the synthetic model paleoceanographic CaCO_3 record) which would reduce the effective magnitude of $x\text{CO}_2$ which can be accounted for consistent with paleoceanographic observations. Model results suggest that perturbations located in the Southern Ocean (aeolian Fe supply, sea ice extent) could potentially account for all of the observed glacial variability in $x\text{CO}_2$ together with the initial deglacial rise. However, longer-term changes in the system routed in oceanic CaCO_3 and silicic acid cycles probably play an important role in defining the envelope of gradual $x\text{CO}_2$ draw-down immediately following each interglacial period. Driving mechanisms for this probably include decreasing neritic CaCO_3 ('Coral Reef Hypothesis') and organic matter ('Phosphate Extraction Model') accumulation rates (as sea level falls), together with increasing dissolved Si supply. Considering the difficulties in generating a sufficient amplitude of $x\text{CO}_2$ variability without contravening paleoceanographic CaCO_3 constraints, it is not easy to reconcile deglacial increases in the carbon inventory of the terrestrial biosphere substantially more than the 500 GtC assumed here.

(vii) dust supply and the ice age cycles

Solely on the basis of its being the only boundary condition to substantially change prior to initial deglacial rise in $x\text{CO}_2$, variability in dust deposition rates to the world ocean would seem likely to be a key element in glacial-interglacial change. This is supported by model results presented here of the effect on $x\text{CO}_2$ of variable aeolian iron supply, either to the Southern Ocean or to the ocean as a whole. These results demonstrate that the apparent lag observed in ice cores between the start of declining aeolian deposition rates and initial deglacial $x\text{CO}_2$ rise can be accounted for as a result of non-linearities inherent in the ocean biogeochemical system. If variability in aeolian iron supply to the ocean does play such a critical role in glacial-interglacial change then it is important that processes controlling dust sources, atmospheric transport, and deposition (including issues of iron solubility) all be understood more fully. It is suggested here that the decline in aeolian deposition rates in the Antarctic towards the end of Stage 2 is inexorably linked to a maximum in global (or local) ice volume having been obtained. Understanding the determinants of dust supply could potentially reveal the reasons for the timing of deglaciation, thus unlocking the secrets of the 100 ka ice age cycles.

References

- Abraham, E. R., et al., Importance of stirring in the development of an iron-fertilized phytoplankton bloom, *Nature*, 407, 727-730, 2000.
- Adams, J. M., H. Faure, L. Faure-Denard, J. M. McGlade, and F. I. Woodward, Increases in terrestrial carbon storage from the Last Glacial Maximum to the present, *Nature*, 348, 711-714, 1990.
- Adams, J. M., and H. Faure, A new estimate of changing carbon storage on land since the last glacial maximum, based on global land ecosystem reconstruction, *Global and Planetary Change*, 17, 3-24, 1998.
- Adkins, J. F., H. Cheng, E. A. Boyle, E. R. M. Druffel, and R. L. Edwards, Deep-sea coral evidence for rapid change in ventilation of the deep North Atlantic 15,400 years ago, *Science*, 280, 725-728, 1998.
- Aksnes, D. L., and J. K. Egge, A theoretical model for nutrient-uptake in phytoplankton, *Marine Ecology Progress Series*, 70, 65-72, 1991.
- Aksnes, D. L., J. K. Egge, R. Rosland, and B. R. Heimdal, Representation of *Emiliania huxleyi* in phytoplankton simulation models - A 1st approach, *Sarsia*, 79, 291-300, 1994.
- Aksnes, D. L., K. B. Ulvestad, B. M. Balino, J. Berntsen, J. K. Egge, and E. Svendsen, Ecological modelling in coastal waters - Towards predictive physical-chemical-biological simulation models, *Ophelia*, 41, 5-36, 1995.
- Aksnes, D. L., and P. Wassmann, The significance of zooplankton grazing for export production, *Limnology and Oceanography*, 38, 978-985, 1993.
- Altabet, M. A., and W. B. Curry, Testing models of past ocean chemistry using foraminifera $^{15}\text{N}/^{14}\text{N}$, *Global Biogeochemical Cycles*, 3, 107-119, 1989.
- Andersen, K. K., A. Armengaud, and C. Genthon, Atmospheric dust under glacial and interglacial conditions, *Geophysical Research Letters*, 25, 2281-2284, 1998.
- Andersen, K. K., and P. D. Ditlevsen, Glacial/interglacial variations of meridional transport and washout of dust: A one-dimensional model, *Journal of Geophysical Research - Atmospheres*, 103, 8955-8962, 1998.
- Andersen, V., P. Nival, and R. P. Harris, Modelling of a phytoplankton ecosystem in an enclosed water column, *J. Mar. Biol. Ass. U.K.*, 67, 407-430, 1987.
- Anderson, R. F., N. Kumar, R. A. Mortlock, P. N. Froelich, P. Kubik, B. Ditttrich-Hannen, and M. Suter, Late-Quaternary changes in productivity of the Southern Ocean, *Journal of Marine Systems*, 17, 497-514, 1998.
- Archer, D., Modeling the calcite lysocline, *Journal of Geophysical Research*, 96, 17037-17050, 1991.
- Archer, D., A data-driven model of the global calcite lysocline, *Global Biogeochemical Cycles*, 10, 511-526, 1996a.
- Archer, D., An atlas of the distribution of calcium carbonate in sediments of the deep sea, *Global Biogeochemical Cycles*, 10, 159-174, 1996b.
- Archer, D., S. Emerson, and C. Reimers, Dissolution of calcite in deep-sea sediments: pH and O_2 microelectrode results, *Geochimica et Cosmochimica Acta*, 53, 2831-2845, 1989.
- Archer, D. E., E. Gidon, A. Winguth, W. Broecker, R. Pierrehumbert, M. Tobis, and R. Jacob, Atmospheric $p\text{CO}_2$ sensitivity to the biological pump in the ocean, *Global Biogeochemical Cycles*, in press.
- Archer, D. E., and K. Johnson, A Model of the iron cycle in the ocean, *Global Biogeochemical Cycles*, 14, 269-279, 2000.
- Archer, D., H. Kheshgi, and E. Maier-Reimer, Dynamics of fossil fuel CO_2 neutralization by marine CaCO_3 , *Global Biogeochemical Cycles*, 12, 259-276, 1998.
- Archer, D., M. Lyle, K. Rodgers, and P. Froelich, what controls opal preservation in tropical deep-sea sediments, *Paleoceanography*, 8, 7-21, 1993.
- Archer, D., and E. Maier-Reimer, Effect of deep-sea sedimentary calcite preservation on atmospheric CO_2 concentration, *Nature*, 367, 260-263, 1994.
- Archer, D., A. Winguth, D. Lea, and N. Mahowald, What caused the glacial/interglacial atmospheric $p\text{CO}_2$ cycles?, *Reviews in Geophysics*, 38, 159-189, 2000.
- Aumont, O., J. C. Orr, P. Monfray, G. Madec, and E. Maier-Reimer, Nutrient trapping in the equatorial Pacific: The ocean circulation solution, *Global Biogeochemical Cycles*, 13, 351-369, 1999.
- Bacastow, R., The effect of temperature change of the warm surface waters of the oceans on atmospheric CO_2 , *Global Biogeochemical Cycles*, 10, 319-333, 1996.
- Bacastow, R., and E. Maier-Reimer, Ocean-circulation model of the carbon cycle, *Climate Dynamics*, 4, 95-125, 1990.
- Balsam, W. L., Carbonate dissolution on the Muir Seamount (western north Atlantic): Interglacial/glacial changes, *Journal of Sedimentary Petrology*, 53, 719-731, 1983.
- Balsam, W. L., and F. W. McCoy, Atlantic sediments: Glacial/interglacial comparisons, *Paleoceanography*, 2, 531-542, 1987.
- Balsam, W. L., B. L. Otto-Bliesner, and B. C. Deaton, Modern and Last Glacial Maximum eolian sedimentation patterns in the Atlantic Ocean interpreted from sediment iron oxide content, *Paleoceanography*, 10, 493-507, 1995.
- Bareille, G., F. E. Grousset, M. Labracherie, L. D. Labeyrie, and J. R. Petit, Origin of detrital fluxes in the southeast Indian Ocean during the last climatic cycle, *Paleoceanography*, 9, 799-819, 1994.
- Barnola, J. M., D. Raynaud, Y. S. Korotkevich, and C. Lorius, Vostok ice core provides 160,000-year record of atmospheric CO_2 , *Nature*, 329, 408-414, 1987.
- Basile, I., F. E. Grousset, M. Revel, J. R. Petit, P. E. Biscaye, and N. I. Barkov, Patagonian origin of glacial dust deposited in East Antarctica (Vostok and Dome C) during glacial stages 2, 4 and 6, *Earth and Planetary Science Letters*, 146, 573-589, 1997.
- Bentaleb, I., and M. Fontugne, The role of the southern Indian Ocean in the glacial to interglacial atmospheric CO_2 change: organic carbon isotope evidences, *Global and Planetary Change*, 17, 25-36, 1998.
- Berelson, W. M., R. F. Anderson, J. Dymond, D. Demaster, D. E. Hammond, R. Collier, S. Honjo, M. Leinen, J. Mcmanus, R. Pope, C. Smith, and M. Stephens, Biogenic budgets of particle rain, benthic remineralization and sediment accumulation in the equatorial Pacific, *Deep-Sea Research Part II - Topical Studies in Oceanography*, 44, 2251-2282, 1997.
- Berger, A., H. Gallee, T. Fichet, I. Marsiat, and C. Tricot, Testing the astronomical theory with a coupled climate-ice-sheet model, *Paleogeography, Paleoclimatology, Paleoecology*, 89, 125-141, 1990.
- Berger, A., J. Guiot, G. Kukla, and P., Pestiaux, Long-term variations of monthly insolation as related to climatic changes, *Geol. Rundsch.*, 70, 748-758, 1981.
- Berger, A., X. S. Li, and M. F. Loutre, Modelling northern hemisphere ice volume over the last 3 Ma, *Quaternary Science Reviews*, 18, 1-11, 1999.
- Berger, A., and M-F. Loutre, Long-term variations in insolation and their effects on climate, the LLN experiments, *Surveys in Geophysics*, 18, 147-161, 1997a.
- Berger, A., and M-F. Loutre, Palaeoclimate sensitivity to CO_2 and insolation, *Ambio*, 26, 32-37, 1997b.
- Berger, A., M. F. Loutre, H. Gallee, Sensitivity of the LLN climate model to the astronomical and CO_2 forcings over the last 200 ky, *Climate Dynamics*, 14, 615-629, 1998.

- Berger, W. H., Deep-sea carbonate and the deglaciation preservation spike in pteropods and foraminifera, *Nature*, 269, 301-304, 1977.
- Berger, W. H., Increase of carbon dioxide in the atmosphere during deglaciation: The coral reef hypothesis, *Naturwissenschaften*, 69, 87-88, 1982a.
- Berger, W. H., Deglacial CO₂ buildup: Constraints on the coral-reef model, *Palaeogeography, Palaeoclimatology, Palaeoecology*, 40, 235-253, 1982b.
- Berger, W. H., Quaternary fourier stratigraphy: Orbital templates and Milankovitch anomalies, *Mathematical Geology*, 26, 769-781, 1994.
- Berger, W. H., T. Bickert, G. Wefer, and M. K. Yasuda, Brunhes-Matuyama boundary: 790 k.y. date consistent with ODP Leg 130 oxygen isotope records based on fit to Milankovitch template, *Geophysical Research Letters*, 22, 1525-1528, 1995.
- Berger, W. H., T. Bickert, M. K. Yasuda, and G. Wefer, Reconstruction of atmospheric CO₂ from ice-core data and the deep-sea record of Ontong Java plateau: The Milankovitch chron, *Geologische Rundschau*, 85, 466-495, 1996.
- Berger, W. H., and G. R. Heath, Vertical mixing in pelagic sediments, *Journal of Marine Research*, 26, 134-143, 1968.
- Berger, W. H., and J. S. Killingley, Box cores from the Equatorial Pacific: 14C sedimentation rates and benthic mixing, *Marine Geology*, 45, 93-125, 1982.
- Berger, W. H., and E. Vincent, Deep-sea carbonate: Reading the carbon-isotope signal, *Geologische Rundschau*, 75, 249-269, 1986.
- Berger, W. H., and G. Wefer, Productivity of the glacial ocean - Discussion of the iron hypothesis, *Limnology and Oceanography*, 36, 1899-1918, 1991.
- Berger, W. H., M. K. Yasuda, T. Bickert, G. Wefer, and T. Takayama, Quaternary time scale for the Ontong Java Plateau: Milankovitch template for Ocean Drilling Program site 806, *Geology*, 22, 463-467, 1994.
- Berner, R. A., and S. Honjo, Pelagic sedimentation of aragonite: Its geochemical significance, *Science*, 211, 940-942, 1981.
- Bertrand, P., et al., The glacial ocean productivity hypothesis - The important of regional temporal and spatial studies, *Marine Geology*, 130, 1-9, 1996.
- Betzler, P. R., R. H. Byrne, J. G. Acker, C. S. Lewis, and R. R. Jolly, The oceanic carbonate system: A reassessment of biogenic controls, *Science*, 226, 1074-1077, 1984.
- Bidle, K. D., and F. Azam, Accelerated dissolution of diatom silica by marine bacterial assemblages, *Nature*, 397, 508-512, 1999.
- Birchfield, G. E., and M. Gill, Climate evolution in the Pliocene and Pleistocene from marine-sediment records and simulations: Internal variability versus orbital forcing, *Journal of Geophysical Research*, 98, 10385-10399, 1993.
- Birchfield, G. E., J. Weertman, and A. T. Lunde, A paleoclimate model of Northern Hemisphere ice sheets, *Quaternary Research*, 15, 126-142, 1981.
- Birchfield, G. E., J. Weertman, and A. T. Lunde, A model study of the role of high-latitude topography in the climatic response to orbital insolation anomalies, *Journal of the Atmospheric Sciences*, 39, 71-87, 1982.
- Bird, M. I., J. Lloyd, and G. D. Farquhar, Terrestrial carbon storage at the LGM, *Nature*, 371, 566, 1994.
- Blain, S., P. Treguer, and M. Rodier, Stocks and fluxes of biogenic silica in the western oligotrophic equatorial Pacific, *Journal of Geophysical Research - Oceans*, 104, 3357-3367, 1999.
- Blunier, T., J. Chappellaz, J. Schwander, B. Stauffer, and D. Raynaud, Variations in atmospheric methane concentrations during the Holocene epoch, *Nature*, 374, 46-49, 1995.
- Blunier, T., J. Chappellaz, J. Schwander, A. Dallenbach, B. Stauffer, T. F. Stocker, D. Raynaud, J. Jouzel, H. B. Clausen, C. U. Hammer, and S. J. Johnsen, Asynchrony of Antarctic and Greenland climate change during the last glacial period, *Nature*, 394, 739-743, 1998.
- Blunier, T., J. Schwander, B. Stauffer, T. Stocker, A. Dallenbach, A. Indermuhle, J. Tschumi, J. Chappellaz, D. Raynaud, and J. M. Barnola, Timing of the Antarctic cold reversal and the atmospheric CO₂ increase with respect to the Younger Dryas event, *Geophysical Research Letters*, 24, 2683-2686, 1997.
- Bolin, B., A. Bjorkstrom, K. Holmen, and B. Moore, The simultaneous use of tracers for ocean circulation studies, *Tellus*, 35, 206-236, 1983.
- Bolton, E. W., K. A. Maasch, and J. M. Lilly, A wavelet analysis of Plio-Pleistocene climate indicators: A new view of periodicity evolution, *Geophysical Research Letters*, 22, 2753-2756, 1995.
- Bond, G., et al., Evidence for massive discharges of icebergs into the North Atlantic Ocean during the last glacial period, *Nature*, 360, 245-249, 1992.
- Boudreau, B. P., Is burial velocity a master parameter for bioturbation, *Geochimica et Cosmochimica Acta*, 58, 1243-1249, 1994.
- Boyd, P. W. et al., A mesoscale phytoplankton bloom in the polar Southern Ocean stimulated by iron fertilization, *Nature*, 407, 695-702, 2000.
- Boyle, E. A., The role of vertical chemical fractionation in controlling Late Quaternary atmospheric carbon dioxide, *Journal of Geophysical Research*, 93, 15701-15714, 1988.
- Boyle, E. A., Pumping iron makes thinner diatoms, *Nature*, 393, 733-734, 1998.
- Brickman, D., W. Hyde, and D. G. Wright, Filtering of Milankovitch cycles by the thermohaline circulation, *Journal of Climate*, 12, 1644-1658, 1999.
- Broccoli, A. J., and S. Manabe, The influence of continental ice, atmospheric CO₂, and land albedo on the climate of the last glacial maximum, *Climate Dynamics*, 1, 87-99, 1987.
- Broecker, W. S., Glacial to interglacial changes in ocean chemistry, *Prog. Oceanog.*, 11, 151-197, 1982a.
- Broecker, W. S., and G. M. Henderson, The sequence of events surrounding Termination II and their implications for the cause of glacial-interglacial CO₂ changes, *Paleoceanography*, 13, 352-364, 1998.
- Broecker, W. S., M. Klas, E. Clark, G. Bonani, S. Ivy, and W. Wolfli, The influence of CaCO₃ dissolution on core top radiocarbon ages for deep-sea sediments, *Paleoceanography*, 6, 593-608, 1991.
- Broecker, W. S., Y. Lao, M. Klas, E. Clark, G. Bonani, S. Ivy, and C. Chen, A search for an early Holocene CaCO₃ preservational event, *Paleoceanography*, 8, 333-339, 1993.
- Broecker, W., J. Lynch-Stieglitz, D. Archer, M. Hofmann, E. Maier-Reimer, O. Marchal, T. Stocker, and N. Gruber, How strong is the Harvardton-Bear constraint?, *Global Biogeochemical Cycles*, 13, 817-820, 1999a.
- Broecker, W., K. Matsumoto, E. Clark, I. Hajdas, and G. Bonani, Radiocarbon age differences between coexisting foraminiferal species, *Paleoceanography*, 14, 431-436, 1999b.
- Broecker, W. S., and T-H. Peng, *Tracers in the Sea*, Lamont-Doherty Geological Observatory, New York, 1982.
- Broecker, W. S., and T-H. Peng, Glacial to interglacial changes in the operation of the global carbon cycle, *Radiocarbon*, 28, 309-327, 1986.
- Broecker, W. S., and T-H. Peng, The cause of the glacial to interglacial atmospheric CO₂ change: A polar alkalinity hypothesis, *Global Biogeochemical Cycles*, 3, 215-239, 1989.
- Broecker, W. S., and T-H. Peng, What caused the glacial to interglacial CO₂ change? in *The Global Carbon Cycle*, edited by Heimann, M., Springer-Verlag, Berlin, 1993.
- Broecker, W. S., T-H. Peng, G. Ostlund, and M. Stuiver, The distribution of bomb radiocarbon in the ocean, *Journal of Geophysical Research*, 90, 6953-6970, 1985.
- Broecker, W. S., and T. Takahashi, The relationship between lysocline depth and in situ carbonate ion concentration, *Deep-Sea Research*, 25, 65-95, 1978.
- Brovkin, V., M. Claussen, V. Petoukhov, and A. Ganopolski, On the stability of the atmosphere-vegetation system in the Sahara/Sahel region, *Journal of Geophysical Research - Atmospheres*, 103, 31613-31624, 1998.
- Brzezinski, M. A., and D. M. Nelson, The annual silica cycle in the Sargasso Sea near Bermuda, *Deep-Sea Research Part I - Oceanographic Research Papers*, 42, 1215-1237, 1995.
- Burkhardt, S., U. Riebesell, and I. Zondervan, Effects of growth rate, CO₂ concentration, and cell size on the stable carbon isotope fractionation in marine phytoplankton, *Geochimica et Cosmochimica Acta*, 63, 3729-3741, 1999.
- Byrne, R. H., J. G. Acker, R. R. Betzer, R. A. Feely, and M. H. Cates, Water column dissolution of aragonite in the Pacific Ocean, *Nature*, 312, 321-326, 1984.
- Calder, N., Arithmetic of ice ages, *Nature*, 252, 216-218, 1974.
- Catubig, N. R., D. E. Archer, R. Francois, P. DeMenocal, W. Howard, and E. F. Yu, Global deep-sea burial rate of calcium

- carbonate during the last glacial maximum, *Paleoceanography*, 13, 298-310, 1998.
- Charette, M. A. and K. O., Buesseler Does iron fertilization lead to rapid carbon export in the Southern Ocean? *Geochemistry Geophysics Geosystems*, 1, 2000.
- Charles, C. D., P. N. Froelich, M. A. Zibello, R. A. Mortlock, and J. J. Morley, Biogenic opal in Southern Ocean sediments over the last 450,000 years: Implications for surface water chemistry and circulation, *Paleoceanography*, 6, 697-728, 1991.
- Charles, C. D., J. Lynch-Stieglitz, U. S. Ninnemann, and R. G. Fairbanks, Climate connections between the hemisphere revealed by deep sea sediment core ice core correlations, *Earth and Planetary Science Letters*, 142, 19-27, 1996.
- Chester, R., K. J. T. Murphy, F. J. Lin, A. S. Berry, G. A. Bradshaw, and P. A. Corcoran, Factors controlling the solubilities of trace metals from non-remote aerosols deposited to the sea surface by the dry deposition model, *Marine Chemistry*, 42, 107-126, 1993.
- Clark, P. U., R. B. Alley, and D. Pollard, Climatology - Northern hemisphere ice-sheet influences on global climate change, *Science*, 286, 1104-1111, 1999.
- Clark, P. U., and D. Pollard, Origin of the middle Pleistocene transition by ice sheet erosion of regolith, *Paleoceanography*, 13, 1-9, 1998.
- Claussen, M., and V. Gayler, The greening of the Sahara during the mid-Holocene: results of an interactive atmosphere-biome model, *Global ecology and Biogeography Letters*, 6, 369-377, 1997.
- CLIMAP project members, The surface of the ice-age Earth, *Science*, 191, 1131-1137, 1976.
- Coale, K. H., J. S. Johnson, S. E. Fitzwater, R. M. Gordon, S. Tanner, F. P. Chavez, L. Ferioli, C. Sakamoto, P. Rogers, F. Millero, P. Steinberg, P. Nightingale, D. Cooper, W. P. Cochlan, M. R. Landry, J. Constantinou, G. Rollwagen, A. Trasvina, and R. Kudela, A massive phytoplankton bloom induced by an ecosystem-scale iron fertilization experiment in the equatorial Pacific Ocean, *Nature*, 383, 495-501, 1996a.
- Coale, K. H., S. E. Fitzwater, R. M. Gordon, K. S. Johnson, and R. T. Barber, Control of community growth and export production by up-welled iron in the equatorial Pacific Ocean, *Nature*, 379, 621-624, 1996b.
- Codispoti, L. A., Is the ocean losing nitrate?, *Nature*, 376, 724, 1995.
- Conkright, M. E., S. Levitus and T. P. Boyer, World Ocean Atlas 1994 Volume 1: Nutrients, *NOAA Atlas NESDIS 1*, U.S. Department of Commerce, Washington, D.C. 150 pp, 1994.
- Crosta, X., J. J. Pichon, and L. H. Burckle, Application of modern analog technique to marine Antarctic diatoms: Reconstruction of maximum sea-ice extent at the Last Glacial Maximum, *Paleoceanography*, 13, 284-297, 1998a.
- Crosta, X., J. J. Pichon, L. H. Burckle, Reappraisal of Antarctic seasonal sea-ice at the Last Glacial Maximum, *Geophysical Research Letters*, 25, 2703-2706, 1998b.
- Crowley, T. J., Calcium-carbonate preservation patterns in the central north Atlantic during the last 150,000 years, *Marine Geology*, 51, 1-14, 1983.
- Crowley, T. J., Ice age carbon, *Nature*, 352, 575-576, 1991.
- Crowley, T. J., Ice-age terrestrial carbon changes revisited, *Global Biogeochemical Cycles*, 9, 377-389, 1995.
- Crowley, T. J., CLIMAP SSTs re-revisited, *Climate Dynamics*, 16, 241-255, 2000.
- Cullen, J. J., Status of the iron hypothesis after the open-ocean enrichment experiment, *Limnology and Oceanography*, 40, 1336-1343, 1995.
- Cullen, J. T., T. W. Lane, F. M. M. Morel, and R. M. Sherrell, Modulation of cadmium uptake in phytoplankton by seawater CO₂ concentration, *Nature*, 402, 165-167, 1999.
- Curry, W. B., and T. J. Crowley, The $\delta^{13}\text{C}$ of equatorial Atlantic surface waters: Implications for ice age pCO₂ levels, *Paleoceanography*, 2, 489-517, 1987.
- Curry, W. B., J. C. Duplessy, L. D. Labeyrie, and N. J. Shackleton, Changes in the distribution of $\delta^{13}\text{C}$ of deep water ΣCO_2 between the last glaciation and the Holocene, *Paleoceanography*, 3, 317-341, 1988.
- Dansgaard, W., H. B. Claussen, N. Gundestrup, C. U. Hammer, S. F. Johnsen, P. M. Kristinsdottir, and N. Reeh, A new Greenland deep ice core, *Science*, 218, 1273-1277, 1982.
- De Angelis, M., N. I. Barkov, and V. N. Petrov, Aerosol concentrations over the last climatic cycle (160 kyr) from an Antarctic ice core, *Nature*, 325, 318-321, 1987.
- de Baar, H. J. W., and T. M. de Jong, *Distributions, sources and sinks of iron in seawater*, In: Turner, D., and R. Hunter (eds), The biogeochemistry of iron in seawater, John Wiley & Sons, Chichester, England, in press.
- de Baar, H. J. W., J. T. M. de Jong, R. F. Nolting, K. R. Timmermans, M. A. VanLeeuwe, U. Bathmann, M. R. VanderLoeff, and J. Sildam, Low dissolved Fe and the absence of diatom blooms in remote Pacific waters of the Southern Ocean, *Marine Chemistry*, 66, 1-34, 1999.
- Deblonde, G., and W. R. Peltier, A model of late Pleistocene ice sheet growth with realistic geography and simplified cryodynamics and geodynamics, *Climate Dynamics*, 5, 103-110, 1990.
- Deblonde, G., and W. R. Peltier, A one-dimensional model of continental ice volume fluctuations through the Pleistocene: Implications for the origin of the mid-Pleistocene climate transition, *Journal of Climate*, 4, 318-344, 1991.
- Deblonde, G., W. R. Peltier, and W. T. Hyde, Simulations of continental ice sheet growth over the last glacial-interglacial cycle: Experiments with a one level seasonal energy balance model including seasonal ice albedo feedback, *Palaogeography, Paleoclimatology, Paleoecology*, 98, 37-55, 1992.
- Deblonde, G., and W. R. Peltier, Late Pleistocene ice age scenarios based on observational evidence, *Journal of Climate*, 6, 709-727, 1993.
- DeLaRocha, C. L., M. A. Brzezinski, M. J. DeNiro, and A. Shemesh, Silicon-isotope composition of diatoms as an indicator of past oceanic change, *Nature*, 395, 680-683, 1999.
- DeMaster, D. J., Continental margin biogenic silica accumulation: Coupling of the marine cycles of organic matter and biogenic silica (abstract), *Southern Ocean - JGOFS Symposium*, 2000.
- DeMenocal, P. B., Pliopleistocene African Climate, *Science*, 270, 53-59, 1995.
- DeMenocal, P. B., W. F. Ruddiman, and E. M. Pokras, Influences of high-latitude and low-latitude processes on African terrestrial climate - Pleistocene eolian records from equatorial Atlantic Ocean Drilling Program Site 663, *Paleoceanography*, 8, 209-242, 1993.
- DeNoblet, N. I., I. C. Prentice, S. Joussaume, D. Texier, A. Botta, and A. Haxeltine, Possible role of atmosphere-biosphere interactions in triggering the last glaciation, *Geophysical Research Letters*, 23, 3191-3194, 1996.
- Dickson, A. G., An exact definition of total alkalinity and a procedure for the estimation of alkalinity and total inorganic carbon from titration data, *Deep-Sea Research*, 28, 609-623, 1981.
- Dickson, A. G., Thermodynamics of the dissociation of boric acid in synthetic seawater from 273.15 to 318.15 K, *Deep-Sea Research*, 37, 755-766, 1990.
- Donaghay, P. L., P. S. Liss, R. A. Duce, A. K. Kester, A. K. Hanson, T. Villareal, N. W. Tindale, and D. J. Gifford, The role of episodic atmospheric nutrient inputs in the chemical and biological dynamics of oceanic ecosystems, *Oceanography*, 4, 62-70, 1991.
- Driscoll, N. W., and G. H. Haug, A short circuit in thermohaline circulation: A cause for northern hemisphere glaciation?, *Science*, 282, 436-438, 1998.
- Drbohlav, J., and F. F. Jin, Inter-decadal variability in a zonally averaged ocean model: An adjustment oscillator, *Journal of Physical Oceanography*, 28, 1252-1270, 1998.
- DuBois, L. G., and W. L. Prell, Effects of carbonate dissolution on the radiocarbon age structure of sediment mixed layers, *Deep-Sea Research*, 35, 1875-1885, 1988.
- Duce, R. A., et al., The atmospheric input of trace species to the world ocean, *Global Biogeochemical Cycles*, 5, 193-259, 1991.
- Ducklow, H. W., Ocean biogeochemical fluxes - New production and export of organic matter from the upper ocean, *Reviews of Geophysics*, 33, 1271-1276, 1995.
- Dugdale, R. C., Nutrient limitation in the sea: Dynamics, identification, and significance, *Limn. Oceanogr.*, 12, 685-695, 1967.
- Dugdale, R. C., and F. P. Wilkerson, Silicate regulation of new production in the equatorial Pacific up-welling, *Nature*, 391, 270-273, 1998.

- Dugdale, R. C., F. P. Wilkerson, and H. J. Minas, The role of silicate pump in driving new production, *Deep-Sea Research I*, 42, 697-719, 1995.
- Duplessy, J. C., N. J. Shackleton, R. G. Fairbanks, L. Laberyie, D. Oppo, and N. Kallel, Deepwater source variations during the last climatic cycle and their impact on the global deepwater circulation, *Paleoceanography*, 3, 343-360, 1988.
- Edwards, R., P. N. Sedwick, V. Morgan, C. F. Boutron, and S. Hong, Iron in ice cores from Law Dome, East Antarctica: implications for past deposition of aerosol iron, *Annals of Glaciology*, 27, 365-370, 1998.
- EGge, J. K., Are diatoms poor competitors at low phosphate concentrations?, *Journal of Marine Systems*, 16, 191-198, 1998.
- EGge, J. K., and D. L. Aksnes, Silicate as regulating nutrient in phytoplankton competition, *Marine Ecology Progress Series*, 83, 281-289, 1992.
- Elderfield, H., and R. E. M. Rickaby, Oceanic Cd/P ratio and nutrient utilization in the glacial Southern Ocean, *Nature*, 405, 305-310, 2000.
- Eppley, R. W., Temperature and phytoplankton growth in the sea, *Fishery Bulletin*, 70, 1063-1085, 1972.
- Erez, J., K. Takahashi, and S. Honjo, In-situ dissolution experiment of Radiolaria in the central North Pacific Ocean, *Earth and Planetary Science Letters*, 59, 245-254, 1982.
- Erickson, D. J., Variations in the global air-sea transfer velocity field of CO₂, *Global Biogeochemical Cycles*, 3, 37-41, 1989.
- Esser, G., and M. Lautenschlager, Estimating the change of carbon in the terrestrial biosphere from 18000 BP to present using a carbon cycle model, *Environmental Pollution*, 83, 45-53, 1994.
- ETOPO5, Data Announcement 88-MGG-02, Digital relief of the Surface of the Earth. NOAA, National Geophysical Data Centre, Boulder, Colorado, 1988.
- Fairbanks, R. G., A 17,000-year glacio-eustatic sea level record: Influence of glacial melting rates on the Younger Dryas event and deep-ocean circulation, *Nature*, 342, 637-642, 1989.
- Falkowski, P. G., Species variability in the fractionation of C-13 and C-12 by marine phytoplankton, *Journal of Plankton Research*, 13, S21-S28, 1991.
- Falkowski, P. G., Evolution of the nitrogen cycle and its influence on the biological sequestration of CO₂ in the ocean, *Nature*, 387, 272-275, 1997.
- Falkowski, P., et al., The global carbon cycle: A test of our knowledge of earth as a system, *Science*, 290, 291-296, 2000.
- Farrell, J. W., and W. L. Prell, Climatic change and CaCO₃ preservation: An 800,000 year bathymetric reconstruction from the central equatorial Pacific Ocean, *Paleoceanography*, 4, 447-466, 1989.
- Farrell, J. W., and W. L. Prell, Pacific CaCO₃ preservation and $\delta^{18}\text{O}$ since 4 Ma: Paleoceanic and paleoclimatic implications, *Paleoceanography*, 6, 485-498, 1991.
- Fasham, M. J. R., H. W. Ducklow, and S. M. McKelvie, A nitrogen-based model of plankton dynamics in the oceanic mixed layer, *Journal of Marine Research*, 48, 591-639, 1990.
- Faure, H., J. M. Adams, J. P. Debenay, L. FaureDenard, D. R. Grant, P. A. Pirazzoli, B. Thomassin, A. A. Velichko, and C. Zazo, Carbon storage and continental land surface change since the Last Glacial Maximum, *Quaternary Science Reviews*, 15, 843-849, 1996.
- Fichefet, T., S. Hovine, and J. C. Duplessy, A model study of the Atlantic thermohaline circulation during the Last Glacial Maximum, *Nature*, 372, 252-255, 1994.
- Fitzwater, S. E., K. H. Coale, R. M. Gordon, K. S. Johnson, and M. E. Ondrusek, Iron deficiency and phytoplankton growth in the equatorial Pacific, *Deep-Sea Research Part II - Topical Studies in Oceanography*, 43, 995-1015, 1996.
- France-Lanord, C., and L. A. Derry, Organic carbon burial forcing of the carbon cycle from Himalayan erosion, *Nature*, 390, 65-67, 1997.
- Francois, R., M. A. Altabet, E-F. Yu, D. M. Sigman, M. P. Bacon, M. Frank, G. Bohrmann, G. Bareille, and L. D. Laberyie, Contribution of Southern Ocean surface-water stratification to low atmospheric CO₂ concentrations during the last glacial period, *Nature*, 389, 929-935, 1997.
- Francois, L. M., C. Delire, P. Warnant, and G. Munhoven, Modelling the glacial-interglacial changes in the continental biosphere, *Global and Planetary Change*, 17, 37-52, 1998.
- Francois, L. M., Y. Godderis, P. Warnant, G. Ramstein, N deNoblet, and S. Lorenz, Carbon stocks and isotopic budgets of the terrestrial biosphere at mid-Holocene and last glacial maximum times, *Chemical Geology*, 159, 163-189, 1999.
- Friedlingsteir, P., C. Delire, J. F. Muller, and J. C. Gerard, The climate induced variation of the continental biosphere - A model simulation of the Last Glacial Maximum, *Geophysical Research Letters*, 19, 897-900, 1992.
- Froelich, P. N., V. Blanc, R. A. Mortlock, S. N. Chillrud, W. Dunstan, A. Udomkit, and T-H. Peng, River fluxes of dissolved silica to the ocean were higher during glacial: Ge/Si in diatoms, rivers, and oceans, *Paleoceanography*, 7, 739-767, 1992.
- Fung, I. Y., S. K. Meyn, I. Tegen, S. C. Doney, J. G. John, and J. K. B. Bishop, Iron supply and demand in the upper ocean, *Global Biogeochemical Cycles*, 14, 281-295, 2000.
- Gallimore, R. G., and J. E. Kutzbach, Role of orbitally induced changes in tundra area in the onset of glaciation, *Nature*, 381, 503-505, 1996.
- Ganeshram, R. S., T. F. Pedersen, S. E. Calvert, and J. W. Murray, Large changes in oceanic nutrient inventories from glacial to interglacial periods, *Nature*, 376, 755-758, 1995.
- Ganopolski, A., C. Kubatzki, M. Claussen, V. Brovkin, and V. Petoukhov, The influence of vegetation-atmosphere-ocean interaction on climate during the mid-Holocene, *Science*, 280, 1916-1919, 1998a.
- Ganopolski, A., S. Rahmstorf, V. Petoukhov, and M. Claussen, Simulation of modern and glacial climates with a coupled global model of intermediate complexity, *Nature*, 391, 351-356, 1998b.
- Genthon, C., Simulations of desert dust and sea salt aerosols in Antarctic with a General Circulation Model of the atmosphere, *Tellus Series B*, 44, 371-389, 1992.
- Gerringa, L. J. A., H. J. W. de Baar, and K. R. Timmermans, A comparison of iron limitation of phytoplankton in natural oceanic waters and laboratory media conditioned with EDTA, *Marine Chemistry*, 68, 335-346, 2000.
- Gnanadesikan, A., A global model of silicon cycling: Sensitivity to eddy parameterization and dissolution, *Global Biogeochemical Cycles*, 13, 199-220, 1999a.
- Goericke, R., and B. Fry, Variations of marine plankton $\delta^{13}\text{C}$ with latitude, temperature, and dissolved CO₂ in the world ocean, *Global Biogeochemical Cycles*, 8, 85-90, 1994.
- Gordon, R. M., K. H. Coale, and K. S. Johnson, Iron distributions in the equatorial Pacific: Implications for new production, *Limnol. Oceanogr.*, 42, 419-431, 1997.
- Greene, R. M., R. J. Geider, and P. G. Falkowski, Effect of iron limitation on photosynthesis in a marine diatom, *Limnology and Oceanography*, 36, 1772-1782, 1991.
- Grousset, F. E., P. E. Biscaye, M. Revel, J. R. Petit, K. Pye, S. Joussaume, and J. Jouzel, Antarctic (Dome C) ice core dust at 18 ky BP - Isotopic constraints on origins, *Earth and Planetary Science Letters*, 111, 175-182, 1992.
- Guilerson, T. P., R. G. Fairbanks, and J. L. Rubenstone, Tropical temperature variations since 20,000 years ago: Modulating inter-hemispheric climate change, *Science*, 263, 663-665, 1994.
- Guinasso, N. L., and D. R. Schink, Quantitative estimates of biological mixing rates in abyssal sediments, *Journal of Geophysical Research*, 80, 3032-3043, 1975.
- Hagelberg, T., N. Piasias, and S. Elgar, Linear and nonlinear couplings between orbital forcing and the marine $\delta^{18}\text{O}$ record during the late Neogene, *Paleoceanography*, 6, 729-746, 1991.
- Hales, S., and S. Emerson, Calcite dissolution in sediments on the Ontong-Java Plateau - *in situ* measurements of pore-water O₂ and pH, *Global Biogeochemical Cycles*, 10, 527-541, 1996.
- Hales, S., S. Emerson, and D. Archer, Respiration and dissolution in the sediments of the western north Atlantic - Estimates from models of *in situ* microelectrode measurements of pore-water oxygen and pH, *Deep-Sea Research Part I - Oceanographic Research Papers*, 41, 695-719, 1994.
- Harrison, K. G., Role of increased marine silica input on paleo-pCO₂ levels, *Paleoceanography*, 15, 292-298, 2000.
- Hausman, E. D., and M. B. McElroy, Role of sea-surface temperature and ocean circulation changes in the reorganization of the global carbon cycle at the last glacial termination, *Global Biogeochemical Cycles*, 13, 371-381, 1999.
- Hay, W. W., The role of polar deep water formation in global climate change, *Annu. Rev. Earth Planet. Sci.*, 21, 227-254, 1993.

- Hay, W. W., Tectonics and climate, *Geol. Rundsch.*, 85, 409-437, 1996.
- Heinze, C., Glacial ocean carbon cycle modeling, in *Carbon cycling in the glacial ocean: Constraints on the ocean's role in global change*, edited by Zahn, R., T. F. Pedersen, M. A. Kaminski, and L. Labeyrie, Springer-Verlag, Berlin, 1994.
- Heinze, C., and T. J. Crowley, Sedimentary response to ocean gateway circulation changes, *Paleoceanography*, 12, 742-754, 1997.
- Heinze, C., E. Maier-Reimer, A. M. E. Winguth, and D. Archer, A global oceanic sediment model for long-term climate studies, *Global Biogeochemical Cycles*, 13, 221-250, 1999.
- Heinze, C., E. Maier-Reimer, and K. Winn, Glacial $p\text{CO}_2$ reduction by the world ocean: Experiments with the Hamburg carbon cycle model, *Paleoceanography*, 6, 395-430, 1991.
- Hendersen, H. M. And N. C., Slowey, Evidence from U-Th dating against Northern Hemisphere forcing of the penultimate deglaciation, *Nature*, 404, 61-66, 2000.
- Hensen, C., H. Landenberger, M. Zabel, and H. D. Schulz, Quantification of diffusive benthic fluxes of nitrate, phosphate, and silicate in the southern Atlantic Ocean, *Global Biogeochemical Cycles*, 12, 193-210, 1998.
- Hinga, K. R., M. A. Arthur, M. E. Q. Pilon, and D. Whitaker, Carbon isotope fractionation by marine phytoplankton in culture - The effects of CO_2 concentration, pH, temperature, and species, *Global Biogeochemical Cycles*, 8, 91-102, 1994.
- Hofmann, M., W. S. Broecker, and J. Lynch-Stieglitz, Influence of a $[\text{CO}_2]_{\text{atm}}$ dependent biological C-isotope fractionation on glacial $^{13}\text{C}/^{12}\text{C}$ ratios in the ocean, *Global Biogeochemical Cycles*, 13, 873-883, 2000.
- Holligan, P. M., and J. E. Robertson, Significance of ocean carbonate budgets for the global carbon cycle, *Global Change Biology*, 2, 85-95, 1996.
- Holtlag, A. A. M., and A. P. VanUlden, A simple scheme for daytime estimates of the surface fluxes from routine weather data, *Journal of Climate and Applied Meteorology*, 22, 517-529, 1983.
- Honjo, S., Material fluxes and modes of sedimentation in the mesopelagic and bathypelagic zones, *Journal of Marine Research*, 38, 53-97, 1980.
- Honjo, S., S. J. Manganini, and J. J. Cole, Sedimentation of biogenic matter in the deep ocean, *Deep Sea Research*, 29, 609-625, 1982.
- Honjo, S., and S. J. Manganini, Annual biogenic particulate fluxes to the interior of the north Atlantic Ocean studies at 34°N 21°W and 48°N 21°W, *Deep-Sea Research Part II - Topical Studies in Oceanography*, 40, 587-607, 1993.
- Hotinski, R. M., L. R. Kump, and R. G. Najjar, Opening Pandora's Box: The impact of open system modeling on interpretations of anoxia, *Paleoceanography*, 15, 267-279, 2000.
- Howard, W. R., and W. L. Prell, Late Quaternary CaCO_3 production and preservation in the Southern Ocean: Implications for oceanic and atmospheric carbon cycling, *Paleoceanography*, 9, 453-482, 1994.
- Hovine, S., and T. Fichfet, A zonally averaged 3-basin ocean circulation model for climate studies, *Climate Dynamics*, 10, 313-331, 1994.
- Hughes, T., Abrupt climatic change related to unstable ice-sheet dynamics: Toward a new paradigm, *Palaeogeography, Palaeoclimatology, Palaeoecology*, 97, 203-234, 1992.
- Hurtt, G. C., and R. A. Armstrong, A pelagic ecosystem model calibrated with BATS data, *Deep-Sea Research Part II - Topical Studies in Oceanography*, 43, 653-683, 1996.
- Hurtt, G. C., and R. A. Armstrong, A pelagic ecosystem model calibrated with BATS and OWSI data, *Deep-Sea Research Part I - Oceanographic Research Papers*, 46, 27-61, 1999.
- Hutchins, D. A., and K. W. Bruland, Iron-limited diatom growth and Si:N uptake ratios in a coastal up-welling regime, *Nature*, 393, 561-564, 1998.
- Hutchins, D. A., G. R. DiTullio, Y. Zhang, and K. W. Bruland, An iron limitation mosaic in the California up-welling regime, *Limnology and Oceanography*, 43, 1037-1054, 1998.
- Hutson, W. H., Bioturbation of deep-sea sediment: Oxygen isotopes and stratigraphic uncertainty, *Geology*, 8, 127-130, 1980.
- Ikehara, M., K. Kawamura, N. Ohkouchi, M. Murayama, T. Nakamura, and A. Taira, Variations of terrestrial input and marine productivity in the Southern Ocean (48 degrees S) during the last two deglaciations, *Paleoceanography*, 15, 170-180, 2000.
- Imbrie, J. et al., The orbital theory of Pleistocene climate: Support from a revised chronology of the marine $\delta^{18}\text{O}$ record, in *Milankovitch and Climate, Part I*, edited by Berger, A., J. Imbrie, J. Hayes, G. Kukla, and B. Saltzman, D. Reidel, Norwell, Mass., 1984.
- Imbrie, J., A. Berger, E. A. Boyle, S. C. Clemens, A. Duffy, W. R. Howard, G. Kukla, J. Kutzbach, D. G. Martinson, A. McIntyre, A. C. Mix, B. Molina, J. J. Morley, L. C. Peterson, N. G. Pisias, W. L. Prell, M. E. Raymo, N. J. Shackleton, and J. R. Toggweiler, On the structure and origin of major glaciation cycles 2. The 100,000-year cycle, *Paleoceanography*, 8, 669-735, 1993.
- Imbrie, J., and K. P. Imbrie, *Ice ages: Solving the mystery*, Harvard University Press, Cambridge, Mass., 1979.
- Imbrie, J., and J. Z. Imbrie, Modeling the climatic response to orbital variations, *Science*, 207, 943-953, 1980.
- Indermuhle, A., T. F. Stocker, F. Joos, H. Fischer, H. J. Smith, M. Wahlen, B. Deck, D. Mastroianni, J. Tschumi, T. Blunier, R. Meyer, and B. Stauffer, Holocene carbon-cycle dynamics based on CO_2 trapped in ice at Taylor Dome, Antarctica, *Nature*, 398, 121-126, 1999.
- Ingle, S. E., Solubility of calcite in the ocean, *Marine Chemistry*, 3, 301-319, 1975.
- IPCC, (Intergovernmental Panel on Climate Change), *Climatic Change: The IPCC Scientific Assessment*, Houghton, J. T., G. J. Jenkins, and J. J. Ephraums (eds), Cambridge University Press, Cambridge, UK, 1990.
- Iriondo, M., Patagonian dust in Antarctica, *Quaternary International*, 68-71, 83-86, 2000.
- Iriondo, M., and N. O. Garcia, Climatic variations in the Argentine plains during the last 18,000 years, *Palaeogeography, Palaeoclimatology, Palaeoecology*, 101, 209-220, 1993.
- Jahnke, R. A., D. B. Craven, D. C. McCorkle, and C. E. Reimers, CaCO_3 dissolution in California continental margin sediments: The influence of organic matter remineralization, *Geochimica et Cosmochimica Acta*, 61, 3587-3604, 1997.
- Jickells, T. D., The inputs of dust derived elements to the Sargasso Sea; a synthesis, *Marine Chemistry*, 68, 5-14, 1999.
- Jickells, T. D., and L. J. Spokes, Atmospheric iron inputs to the oceans, in *The biogeochemistry of iron in seawater*, edited by Turner, D., and R. Hunter, John Wiley & Sons, Chichester, England, in press.
- Johnsen, S. J., et al., The $\delta^{18}\text{O}$ record along the Greenland Ice Core Project deep ice core and the problem of possible Eemian climatic instability, *Journal of Geophysical Research*, 102, 26397-26410, 1997.
- Johnson, K. S., R. M. Gordon, and K. H. Coale, What controls dissolved iron concentrations in the world ocean?, *Marine Chemistry*, 57, 137-161, 1997a.
- Joos, F., J. C. Orr, and U. Siegenthaler, Ocean carbon transport in a box-diffusion versus a general circulation model, *Journal of Geophysical Research-Oceans*, 102, 12367-12388, 1997.
- Joussaume, S., Paleoclimatic tracers - An investigation using an Atmospheric General Circulation Model under ice age conditions. I. Desert dust, *Journal of Geophysical Research*, 98, 2767-2805, 1993.
- Jouzel, J., N. I. Barkov, J. M. Barnola, M. Bender, J. Chappellaz, C. Genthon, V. M. Kotlyakov, V. Lipenkov, C. Lorius, J. R. Petit, D. Raynaud, G. Raisneck, C. Ritz, T. Sowers, M. Stievenard, F. Yiou, and P. Yiou, Extending the Vostok ice-core record of paleoclimate to the penultimate glacial period, *Nature*, 364, 407-412, 1993.
- Jouzel, J., C. Lorius, J. R. Petit, C. Genthon, N. I. Barkov, V. M. Kotlyakov, and V. M. Petrov, Vostok ice core: A continuous isotope temperature record over the last climatic cycle (160,000 years), *Nature*, 329, 403-408, 1987.
- Jouzel, J., et al., The 2-step shape and timing of the last deglaciation in Antarctica, *Climate Dynamics*, 11, 151-161, 1995.
- Kamatani, A., Dissolution rates of silica from diatoms decomposing at various temperatures, *Marine Biology*, 68, 91-96, 1982.
- Karlin, R., M. Lyle, and R. Zahn, Carbonate variations in the northeast Pacific during the late Quaternary, *Paleoceanography*, 7, 43-61, 1992.
- Keir, R. S., The dissolution kinetics of biogenic calcium carbonates in seawater, *Geochimica et Cosmochimica Acta*, 44, 241-252, 1980.
- Keir, R. S., On the late Pleistocene ocean geochemistry and circulation, *Paleoceanography*, 3, 413-445, 1988.

- Keir, R. S., Cold surface ocean ventilation and its effect on atmospheric CO₂, *Journal of Geophysical Research*, 98, 849-856, 1993a.
- Keir, R. S., Are atmospheric CO₂ content and Pleistocene climate connected by wind-speed over a polar Mediterranean Sea, *Global and Planetary Change*, 8, 59-68, 1993b.
- Keir, R. S., Is there a component of Pleistocene CO₂ change associated with carbonate dissolution cycles?, *Paleoceanography*, 10, 871-880, 1995.
- Keir, R. S., and W. H. Berger, Atmospheric CO₂ content in the last 120,000 years: The phosphate-extraction model, *Journal of Geophysical Research*, 88, 6027-6038, 1983.
- Keir, R. S., and W. H. Berger, Late Holocene carbonate dissolution in the equatorial Pacific: Reef growth or neoglaciation, *American Geophysical Union Geophysical Monograph*, 32, 208-219, 1985.
- Keir, R. S., and R. L. Michel, Interface dissolution control of the ¹⁴C profile in marine sediment, *Geochimica et Cosmochimica Acta*, 57, 3563-3573, 1993.
- Kim, S.-J., T. J. Crowley, and A. Stossel, Local orbital forcing of Antarctic climate change during the last interglacial, *Science*, 280, 728-730, 1998.
- Klepper, O., B. J. Dehaan, and H. Vanhuet, Biochemical feedbacks in the oceanic carbon cycle, *Ecological Modelling*, 75, 459-469, 1994.
- Kleypas, J. A., Modelled estimates of global reef habitat and carbonate production since the last glacial maximum, *Paleoceanography*, 12, 533-545, 1997.
- Klinger, L. F., J. A. Taylor, and L. G. Franzen, The potential role of peatland dynamics in ice-age initiation, *Quaternary Research*, 45, 89-92, 1996.
- Knox, F., and M. B. McElroy, Changes in atmospheric CO₂: Influence of the marine biota at high latitudes, *Journal of Geophysical Research - Atmospheres*, 89, 4629-4637, 1984.
- Kriest, I., and G. T. Evans, Representing phytoplankton aggregates in biogeochemical models, *Deep-Sea Research Part I - Oceanographic Research Papers*, 46, 1841-1859, 1999.
- Kukla, G., A. Berger, R. Lotti, and J. Brown, Orbital signature of interglacials, *Nature*, 290, 295-300, 1981.
- Kuma, K., A. Katsumoto, H. Kawakami, F. Takatori, and K. Matsunaga, Spatial variability of Fe(III) hydroxide solubility in the water column of the northern North Pacific Ocean, *Deep-Sea Research Part I - Oceanographic Research Papers*, 45, 91-113, 1998.
- Kumar, N., R. F. Anderson, R. A. Mortlock, P. N. Froelich, P. Kubik, B. Ditttrich-Hannen, and M. Suter, Increased biological productivity and export production in the glacial Southern Ocean, *Nature*, 378, 675-680, 1995.
- Kump, L., Oceans of change, *Nature*, 361, 592-593, 1993.
- Kurz, K. D., and E. Maier-Reimer, Iron fertilization of the Austral Ocean - The Hamburg model assessment, *Global Biogeochemical Cycles*, 7, 229-244, 1993.
- Lambeck, K., and M. Nakada, Constraints on the age and duration of the last interglacial period and on sea-level variations, *Nature*, 357, 125-128, 1992.
- Laskar, J., F. Joutel, and F. Boudin, Orbital, precessional, and insolation quantities for the Earth from -20Myr to +10 Myr, *Astron. Astrophys.*, 270, 522-533, 1993.
- Lau, K. M., and H. Weng, Climate signal detection using wavelet transform: How to make a time series sing, *Bulletin of the American Meteorological Society*, 76, 2391-2402, 1995.
- Ledley, T. S., and S. Chu, The initiation of ice sheet growth, Milankovitch solar radiation variations, and the 100 ky ice age cycle, *Climate Dynamics*, 11, 439-445, 1995.
- Lefevre, N., and A. J. Watson, Modelling the geochemical cycle of iron in the oceans and its impact on atmospheric CO₂ concentrations, *Global Biogeochemical Cycles*, 13, 715-736, 1999.
- Legeleux, F., J. L. Reyss, and S. Schmidt, Particle mixing rates in sediments of the northeast tropical Atlantic - Evidence from Pb₂₁₀_{xs}, Cs₁₃₇, Th₂₂₈_{xs}, and Th₂₃₄_{xs} downcore distributions, *Earth and Planetary Science Letters*, 128, 545-562, 1994.
- LeTreau, H., and M. Ghil, Orbital forcing, climatic interactions, and glaciation cycles, *Journal of Geophysical Research*, 88, 5167-5190, 1983.
- Leuenberger, M., U. Siegenthaler, and C. C. Langway, Carbon isotope composition of atmospheric CO₂ during the last ice age from an Antarctic ice core, *Nature*, 357, 488-490, 1992.
- Levitus S. and T.P. Boyer, World Ocean Atlas 1994 Volume 2: Oxygen, *NOAA Atlas NESDIS 2*, U.S. Department of Commerce, Washington, D.C. 186 pp, 1994a.
- Levitus S., R. Burgett and T. P. Boyer, World Ocean Atlas 1994 Volume 3: Salinity, *NOAA Atlas NESDIS 3*, U.S. Department of Commerce, Washington, D.C. 99 pp, 1994b.
- Levitus S. and T. P. Boyer, World Ocean Atlas 1994 Volume 4: Temperature, *NOAA Atlas NESDIS 4*, U.S. Department of Commerce, Washington, D.C. 117 pp, 1994c.
- Leynaert, A., D. M. Nelson, B. Queguiner, and P. Treguer, The silica cycle in the Antarctic Ocean - Is the Weddell Sea atypical?, *Marine Ecology Progress Series*, 96, 1-15, 1993.
- Li, X. S., A. Berger, and M. F. Loutre, CO₂ and Northern Hemisphere ice variations over the middle and late Quaternary, *Climate Dynamics*, 14, 537-544, 1998a.
- Li, X. S., A. Berger, M. F. Loutre, M. A. Maslin, G. H. Haug, and R. Tiedemann, Simulating late Pliocene northern hemisphere climate with the LLN 2-D model, *Geophysical Research Letters*, 25, 915-918, 1998b.
- Lindzen, R. S., A simple model for 100k-year oscillations in glaciation, *Journal of Atmospheric Sciences*, 43, 986-996, 1986.
- Loehle, C., Geologic methane as a source for postglacial CO₂ increases - The hydrocarbon pump hypothesis, *Geophysical Research Letters*, 20, 1415-1418, 1993.
- Lorius, C., J. Jouzel, D. Raynaud, J. Hansen, and H. L. Treut, The ice-core record: Climate sensitivity and future greenhouse warming, *Nature*, 347, 139-145, 1990.
- Loutre, M. F., and A. Berger, No glacial-interglacial cycle in the ice volume simulated under a constant astronomical forcing and a variable CO₂, *Geophysical Research Letters*, 27, 783-786, 2000.
- Lynch-Stieglitz, J., T. F. Stocker, W. S. Broecker, and R. G. Fairbanks, The influence of air-sea exchange on the isotopic composition of oceanic carbon - Observations and modelling, *Global Biogeochemical Cycles*, 9, 653-665, 1995.
- Maasch, K. A., Statistical detection of the mid-Pleistocene transition, *Climate Dynamics*, 2, 133-143, 1988.
- Mackensen, A., H. W. Hubberten, T., Bickert, G. Fischer, and D. K. Futterer, The δ¹³C in benthic foraminiferal tests of *Fontbotia wuellerstorfi* relative to the δ¹³C of dissolved inorganic carbon in Southern Ocean deep-water - Implications for glacial ocean circulation models, *Paleoceanography*, 8, 587-610, 1993.
- Mahowald, N., K. Kohfeld, M. Hansson, Y. Balkanski, S. P. Harrison, I. C. Prentice, M. Schulz, and H. Rodhe, Dust sources and deposition during the last glacial maximum and current climate: A comparison of model results with paleodata from ice cores and marine sediments, *Journal of Geophysical Research - Atmospheres*, 104, 15895-15916, 1999.
- Maier-Reimer, E., Geochemical cycles in an ocean general circulation model. Pre-industrial tracer distributions, *Global Biogeochemical Cycles*, 7, 645-677, 1993.
- Maier-Reimer, E., and K. Hasselmann, Transport and storage of CO₂ in the ocean - and inorganic ocean-circulation carbon cycle model, *Climate Dynamics*, 2, 63-90, 1987.
- Mangini, A., A. Eisenhauer, and P. Walter, A spike of CO₂ in the atmosphere at glacial-interglacial boundaries induced by rapid deposition of manganese in the oceans, *Tellus Series B*, 43, 97-105, 1991.
- Mann, M. E., and J. M. Lees, Robust estimation of background noise and signal detection in climatic time series, *Climate Dynamics*, 33, 409-445, 1996.
- Marchal, O., T. F. Stocker, and F. Joos, Impact of oceanic reorganizations on the ocean carbon cycle and atmospheric carbon dioxide content, *Paleoceanography*, 13, 225-244, 1998a.
- Marchal, O., T. F. Stocker, and F. Joos, A latitude-depth, circulation biogeochemical ocean model for paleoclimate studies. Development and sensitivities, *Tellus Series B - Physical and Physical Meteorology*, 50B, 290-316, 1998b.
- Marchal, O., T. F. Stocker, F. Joos, A. Indermuhle, T. Blunier, and J. Tschumi, Modelling the concentration of atmospheric CO₂ during the Younger Dryas climate event, *Climate Dynamics*, 15, 341-354, 1999.
- Marino, B. D., M. B. McElroy, R. J. Salawitch, and W. G. Spaulding, Glacial-to-interglacial variations in the carbon isotopic composition of atmospheric CO₂, *Nature*, 357, 461-466, 1992.
- Martin, J. H., Glacial-interglacial CO₂ change: The iron hypothesis, *Paleoceanography*, 5, 1-13, 1990.

- Martin, J. H. and S. E. Fitzwater, Iron deficiency limits phytoplankton growth in the northeast Pacific subantarctic, *Nature*, 331, 341-343, 1988.
- Martin, J. H., S. E. Fitzwater, R. M. Gordon, C. N. Hunter, and S. J. Tanner, Iron, primary production and carbon nitrogen flux studies during the JGOFS North Atlantic Bloom Experiment, *Deep-Sea Research Part II - Topical Studies in Oceanography*, 40, 115-134, 1993.
- Martin, J. H., and R. M. Gordon, Northeast Pacific iron distributions in relation to phytoplankton productivity, *Deep-Sea Research*, 35, 177-196, 1988.
- Martin, J. H., R. M. Gordon, and S. E. Fitzwater, Iron in Antarctic waters, *Nature*, 345, 156-158, 1990.
- Martin, J. H., R. M. Gordon, and S. E. Fitzwater, and W. W. Broenkow, VERTEX - Phytoplankton iron studies in the gulf of Alaska, *Deep-Sea Research Part A - Oceanographic Research Papers*, 36, 649-680, 1989.
- Martin, J. H., G. A. Knauer, D. M. Karl, and W. W. Broenkow, VERTEX: Carbon cycling in the northeast Pacific, *Deep-Sea Research*, 34, 267-285, 1987.
- Martin, W. R., M. Bender, M. Leinen, and J. Orchardo, Benthic organic carbon degradation and biogenic silica dissolution in the central equatorial Pacific, *Deep-Sea Research Part A - Oceanographic Research Papers*, 12, 1481-1516, 1991.
- Martin, W. R., A. P. McNichol, and D. C. McCorkle, The radiocarbon age of calcite dissolving at the sea floor: Estimates from pore water data, *Geochimica et Cosmochimica Acta*, 64, 1391-1404, 2000.
- Martin, W. R., and F. L. Sayles, CaCO₃ dissolution in sediments of the Ceara Rise, western equatorial Atlantic, *Geochimica et Cosmochimica Acta*, 60, 243-263, 1996.
- Maslin, M. A., J. Adams, E. Thomas, H. Faure, and R. Haines-Young, Estimating the carbon transfer between the ocean, atmosphere and the terrestrial biosphere since the Last Glacial Maximum, *Terra Nova*, 7, 358-366, 1995.
- Maslin, M. A., X. S. Li, M. F. Loutre, and A. Berger, The contribution of orbital forcing to the progressive intensification of Northern Hemisphere glaciation, *Quaternary Science Reviews*, 17, 411-426, 1998.
- Matsumoto, K., and J. Lynch-Stieglitz, Similar glacial and Holocene deep water circulation inferred from southeast Pacific benthic foraminiferal carbon isotope composition, *Paleoceanography*, 14, 149-163, 1999.
- Matteucci, G., Orbital forcing in a stochastic resonance model of the Late-Pleistocene climatic variations, *Climate Dynamics*, 3, 179-190, 1989.
- Matteucci, G., Analysis of the probability distribution of the late Pleistocene climatic record: Implications for model validation, *Climate Dynamics*, 5, 35-52, 1990.
- McElroy, M. B., Marine biological controls on atmospheric CO₂ and climate, *Nature*, 302, 328-329, 1993.
- McGuffie, K. and A. Henderson-Sellers, *A climate modelling primer*, John Wiley & Sons, Chichester, England, 1996.
- McManus, J., D. E. Hammond, W. M. Berelson, T. E. Kilgore, D. J. Demaster, O. G. Ragueneau, and R. W. Collier, Early diagenesis of biogenic opal - Dissolution rates, kinetics, and paleoceanographic implications, *Deep-Sea Research Part II - Topical Studies in Oceanography*, 42, 871-903, 1995.
- Michel, E., L. D. Labeyrie, J. C. Duplessy, N. Gortfi, M. Labracherie, and J. L. Turon, Could deep sub-Antarctic convection feed the world deep basins during the Last Glacial Maximum, *Paleoceanography*, 10, 927-941, 1995.
- Mikolajewicz, U., T. J. Crowley, A. Schiller, and R. Voss, Modelling teleconnections between the North Atlantic and North Pacific during the Younger Dryas, *Nature*, 387, 384-387, 1997.
- Millero, F. J., The thermodynamics of the carbonate system in seawater, *Geochimica et Cosmochimica Acta*, 43, 1651-1661, 1979.
- Millero, F. J., The thermodynamics of seawater. Part I. The PVT properties, *Ocean Science and Engineering*, 7, 403-460, 1982.
- Millero, F. J., Thermodynamics of the carbon dioxide system in the oceans, *Geochimica et Cosmochimica Acta*, 59, 661-677, 1995.
- Millero, F. J., and M. L. Sohn, *Chemical Oceanography*, 531 pp., CRC, Boca Raton, Fla., 1992.
- Milliman, J. D., Production and accumulation of calcium carbonate in the ocean: Budget of a nonsteady state, *Global Biogeochemical Cycles*, 7, 927-957, 1993.
- Milliman, J. D., P. J. Troy, W. M. Balch, A. K. Adams, Y. H. Li, and F. T. Mackenzie, Biologically mediated dissolution of calcium carbonate above the chemical lysocline?, *Deep-Sea Research Part I - Oceanographic Research Papers*, 46, 1653-1669, 1999.
- Moldrup, P., C. W. Kruse, T. Yamaguchi, and D. E. Rolston, Modeling diffusion and reaction in soils: I. A diffusion and reaction corrected finite difference calculation scheme, *Soil Science*, 161, 347-354, 1996.
- Monnin, E., et al., Atmospheric CO₂ concentrations over the last glacial termination, *Science*, 291, 112-114, 2001.
- Mook, W. G., ¹³C in atmospheric CO₂, *Netherlands Journal of Sea Research*, 20, 211-223, 1986.
- Mook, W. G., J. C. Bommerson, and W. H. Staverman, Carbon isotope fractionation between dissolved bicarbonate and gaseous carbon dioxide, *Earth and Planetary Science Letters*, 22, 169-176, 1974.
- Moore, J. K., M. R. Abbott, J. G. Richman, and D. M. Nelson, The Southern Ocean at the last glacial maximum: A strong sink for atmospheric carbon dioxide, *Global Biogeochemical Cycles*, 14, 455-475, 2000.
- Mortlock, R. A., C. D. Charles, P. N. Froelich, M. A. Zibello, J. Saltzman, J. D. Hays, and L. H. Burckle, Evidence for lower productivity in the Antarctic Ocean during the last glaciation, *Nature*, 351, 220-222, 1991.
- Mucci, A., The solubility of calcite and aragonite in seawater at various salinities, temperatures and one atmosphere total pressure, *American Journal of Science*, 283, 780-799, 1983.
- Mudelsee, M., and M. Schulz, The Mid-Pleistocene climate transition: onset of 100 ka cycle lags ice volume build-up by 280 ka, *Earth and Planetary Science Letters*, 151, 117-123, 1997.
- Mudelsee, M., and K. Stattegger, Exploring the structure of the mid-Pleistocene revolution with advanced methods of time series analysis, *Geologische Rundschau*, 86, 499-511, 1997.
- Muggli, D. L., M. Lecourt, and P. J. Harrison, Effects of iron and nitrogen source on the sinking rate, physiology and metal composition of an oceanic diatom from the subarctic Pacific, *Marine Ecology Progress Series*, 132, 215-227, 1996.
- Muller, R. A., and G. J. MacDonald, Simultaneous presence of orbital inclination and eccentricity in proxy climate records from Ocean Drilling Program Site 806, *Geology*, 25, 3-6, 1997a.
- Muller, R. A., and G. J. MacDonald, Glacial cycles and astronomical forcing, *Science*, 277, 215-218, 1997b.
- Muller, R. A., and G. J. MacDonald, Spectrum of 100-kyr glacial cycle: Orbital inclination, not eccentricity, *Proc. Natl. Acad. Sci.*, 94, 8329-8334, 1997c.
- Munhoven, G., and L. M. Francois, Glacial-interglacial changes in continental weathering: Possible implications for atmospheric CO₂, in *Carbon cycling in the glacial ocean: Constraints on the ocean's role in global change*, edited by Zahn, R., T. F. Pedersen, M. A. Kaminski, and L. Labeyrie, Springer-Verlag, Berlin, 1994.
- Munhoven, G., and L. M. Francois, Glacial-interglacial variability of atmospheric CO₂ due to changing continental silicate rock weathering: A model study, *Journal of Geophysical Research*, 101, 21423-21437, 1996.
- Najjar, R. G., J. L. Sarmiento, and J. R. Toggweiler, Downward transport and fate of organic matter in the ocean: Simulations with a General Circulation Model, *Global Biogeochemical Cycles*, 6, 45-76, 1992.
- Neftel, A., H. Oeschger, T. Staffelbach, and B. Stauffer, CO₂ record in the Byrd ice core 50,000-5,000 years BP, *Nature*, 331, 609-611, 1985.
- Nelson D. M., J. J. Goering, S. S. Kilham, and R. R. L. Guillard, Kinetics of silicic acid uptake and rates of silica dissolution in the marine diatom *Thalassiosira pseudonana*, *J. Phycol.*, 12, 246-252, 1976.
- Ninnemann, U. S., and C. D. Charles, Regional differences in Quaternary Subantarctic nutrient cycling: Link to intermediate and deep water ventilation, *Paleoceanography*, 12, 560-567, 1999.
- Noriki, S., and S. Tsunogai, Particulate fluxes and major components of settling particles from sediment trap experiments in the Pacific Ocean, *Deep-Sea Research*, 33, 903-912, 1986.
- Nozaki, Y., J. K. Cochran, K. K. Turekian, and G. Keller, Radiocarbon and ²¹⁰Pb distributions in submersible-taken

- deep-sea cores from project FAMOUS, *Earth and Planetary Science Letters*, 34, 167-173, 1977.
- Oerlemans, J., Model experiments on the 100,000-kyr cycle, *Nature*, 287, 430-432, 1980.
- Oerlemans, J., Glacial cycles and ice-sheet modelling, *Climatic Change*, 4, 353-374, 1982.
- Oerlemans, J., The role of ice sheets in the Pleistocene climate, *Norsk Geologisk Tidsskrift*, 71, 155-161, 1991.
- Oeschger, H., J. Beer, U. Siegenthaler, B. Stauffer, W. Dansgaard, and C. C. Langway, Late glacial climate history from ice cores, *American Geophys. Un. Monogr. Ser.*, 29, 299-306, 1984.
- Oeschger, H., U. Siegenthaler, U. Schotterer, A. Gugelmann, A box diffusion model to study the carbon dioxide exchange in nature, *Tellus*, 2, 168-192, 1975.
- Officer, C. B., and D. R. Lynch, Determination of mixing parameters from tracer distributions in deep-sea sediment cores, *Marine Geology*, 52, 59-74, 1983.
- Officer, C. B., and J. H. Ryther, The possible importance of silicon in marine eutrophication, *Marine Ecology Progress Series*, 3, 83-91, 1980.
- Opdyke, B. N., and J. C. G. Walker, Return of the coral reef hypothesis: Basin to shelf partitioning of CaCO₃ and its effect on atmospheric CO₂, *Geology*, 20, 730-736, 1992.
- Oschlies, A., and V. Garçon, An eddy-permitting coupled physical-biological model of the North Atlantic - 1. Sensitivity to advection numerics and mixed layer physics, *Global Biogeochemical Cycles*, 13, 135-160, 1999.
- Oxburgh, R., The Holocene preservation history of equatorial Pacific sediments, *Paleoceanography*, 13, 50-62, 1998.
- Oxburgh, R., and W. S. Broecker, Pacific carbonate dissolution revisited, *Palaeogeography, Palaeoclimatology, Palaeoecology*, 103, 31-39, 1993.
- Paillard, D., The timing of Pleistocene glaciations from a simple multiple-state climate model, *Nature*, 391, 378-381, 1998.
- Paillard, D., M. Ghil, and H. Treut, Dissolved organic matter and the glacial-interglacial pCO₂ problem, *Global Biogeochemical Cycles*, 7, 901-914, 1993.
- Palmer, M. R., P. N. Pearson, and S. J. Cobb, Reconstructing past ocean pH-depth profiles, *Science*, 282, 1468-1471, 1998.
- Palmer, M. R., and G. H. Swihart, Boron isotope geochemistry: An overview, *Rev. Mineralogy*, 33, 709-744, 1996.
- Park, J., and K. A. Maasch, Plio-Pleistocene time evolution of the 100-kyr cycle in marine paleoclimate records, *Journal of Geophysical Research*, 98, 447-461, 1993.
- Peltier, W. R., and S. Marshall, Coupled energy-balance/ice-sheet model simulations of the glacial cycle: A possible connection between terminations and terrigenous dust, *Journal of Geophysical Research*, 100, 14269-14289, 1995.
- Peng, C. H., J. Guiot, and E. VanCampo, Estimating changes in terrestrial vegetation and carbon storage: Using palaeoecological data and models, *Quaternary Science Reviews*, 17, 719-735, 1998.
- Peng, T.-H., W. S. Broecker, and W. H. Berger, Rates of benthic mixing in deep-sea sediments as determined by radioactive tracers, *Quaternary Research*, 11, 141-149, 1979.
- Petit, J. R., M. Briat, and A. Royer, Ice age aerosol content from East Antarctic ice core samples and past wind strength, *Nature*, 293, 391-394, 1981.
- Petit, J. R., et al., Climate and atmospheric history of the past 420000 years from the Vostok ice core, Antarctica, *Nature*, 399, 429-436, 1999.
- Pisias, N. G., and T. C. Moore, The evolution of Pleistocene climate: A time series approach, *Earth and Planetary Science Letters*, 52, 450-458, 1991.
- Pisias, N. G., and N. J. Shackleton, Modelling the global climate response to orbital forcing and atmospheric carbon dioxide changes, *Nature*, 310, 757-759, 1984.
- Pollard, D., An investigation of the astronomical theory of the ice ages using a simple climate-ice sheet model, *Nature*, 272, 233-235, 1978.
- Pollard, D., A simple ice sheet model yields realistic 100 kyr glacial cycles, *Nature*, 296, 334-338, 1982.
- Pollard, D., Ice-age simulations with a calving ice-sheet model, *Quaternary Research*, 20, 30-48, 1983.
- Pondaven, P., C. Fravallo, D. Ruiz-Pino, P. Treguer, B. Queguiner, and C. Jeandel, Modelling the silica pump in the Permanently Open Ocean Zone of the Southern Ocean, *Journal of Marine Systems*, 17, 587-619, 1998.
- Pondaven, P., D. Ruiz-Pino, J. N. Druon, C. Fravallo, and P. Treguer, Factors controlling silicon and nitrogen biogeochemical cycles in high nutrient, low chlorophyll systems (the Southern Ocean and the North Pacific): Comparison with a mesotrophic system (the North Atlantic), *Deep-Sea Research Part I - Oceanographic Research Papers*, 46, 1923-1968, 1999.
- Pope, R. H., D. J. Demaster, C. R. Smith, and H. Seltmann, Rapid bioturbation in equatorial Pacific sediments - Evidence from excess Th234 measurements, *Deep-Sea Research Part II - Topical Studies in Oceanography*, 43, 1339-1364, 1996.
- Popova, E. E., V. A. Ryabchenko, and M. J. R. Fasham, Biological pump and vertical mixing in the Southern Ocean: Their impact on atmospheric CO₂, *Global Biogeochemical Cycles*, 14, 477-498, 2000.
- Popp, B. N., T. Trull, F. Kenig, S. G. Wakeham, T. M. Rust, B. Tilbrook, F. B. Griffiths, S. W. Wright, H. J. Marchant, R. R. Bidigare, and E. A. Laws, Controls on the carbon isotopic composition of Southern Ocean phytoplankton, *Global Biogeochemical Cycles*, 13, 827-843, 1999.
- Prentice, K. C., and I. Y. Fung, The sensitivity of terrestrial carbon storage to climate change, *Nature*, 346, 48-51, 1990.
- Price, N. M., B. A. Ahner, and F. M. M. Morel, The equatorial Pacific Ocean - Grazer-controlled phytoplankton populations in an iron-limited ecosystem, *Limnology and Oceanography*, 39, 520-534, 1994.
- Pye, K., Processes of fine particle formation, dust source regions, and climatic changes, in *Paleoclimatology and Paleometrology: Modern and Past Patterns of Global Atmospheric Transport*, edited by Leiner, M. and M. sarnthein, Kluwer Academic Publishers, 1989.
- Rabouille, C., and J. F. Gaillard, The validity of steady-state flux calculations in early diagenesis - A computer simulation of deep-sea silica diagenesis, *Deep-Sea Research Part A - Oceanographic Research Papers*, 37, 625-646, 1990.
- Rabouille, C., J. F. Gaillard, P. Treguer, and M. A. Vincendeau, Biogenic silica recycling in surficial sediments across the Polar Front of the Southern Ocean (Indian Sector), *Deep-Sea Research Part II - Topical Studies in Oceanography*, 44, 1151-1176, 1997.
- Rau, G. H., U. Riebesell, and D. Wolf-Gladrow, A model of photosynthetic ¹³C fractionation by marine phytoplankton based on diffusive molecular CO₂ uptake, *Marine Ecology Progress Series*, 133, 275-285, 1996.
- Rau, G. H., U. Riebesell, and D. Wolf-Gladrow, CO_{2(aq)}-dependent photosynthetic ¹³C fractionation in the ocean: A model versus measurements, *Global Biogeochemical Cycles*, 11, 267-278, 1997.
- Rau, G. H., T. Takahashi, and D. J. Des Marais, Latitudinal variations in plankton ^δ¹³C: Implications for CO₂ and productivity in past oceans, *Nature*, 341, 516-518, 1989.
- Rau, G. H., T. Takahashi, D. J. Des Marais, D. J. Repeta, and J. H. Martin, The relationship between ^δ¹³C: of organic matter and [CO_{2(aq)}] in ocean surface water: Data from a JGOFS site in the northeast Atlantic Ocean and a model, *Geochimica et Cosmochimica Acta*, 56, 1413-1419, 1992.
- Raymo, M. E., The Himalayas, organic carbon burial, and climate change in the Miocene, *Paleoceanography*, 9, 399-404, 1994.
- Raymo, M. E., The timing of major climate terminations, *Paleoceanography*, 12, 577-585, 1997.
- Raymo, M. E., and W. F. Ruddiman, Tectonic forcing of late Cenozoic climate, *Nature*, 359, 117-122, 1992.
- Raymo, M. E., W. F. Ruddiman, and P. N. Froelich, Influence of late Cenozoic mountain building on ocean geochemical cycles, *Geology*, 16, 649-653, 1988.
- Rea, D. K., Aspects of atmospheric circulation - The late Pleistocene (0 - 950,000 yr) record of eolian deposition in the Pacific Ocean, *Palaeogeography, Palaeoclimatology, Palaeoecology*, 78, 217-227, 1990.
- Rea, D. K., The paleoclimatic record provided by eolian deposition in the deep-sea - The geologic history of wind, *Reviews of Geophysics*, 32, 159-195, 1994.
- Rea, D., L. W. Chambers, J. M. Chuey, T. R. Janecek, M. Leinen, and N. G. Pisias, A 420,000-year record of cyclicity in oceanic and atmospheric processes from the eastern equatorial Pacific, *Paleoceanography*, 1, 577-586, 1986.

- Reader, M. C., I. Fung, and N. McFarlane, The mineral dust aerosol cycle during the Last Glacial Maximum, *Journal of Geophysical Research - Atmospheres*, 104, 9381-9398, 1999.
- Redfield, A. C., B. H. Ketchum, and F. A. Richards, The influence of organisms in the composition of sea water, In: Hill, N. M. (eds), *The Sea*, pp. 26-77, Wiley-Interscience, New York, 1963.
- Rich, J. J., D. Hollander, and G. E. Birchfield, Role of regional bioproductivity in atmospheric CO₂ changes, *Global Biogeochemical Cycles*, 13, 531-553, 1999.
- Rickaby, R. E. M., and H. Elderfield, Planktonic foraminiferal Cd/Ca: Paleonutrients or paleotemperature?, *Paleoceanography*, 14, 293-303, 1999.
- Ridgwell, A. J., Comment on "Does iron fertilization lead to rapid carbon export in the Southern Ocean?" by Matthew A. Charette and Ken O. Buesseler, *Geochemistry Geophysics Geosystems*, 1, 2000.
- Ridgwell, A. J., A. J. Watson, and M. E. Raymo, Is the spectral signature of the 100 kyr glacial cycle consistent with a Milankovitch origin?, *Paleoceanography*, 14, 437-440, 1999.
- Ruddiman, W. F., Tropical Atlantic terrigenous fluxes since 25,000 yrs BP, *Marine Geology*, 136, 189-207, 1997.
- Ruddiman, W. F., G. A. Jones, T-H. Peng, L. K. Glover, B. P. Glass, and P. J. Liebertz, Tests for size and shape dependency in deep-sea mixing, *Sedimentary Geology*, 25, 257-276, 1980.
- Ruddiman, W. F., and M. E. Raymo, Northern hemisphere climate regimes during the past 3 Ma: Possible tectonic connections, *Philosophical Transaction of the Royal Society of London Series B*, 318, 441-430, 1988.
- Rue, E. L., and K. W. Bruland, The role of organic complexation on ambient iron chemistry in the equatorial Pacific Ocean and the response of a mesoscale iron addition experiment, *Limnology and Oceanography*, 42, 901-910, 1997.
- Russell, A. D., and H. J. Spero, Field examination of the oceanic carbonate ion effect on stable isotopes in planktonic foraminifera, *Paleoceanography*, 15, 43-52, 2000.
- Rutherford, S., and S. D'Hondt, Early onset and tropical forcing of 100,000-year Pleistocene glacial cycles, *Nature*, 408, 72-75, 2000.
- Sakai, K., and W. R. Peltier, A simple model of the Atlantic thermohaline circulation - Internal and forced variability with paleoclimatological implications, *Journal of Geophysical Research*, 100, 13455-13479, 1995.
- Sakai, K., and W. R. Peltier, Dansgaard-Oeschger oscillations in a coupled atmosphere-ocean climate model, *Journal of Climate*, 10, 949-970, 1997.
- Sakai, K., and W. R. Peltier, Deglaciation-induced climate variability: An explicit model of the glacial-interglacial transition that simulates both the Bolling/Allerod and Younger-Dryas events, *Journal of the Meteorological Society of Japan*, 76, 1029-1044, 1998.
- Saltzman, B., Carbon dioxide and the $\delta^{18}\text{O}$ record of late-Quaternary climatic change: A global model, *Climate Dynamics*, 1, 77-85, 1987.
- Saltzman, B., Three basic problems of paleoclimatics modeling: A personal perspective and review, *Climate Dynamics*, 5, 67-78, 1990.
- Saltzman, B., and K. A. Maasch, Carbon cycle instability as a cause of the late Pleistocene ice age oscillations: Modelling the asymmetric response, *Global Biogeochemical Cycles*, 2, 177-185, 1988.
- Saltzman, B., and K. A. Maasch, A first-order global model of late Cenozoic climatic change, *Transactions of the Royal Society of Edinburgh: Earth Sciences*, 81, 315-325, 1990.
- Saltzman, B., and K. A. Maasch, A first-order global model of late Cenozoic climatic change II. Further analysis based on a simplification of CO₂ dynamics, *Climate Dynamics*, 5, 201-210, 1991.
- Saltzman, B., K. A. Maasch, and M. Y. Verbitsky, Possible effects of anthropogenically-increased CO₂ on the dynamics of climate: Implications for ice age cycles, *Geophysical Research Letters*, 20, 1051-1054, 1993.
- Saltzman, B., and A. Sutera, A model of the internal feedback system involved in late Quaternary climatic change, *Journal of the Atmospheric Sciences*, 41, 736-745, 1984.
- Saltzman, B., and A. Sutera, The mid-Quaternary climatic transition as the free response of a three-variable dynamical model, *Journal of the Atmospheric Sciences*, 44, 236-241, 1987.
- Saltzman, B., and M. Y. Verbitsky, Asthenospheric ice-load effects in a global dynamical-system model of the Pleistocene climate, *Climate Dynamics*, 8, 1-11, 1992.
- Saltzman, B., and M. Y. Verbitsky, Multiple instabilities and modes of glacial rhythmicity in the Plio-Pleistocene: A general theory of late Cenozoic climatic change, *Climate Dynamics*, 9, 1-15, 1993.
- Saltzman, B., and M. Y. Verbitsky, CO₂ and glacial cycles, *Nature*, 367, 419, 1994a.
- Saltzman, B., and M. Y. Verbitsky, Late Pleistocene climatic trajectory in the phase space of global ice, ocean state, and CO₂: Observations and theory, *Paleoceanography*, 9, 767-779, 1994b.
- Sanyal, A., N. G. Hemming, W. S. Broecker, D. W. Lea, H. J. Spero, and G. N. Hanson, Oceanic pH control on the boron isotopic composition of foraminifera: Evidence from culture experiments, *Paleoceanography*, 11, 513-517, 1996.
- Sanyal, A., N. G. Hemming, W. S. Broecker, and G. N. Hanson, Changes in pH in the eastern equatorial Pacific across stage 5-6 boundary based on boron isotopes in foraminifera, *Global Biogeochemical Cycles*, 11, 125-133, 1997.
- Sanyal, A., N. G. Hemming, G. N. Hanson, W. S. Broecker, Evidence for a higher pH in the glacial ocean from boron isotopes in foraminifera, *Nature*, 373, 234-236, 1995.
- Sarmiento, J. L., J. C. Orr, and U. Siegenthaler, A perturbation simulation of CO₂ uptake in an Ocean General Circulation Model, *Journal of Geophysical Research*, 97, 3621-3645, 1992.
- Sarmiento, J. L., R. D. Slater, M. J. R. Fasham, H. W. Ducklow, J. R. Toggweiler, and G. T. Evans, A seasonal 3-dimensional ecosystem model of nitrogen cycling in the north Atlantic euphotic zone, *Global Biogeochemical Cycles*, 7, 417-450, 1993.
- Sarmiento, J. L., and E. T. Sundquist, Revised budget for the oceanic uptake of anthropogenic carbon dioxide, *Nature*, 356, 589-593, 1992.
- Sarmiento, J. L., and J. R. Toggweiler, A new model for the role of the oceans in determining atmospheric pCO₂, *Nature*, 308, 621-624, 1984.
- Sarmiento, J. L., J. R. Toggweiler, and R. Najjar, Ocean carbon-cycle dynamics and atmospheric pCO₂, *Phil. Trans. R. Soc. Lond. A*, 325, 3-21, 1988.
- Sayles, F. L., W. G. Deuser, J. E. Goudeau, W. H. Dickinson, T. D. Jickells, and P. King, The benthic cycle of biogenic opal at the Bermuda Atlantic Time Series site, *Deep-Sea Research Part I - Oceanographic Research Papers*, 43, 383-409, 1996.
- Schiffelbein, P., Effect of benthic mixing on the information content of deep-sea stratigraphical signals, *Nature*, 311, 651-653, 1984.
- Schink, D. R., N. L. Guinasso, and K. A. Fanning, Processes affecting the concentration of silica at the sediment-water interface of the Atlantic Ocean, *Journal of Geophysical Research*, 80, 3013-3031, 1975.
- Schluter, M., and E. Sauter, Biogenic silica cycle in surface sediments of the Greenland Sea, *Journal of Marine Systems*, 23, 333-342, 2000.
- Seidov, D., and B. J. Haupt, Last glacial and meltwater interbasin water exchanges and sedimentation in the world ocean, *Paleoceanography*, 14, 760-769, 1999.
- Shackleton, N. J., Carbon-13 in *Uvigerina*: Tropical rainforest history and the equatorial Pacific carbonate dissolution cycles, in *The fate of fossil fuel CO₂ in the oceans*, edited by Andersen, N. R., and A. Malahoff, Plenum Press, New York, 1977.
- Shackleton, N. J., J. Backman, H. Zimmerman, D. V. Kent, M. A. Hall, D. G. Roberts, D. Schmitker, J. G. Baldauf, A. Desprairies, R. Homrighausen, P. Huddleston, J. B. Keene, A. J. Kaltenback, A. O. Krumsiek, A. C. Morton, J. W. Murray, and J. Westberg-Smith, Oxygen isotope calibration of the onset of ice-rafting and history of glaciation in the North Atlantic region, *Nature*, 307, 620-623, 1984.
- Shackleton, N. J., M. A. Hall, J. Line, and C. Shuxi, Carbon isotope data in core V19-30 confirm reduced carbon dioxide concentration in the ice age atmosphere, *Nature*, 306, 319-322, 1983.
- Shackleton, N. J., and N. D. Opdyke, Oxygen isotope and paleomagnetic stratigraphy of equatorial Pacific core V28-238: Oxygen isotope temperature and ice volumes on a 10⁵ and 10⁶ year scale, *Quaternary Research*, 3, 39-55, 1973.
- Shaffer, G., A model of biogeochemical cycling of phosphorous, nitrogen, oxygen, and sulphur in the ocean: One step toward a

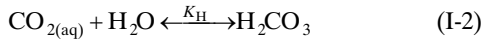
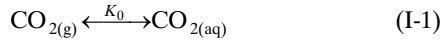
- global climate model, *Journal of Geophysical Research*, 94, 1979-2004, 1989.
- Shaffer, G., A non-linear climate oscillator controlled by biogeochemical cycling in the ocean: An alternative model of Quaternary ice age cycles, *Climate Dynamics*, 4, 127-143, 1990.
- Shaffer, G., Effects of the marine biota on global carbon cycling, in *The Global Carbon Cycle*, edited by Heimann, M., Springer-Verlag, Berlin, 1993.
- Shaffer, G., Biogeochemical cycling in the global ocean 2. New production, Redfield ratios, and the remineralization in the organic pump, *Journal of Geophysical Research*, 101, 3723-3745, 1996.
- Shaffer, G., and J. L. Sarmiento, Biogeochemical cycling in the global ocean 1. A new, analytical model with continuous vertical resolution and high-latitude dynamics, *Journal of Geophysical Research*, 100, 2659-2672, 1995.
- Short, D. A., J. G. Mengel, T. J. Crowley, W. T. Hyde, and G. R. North, Filtering of Milankovitch cycles by Earth's geography, *Quaternary Research*, 35, 157-173, 1991.
- Siegel, D. A., T. C. Granata, A. F. Michaels, and T. D. Dickey, Mesoscale eddy diffusion, particle sinking, and the interpretation of sediment trap data, *Journal of Geophysical Research*, 95, 5305-5311, 1990.
- Siegenthaler, U., and F. Joos, Use of a simple model for studying oceanic tracer distributions and the global carbon cycle, *Tellus*, 44, 186-207, 1992.
- Siegenthaler, U., and Th. Wenk, Rapid atmospheric CO₂ variations and ocean circulation, *Nature*, 308, 624-626, 1984.
- Sigman, D. M., M. A. Altabet, R. Francois, D. C. McCorkle, and J. F. Gaillard, The isotopic composition of diatom-bound nitrogen in Southern Ocean sediments, *Paleoceanography*, 14, 118-134, 1999a.
- Sigman, D. M., M. A. Altabet, D. C. McCorkle, R. Francois, and G. Fischer, The delta N-15 of nitrate in the Southern Ocean: Consumption of nitrate in surface waters, *Global Biogeochemical Cycles*, 13, 1149-1166, 1999b.
- Sigman, D. M., and E. A. Boyle, Glacial/interglacial variations in atmospheric carbon dioxide, *Nature*, 407, 859-869, 2000.
- Sigman, D. M., D. C. McCorkle, and W. R. Martin, The calcite lysocline as a constraint on glacial/interglacial low-latitude production changes, *Global Biogeochemical Cycles*, 12, 409-427, 1998.
- Six, K. D., and E. Maier-Reimer, Effects of plankton dynamics on seasonal carbon fluxes in an ocean general circulation model, *Global Biogeochemical Cycles*, 10, 559-583, 1996.
- Smith, H. J., M. Wahlen, D. Mastroianni, and K. C. Taylor, The CO₂ concentration of air trapped in GISP2 ice from the Last Glacial Maximum-Holocene transition, *Geophysical Research Letters*, 24, 1-4, 1997.
- Smith, H. J., H. Fischer, M. Wahlen, D. Mastroianni, and B. Deck, Dual modes of the carbon cycle since the Last Glacial Maximum, *Nature*, 400, 248-250, 1999.
- Snieder, R. K., The origin of the 100,000 year cycle in a simple ice age model, *Journal of Geophysical Research*, 90, 5661-5664, 1985.
- Soetaert, K., P. M. J. Herman, J. J. Middelburg, C. Heip, H. S. DeStigter, T. C. E. VanWeering, E. Epping, and W. Helder, Modeling Pb-210-derived mixing activity in ocean margin sediments: Diffusive versus nonlocal mixing, *Journal of Marine Research*, 54, 1207-1227, 1996.
- Sohrin, Y., S. Iwamoto, M. Matsui, H. Obata, E. Nakayama, K. Suzuki, N. Handa, and M. Ishii, The distribution of Fe in the Australian sector of the Southern Ocean, *Deep-Sea Research Part I - Oceanographic Research Papers*, 47, 55-84, 2000.
- Sowers, T., M. Bender, L. Labeyrie, D. Martinson, J. Jouzel, D. Raynaud, J. J. Pochon, and Y. S. Korotkevich, A 135,000-year Vostok-SPECMAP common temporal framework, *Paleoceanography*, 8, 737-766, 1993.
- Sowers, T., M. Bender, D. Raynaud, Y. S. Korotkevich, and J. Orcharto, The $\delta^{18}\text{O}$ of atmospheric O₂ from air inclusions in the Vostok ice core: Timing of CO₂ and ice volume changes during the penultimate deglaciation, *Paleoceanography*, 6, 679-696, 1991.
- Spero, H. J., J. Bijma, D. W. Lea, and B. E. Bemis, Effect of seawater carbonate concentration on foraminiferal carbon and oxygen isotopes, *Nature*, 390, 497-500, 1997.
- Spokes, L. J., and T. D. Jickells, Factors controlling the solubility of aerosol trace metals in the atmosphere and on mixing into seawater, *Aquatic Geochemistry*, 1, 355-374, 1996.
- Stein, M., G. J. Wasserburg, P. Aharon, J. H. Chen, Z. R. Zhu, A. Bloom, and J. Chappell, TIMS U-series dating and stable isotopes of the last interglacial event in Papua New Guinea, *Geochimica et Cosmochimica Acta*, 57, 2541-2254, 1993.
- Stephens, M. P., and D. C. Kadko, Glacial-Holocene calcium carbonate dissolution at the central equatorial Pacific sea floor, *Paleoceanography*, 12, 797-804, 1997.
- Stephens, B. B., and R. F. Keeling, The influence of Antarctic sea ice on glacial-interglacial CO₂ variations, *Nature*, 404, 171-174, 2000.
- Stocker, T. F., W. S. Broecker, and D. G. Wright, Carbon uptake experiments with a zonally-averaged global ocean circulation model, *Tellus Series B*, 46, 103-122, 1994.
- Stocker, T. F., and D. G. Wright, A zonally averaged ocean model for the thermohaline circulation. 2. Inter-ocean circulation in the Pacific Atlantic basin system, *Journal of Physical Oceanography*, 21, 1725-1739, 1991a.
- Stocker, T. F., and D. G. Wright, Rapid transitions of the ocean's deep circulation induced by changes in surface water fluxes, *Nature*, 351, 729-732, 1991b.
- Stocker, T. F., and D. G. Wright, Rapid changes in ocean circulation and atmospheric radiocarbon, *Paleoceanography*, 11, 773-795, 1996.
- Stocker, T. F., D. G. Wright, and L. A. Mysak, A zonally averaged, coupled ocean atmosphere model for paleoclimate studies, *Journal of Climate*, 5, 773-797, 1992.
- Suarez, M. J., and I. M. Held, Modelling climatic response to orbital parameter variations, *Nature*, 263, 46-47, 1976.
- Suess, E., Particulate organic carbon flux in the oceans - surface productivity and oxygen utilization, *Nature*, 288, 260-263, 1980.
- Sunda, W. G., and S. A. Huntsman, Iron uptake and growth limitation in oceanic and coastal phytoplankton, *Marine Chemistry*, 50, 189-206, 1995.
- Sunda, W. G., D. G. Swift, and S. A. Huntsman, Low iron requirement for growth in oceanic phytoplankton, *Nature*, 351, 55-57, 1991.
- Sundquist, E. T., Influence of deep-sea benthic processes on atmospheric CO₂, *Phil. Trans. R. Soc. Lond. A*, 331, 155-165, 1990.
- Takahashi, K., Seasonal fluxes of pelagic diatoms in the sub-Arctic Pacific, 1982-1983, *Deep-Sea Research Part A - Oceanographic Research Papers*, 33, 1225-1251, 1986.4
- Takeda, S., Influence of iron availability on nutrient consumption ratio of diatoms in oceanic waters, *Nature*, 393, 774-777, 1998.
- Tans, P. P., I. Y. Fung, and T. Takahashi, Observational constraints on the global atmospheric CO₂ budget, *Science*, 247, 1431-1438, 1990.
- Tarasov, L., and W. R. Peltier, Terminating the 100 kyr ice age cycle, *Journal of Geophysical Research*, 102, 21665-21693, 1997.
- Taylor, A. H., and I. Joint, A steady-state analysis of the 'microbial loop' in stratified systems, *Marine Ecology Progress Series*, 59, 1-17, 1990.
- Taylor, A. H., A. J. Watson, M. Ainsworth, J. E. Robertson, and D. R. Turner, A modelling investigation of the role of phytoplankton in the balance of carbon at the surface of the North Atlantic, *Global Biogeochemical Cycles*, 5, 151-171, 1991.
- Taylor, S. R., and S. M. McLennan, *The continental crust, its composition and evolution: An examination of the geochemical record preserved in sedimentary rocks*, Blackwell, Oxford, 1985.
- Thompson, L. G., E. Mosey-Thompson, M. W. Davis, P. N. Lin, K. A. Henderson, J. Coledai, J. F. Bolzan, and K. B. Liu, Late glacial stage and Holocene tropical ice core records from Huascarán, Peru, *Science*, 269, 46-50, 1995.
- Tiedemann, R., M. Sarntheim, and N. J. Shackleton, Astronomic timescale for the Pliocene Atlantic $\delta^{18}\text{O}$ and dust flux records of Ocean Drilling Program site 659, *Paleoceanography*, 9, 619-638, 1994.
- Toggweiler, J. R., Variation of atmospheric CO₂ by ventilation of the ocean's deepest water, *Paleoceanography*, 14, 571-588, 1999.
- Trauth, M. H., TURBO: A dynamic-probabilistic simulation to study the effects of bioturbation on paleoceanographic time series, *Computers & Geosciences*, 24, 433-441, 1998.

- Trauth, M. H., M. Sarnthein, M. Arnold, Bioturbational mixing depth and carbon flux at the sea floor, *Paleoceanography*, 12, 517-526, 1997.
- Treguer, P., D. M. Nelson, A. J. VanBennekom, D. J. Demaster, A. Leynaert, and B. Queguiner, The silica balance in the world ocean - A re-estimate, *Science*, 268, 375-379, 1995.
- Treguer, P., and P. Pondaven, Silica control of carbon dioxide, *Nature*, 406, 358-359, 2000.
- Tsunogai, S., and S. Noriki, Particulate fluxes of carbonate and organic carbon in the ocean - Is the marine biological activity working as a sink of the atmospheric carbon?, *Tellus Series B*, 43, 256-266, 1991.
- Trenberth, K., J. Olson, and W. Large, *A Global Ocean Wind Stress Climatology based on ECMWF Analyses*. Tech. Rep. NCAR/TN-338+STR, National Centre for Atmospheric Research, Boulder, Colorado, 1989.
- Tromp, T. K., P. VanCappellen, and R. M. Key, A global model for the early diagenesis of organic carbon and organic phosphorous in marine sediments, *Geochimica et Cosmochimica Acta*, 59, 1259-1284, 1995.
- Tyrrell, T., The relative influences of nitrogen and phosphorous on oceanic primary production, *Nature*, 400, 525-531, 1999.
- Tyrrell, T., and A. H. Taylor, A modelling study of *Emiliania huxleyi* in the NE Atlantic, *Journal of Marine Systems*, 9, 83-112, 1996.
- Ullman, W. J., and R. C. Aller, Diffusion coefficient in nearshore marine sediments, *Limnol. Oceanogr.*, 27, 552-556, 1982.
- VanBennekom, A. J., G. W. Berger, S. J. VanDerGaast, and R. T. P. Devries, Primary productivity and the silica cycle in the Southern Ocean (Atlantic sector), *Palaeogeography, Palaeoclimatology, Palaeoecology*, 67, 19-30, 1988.
- VanCampo, E., J. Guiot, and C. Peng, A data-based reappraisal of the terrestrial carbon budget at the Last Glacial Maximum, *Global and Planetary Change*, 8, 189-201, 1993.
- VanCappellen, P., and L. Q. Qiu, Biogenic silica dissolution in sediments of the Southern Ocean .1. Solubility, *Deep-Sea Research Part II - Topical Studies in Oceanography*, 44, 1109-1128, 1997a.
- VanCappellen, P., and L. Q. Qiu, Biogenic silica dissolution in sediments of the Southern Ocean .2. Kinetics, *Deep-Sea Research Part II - Topical Studies in Oceanography*, 44, 1129-1149, 1997b.
- VanderSluys, J. P., G. J. DeBruyn, and P. Westbroek, Biogenic feedbacks in the carbonate-silicate geochemical cycle and the global climate, *American Journal of Science*, 296, 932-953, 1996.
- Vengosh, A. Y. Kolodny, A. Starinsky, A. R. Chivas, and M. T. McCulloch, Co-precipitation and isotopic fractionation of boron in modern biogenic carbonates, *Geochimica et Cosmochimica Acta*, 55, 2901-2910, 1991.
- Volk, T., and M. I. Hoffert, Ocean carbon pumps: Analysis of relative strengths and efficiencies in ocean-driven atmospheric CO₂ changes, *Geophys. Monogr.*, 32, 99-110, 1985.
- Walker, J. C. G., and B. C., Opdyke, Influence of variable rates of netric carbonate deposition on atmospheric carbon dioxide and pelagic sediments, *Paleoceanography*, 10, 415-427, 1995.
- Wanninkhof, R. Relationship between wind-speed and gas-exchange over the ocean, *Journal of Geophysical Research*, 97, 7373-7382, 1992.
- Watson, A. J., D. C. E. Bakker, A. J. Ridgwell, P. W. Boyd, and C. S. Law, Effect of iron supply on Southern Ocean CO₂ uptake and implications for glacial atmospheric CO₂, *Nature*, 407, 730-733, 2000.
- Watson, A. J., and N. Lefèvre, The sensitivity of atmospheric CO₂ concentrations to input of iron to the oceans, *Tellus*, 51, 543-460, 1999.
- Weaver, A. J., and E. S. Sarachik, The role of mixed boundary conditions in numerical models of the oceans climate, *Journal of Physical Oceanography*, 21, 1470-1493, 1991.
- Weertman, J., Milankovitch solar radiation variations and ice age ice sheet sizes, *Nature*, 261, 17-20, 1976.
- Weiss, R. F., Carbon dioxide in water and seawater: The solubility of a non-ideal gas, *Marine Chemistry*, 2, 203-215, 1974.
- Wheatcroft, R. A., Experimental tests for particle size-dependent bioturbation in the deep ocean, *Limnology and Oceanography*, 37, 90-104, 1992.
- Wheatcroft, R. A., P. A. Jumars, C. R. Smith, and A. R. M. Nowell, A mechanistic view of the particulate biodiffusion coefficient: Step lengths, rest periods and transport directions, *Journal of Marine Research*, 48, 177-207, 1990.
- Wigley, T. M. L., Spectral analysis and the astronomical theory of climatic change, *Nature*, 264, 629-631, 1976.
- Winton, M., and E. S. Sarachik, Thermohaline oscillations induced by strong steady salinity forcing of Ocean General Circulation Models, *Journal of Physical Oceanography*, 23, 1389-1410, 1993.
- WolfGladrow, D. A., J. Bijma, and R. E. Zeebe, Model simulation of the carbonate chemistry in the microenvironment of symbiont bearing foraminifera, *Marine Chemistry*, 64, 181-198, 1999a.
- WolfGladrow, D. A., U. Riebesell, S. Burkhardt, and J. Bijma, Direct effects of CO₂ concentration on growth and isotopic composition of marine plankton, *Tellus Series B - Chemical and Physical Meteorology*, 51, 461-476, 1999b.
- Wollast, R., and L. Chou, Kinetic study of the dissolution of albite with a continuous flow-through fluidized bed reactor, in *The chemistry of weathering*, edited by Drever, J. I., D. Reidel, Norwell, Mass., 1985.
- Wright, D. G., and T. F., Stocker, A zonally averaged ocean model for the thermohaline circulation. I. Model development and flow dynamics, *Journal of Physical Oceanography*, 21, 1713-1724, 1991.
- Wright, D. G., and T. F., Stocker, Sensitivities of a zonally averaged global circulation model, *Journal of Geophysical Research*, 97, 12707-12730, 1992.
- Yamanaka, Y., and E. Tajika, The role of the vertical fluxes of particulate organic matter and calcite in the oceanic carbon cycle: Studies using an ocean biogeochemical general circulation model, *Global Biogeochemical Cycles*, 10, 361-382, 1996.
- Yamanaka, Y., and E. Tajika, Role of dissolved organic matter in the marine biogeochemical cycle: Studies using an ocean biogeochemical general circulation model, *Global Biogeochemical Cycles*, 11, 599-612, 1997.
- Yang, J. Y., and J. D. Neelin, Sea-ice interaction with the thermohaline circulation, *Geophysical Research Letters*, 20, 217-220, 1993.
- Yang, J. Y., and R. X. Huang, Decadal oscillations driven by the annual cycle in a zonally- averaged coupled ocean-ice model, *Geophysical Research Letters*, 23, 269-272, 1996.
- Yiou, P., E. Baert, M. F. Loure, Spectral analysis of climate data, *Surveys in Geophysics*, 17, 619-663, 1996.
- Yokoyama, Y., K. Lambeck, P. De Deckker, P. Johnston, and L. K. Fifield, Timing of the Last Glacial Maximum from observed sea-level minima, *Nature*, 406, 713-716, 2000.
- Yung, Y. L., T. Lee, C. H. Wang, and Y. T. Shieh, Dust: A diagnostic of the hydrologic cycle during the last glacial maximum, *Science*, 271, 962-963, 1996.
- Zeebe, R. E., J. Bijma, D. A. WolfGladrow, A diffusion-reaction model of carbon isotope fractionation in foraminifera, *Marine Chemistry*, 64, 199-227, 1999.
- Zhaung, G., R. A. Duce, and D. R. Kester, The dissolution of atmospheric iron in surface seawater of the open ocean, *Journal of Geophysical Research*, 95, 16207-16216, 1990.
- Zhang, J., P. D. Quay, and D. O. Wilbur, Carbon isotope fractionation during gas-water exchange and dissolution of CO₂, *Geochimica et Cosmochimica Acta*, 59, 107-115, 1995.

Appendix I

Carbonate system thermodynamics

The inorganic aqueous carbonate system in the ocean comprises four dissolved species, CO_2 , H_2CO_3 , HCO_3^- , and CO_3^{2-} , characterized by the following series of reactions



where K_0 is the solubility coefficient of CO_2 , K_{H} is the dissociation constant of H_2O , and K_1 and K_2 are the first and second dissociation constants of carbonic acid, respectively, all referenced to seawater. Given the total dissolved inorganic CO_2 (ΣCO_2) and carbonate alkalinity (A_{C}) concentration in seawater, this system can be defined [Millero and Sohn, 1992] by solving for three of the dissolved carbonate species

$$[\text{CO}_2] = \Sigma\text{CO}_2 - A_{\text{C}} +$$

$$\frac{A_{\text{C}} \cdot K - \Sigma\text{CO}_2 \cdot K - 4 \cdot A_{\text{C}} + Z}{2 \cdot (K - 4)} \quad (\text{I-5})$$

$$[\text{HCO}_3^-] = \frac{\Sigma\text{CO}_2 \cdot K - Z}{K - 4} \quad (\text{I-6})$$

$$[\text{CO}_3^{2-}] = \frac{A_{\text{C}} \cdot K - \Sigma\text{CO}_2 \cdot K - 4 \cdot A_{\text{C}} + Z}{2 \cdot (K - 4)} \quad (\text{I-7})$$

where

$$K = \frac{K_1}{K_2} \quad (\text{I-8})$$

and

$$Z = \left((4 \cdot A_{\text{C}} + \Sigma\text{CO}_2 \cdot K - A_{\text{C}} \cdot K)^2 + 4 \cdot (K - 4) \cdot A_{\text{C}}^2 \right)^{0.5} \quad (\text{I-9})$$

The total alkalinity (A_{T}) of seawater is defined as the “concentration of all the bases that can accept H^+ when a titration is made with HCl to the carbonic acid endpoint” [Millero and Sohn, 1992]. However, in order to improve overall model computational efficiency, the exact definition of Dickson [1981] is simplified by omitting the relatively

minor contributions made by S, F, and N species. In addition, since the contribution from phosphoric acid to total alkalinity is relatively small and exhibits very little temperature or pressure dependence, this is approximated by a simple linear dependence on ambient PO_4^{3-} concentration (producing an additional error in A_{T} of $\leq 0.01\%$). A_{T} is therefore written

$$A_{\text{T}} = [\text{HCO}_3^-] + 2[\text{CO}_3^{2-}] + [\text{H}_4\text{BO}_4^-] + [\text{H}_3\text{SiO}_4^-] + [\text{OH}^-] + 1.1[\text{PO}_4^{3-}] \quad (\text{I-10})$$

Carbonate alkalinity (A_{C}) is defined as

$$A_{\text{C}} = [\text{HCO}_3^-] + 2[\text{CO}_3^{2-}] \quad (\text{I-11})$$

and thus can be approximated by

$$A_{\text{C}} = A_{\text{T}} - \left([\text{H}_4\text{BO}_4^-] + [\text{H}_3\text{SiO}_4^-] + [\text{OH}^-] + 1.1[\text{PO}_4^{3-}] \right) \quad (\text{I-12})$$

The concentrations of HCO_3^- , CO_3^{2-} , OH^- , H_4BO_4^- , and H_3SiO_4^- are calculated via their respective dissociation constants, K_1 , K_2 , K_{H} , K_{B} , and K_{Si} , defined by

$$K_1 = \frac{[\text{H}^+][\text{HCO}_3^-]}{[\text{H}_2\text{O}][\text{CO}_2]} \quad (\text{I-13})$$

$$K_2 = \frac{[\text{H}^+][\text{CO}_3^{2-}]}{[\text{HCO}_3^-]} \quad (\text{I-14})$$

$$K_{\text{B}} = \frac{[\text{H}^+][\text{H}_4\text{BO}_4^-]}{[\text{H}_2\text{O}][\text{H}_3\text{BO}_3]} \quad (\text{I-15})$$

$$K_{\text{H}} = \frac{[\text{H}^+][\text{OH}^-]}{[\text{H}_2\text{O}]} \quad (\text{I-16})$$

$$K_{\text{Si}} = \frac{[\text{H}^+][\text{H}_3\text{SiO}_4^-]}{[\text{H}_4\text{SiO}_4]} \quad (\text{I-17})$$

where $[\text{H}_2\text{O}] \equiv 1$. Dissociation constants are typically written as empirically-determined multi-variate regressions of temperature and salinity (or total ionic strength), detailed in Table I-1. All calculations assume the same seawater $p\text{H}$ scale ($p\text{H}_{\text{SWS}}$) [Millero, 1995]. It is therefore necessary to make a correction to K_{B} to account for its being determined

on the total pH (pH_{tot}) scale. Rather than make an explicit conversion from a pH_{tot} to pH_{SWS} basis, which requires consideration of the dissociation of HF and H_2SO_4 [Millero, 1995], since there is little dependence on salinity a simple linear dependence on temperature is made. A correction must also be made to K_{Si} since it was not determined in seawater. The concentration of silicic acid and phosphoric acids are taken directly from the ocean tracer field, while that of boric acid in seawater is simply estimated from salinity [Millero, 1982].

The fugacity of CO_2 in seawater (fCO_2) rather than the partial pressure (pCO_2) is calculated as the CO_2 -seawater system exhibits considerable non-ideality, with the value of fCO_2 in air about 0.3% lower than that of pCO_2 at pressures of order of 1 atm. fCO_2 is given by Weiss [1974]

$$fCO_2 = \frac{[CO_2]}{Q_{CO_2}} \quad (\text{I-18})$$

The thermodynamics of the solid-aqueous system are defined by the solubility products for the two solid phases of calcium carbonate ($CaCO_3$), calcite (K_{cal}) and aragonite (K_{arg}), and calculated using empirical functions of temperature and salinity [Mucci, 1983] (given in Table I-1). From these, the saturation state of $CaCO_3$ in seawater can be obtained, which is defined in terms of a solubility ratio (Ω) for each phase

$$\Omega_{\text{cal}} = \frac{[Ca^{2+}][CO_3^{2-}]}{K_{\text{cal}}} \quad (\text{I-19})$$

$$\Omega_{\text{arg}} = \frac{[Ca^{2+}][CO_3^{2-}]}{K_{\text{arg}}} \quad (\text{I-20})$$

Determination of pH

It remains to determine the hydrogen ion concentration ($[H^+]$) and thus the pH of the system. Since there is no analytical solution, this is estimated by means of an iterative numerical approximation. The sequence of stages in this is as follows

1. An initial guess made of $[H^+]$; at model spin-up this is taken to be 7×10^{-9} , otherwise the equilibrium value from the previous time step is assumed.
2. CO_2 alkalinity is estimated from the current value of $[H^+]$, from which the concentrations of HCO_3^- , CO_3^{2-} , and $CO_{2(aq)}$ are calculated.
3. $[HCO_3^-]$, $[CO_3^{2-}]$, and $[CO_2]$ calculated in (2) are used in conjunction with the two dissociation constants of carbonic acid (K_1 , K_2) to produce two different estimates for $[H^+]$

$$[H^+]_1 = K_1 \cdot \frac{[CO_2]}{[HCO_3^-]} \quad (\text{I-21})$$

$$[H^+]_2 = K_2 \cdot \frac{[HCO_3^-]}{[CO_3^{2-}]} \quad (\text{I-22})$$

4. A new estimate of $[H^+]$ is then made by combining the two estimates made above

Table I-1 Empirical Descriptions of Aqueous Carbonate System Dissociation Constants

Constant	Thermodynamic approximation	Reference
K_1	$\ln(K_1) = 2.18867 - 2275.036 / T - 1.468591 \cdot \ln(T) +$ $(-0.138681 - 9.33291 / T) \cdot S^{0.5} + 0.0726483 \cdot S - 0.00574938 \cdot S^{1.5}$	Millero [1995]
K_2	$\ln(K_2) = -0.84226 - 3741.1288 / T - 1.437139 \cdot \ln(T) +$ $(-0.128417 - 24.41239 / T) \cdot S^{0.5} + 0.1195308 \cdot S - 0.00912840 \cdot S^{1.5}$	Millero [1995]
K_B	$\ln(K_B) = 148.0248 + 137.1942 \cdot S^{0.5} + 1.62142 \cdot S +$ $(-8966.90 - 2890.53 \cdot S^{0.5} - 77.942 \cdot S + 1.728 \cdot S^{1.5} - 0.0996 \cdot S^2) / T +$ $(-24.4344 - 25.085 \cdot S^{0.5} - 0.2474 \cdot S) \cdot \ln(T) + 0.053105 \cdot S^{0.5} \cdot T$	Dickson [1990]
K_H	$\ln(K_H) = 148.9802 - 13847.26 / T - 23.6521 \cdot \ln(T) +$ $(-5.977 + 118.67 / T + 1.0495 \cdot \ln(T)) \cdot S^{0.5} - 0.01615 \cdot S$	Millero [1992]
K_{Si}	$\ln(K_{\text{Si}}) = 117.40 - 8904.2 / T - 19.334 \ln(T) +$ $(3.5913 - 458.79 / T) \cdot I^{0.5} + (-1.5998 + 188.74 / T) \cdot I + (0.07871 - 12.1652 / T) \cdot I^2$ ¹	Millero [1995]
K_{cal}	$\log_{10}(K_{\text{cal}}) = -171.9065 - 0.077993 \cdot T + 2839.319 / T + 71.595 \cdot \log_{10}(T) +$ $(-0.77712 + 0.0028426 \cdot T + 178.34 / T) \cdot S^{0.5} - 0.07711 \cdot S + 0.0041249 \cdot S^{1.5}$	Mucci [1983]
K_{arg}	$\log_{10}(K_{\text{cal}}) = -171.9450 - 0.077993 \cdot T + 2903.293 / T + 71.595 \cdot \log_{10}(T) +$ $(-0.068393 + 0.0017276 \cdot T + 88.135 / T) \cdot S^{0.5} - 0.10018 \cdot S + 0.0059415 \cdot S^{1.5}$	Mucci [1983]

¹ I is the ionic strength, defined [Millero, 1982]; $I = 19.92 \cdot S / (10000 - 1005 \cdot S)$

$$[\text{H}^+] = \left([\text{H}^+]_1 \cdot [\text{H}^+]_2 \right)^{0.5} \quad (\text{I-23})$$

5. If the difference between new and old estimates of $[\text{H}^+]$ is greater than 0.1% (equivalent to an error in $f\text{CO}_2$ of 0.6 ppmv under typical oceanic conditions), steps #2 through #5 are repeated until an approximate convergence is obtained.

Pressure-dependence of system thermodynamics

Pressure correction of dissociation constants is carried out assuming a conversion between depth and pressure of 1 dbar m^{-1} . The error in this is no more than $\sim 3\%$, even at the deep ocean depths (10000 m). Corrections are applied to all of K_1 , K_2 , K_w , K_B , and K_{Si} . However, the influence on the carbonate system as a whole of pressure effects on the dissociation constants of HF and H_2SO_4 (used in converting between different pH scales) are insignificant, and as such are omitted. The general form of the pressure correction factor is [Millero, 1979]

$$\ln \left(\frac{K(P)}{K(0)} \right) = - \left(\frac{\Delta V}{RT} \right) \cdot P + \left(\frac{0.5 \cdot \Delta \kappa}{RT} \right) \cdot P^2 \quad (\text{I-24})$$

where P is the applied pressure in bars, T is the temperature ($^{\circ}\text{C}$), ΔV and $\Delta \kappa$ are the molar volume and compressibility change for the dissociation reactions, respectively, and R is the gas constant ($83.145 \text{ bar cm}^3 \text{ mol}^{-1} \text{ K}^{-1}$). For each dissociation reaction the values of ΔV and $\Delta \kappa$ in seawater are approximated as function only of temperature (assuming a salinity of 35‰) by

$$\Delta V = a_0 + a_1 \cdot T + a_2 \cdot T^2 \quad (\text{I-25})$$

$$10^3 \cdot \Delta \kappa = b_0 + b_1 \cdot T \quad (\text{I-26})$$

with the coefficients $a_0 \dots b_1$ given in Table I-2. There is no available relationship describing the effect of pressure on the dissociation of silicic acid. The same pressure effect as for boric acid is therefore assumed.

Table I-2 Coefficients for Describing Dissociation Constants as a Function of Pressure

Acid	a_0	a_1	a_2	b_0	b_1	Reference
H_2CO_3	-2.55E+01	+1.27E-01	+0.00E+00	-3.08E+00	+8.77E-02	Millero [1995]
HCO_3^-	-1.58E+01	-2.19E-02	+0.00E+00	+1.13E+00	-1.47E-01	Millero [1995]
H_3BO_3	-2.86E+01	+1.21E-01	-3.21E-04	-3.00E+00	+4.27E-02	Millero [1982]
H_2O	-2.00E+01	+1.12E-01	-1.41E-03	-5.13E+00	+7.49E-02	Millero [1982]
CaCO_3 (calcite)	-4.88E+01	+5.30E-01	+0.00E+00	-1.18E+01	+3.69E-01	Ingle [1975], Millero [1979]
CaCO_3 (aragonite)	-4.60E+01	+5.30E-01	+0.00E+00	-1.18E+01	+3.69E-01	Millero [1979]

Appendix II

Insolation

Light limitation of new production is parameterized in a similar manner to *Bacastow and Maier-Reimer* [1990], based on a normalized incident light factor, calculated from estimated solar elevation summed over each day [*Holtslag and van Ulden*, 1983]. However, no account is taken of the reduction of radiation incident at the ocean surface with increasing solar elevation due to reflectance at the air-sea interface.

Incoming solar radiation at the ocean surface assuming clear sky conditions, is given by

$$K = a_1 \cdot \sin \phi + a_2 \quad (\text{II-1})$$

where ϕ is the solar elevation, and a_1 and a_2 are empirical coefficients, taking values of 1041 and -69 W m^{-2} , respectively [*Holtslag and van Ulden*, 1983]. Solar elevation follows *Holtslag and van Ulden* [1983];

$$\sin \phi = \sin \delta \cdot \sin \psi + \cos \delta \cdot \cos \psi \cdot \cos h \quad (\text{II-2})$$

where ψ is the latitude of the location (radians), δ the solar declination

$$\delta = \arcsin(0.398 \cdot \sin(SL)) \quad (\text{II-3})$$

where SL is the solar longitude

$$SL = 4.871 + 0.0175 \cdot d + 0.033 \cdot \sin(0.0175 \cdot d) \quad (\text{II-4})$$

with d , is the day number. Finally, h , the hour angle is described by

$$h = -\lambda_w + 0.043 \cdot \sin(2 \cdot SL) - 0.033 \cdot \sin(0.0175 \cdot d) + 0.262 \cdot t - \pi \quad (\text{II-5})$$

where λ_w is the western longitude (radians) of the location and t is the universal time (hours).

For each time step in the biological scheme (Δt), the reduction in new production due to sub-optimal insolation is calculated by

$$I_{t,lat} = \sum_{t-\Delta t/2}^{t+\Delta t/2} H(K_{t,lat}) \quad (\text{II-6})$$

where the mean hourly insolation is summed over the length of the new production time step at the mean latitude of each grid point, and H is the Heavyside function. I is then normalized to a value of unity at the time and location of maximum calculated insolation on Earth to give $\mu_{(t)}$. No account is taken of past variations in the Earth's orbital parameters.

Appendix III

Opal diagenesis core data

Core ID	opal (wt%)	CaCO ₃ (wt%)	opal rain rate ($\mu\text{mol cm}^{-2} \text{ a}^{-1}$)	opal burial rate ($\mu\text{mol cm}^{-2} \text{ a}^{-1}$)	opal dissolution rate ($\mu\text{mol cm}^{-2} \text{ a}^{-1}$)	opal preservation (%)	[H ₄ SiO ₄] _{diagen} ($\mu\text{mol kg}^{-1}$)	Reference
HAP	3	21	6	4.32 ¹	1.68 ¹	72		1
NAP	0	6	4	0.04 ¹	3.96 ¹	1		1
E	2	28	5					1
MFZ	3	2	11	1.21 ¹	9.79 ¹	11		1
ER	9	46	9					1
NS	10	9	44	8.80 ¹	35.20 ¹	20		1
MW	6	1	14	1.96 ¹	12.04 ¹	14		1
G	3	25	5	0.20 ¹	4.80 ¹	4		1
H	15	1	7	0.28 ¹	6.72 ¹	4		1
M	11	15	12	0.48 ¹	11.52 ¹	4		1
S	16	1	3	0.03 ¹	2.97 ¹	1		1
C	13	75	11	1.10 ¹	10.90 ¹	10		1
EP1	0	9	2					1
PB	7	22	31					1
T9	3.2	6.8						2
T12	6.3	8.4						2
T16	6.4	11.9						2
T31	9.1	16.4						2
T36	12.2	20.3						2
T42	9.6	20.3						2
T47	15.2	17.8						2
T62	13.7	10.7						2
T68	11.4	10.7						2
T69	20.7	12.9						2
T89	17.2	7.0						2
T92	17.9	14.7						2

References: 1, *Archer et al.* [1993]; 2, *Martin et al.* [1991]; 3, *McManus et al.* [1995].

¹ Calculated from published opal rain rates and percentage opal preservation.

² Estimated from similarly located cores.

Core ID	opal (wt%)	CaCO ₃ (wt%)	opal rain rate ($\mu\text{mol cm}^{-2} \text{ a}^{-1}$)	opal burial rate ($\mu\text{mol cm}^{-2} \text{ a}^{-1}$)	opal dissolution rate ($\mu\text{mol cm}^{-2} \text{ a}^{-1}$)	opal preservation (%)	[H ₄ SiO ₄] _{asym} ($\mu\text{mol kg}^{-1}$)	Reference
04-12S		~70 ²			1.8		266	3
10-12S		~70 ²			2.9		241	3
34-05S		~74 ²			8.4		407	3
39-05S		~74 ²			8.8		424	3
27-03S	3.3	~84 ²			12.8		492	3
19-02S		~84 ²			14.2		542	3
23-02S	7.0	~84 ²			11.3		521	3
48-00		~80 ²			14.6		537	3
58-00		~80 ²			17.5		564	3
77-02N		~80 ²			16.8		530	3
82-02N	9.7	~80 ²			19.0		543	3
113-04N	8.2	~80 ²			9.5		404	3
104-05N	5.5	~60 ²			9.5		398	3
108-05N		~60 ²			7.3		419	3
132-09N	11.0	~0 ²			3.3		282	3
135-09N		~0 ²			3.3		309	3
Z-9		~58 ²			18.3		508	3
X-5		~50 ²			17.2		474	3
W-3		~80 ²			24.5		546	3
PFC	7.8	~76 ²			11.3		461	3
PFSC	9.6	~65 ²			5.1		415	3
PFS	10.8	~0 ²			21.6		582	3

Appendix IV

Model parameter values (baseline scenario)

Parameter Description	Symbol (where applicable)	Equation number (where applicable)	Value
Model time step: primary (ocean-sediment) interactions	-	-	1 year
Model time step: intra-ocean and ocean-atmosphere interactions	-	-	1 month
Model time step: biological uptake and export	-	-	1 day
Horizontal eddy diffusivity	-	-	$200.0 \times 10^6 \text{ cm}^2 \text{ s}^{-1}$
Minimum (at surface) vertical eddy diffusivity	-	-	$0.33 \text{ cm}^2 \text{ s}^{-1}$
Maximum (at depth) vertical eddy diffusivity	-	-	$1.25 \text{ cm}^2 \text{ s}^{-1}$
Depth of the euphotic zone	D_{euph}	2-14a, 2-14b	47 m
PO ₄ uptake rate Q ₁₀ temperature dependency (SP)	Q ₁₀	2-9, 2-10	1.88
PO ₄ uptake rate Q ₁₀ temperature dependency (NSP)	Q ₁₀	2-9, 2-10	1.88
Base PO ₄ uptake rate (SP)	$u_{\text{SP}}^{\text{PO}_4}$	2-8a	$5.0 \mu\text{mol kg}^{-1} \text{ a}^{-1}$
Base PO ₄ uptake rate (NSP)	$u_{\text{NSP}}^{\text{PO}_4}$	2-8b	$0.25 \mu\text{mol kg}^{-1} \text{ a}^{-1}$
PO ₄ half-saturation constant (SP)	$K_{\text{S,SP}}^{\text{PO}_4}$	2-11	$0.1 \mu\text{mol kg}^{-1}$
H ₄ SiO ₄ half-saturation constant (SP)	$K_{\text{S,SP}}^{\text{H}_4\text{SiO}_4}$	2-12	$4.0 \mu\text{mol kg}^{-1}$
Fe half-saturation constant (SP)	$K_{\text{S,SP}}^{\text{Fe}}$	2-13	$0.125 \text{ nmol kg}^{-1}$
PO ₄ half-saturation constant (NSP)	$K_{\text{S,NSP}}^{\text{PO}_4}$	-	$0.05 \mu\text{mol kg}^{-1}$
Fe half-saturation constant (NSP)	$K_{\text{S,NSP}}^{\text{Fe}}$	-	$0.068 \text{ nmol kg}^{-1}$
Particulate organic matter export partition coefficient (SP)	λ_{SP}	2-16a	1.0
Particulate organic matter export partition coefficient (NSP)	λ_{NSP}	2-16b	1.0
Particulate organic matter N:P export ratio (SP)	$r_{\text{SP}}^{\text{PON:POP}}$	2-18	16
Particulate organic matter C:P export ratio (SP)	$r_{\text{SP}}^{\text{POC:POP}}$	2-17	106
Particulate organic matter O ₂ :P export ratio (SP)	-	-	177
Opal:POC export ratio value under Fe-replete conditions (SP)	$r_{\text{0,SP}}^{\text{opal:POC}}$	2-26	0.175
Opal:POC export ratio function [Fe] half-saturation constant	K_{S}^{Fe}	2-26	$0.25 \text{ nmol kg}^{-1}$
Opal:POC export ratio function [Fe] off-set	$[\text{Fe}]_{\text{off}}$	2-26	$0.125 \text{ nmol kg}^{-1}$
Particulate organic matter N:P export ratio (NSP)	$r_{\text{NSP}}^{\text{PON:POP}}$	2-22	16
Particulate organic matter C:P export ratio (NSP)	$r_{\text{NSP}}^{\text{POC:POP}}$	2-21	106
Particulate organic matter O ₂ :P export ratio (NSP)	-	-	177
CaCO ₃ :POC export ratio (NSP)	$r_{\text{NSP}}^{\text{CaCO}_3:\text{POC}}$	2-22	0.3
Base POM remineralization depth	z_0	2-28a, 2-28b	97 m
Base calcite remineralization depth	z_0	2-29a, 2-29b	97 m
Opal settling velocity	-	2-35	125 m s^{-1}
Opal water-column base dissolution rate constant	k_0^{opal}	2-33	0.019 d^{-1}
Minimum allowed oceanic O ₂ concentration	-	-	$25.0 \mu\text{mol kg}^{-1}$
Fe scavenging rate: by POC	$k_{\text{scav}}^{\text{Fe}}_{\text{POC}}$	2-38	$0.0025 \text{ a}^{-1} (\text{mol C m}^{-2} \text{ a}^{-1})^{-1}$
Fe scavenging rate: by opal	$k_{\text{scav}}^{\text{Fe}}_{\text{opal}}$	2-38	$0.00025 \text{ a}^{-1} (\text{mol C m}^{-2} \text{ a}^{-1})^{-1}$
Fe scavenging rate: by calcite	$k_{\text{scav}}^{\text{Fe}}_{\text{cal}}$	2-38	$0.00025 \text{ a}^{-1} (\text{mol C m}^{-2} \text{ a}^{-1})^{-1}$
Fe scavenging rate: by aragonite	$k_{\text{scav}}^{\text{Fe}}_{\text{arg}}$	2-38	$0.00025 \text{ a}^{-1} (\text{mol C m}^{-2} \text{ a}^{-1})^{-1}$
Fe 'self-scavenging' rate (by dust)	$k_{\text{scav}}^{\text{Fe}}_{\text{dust}}$	2-43	$0.0750 \text{ a}^{-1} (\text{mol C m}^{-2} \text{ a}^{-1})^{-1}$
Fe abundance in dust	$Fe_{\text{frac}}^{\text{dust}}$	2-43	3.5%

Parameter Description	Symbol (where applicable)	Equation number (where applicable)	Value
Enzymic ¹³ C fraction factor (SP)	ϵ_f	2-56, 2-58	25‰
Enzymic ¹³ C fraction factor (NSP)	ϵ_f	2-56, 2-58	20‰
CO _{2(aq)} diffusion ¹³ C fraction factor	ϵ_d	2-56, 2-58	0.7‰
CO _{2(aq)} uptake rate per cell surface area	Q_s	2-56, 2-59	$1.62 \times 10^{-7} \text{ mol C m}^{-2} \text{ s}^{-1}$
Surface area equivalent cell radius	r	2-56, 2-59	$5.0 \times 10^{-5} \text{ m}$
Reacto-diffusive length	r_k	2-56, 2-59	$2.06 \times 10^{-4} \text{ m}$
Cell wall permeability to CO _{2(aq)}	P	2-56, 2-59	10^{-4} m s^{-1}
Activation energy of diffusion	E_d	2-57	19510 J mol^{-1}
Prescribed POC sedimentary preservation efficiency	-	-	5%
Prescribed additional sedimentary rain flux of detrital material	-	-	$0.167 \text{ g cm}^{-2} \text{ ka}^{-1}$
Thickness of 'well mixed' surface sediment layer	-	-	5 cm
Porosity of 'well mixed' surface sediment layer	ϕ	3-4	$0.776 \text{ cm}^3 \text{ cm}^{-3}$
Thickness of (complete) sedimentary stack layers	-	-	1 cm
Porosity of sedimentary stack	ϕ	3-4	$0.705 \text{ cm}^3 \text{ cm}^{-3}$
Bioturbation rate at top of sedimentary stack	-	-	$120 \text{ cm}^2 \text{ ka}^{-1}$
Calcite dissolution rate constant	-	-	$20 \% \text{ d}^{-1}$
Calcite dissolution power	-	-	4.5
Aragonite dissolution rate constant	-	-	$20 \% \text{ d}^{-1}$
Aragonite dissolution power	-	-	4.2
Riverine input of carbon	-	-	15 Tmol a^{-1}
¹³ C isotopic signature of riverine carbon	-	-	3.1‰
Volcanic input of carbon	-	-	5 Tmol a^{-1}
¹³ C isotopic signature of volcanic carbon	-	-	3.1‰
Riverine input of alkalinity	-	-	$40 \text{ Tmol eq a}^{-1}$
Total input of dissolved silica	-	-	6 Tmol a^{-1}
Accumulation rate of neritic CaCO ₃	-	-	10 Tmol a^{-1}
¹³ C isotopic signature of neritic CaCO ₃	-	-	3.1‰